CHARACTERIZATION OF THE SPATIAL DISTRIBUTION OF THE ELECTRIC FIELD STRENGTH IN INDOOR PROPAGATION AT 2.45 GHz

TIAGO FREIRE CARNEIRO LEAO

A THESIS
IN
THE DEPARTMENT
OF
ELECTRICAL AND COMPUTER ENGINEERING

PRESENTED IN PARTIAL FULFILLMENT OF THE REQUIREMENTS
FOR THE DEGREE OF DOCTOR OF PHILOSOPHY
CONCORDIA UNIVERSITY
MONTREAL, QUEBEC, CANADA

JUNE 2014

CONCORDIA UNIVERSITY
SCHOOL OF GRADUATE STUDIES

This is to certify that the thesis prepared

By: Tiago Freire Carneiro Leao

Entitled: Characterization of the Spatial Distribution of the Electric Field Strength in Indoor Propagation at 2.45 GHz

and submitted in partial fulfillment of the requirements for the degree of

Doctor of Philosophy (Electrical & Computer Engineering)

complies with the regulations of the University and meets the accepted standards with respect to originality and quality.

Signed by the final examining committee:

_____ Chair
Dr. G. Grahne

_____ External Examiner
Dr. M.J. Neve

_____ External to Program
Dr. R. Ganesan

_____ Examiner
Dr. R. Paknys

_____ Examiner
Dr. A.R. Sebak

_____ Thesis Supervisor
Dr. C.W. Trueman

Approved by: _____
Dr. A.R. Sebak, Graduate Program Director

June 26, 2014

_____
Dr. C.W. Trueman, Interim Dean
Faculty of Engineering & Computer Science

Abstract

Characterization of the Spatial Distribution of the Electric Field Strength in Indoor Propagation at 2.45 GHz

Tiago Freire Carneiro Leao, Ph.D

Concordia University, 2014

Small-scale spatial variations of the electric field strength or "fast fading" are encountered in indoor environments, and are of particular concern for indoor wireless communication applications as well as for electromagnetic compatibility assessment. This thesis is motivated by the problem of electromagnetic interference with a critical-care medical equipment caused by fields radiated by portable electronic devices such as cell phones and tablet computers. Measurement and computer simulation of the electric field strength, in both controlled and real-world scenarios, are explored to estimate parameter values of statistical models for the fast fading in a region of interest inside a building.

First, a method for measuring the dielectric constant of wall construction materials is developed for two reasons: little information available on electrical properties of such

materials in the frequency range of interest, 2.4 GHz ISM band, and variations in material properties caused by different manufacturing processes employed by different manufacturers. The proposed technique, referred to as the parallel-path method, falls into the category of free-space methods and is shown to be more sensitive to the dielectric constant than free-space methods based on normal incidence only.

Having determined the dielectric constant of gyproc slabs and of a wooden door, a controlled multipath environment is built inside an anechoic chamber. Two line-of-sight and a non-line-of-sight scenarios, each with about 4000 measurement points, are studied. We apply the Friedman's goodness-of-fit test at 5% significance level to show that a ray-tracing technique based only on 3D geometrical optics is suitable for estimating the fast fading of the electromagnetic field at 2.45 GHz in a very controlled situation. Then the Anderson-Darling goodness-of-fit test, also at 5% significance level, is applied to show that in the vicinity of a transmitter the Ricean, Normal, Nakagami, and Weibull distributions can be equivalently used to represent the spatial fast fading for both line and non-line-of-sight scenarios. Furthermore, the effects of metal studs are shown to worsen not only point-by-point agreement between measurement and GO simulation, but also the agreement on the statistics of the fast fading in a 65 by 65 cm region.

Another aspect of this thesis is the development of a new method for estimating the parameters of the Ricean probability density function. This new method is compared to the maximum-likelihood method, and is shown to provide accurate estimates with samples containing as few as 36 data points for regions within 2 m from a transmitter,

and as few as 9 data points for regions farther away. This is a considerable improvement in term of computation time when compared to estimates based on approximately 4000 points, or even 200 data points. Together with GO simulations, this method reduces the initial and elaborated measurement approach to only a few simulated points and a statistical model.

Finally, this methodology is extended and applied to real-world scenarios such as a long hallway and a conventional laboratory room. The agreement between measurement and GO simulation is not as good as that of the experiment conducted in a shielded anechoic chamber, but it is still reasonable, especially because the interior structures of walls such as metal studs are not modeled by the GO code. As for the statistical models used to describe the electric field strength variation in a region, it is shown that the Ricean, Normal, Nakagami, and the Weibull distributions can be employed. However, for the data collected in this work, the Normal distribution is the one that results in the worst fit to measured data for most of the cases. It is demonstrated that, even though diffracted rays are not taken into account, GO simulation allows for an accurate estimation of the parameters of a statistical model for the fast fading, for both controlled and most real-world scenarios, provided that the site geometry and electrical properties of walls, floor, and ceiling are known.

Acknowledgments

I would like to express my sincere gratitude to my supervisor Dr. Christopher W. Trueman for providing me with this incredible opportunity, from which I have learned so much. I deeply appreciate his guidance and encouragement. Without his contribution, sound advice, and support this work would not have been completed.

I would also like to thank Mr. Vincent Mooney Chopin for his friendship and fundamental participation in the design and development of the measurement system. Without his hard work and efforts towards the implementation of the measurement system, this work would not have been possible. Further, I would like to thank Mr. Dmitry Rozhdestvenskiy and Mr. Jeffrey Landry for their technical guidance and many helpful suggestions regarding the development of the measurement system.

I have enjoyed to a great extent my experience as a teaching assistant throughout my program. On this front, I would like to thank my friends Donald Davis and Ted Obuchowicz for encouraging and providing me with opportunities to develop my teaching skills.

I would like to thank my friends Ayman Elboushi and Zouhair Briqech for their friendship and support over the years. Further, I would like to thank all my friends from Space Concordia.

I would like to express a special thanks to Dr. Sergio Muhlen for having introduced me to Dr. Trueman and encouraged me to come to Canada to pursue my PhD degree.

Finally, I wish to thank my wife and best friend for all the moral support and dedication, over the past 15 years, to help me fulfill my dreams in this life. It has been a long journey and I could not have wished for a better person to share my life with. Carolina, I love you!

The work undertaken in this thesis was funded by the Natural Sciences and Engineering Research Council of Canada (NSERC) and the National Council for Technological and Scientific Development (CNPq), Brazil.

Table of Contents

List of Figures

List of Tables

List of Abbreviations

2D – Two-dimensional

3D – Three-dimensional

AD – Anderson-Darling

ADC – Analog-to-digital converter

ANSI – American National Standards Institute

CDF – Cumulative distribution function

CDMA – Code division multiple access

CW – Continuous wave

ECG - Electrocardiography

ED – Emergency department

EEG – Electroencephalography

EMI – Electromagnetic interference

FDTD – Finite-Difference Time Domain

FEM – Finite element method

FFT – Fast Fourier transform

GF/MoM – Green's function/method of moments

GO – Geometrical optics

GO/UTD – Geometrical optics/ uniform theory of diffraction

GPRS – General packet radio service

GSM – Global system for mobile communication

GTD – Geometrical theory of diffraction

HFSS – High frequency structural simulator

ICU – Intense care unit

IEC – International electrotechnical commission

IFFT – Inverse fast Fourier transform

LED – Light-emitting diode

LOS – Line of sight

LTI – Linear time-invariant

MLE – Maximum likelihood estimation method

MM – Moment method

MoM – Method of moments

MoM/GO – Method of moments/geometrical optics

MoM/PO – Method of moments/ physical optics

MoM/UTD – Method of moments/ uniform theory of diffraction

MS – Minimum separation

NLOS – Non line of sight

OR – Operation room

PCS – Personal Communications Services

PDF – Probability density function

PMM – Periodic moment method

RF – Radio frequency

RMS – Root mean square

RMSE – Root-mean-square error

RT – Ray tracing

Rx – Receiver

SD – Secure digital

SIE/MoM – Surface integral equation/method of moments

SNR – Signal-to-noise ratio

SWR – Standing-wave ratio

TDMA – Time division multiple access

Tx - Transmitter

UMTS – Universal mobile telecommunications system

UTD – Uniform theory of diffraction

UWB – Ultrawideband

WLAN – Wireless local area network

Chapter 1: Introduction

This chapter describes the motivation for this research project, the research hypothesis, and the objectives of this thesis. Then we present the outline of the remaining chapters, followed by a description of the contributions of this work.

1.1 Motivation and Research Hypothesis

The motivation for this work is the problem of electromagnetic interference in critical-care medical equipment caused by electromagnetic waves radiated by mobile communication devices. An important aspect of any possible solution for this problem is the understanding of the mechanisms of propagation of radio waves in an indoor environment. Consequently, this research is focused on indoor propagation, more precisely, on the study of the spatial distribution of the electric field strength. We aim to measure, model, and statistically characterize the small scale spatial variation or "fast fading" of the electric field strength in indoor environments.

Our hypothesis is that statistical models for an accurate characterization of the spatial variation of the electric field can be applied to the underlying problem, namely that of estimating the risk of exceeding immunity of medical devices. Our hope is that the work on propagation modeling, electromagnetic characterization of construction walls and internal metal studs, and the statistical approach based on the Ricean distribution and geometrical optics presented in this thesis will lead to minimization of the risk of electromagnetic interference, for instance, by helping engineers better design wireless

networks in hospitals. Furthermore, we hope that this work will serve as a basis for more complex indoor propagation modeling.

It should be noted that the scientific methodology and investigation approach adopted in this thesis, as well as its conclusions, are not restricted to the problem of electromagnetic interference in critical-care medical equipment. The same principles can be applied to the field of wireless communication and channel characterization. The Ricean probability distribution is widely used in wireless communications to calculate the probability that the field strength is above a minimum threshold value, and to estimate the amount of co-channel interference expected when frequency re-use is used in wireless local area network (WLAN) systems.

1.2 Objectives

The broad aim of this work is to study the behavior of radio waves in indoor environments by means of measurement, geometrical optics simulation, Sabine method simulation, and statistical analysis of the electric field strength distribution. With this in mind, we define the following objectives:

1. Design and build an automated measurement system capable of accurately positioning the detection antenna at the desired location and sampling electric field strength. The system must be able to take measurements along a 20-m straight path and over a 65 by 65 cm horizontal region. At 2.45 GHz the 20-m path is approximately 163 wavelengths and the horizontal region is 5 by 5

wavelengths. The separation between data points should be defined by the user and be 1 cm or larger. This would allow us to study the spatial distribution of the electric field strength by straight line path measurements and by measurements over an area.

2. Study reflection and transmission properties of wall constructions and doors. A typical wall construction is comprised of two gyproc panels separated by an air layer with metal studs. We apply geometrical optics to the characterization of layered structures for indoor propagation applications.
3. Evaluate the effect of metal studs in between drywall (gyproc) panels on the net electric field strength and its statistics.
4. Evaluate the accuracy of the geometrical-optics indoor propagation models at 2.45 GHz.
5. Identify statistical models for fast fading in indoor environments, and evaluate their applicability.
6. Study the effect of the sample size and data point separation on the accuracy of the estimate of the statistics of the fast fading.
7. Develop a simple and accurate method for estimating the parameters of the Ricean probability distribution based on a minimum number of calculated or measured field samples, which works for regions both close and well separated from the transmitter.

1.3 Thesis Outline

Chapter 2 is the literature review and provides a summary of the physics of indoor propagation. It includes a review on electromagnetic interference of wireless devices with medical equipment in order to show evidence of the problem. Moreover, it presents descriptions of several techniques for field measurements in indoor environments. Computational models to predict electric field strength in indoor environments are reviewed, as well as statistical distributions commonly used to model the fast fading. We also briefly describe the maximum likelihood method and the moment method, which are techniques for estimating the parameters of a distribution from a set of samples of data. Finally, we summarize the Anderson-Darling goodness-of-fit test which is used to assess the extent to which a statistical model agrees with the observed data.

Chapter 3 describes the automated measurement system that was developed for this project. It moves a probe along a 20-m path or over a 65 by 65 cm grid in accurate steps of 1 cm or larger.

Chapter 4 presents a new method, called parallel-path method, for measuring the dielectric constant of construction materials used to build walls and building structures.

Chapter 5 describes and presents the results of experiments conducted in a shielded controlled environment, where different scenarios were built and used to validate the geometrical optics model used throughout this research work.

Chapter 6 contains the statistical analysis of the fast fading of the field for the area experiments conducted in a shielded anechoic chamber. The Anderson-Darling goodness-of-fit test is used to compare the best fits to the measured data, based on the maximum likelihood estimation method and the Ricean, Normal, Nakagami, and Weibull distributions.

Chapter 7 presents the proposed Ricean parameter estimation method and compares its performance to those of the maximum likelihood method and moment method. We show excellent agreement between measurement and predictions made with geometrical optics simulation.

Chapter 8 presents a study made in a real indoor scenario: a hallway on the 15th floor of the EV Building at Concordia University.

Chapter 9 provides a study similar to the one described in Chapter 8, but in a conventional laboratory room instead. The geometry and type of walls of this particular room are drastically different from those of the corridor. Besides, this laboratory room has several features, such as furniture and lab equipment on the workbenches, which are not present in the hallway experiment.

Chapter 10 provides the conclusions of this thesis. We summarize our contributions and examine the strong and limited aspects of our techniques, including recommendations for future work.

1.4 Contributions

We developed a versatile and complete automated measurement system which can be used in extensive electric field strength measurement campaigns and easily modified to add new functionalities.

We took measurements of electric field strength over a horizontal region of approximately 5 by 5 wavelengths in size for a dense grid of points separated by 1 cm. This allowed us to obtain excellent correspondence between measurement and geometrical optics simulation in experiments conducted in a shielded anechoic chamber, as well as reasonable correspondence of the statistics of fast fading obtained by measurement and geometrical optics simulation for real indoor environments.

We demonstrated by applying the Anderson-Darling goodness-of-fit test that, for all type of indoor environment considered in this research work, the distribution of the electric field strength can be successfully modeled with the following statistical distributions: Ricean, Normal, Nakagami, and Weibull. Nevertheless, for the majority of regions considered, the Normal models were the ones that consistently resulted in the worst fit to the measured data, even though the models were shown not to be statistically different from measured data. The Ricean, Nakagami, and Weibull all represent the data equally well for 100 % of the cases.

We demonstrated that accurate predictions of the electric field strength with geometrical optics only is not sufficient to capture the fields scattered by metal studs, not even the

statistics of the fast fading in regions close to walls containing studs. It is clear that to improve point-by-point agreement between measurement and simulation, metal studs must be accounted for in the model. However, when the angle of incidence on the wall approaches grazing, only a small fraction of the incident field strength makes its way to the studs, and then geometrical optics starts to provide accurate results even for real indoor environments.

We described a new method for estimating the parameters of the Ricean probability distribution based on the spatial variation of the field. This method presents comparable performance to the maximum likelihood method and moment method, and is straightforward and easier to implement. We also showed that it can be used with a sample containing as few as 36 field strength observations evenly spaced across a 65 by 65 cm region. In other words, we recommend to use the new method with a sample whose points are separated by a wavelength.

We demonstrated that useful information can be obtained from indoor propagation studies based on geometrical optics simulation, especially when a prediction of the slow fading is desired. Moreover, the Sabine method was shown to be extremely good and efficient to predict the slow fading or mean electric field strength in real indoor environments, and that it can be applied to accurately estimate the path loss exponent.

Finally, we described a new method for measuring the dielectric constant of construction materials. The automated measurement system was fundamental for this method to be feasible, which demonstrated its versatility. This method is based on electric field

strength measurements along a path parallel to the surface of the material under test, and takes advantage of the sensitivity of the reflection coefficient to the angle of incidence. It was proven to be more accurate than free-space methods based on normal incidence only.

In the next chapter, we provide a review on the theory and main techniques used to investigate indoor propagation. The chapter begins with a summary of studies reporting problems in the operation of critical-care medical equipment caused by electromagnetic interference with mobile communication devices.

Chapter 2: Literature Review

In this chapter, a summary of what has been published in the field of indoor radio propagation and electromagnetic compatibility of medical equipment over the past few years is provided. This includes the motivation of this work, and a description of the mechanisms of propagation, measurement techniques, simulation tools, and statistical models and tests used in the study of indoor propagation.

2.1 Electromagnetic Interference in Critical-Care Medical Equipment

Electromagnetic interference (EMI), a harmful effect on the performance of an electrical circuit caused by its exposure to electromagnetic radiation, has been verified to cause a significant number of medical devices to malfunction, imposing health hazards to patients who depend on life-supporting equipment. Many studies have not only shown an increasing number of wireless devices such as wireless local area networks (WLANs) being installed in hospitals, and of personnel hand-held wireless transmitters used by medical staff; but also presented alarming results concerning the critical-care devices' immunity level being exceeded by the electric field strength emitted by such devices [1], [2], [3], [4].

Many standards, such as the International Electrotechnical Commission (IEC) 60601-1-2 and the American National Standards Institute (ANSI) C63.18-1997, present guidelines and recommendation of standardized immunity level tests in attempt to guarantee patient's safety [5], [6]. These standards rely on a criterion based on maintaining a

physical separation between the radiofrequency (RF) transmitter and the medical device, known as minimum separation (MS). However, Davis *et al.* in [7], [8], and [9], have demonstrated that this criterion is not valid in various indoor scenarios commonly encountered in a hospital, since the free-space propagation, which is assumed by this criterion, is invalid due to the presence of many reflective surfaces such as walls, furniture, and obstructing objects.

This indicates that it is necessary to conduct further research on propagation mechanisms of the radio waves in hospitals, especially in corridors. Furthermore, the knowledge of the electromagnetic field distribution in hospital corridors, patient rooms, or intensive care units, is of great importance so as to minimize the risk of EMI by means of a better design of the placement of both medical equipment and sources of electromagnetic radiation. According to Tan *et al.* in [1], the risk of EMI depends on

- the distance from the radiation source to the medical device;
- the distance at which the wireless hand-held device is from the base station or access point, since it determines the power output of the hand-held device;
- the operating frequency of the wireless device;
- the transmitting time (some cases);
- the shielding of the medical device and cables.

In addition, after testing 106 medical devices to assess their susceptibility to EMI from two WLAN systems operating at 2.42 GHz and one medical telemetry system operating at 466 MHz, random static noise was observed in hand-held Doppler units placed within

10 cm of WLAN system. In general, it was concluded that the low electric field emitted by these devices does not cause EMI in medical devices, especially at 466 MHz [1]. In contrast, Tang *et al.* in [2], observed EMI to occur at field strengths as low as 0.02 V/m in a study regarding cell phones. Their results can be seen in Table 2.1.

Table.2.1: EMI caused by second- and Third-Generation Mobile Phones *[2]*.

Type of equipment	**Abnormal response**	**Measured E-field**
ECG Monitor	Noise is generated inside the equipment. Waveform of the ECG signal shown on the monitor is distorted.	0.266
Mobile radiographic/ fluoroscopic unit	Image distortion on the monitor.	GSM 900 1.69 V/m PCS 1800 0.02 V/m
Audio evoked potential system	Abnormal pulse shown on monitor. Input EEG signal are affected, and system indicated "rejected".	GSM 900 10 V/m PCS 1800 5.4 V/m
Wireless ECG monitor system	Noise is generated inside the equipment.	GSM 900 0.0062 V/m PCS 1800 0.501 V/m
Wireless ECG monitor	Noise is generated inside the equipment. Waveform of the ECG signal is distorted.	GSM 900 0.71 V/m PCS 1800 0.67 V/m
Ultrasonic fetal heart detector A	Noise is generated from the speaker.	GSM 900 0.012 V/m PCS 1800 0.2 V/m
Ultrasonic fetal heart detector B	Noise is generated from the speaker.	GSM 900 0.63 V/m PCS 1800 0.35 V/m 3G 0.006 V/m

Ultrasonic fetal heart detector C	Noise is generated from the speaker.	GSM 900 0.0004 V/m PCS 1800 0.23 V/m
Ultrasonic fetal heart detector D	Noise is generated	GSM 900 0.14 V/m PCS 1800 0.6 V/m

As can be seen, these values are astonishingly lower than the typical critical-care devices' immunity levels reported in the literature, supporting the evidence that the indiscriminate use of wireless devices for communication in certain areas of a hospital poses serious health hazards to patients. Table 2.2 summarizes the typical immunity levels of critical-care devices [10].

Typical transmitters used for wireless communications are paging transmitters, mobile radios, hand-held transceivers, WLANs, personal digital assistants, and radio modems. The frequency range at which these transmitters operate goes from 49 to 5800 MHz. The maximum output power radiated by a WLAN is about 100 mW which corresponds to an electric field strength of 2.2 V/m at 1 m from the source [6] with the directivity of a half-wave dipole antenna of 1.64. When comparing the latter with the immunity levels in Tables 2.1 and 2.2, the problem becomes evident, since the electric field strength created by most wireless devices can reach levels above the typical immunity level of critical-care medical equipment.

Table 2.2: Typical values of medical devices' immunity level.

EQUIPMENT	FREQ. RANGE	IMMUNITY LEVEL	COMMENTS – failure
570 Infusion Pump	30 – 150 MHz	9.8 V/m	Spurious generation of the FIX ME error code.
LP6 Plus Ventilator	150 – 1000 MHz	5.8 V/m	Spurious illumination of the breathing effort warning light.
Lifepak-6S Defibrillator with ECG Monitor	30 – 350 MHz	3 V/m	A keyed radiated electric field of 0.9 V/m shifted the baseline of the device's ECG monitor.
N-200 Pulse oximeter	7.5 – 600 MHz	1.6 V/m	
C100 Infant Incubator	30 – 2000 MHz	0.2 V/m	Erroneous temperature readings and spurious operation of internal heater.
Bear 5 Ventilator	30 – 1000 MHz	0.9 V/m	Spurious activation of the humidifier alarm, interference with several of the main readouts, and stopped the ventilator.
HP 78534B Physio. Monitor	7.5 – 350 MHz	1.1 V/m	Spurious operation of alarms.

Chimeno *et al.* in [3] present a review of published works on the effect of electromagnetic interferences caused by mobile phones on both medical equipment placed in critical hospital areas and implantable devices. Their conclusions are the following. As for the implantable devices, the EMI caused by mobile phones are not severe, but a safety distance must be kept. As for the medical equipment placed in critical areas, EMI occurs more frequently than in the case of pacemakers. It is also mentioned that the conclusions are not clear as to whether or not the mobile phones should be used in critical areas, which means that after all these years of research, this question remains unanswered. The authors recommended the development of clearer policies for the use of

wireless devices in intense care units (ICU), in operating rooms (OR) and in emergency departments (ED). Yet, the most important comment was that the development of such a policy is only possible if the electromagnetic environments in these areas are reliably characterized for each particular case. Table 2.3 presents a summary of studies on EMI caused by wireless devices in medical equipment placed in critical areas of a hospital.

Table 2.3: Summary of studies on EMI caused by mobile phones in medical equipment *[3]*.

Reference (year)	**Telephone frequency band**	**Mean distance where EMI occurs (cm)**	**# equipment Malfunctions**
Lieshout (2007)	GPRS/UMTS 900-1947,2 MHz	3	26 of 61 (43%)
Hans (2009)	GSM/CDMA bands	30.5	2 of 3 (66%)
Tri (2005)	CDMA/GSM/ TDMA/ANALOGUE	3.2	7 of 16 (44%)
Tang (2009)	GSM900/PCS1800/ 3G	328	18 of 532 (33%)
Dang (2007)	GSM/TDMA	50	1 of 7 (14.3%)
Shaw (2004)	GSM	15	6 of 14 (43%)
Jones (2005)	GSM	100	5 of 5 (100%)
Calcagnini (2008)	GSM/DECT/WiFi	9.1	5 of 17 (30%)

In summary, wireless technology has become more and more attractive to hospitals partly due to its capacity of providing physicians with instant information on patients, and to the benefit of reducing the amount of paper files and physical space to store the information. However, this technology transmits information wirelessly by means of electromagnetic radiation created by an access point and detected by the user's handheld. Therefore, it is important to investigate how this technology, or rather, the electromagnetic radiation affects the existing medical equipment in a hospital.

It is generally agreed that part of the solution to this problem relies on a better understanding of radio wave propagation in indoor environments. For this reason, this thesis addresses some of the important issues in electromagnetic propagation and channel characterization, by investigating the electric field strength spatial distribution – fast fading – in corridors and laboratory rooms at 2.45 GHz, as well as the influence of walls and their internal structures, more precisely periodic metal studs, on the field statistics.

2.2 Propagation in Indoor Environments

The use of wireless devices for data or voice communication in the context of indoor environments such as office buildings, warehouses, factories, convention centers, apartment buildings, and hospitals has become more and more popular over the past few years [7], [11], [12], [13]. Power distributed over a volume is an essential requirement for reliable communication. In a typical indoor wireless system a fixed antenna called an "access point" or "base station" communicates with a number of users' handhelds (forward link) inside the site in question. In the context of EMI in medical equipment, the

radiation from the user's tablet or smartphone (reverse link) is more likely to be important given that these are more likely to be much closer to a medical device than access points. Due to reflection, refraction and scattering of radio waves by structures present in the environment, the transmitted signal most often reaches a specific point, the receiver, by more than one path, with different amplitudes, phases, and time delays; resulting in multipath fading, also known as multipath interference [7], [11], [12], [14], [15].

The signal contributions arriving from the direct path and from the indirect paths combine vectorially and produce a distorted version of the transmitted signal. Due to the interference caused by the multipath contribution, not only the mean power is important, but also the statistical distribution of the electric field strength. The multipath interference creates small regions of intense electrical field strength and small region of weak electric field strength within any indoor environment, which may seriously degrade the performance of communication systems [12], [14], [15]. From a communications perspective the idea of coverage is not usually a problem in indoor wireless systems because the signal strength is usually adequate. Conversely, keeping the level of co-channel interference from another transmitter using the same frequency under control is a limiting factor in attaining good overall performance of the wireless systems.

It seems to be a generally agreed point that little can be done to eliminate multipath interference. In a hospital, not only the communication system is affected by the multipath interference, but there is also an increase in the probability that a local electric

field exceeds the immunity of a critical-care medical device placed at that location. Therefore, the characterization of the multipath medium and the knowledge of the propagation mechanisms will not only influence the design of the communication system and then, help achieve a better quality of service; but also provide design guidelines for minimizing EMI effects on medical devices.

Two important types of fading in indoor propagation are the "fast" fading and the "slow" fading of the field. The former accounts for the very rapid variation of the electric field strength over sub-wavelength distances due to multipath interference, whereas the latter refers to the slowly varying local mean of the fading envelope over distances of several wavelengths.

The path loss is a measure of the average attenuation of a RF signal after traveling down a path of several wavelengths from the transmitter to the receiver, and thus represents the mean of the slow fading. The mean power is approximated by [16]

$$P(r) = \frac{P_0}{r^n} \tag{2.1}$$

where n is the path loss exponent, r is the distance between the transmitter and the receiver, and P_0 is the received power at 1 m from the transmitter.

The path loss is associated with the design of base stations in order to service a certain region [12], [14], [17]. It is known that the path loss not only depends on the geometry of the indoor environment, but also varies with frequency. Statistical path loss models have

been proven to be useful for understanding the propagation of electromagnetic waves in indoor environment, however it usually requires extensive amount of measured data in order to obtain the appropriate parameters for the model of a particular building [7].

The existing propagation models can be classified into two groups: statistical models (empirical) and site-specific models (deterministic). The former are based on the statistics of the received signal, and are relatively easy to implement and requires less computational effort. The latter requires detailed information on the geometry of the environment, the electrical properties of the materials of which the walls and furniture are composed, and so on.

The characteristics of electromagnetic waves can be, in theory, exactly computed by any numerical method, such as finite-difference time domain (FDTD), method of moments (MoM), and finite element method (FEM), capable of solving Maxwell's equations with boundary conditions that define the building geometry. Buildings are many wavelengths in size, and thus are too big to be modeled with methods that cover surfaces with unknown surface currents to be found by the MoM or fill volumes with unknown field strengths to the found by FEM. These methods lead to impractical numbers of unknowns for indoor propagation problems. Therefore, pure numerical solvers based on these methods are not preferable, making approximate numerical methods, such as ray-tracing based on geometrical optics (GO) and uniform theory of diffraction (UTD), appealing. In particular, ray-tracing models have been demonstrated to be reliable and effective tools for designing indoor communication systems [15].

It is interesting to point out that Dagefu *et al.* in [18] claim that the existing models, including various ray-tracing and hybrid techniques, are inadequate for evaluating electromagnetic field levels at near-ground networks because near-ground propagation is dominated by Norton surface waves, with or without the presence of building walls. To solve this problem, these authors relied on an approach based on a hybrid physical optics and asymptotic expansion of the dyadic Green's function for a half-space dielectric. Davis's results in [7] support the claims in [18], since it showed that the values of the near-ground fields obtained with a GO-based ray-tracing and measurements did not agree. In this thesis, Norton waves are not a concern because all field measurements were taken at points located several wave lengths above the floor.

In summary, electromagnetic field prediction models for indoor environments present a wide range of applications such as wireless channel characterization for both communications and EMI purposes, through-wall imaging, and positioning and tracking. Besides, indoor propagation models have relied more and more on a combination of a ray-tracing technique and a statistical distribution. In the next subsections, we explore the physics behind indoor wave propagation, and present some of the most used and promising techniques applied to problems related to this topic.

2.2.1 Basic Mechanisms of Propagation

The three main mechanisms of propagation in an indoor environment are reflection, diffraction, and scattering [17].

2.2.1.1 *Reflection*

Reflection occurs whenever an electromagnetic wave impinges on a smooth object that has very large dimensions compared to the wavelength of the propagating wave. Actually, when reflection occurs, a fraction of the wave intensity is reflected and the other part is transmitted (refracted). The reflection and transmission (refraction) coefficients depend on the electrical properties of the media such as the electrical permittivity, magnetic permeability, and conductivity; and on the wave polarization, angle of incidence, and frequency [14], [19]. Usually reflection occurs from the surface of the walls, ground, and furniture.

2.2.1.2 *Diffraction*

Diffraction occurs whenever the electromagnetic wave hits an object which has sharp edges. At the point of interaction, diffracted waves are created and radiated throughout the space, given rise to the "bending" of the waves around obstructing objects, even when a line of sight (LOS) between the transmitter and receiver does not exist. Diffraction depends on the amplitude, phase, and polarization of the incident wave at the point of interaction, as well as on the geometry of the object [14], [19]. Diffraction is not limited to objects with sharp edges, but can also occur in curved surfaces.

2.2.1.3 *Scattering*

Scattering occurs whenever the medium through which the electromagnetic wave propagates consists of objects which are small compared to the wavelength of the wave,

and the number of obstacles per unit volume is large. Moreover, scattered waves are produced by the interaction of the incident wave with rough surfaces, small objects, or with irregularities in the propagating medium (channel). The accurate prediction of the scattered signal strength requires the knowledge of the object geometry [19]. In most cases, the scattering is neglected [14].

2.2.2 Ray-Tracing Technique

Three-dimensional (3D) ray-tracing techniques based on geometrical optics (GO) and the uniform theory of diffraction (UTD) have proven to be useful simulation tools for predicting high-frequency radio wave propagation in indoor environments [20], [21], [22], [23], [24], [25].

The total field at an observation point is the vector sum of the fields associated with the direct field, all the reflected and transmitted fields, and all the diffracted fields.

$$\vec{E}_t = \vec{E}_{direct} + \vec{E}_{reflected} + \vec{E}_{transmitted} + \vec{E}_{diffracted} \tag{2.2}$$

The field contribution due to the direct ray is given by [21]

$$\vec{E}_{direct} = \sqrt{\frac{\eta_0 P_{rad} G}{4\pi}} \vec{F}(\theta, \phi) \frac{\exp(-jk_0 r)}{r} \tag{2.3}$$

where k_0 is the free-space wavenumber, r is the distance between the transmitter and the observation point, η_0 is the intrinsic impedance of free space, P_{rad} is the power radiated

by the transmitter, G is the gain of the transmit antenna, and $\vec{F}(\theta, \phi)$ is the normalized radiation pattern of the transmit antenna.

The perpendicular and parallel components of the reflected field are found by multiplying the perpendicular and parallel components of the incident field on the point of reflection by their respective reflection coefficient. As for the transmitted field, the perpendicular and parallel transmission coefficients are used. To obtain the field diffracted by an edge, the diffraction coefficients [26] are employed.

We usually describe the total field at an observation point in terms of its direct and multipath components. Therefore, we define the multipath field as the vector sum of all reflected, transmitted, and diffracted rays.

$$\vec{E}_m = \vec{E}_{reflected} + \vec{E}_{transmitted} + \vec{E}_{diffracted} \tag{2.4}$$

Thus, we can write (2.1) as follows

$$\vec{E}_t = \vec{E}_{direct} + \vec{E}_m \tag{2.5}$$

Although point-by-point agreement between measurements and GO/UTD simulations is difficult to attain for a complex indoor environment such as that in [21], the fading statistics obtained from these simulation methods can be similar to those obtained by measurements. Even spatial correlation is well reproduced by ray-tracing methods [22]. For example, in [23], a five-wavelength sliding window is applied to GO/UTD data to

remove the fast fading, and agreement between measured and simulated slow fading is achieved with rms errors less than 7 dB for a 55-m long measurement path. Furthermore, agreement is found between predicted and measured rms delay spread with a normalized error less than 13%. A similar study is found in [24], which shows narrowband and wideband analyses at 1.8 and 2.45 GHz, and the usefulness of GO/UTD simulation for predicting the local mean power, the fading statistics, and the second-order statistics is demonstrated. Moreover, both the simulated and measured data are used to find the best estimate of the Ricean probability distribution function parameter, known as *K*-factor. Three different methods that rely on ray tracing are used in [20] to estimate the Ricean *K*-factor in attempt to model the local fast fading.

A ray-tracing method based only on GO is presented in [25]. The solutions are compared to those obtained from MoM and measurements. Aside from the presence of some field discontinuities in the GO approximation, agreement between measurement and GO simulation is obtained, since the overall field variations are similar.

If the main purpose of diffracted rays is to remove the field discontinuities in the GO shadow boundaries, these rays should not affect considerably the field statistics in a LOS region that is several wavelengths in size, especially if field data is averaged, which is the case when the slow fading is predicted. If the results presented in [25] are compared to those in [21], [22], [23], [24], the point-by-point disagreement does not seem to be different whether or not diffracted rays are taken into account. Diffracted rays are certainly important, but the errors due to modeling the environment geometry, to the not-

precisely-known electrical properties of the building materials, and to the uncertainties in the position of the transmitter and receiver, have a stronger impact on the final prediction than the diffracted rays. This suggests that GO is as good as GO/UTD for most practical purposes regarding indoor propagation.

In support of this idea, we have used the GO code described in [27] to compute the magnitude and phase of the electric field vector at closely-spaced points both along a straight line and over an area to assess the fast fading of the field strength in indoor environments [28], [29], [30], and have obtained satisfactory results. This code has also been used to predict the parameters of the Ricean probability distribution function in order to assess the probability that the field strength will exceed the immunity of medical devices [31]. The GO code [27] is the main simulation tool used in this thesis and is thus further described in the following.

2.2.2.1 *GO_3D program*

The GO_3D code [27] implements a 3D ray-tracing technique that is based on geometrical optics (GO). At an observation point, this code approximates the net electric field as the vector sum of the fields associated with the direct ray and multipath rays, but omits diffracted fields. It can compute the electric field either along a straight line or over a grid of points defined by the user. GO_3D usually models the transmit antenna as a half-wave dipole, however the radiation pattern of any antenna obtained by FDTD or MoM can easily be imported into the code.

Walls are modeled as uniform layered structures [32], [33], accounting for the angle and polarization dependencies of the plane-wave reflection and transmission coefficients. The code requires accurate values for the dielectric constants of the layers [34]. This ray-tracing technique has been demonstrated to be useful for predicting the electric field strength in site-specific environments [28], [29], [30], as well as the slow fading of the field even though internal structures of walls such as studs, wiring and ducting are not accounted for [7], [35].

The accuracy of the simulation depends on the number of reflections that is taken into account by the model. On the other hand, the cost of the ray-tracing computation increases as the number of reflections increases. In theory the field goes on to be reflected an infinite number of times and its amplitude gradually dies away. For practical computational purposes, the number of reflections required to accurately predict the electric field strength depends on a threshold amplitude defined by the user. When the field strength of a ray reflected from a surface is less than the threshold value, the ray is not taken into account in the computation. That is a suitable criterion because eventually the contribution of a ray that undergoes many reflections becomes negligible.

GO_3D controls the maximum number of reflections that are considered in the field computation by allowing the user to specify a threshold field strength. The code keeps generating as many reflections as required until the estimated field strength of the reflected ray drops below a pre-set threshold value. This approach helps avoid potential mistakes that result from the difficulty in determining the number of reflections required

prior to simulation. For example, these mistakes happen particularly in environments where rays undergo reflection at near-grazing angles, since the reflection coefficient is close to unity for all construction materials and wave polarizations.

Reflected and transmitted fields are obtained by accounting for their parallel and perpendicular vector components. First, the incident field is decomposed into its parallel and perpendicular components. Next, the magnitude and phase of both the parallel and perpendicular reflection coefficients, as well as those of the transmission coefficient, are computed. The x, y, and z components of the reflected and transmitted fields are then constructed by combining their parallel and perpendicular components. The reflection and transmission coefficients are functions not only of frequency but also of incidence angle. Moreover, since these coefficients depend on the impedances of the media in question, they also depend on the media electrical properties such as relative permittivity (dielectric constant), relative magnetic permeability, and conductivity [19], [36]. For this reason, we present in Chapter 4 a new method for measuring the dielectric constant of construction materials.

2.2.3 Finite-Difference Time-Domain (FDTD)

Finite-difference time-domain (FDTD) method is a full-wave analysis tool used to obtain numerical solutions of Maxwell's equations and, therefore, is an alternative approach used to study fairly complex indoor environments containing irregular lossy structures. It is more accurate than GO because all propagation phenomena, such as reflection, transmission, diffraction, and surface wave effects are taken into consideration, whereas

GO considers only reflection and transmission, as discussed in the section 2.2.2 [14]. Besides, ray-tracing models assume that reflections from objects are specular, ignoring internal structures of walls.

As a matter of fact, another important problem where FDTD can add substantial improvement is whenever the internal structures of walls play an important role in the indoor environment channel, which in fact accounts for most cases. Few investigations using ray-tracing methods have paid attention to the inner structures of walls [27], [37], [38], [39].

Ji *et al.* in [40] use FDTD method to study periodic structures of walls and to predict propagation properties for indoor environments. Their results show that the inner structures of the walls have a considerable impact on the prediction of the path loss, and that FDTD produces results with high level of accuracy. On the other hand, it must be emphasized that as a numerical method, FDTD requires large amounts of computer memory and extensive calculations to update the solution at successive instants of time. Thus, using this technique to model the entire area of an environment is extremely time consuming and, therefore, impractical if one is not willing to wait for the answer.

Austin *et al.* in [41] applied a 2D TE_z implementation of the FDTD method to model inter-floor radio-wave propagation in the presence of nearby buildings. They have found that reflections from nearby buildings increase the mean received power in adjacent floors. They claimed that the FDTD method has the advantage of being capable of modeling propagation in the presence of inhomogeneous dielectric structures with

complex geometry, and that this method is becoming more and more suitable to solve electrically large problems, given the recent advances in processing capabilities. Yet, based on the accurate results obtained with FDTD method, the authors developed simple mechanistic models based on GO that are accurate and less time-consuming. These models involved the direct ray penetrating through the floors and reflected rays by nearby buildings. These mechanistic models were then compared to narrowband measurements of path gains of adjacent floors at 4.5 GHz, and an RMS error of 3.5 dB was obtained. An interesting point observed in this study is that, even though double-reflections and edge diffraction can increase the received power, their contribution is not important and thus not included in the mechanistic models.

Austin *et al.* in a more recent work [42] used a 3D implementation of the FDTD method to identify and isolate the dominant propagation mechanisms in a multistorey building at 1 GHz. They found that the presence of metallic and lossy dielectric clutter in the environment increases attenuation, which in turn increases the path loss exponent of the floor. Moreover, the FDTD simulations underestimated the path loss for many regions when compared to measurements. This disagreement is largest in regions that are far from the transmitter and with a lot of clutter, particularly for paths shadowed by the shaft and passing through many partitions. In this particular work, the RMS error between measurement and FDTD simulation is 14.4 dB and is improved to 10.5 dB when more clutter is included in the FDTD model. This result is significant and shows the difficulty in characterizing an indoor environment with a fully deterministic model, given the random nature of the clutter. Another important observation in this study is that

diffraction is dominant in the shadow regions when shelves and books are included in the model because of extra attenuation of the reflected fields, but contributes a small proportion of the total power in other regions.

Ying *et al.* in [43] created a hybrid technique based on the combination of a ray-tracing method with FDTD. In short, ray-tracing was used to analyze wide areas, and FDTD to study areas close to structures with complex material properties, where ray-tracing fails to provide sufficiently accurate solutions.

2.2.4 Method of Moments (MoM)

The Method of Moments (MoM) is a numerical method for solving Maxwell's equations, formulated as integral equations. It calculates only boundary values and, therefore, it requires less computational resources than FDTD, especially for problems in which objects are tens of wavelengths in size [14], [19]. Furthermore, the solutions obtained with MoM are accurate provided that the spatial segmentation used for the objects is sufficiently small.

Sandor *et al.* in [44] proposed a hybrid model based on both ray-tracing method and Periodic Moment Method (PMM) to study indoor propagation, penetration, as well as scattering due to periodic structures in buildings. In [44], the PMM was applied to evaluate the specular and grating transmission and reflection coefficients of the periodic structures. Then, those values were used in the ray-tracing code to find the specular and grating rays for each ray tube impinging on one of the periodic structures.

Parsa [45] studied electromagnetic propagation through reinforced concrete slabs. This was an important work because reinforced concrete is used in ceilings, walls, floors, and in columns in order to provide more strength to indoor structures. Moreover, the metallic bars inside the concrete were taken into consideration and their effects on the reflection and transmission of electromagnetic waves were investigated. The author approached this problem by developing a 2D hybrid method called the Green's function/method of moments (GF/MoM) in order to minimize the large number of unknowns usually generated by an accurate full wave computational technique whenever modeling electrically large structures. The results successfully agreed with those obtained by the surface integral equation/method of moments (SIE/MoM) technique.

2.2.5 Sabine's Method

Sabine's theory of reverberation in acoustics has been extended to electromagnetics, and provides an estimate of the spatially-averaged electric field strength in an indoor environment such as a conventional laboratory room and a corridor [7], [46], [47]. The mean electric field in a volume of space is given by the combinations of the direct and multipath fields on an energy basis:

$$\tilde{E}_t(r) = \sqrt{E_{dir}^2(r) + \tilde{E}_m^2(r)} = \sqrt{\frac{\eta_0 DP}{4\pi r^2} + \frac{4\eta_0 P}{A_m}} \tag{2.6}$$

where the tilde signifies a spatially-averaged value, r is the distance between the antenna and the receiver, D is the directive gain of the antenna in the direction of the observer, P

is the radiated power, η_0 is the intrinsic impedance of the medium, and A_m is the multipath room absorption.

The FINDEMI code is based on the Sabine's method which assumes that the electric field radiated by the source undergoes numerous reflections from the walls, causing the energy density to become uniform throughout the room at steady state [46], [48]. This assumption is valid when the walls of the room are sufficiently reflective that the field undergoes many reflections before being reduced to a negligible value. Thus, if one wall of the room is highly absorptive then this assumption is violated. In the Sabine approximation, the multipath field is constant throughout the room and depends on the absorption characteristics of the walls. Furthermore, its contribution to the mean field accounts for the characterization of the room by means of the multipath room absorption, A_m, given by

$$A_m = \frac{AS_T}{S_T - A} \tag{2.7}$$

where S_T is the surface area of the walls, floor and ceiling, whereas A is the Sabine room absorption given by

$$A = \sum_{k=1}^{N} S_k \tilde{\alpha}_k \tag{2.8}$$

where N is the total number of surfaces in the room, S_k is the area of the kth surface in the model, and $\tilde{\alpha}_k$ is the angle-averaged power absorption coefficient of kth surface given by

$$\tilde{\alpha} = 2\int_{0}^{\pi/2} \left[1 - \frac{1}{2}\left(\left|\Gamma_{\parallel}\right|^2 + |\Gamma_{\perp}|^2\right)\right] \sin\theta \cos\theta \, d\theta \tag{2.9}$$

where $\Gamma_{\parallel}$ and $\Gamma_{\perp}$ are the angle-dependent reflection coefficients for the parallel and perpendicular polarization respectively. Equation (2.9) assumes that both polarizations are equally likely to occur. FINDEMI accepts the electrical properties of materials used to create the walls as inputs, evaluate the angle-dependent reflection coefficients every one degree for each type of wall construction included in the model of the indoor environment in question, and then uses (2.9) to compute the angle-averaged power absorption coefficient.

A distance correction is required when the transmitter and receiver are well separated in a large room or corridor. This is necessary because some power is absorbed by the walls as the field propagates from the transmitter to the receiver. A penetration depth (2.10) is defined so that the power in (2.6) can be corrected (2.11).

$$\delta = \frac{S_T}{2\sqrt{h^2 + \frac{S_T}{2}}} \tag{2.10}$$

where S_T is the area of the walls of the room, floor and ceiling, and h the ceiling height.

$$P(z) = P_r \exp\left(-\frac{z}{\delta}\right) \tag{2.11}$$

where z is the distance along the path between the transmitter and receiver, and P_r the radiated power by the source at $z = 0$.

In summary, FINDEMI implements the Sabine's method and estimates the mean electric field at any point in an indoor environment. In order to do so, the code uses (2.9) to compute the angle and polarization averaged absorption coefficient, (2.8) to evaluate the room absorption, and then (2.7) to find the multipath room absorption. Finally, the mean value of the field strength is obtained with (2.6). Distance correction can be applied depending on the geometry of the environment [49].

2.2.6 Measurement Techniques

In this section a few works on indoor radio propagation found in the literature are presented and discussed. The focus here is on the description of the measurement systems and results. The purpose is to provide an overview of equipment and measurement methods most used in indoor propagation research. This helps us understand the design choices for the automated measurement system designed and built for this work.

In most propagation models for mobile communication, the characterization of a complex radio-propagation channel consists in measuring the channel impulse response at each point in a three-dimensional environment. This is useful because the impulse response of a linear time-invariant system (LTI) contains all of the information necessary to analyze any type of channel.

$$h(t) = \sum_{k} A_k e^{j\theta_k} \delta(t - \tau_k) \tag{2.12}$$

where A_k, θ_k, and τ_k, represent the attenuation, phase, and delay in time of arrival or propagation delay, respectively.

Evidently, the condition that the channel is a LTI system must be valid so that this approach can be successfully applied. However, all of the three parameters attenuation, phase, and propagation delay are randomly time-varying functions due to motion of people and equipment in and around the indoor environment under study. Then, the question is: under what condition, for communications purposes, is the LTI-system assumption valid, or rather, can the parameters be thought of as time-invariant random variables? Saleh *et al.* in [13] claimed that as long as the rates at which these parameters vary are very slow compared to any useful signaling rates used in communication systems, LTI can be assumed.

The power-delay profile of a channel is determined by taking the spatial average of the $|h(t)|^2$ over a local area or volume, and represents the large-scale multipath effects of the channel. From the power-delay profile two important parameters, that are useful in describing the overall characteristics of the multipath, can be estimated. These are the power gain and the rms delay spread [13], [14]. The former is useful in estimating the signal-to-noise ratio (SNR) of a communication system, while the latter is a measure of the temporal extent of the multipath delay profile, and is related to performance degradation caused by intersymbol interference.

Time-domain analysis of the received field is vital because it provides insight into the various scattering mechanisms [18], allowing the field prediction technique to focus on the dominant contributions. Usually, frequency domain measurements are taken with the aid of either a vector network analyzer or a spectrum analyzer. It means that the field at the receiver, at a fixed position, is measured or computed as a function of frequency. Then, the inverse Fourier transform of this frequency-domain signal is taken so as to recover the time-domain signal. The accuracy depends on the bandwidth chosen for the measurements in the frequency domain, since it dictates the resolution in time-domain. Furthermore, the frequency step of the measurement determines the time extent of the resulting time-domain signal.

Guérin *et al.* in [50] performed indoor propagation measurements for HYPERLAN at 5 GHz. They obtained an empirical path loss formula, as well as some typical delay profiles and delay parameters. The measurement setup consisted of a transmit patch antenna fixed on the ceiling of a meeting room 9 m long, 8 m wide, and with 3 m of height; a receive patch antenna mounted on a circular positioning system with radius equal to 17 cm, 1.5 m above the floor; and a MVNA 605 Network Analyzer to measure the transfer function of the channel. Each measurement consisted of 127 frequency samples within a 50-MHz bandwidth, ranging from 5.105 to 5.155 GHz. A total of 60 measurement points spaced less than $\lambda/3$ apart along the circumference were taken. Then, the impulse response of each measurement point was calculated using inverse fast Fourier transform (IFFT). Finally, the delay profile at the center of circle was obtained by averaging the 60 impulse responses around it. This process was repeated with the receive antenna placed in 9

different locations within the room. As expected, the authors observed that at a few points the received power level differed from that predicted with path loss model because of multipath contributions. Yet, they concluded that the path loss within the room was very close to that of free space for that particular indoor environment, since the measured path loss exponent is equal to 2.22, whereas in free-space it is equal to 2.

Tingley *et al.* in [51] presented a novel technique for the joint measurement of the angles, times, and complex amplitudes of discrete path arrivals in an indoor environment. Their data measurement system consisted of a circular-shaped array comprised of eight normally-identical quarter-wave monopole elements separated by one-third of the wavelength, an eight-channel switch, and an HP8753D vector network analyzer. The center frequency of interest in this work was 2.45 GHz and a series of eight-channel frequency domain measurements were conducted. Essentially, the vector network analyzer provided a synthesized source, which was swept from 2.35 to 2.55 GHz, and then delivered to an omnidirectional antenna by means of a 50-m double-shielded coaxial cable. The transmitted spectrum was intercepted by the array, and then applied to the receive channel of the vector network analyzer, as illustrated in Figure 2.1.

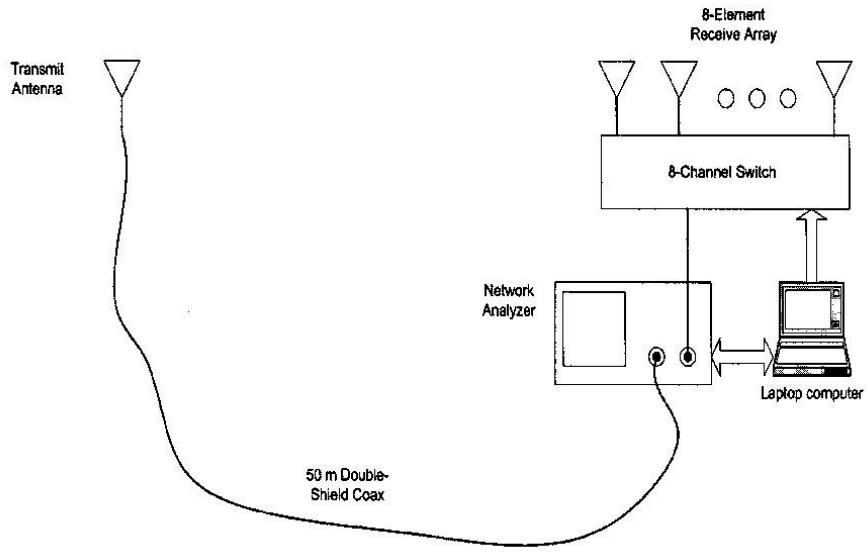

Figure 2.1: Schematic of the measurement setup, from *[51]*.

For each element of the array, the complex-valued transfer function (S_{21}) is retrieved and stored. The authors emphasize that the elements of the array couple strongly with one another, and that there are shielding effects caused by the elements which blocks the line-of-sight view of the source. In addition, we cannot forget to mention the effects caused by the finite dimension of the underlying ground plane, as well as the effects of mismatching of the array elements. The authors presented two signal processing algorithms that eliminate systematic error in their measurement system. Their results show that, in an indoor line-of-sight environment, the first arrival is by far the largest and represents the energy conveyed through the direct path. On the other hand, for a non-line-of-sight environment, the response is quite different. The delay spread is roughly three times longer, and the first arrival is weaker than many subsequent arrivals. These results are expected because in the second scenario there are only multipath fields.

Dagefu *et al.* in [18] used the results from the time-domain analysis to calibrate the results of their measured data. Their experiments were conducted under controlled condition in a laboratory in order to characterize all the parameters well and to suppress features that can lead to uncertainties. Their experimental setup consisted of a single wall built out of concrete and two horn antennas positioned on either side of the wall. A vector network analyzer was used to measure the S_{21} parameter from 1 to 5 GHz, and it was connected to the antennas through long cables, as illustrated in Figure 2.2. Comparison between the proposed approach and measurements showed agreement within 10%.

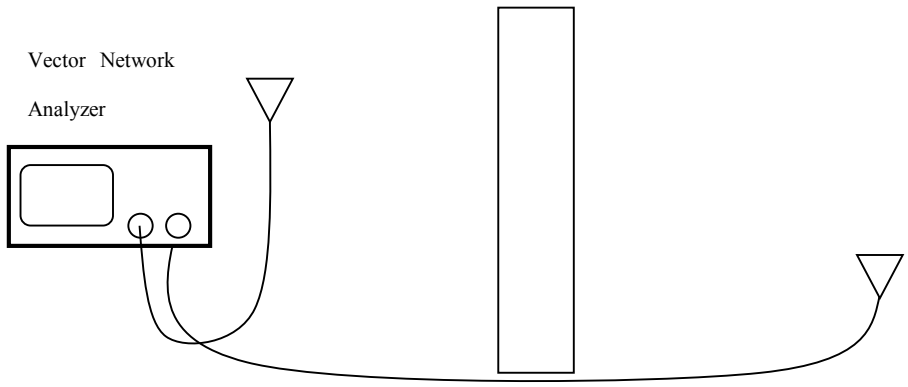

Figure 2.2: Schematic of the measurement setup to measure near-ground fields.

Haneda *et al.* in [52] studied the influence of large- and small-scale propagation behavior on the improvement of receiving signal-to-noise ratio (SNR). Their ultrawideband (UWB) propagation measurements were conducted in an office room, containing desks, chairs, television displays, and metal-furnished shelves. Measurements of the channel

transfer function (S_{21}) were performed with a vector network analyzer connected to two UWB monopole antennas (Tx and Rx), and operating at a frequency range from 3.1 to 10.6 GHz. The heights of the Tx and Rx antennas were both 1.3 m above the floor and their separation varied from 0.6 to 9.3 m. In their experiment setup the Rx antenna was fixed at the corner of the room, whereas the Tx antenna was positioned at almost any place in the room with the aid of a large spatial scanner. There were 1501 frequency sweeping points and the transmitting power was -17 dBm (CW). In order to study the small-scale field distribution in the channel, a small 5 x 5 array of points spaced 25 mm apart from one another was considered. The array measurement was performed in 168 different locations of the room to account for large-scale field distribution within the environment. The authors also mentioned that there was no moving object during the measurements so that the time-invariance characteristic of the channel was ensured. Their results showed that with eight-finger rake reception, 6-dB improvement of the receiving SNR can be expected, and that it is a reasonable number of fingers under practical tradeoffs [52]. They also concluded that larger Tx-Rx separation results in better SNR improvement, whereas its small-scale variation is almost independent on the separation.

Saleh *et al.* in [13] measured the impulse response of the channel in a slightly different way than the previous authors. The rms delay spread and the attenuation within a medium-size office building were calculated from the measured impulse response. Instead of taking frequency-domain measurements and then applying IFFT to obtain the time-domain signal, the detection system in [13] consisted of a square-law envelope

detector connected to an oscilloscope (Tektronix model 7854). Therefore, it is capable of measuring the power profile of the detected signal.

The rest of measurement setup in [13] consisted of an RF source used to generate a 1.5 GHz CW signal, which was modulated by a train of 10 ns pulses with 600 ns repetition period. Two discone antennas were chosen as the transmit and receive antennas due to their superior bandwidth when compared to a vertical dipole antenna. Besides, these two types of antennas have almost the same radiation pattern. For this type of measurement, it is important that the antenna presents a wider bandwidth because a sweeping in the signal frequency is desired. In this experiment the transmitted signal frequency was swept in steps of 100 Hz over ±100 MHz around the 1.5-GHz center frequency. Figure 2.3 shows the schematic representation of the measurement setup.

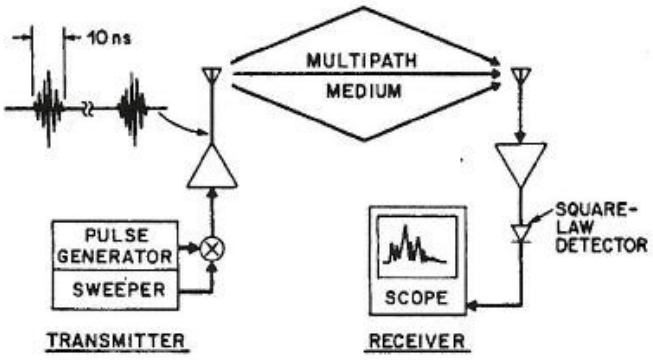

Figure 2.3: Schematic of the measurement setup with square-law detector, from *[13]*.

For each frequency, at each location, the power profile was obtained. Then, the oscilloscope was used to average the received frequency-swept pulse responses, giving rise to the frequency-average power profile, $S(t)$, given by

$$S(t) \equiv \frac{1}{\Delta f} \int_{-\Delta f/2}^{\Delta f/2} |y(t)|^2 \, df \tag{2.13}$$

where Δf is the range of frequencies considered. The extraction of the multipath power gain, *G*, and of the rms delay spread, σ_τ, parameters comes from the frequency-averaged power profile moments and from the transmitted power profile moments

$$M_n \equiv \int_{-\infty}^{\infty} t^n S(t) dt \qquad n = 0, 1, 2 \tag{2.14}$$

$$m_n \equiv \int_{-\infty}^{\infty} t^n x^2(t) dt \qquad n = 0, 1, 2 \ . \tag{2.15}$$

The path gain is given by

$$G = \frac{M_0}{m_0} = \frac{\int_{-\infty}^{\infty} S(t) \, dt}{\int_{-\infty}^{\infty} x^2(t) \, dt} \ . \tag{2.16}$$

The rms delay spread is given by

$$\sigma_\tau^2 = \sigma_s^2 - \sigma_x^2 = \left[\frac{M_2}{M_0} - \left(\frac{M_1}{M_0}\right)^2\right] - \left[\frac{m_2}{m_0} - \left(\frac{m_1}{m_0}\right)^2\right] \ . \tag{2.17}$$

The spatial average of the path gain, $\bar{G}$, around a point at a distance, r, from the source was demonstrated to be, in general, a decreasing function of r.

$$\bar{G}(r) \sim r^{-\alpha} \tag{2.18}$$

In free space, $\alpha = 2$, and the power gain can be obtained from the Friis formula.

$$P_{rec}/P_{trans} = G_t G_r \left[\frac{\lambda_0}{4\pi r}\right]^2 \tag{2.19}$$

The experiment conducted in a hallway [13] resulted in a value of $\alpha < 2$, which according to this author is a result of a waveguiding effect. Depending on the geometry of the room, values of α were found to be between 3 and 4. The results of the rms delay spread shows that this parameter are not correlated with the distance from the transmitter. Rather, it is related to the local surroundings of the transmitter and receiver, such as their proximity to large reflectors.

Esposti *et al.* in [22] performed frequency-domain measurements on a manually moving platform. The transfer function (S_{21}) at several places within a rectangular room (5 m x 5 m) was taken with a HP 8753C vector network analyzer. The frequency swept from 1.7 to 2.2 GHz at a frequency step of 625 kHz, providing a resolution of 2 ns and a maximum nonambiguous echo delay of 1.6 μs. The transmit antenna, a discone copper antenna, was mounted on a wooden circular trolley, 1.6 m above the floor, and was connected to the vector network analyzer through a 80-m-long coaxial cable. The trolley was graduated to

allow a manual 1-cm displacement of the transmit antenna over 72 points along a half-meter diameter semi circumference. The receive antenna was fixed in position at a height of 1.9 m above the floor. The schematic of the measurement system is illustrated in Figure 2.4. Their results show that comparison between measured data and ray-tracing simulation is reliable for both narrow-band and wide-band parameters. In addition, they concluded that even second-order statistics, such as spatial correlation, are well reproduced by ray-tracing technique. Nevertheless, in the case of a non-line-of-sight situation, the agreement is found to be worse. It is also mentioned that the disagreement found when including furniture is due to the lack of refined description of the environment.

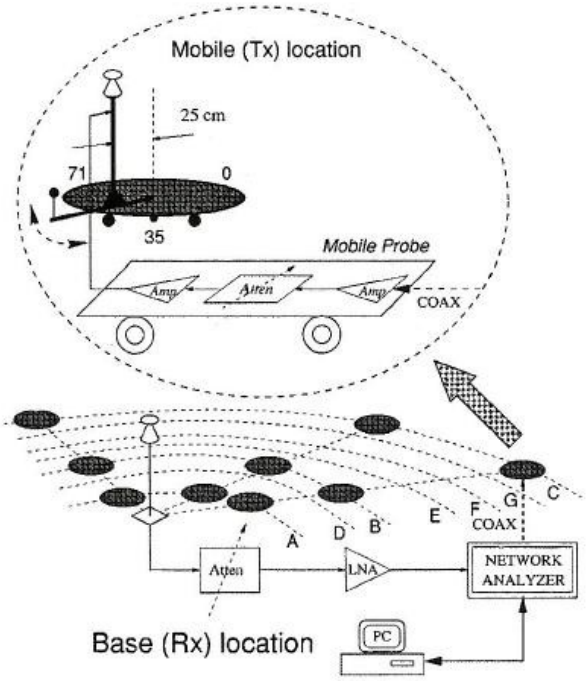

Figure 2.4: Schematic of the manual moving measurement system, from [22].

When it comes to evaluating the risk of EMI in any electronic device, including critical-care medical equipment, the fast fading of the field and its distribution throughout the indoor environment are the parameters of interest. In most immunity tests, the medical device is exposed to either an electromagnetic field of increasing intensity created by a fixed antenna until a malfunction of the equipment is observed, or to a field generated by an uncontrolled source, in which case the distance between the source and the device is changed until a malfunction is observed. Therefore, the condition for observing EMI in medical equipment is that the electric field strength to which they are exposed is greater or equal to their immunity level.

Davis in [7] developed a heuristic model of indoor propagation based on a power law model, as well as on the variability of the field, called residual. This heuristic model was used to quantify the risk of EMI. In order to do that he measured detailed trajectories, planar surfaces, and volume within hospital corridors and rooms so as to acquire practical information on the actual field strength. In his study, the source was kept fixed and a robot measurement system, carrying the receive antenna, performed a large number of efficient and repeatable measurements. This system allowed for both slow fading and fast fading detection. However, in most of his measurements the point spacing used was too wide to evaluate fast fading with confidence. The measurement setup consisted of an RF signal generator (HP616A) connected to a transmit monopole antenna, a receive half-wave dipole antenna, Electromechanics 3121C-db4, and a spectrum analyzer to measure power, which was later converted to electric field strength.

Figure 2.5 shows the robot carrying the receive antenna connected through a cable to a spectrum analyzer. The robot allowed measurements to be taken at a maximum sampling resolution of 3.2 cm (steps), corresponding to about one tenth of the wavelength at 850 MHz and one fifth at 1900 MHz. Then, the robot took measurements along a 50-m corridor in a hospital. The results in [7] show that the attenuation rate of the measured field varies with position in the corridor. Fields near the wall are found to attenuate more rapidly than those near the middle of the corridor. Near-ground fields are weaker than those in the center of the corridor. Besides, they do not attenuate much with distance, which may be explained by the fact that Norton waves are dominant near the floor as discussed above in [18].

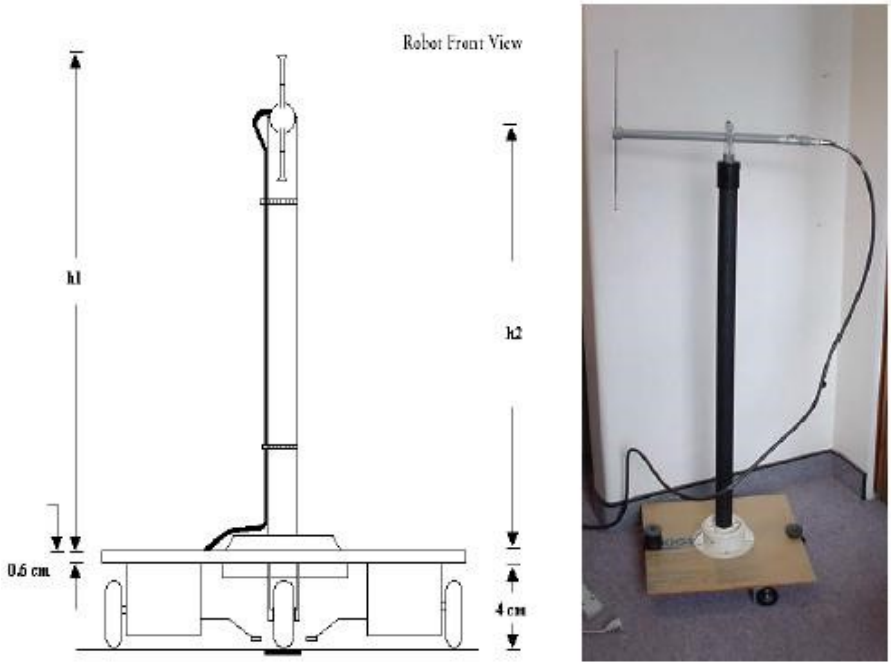

Figure 2.5: Measurement system (robot) with the receive antenna, from *[7]*.

Muneer in [53] studied the behavior of the Ricean-K factor in a long hallway and in a rectangular laboratory room. His study involved two parts: measurement and ray-tracing simulation. His measurements consisted of measuring both spatial and temporal variations of power and, therefore, electric field strength with an automated system containing a transmit unit, a moving platform, a receiving unit, and a control unit. The robot was essentially an automated moving platform equipped with a 900 MHz wireless link in order to communicate with the control unit, and the transmitting monopole antenna. The receive antenna was a calibrated dipole antenna fixed at a location and connected to an HP8569B spectrum analyzer. The frequency range of interest goes from 2.3 to 2.5 GHz. Figure 2.6 shows this measurement system in operation.

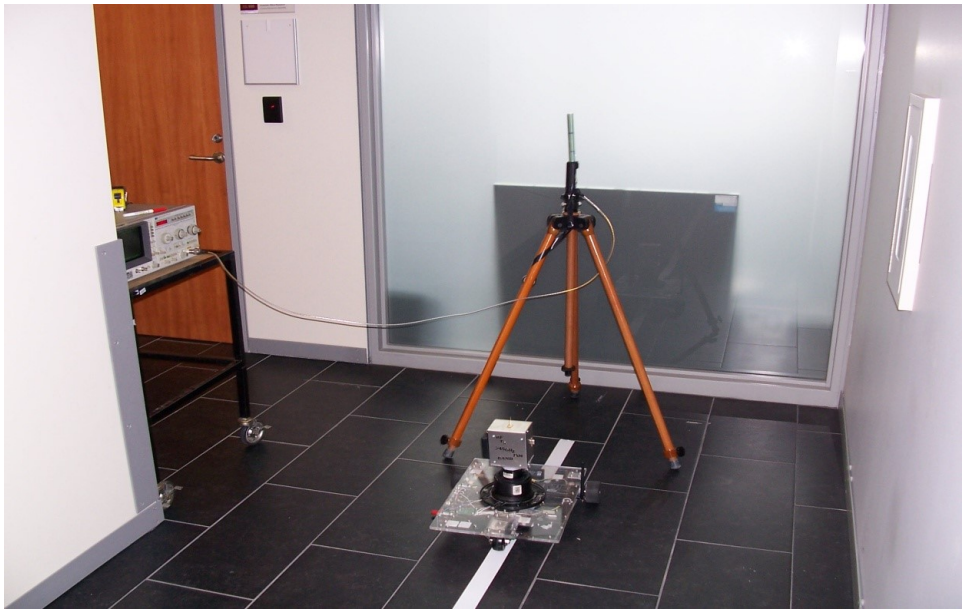

Figure 2.6: Measurement system developed at Concordia University, from *[53]*.

The simulated path loss, spatial Ricean-K factor, and large scale fading data obtained with a GO-based ray-tracing technique were compared to those obtained with the measurement system, and it was concluded that a good match was obtained for the study conducted in the H853 room, whereas that was not the case for the experiment on the 15th floor of the EV Building at Concordia University.

2.3 Electromagnetic Properties of Wall Constructions

The propagation of electromagnetic waves in an indoor environment depends on the properties of the materials in the propagation medium. The most common techniques used to measure electrical properties of materials, such as the dielectric constant and conductivity, are the capacitor method, waveguide resonator method, coaxial cavity method, and the free-field or radiated technique [54], [55]. The first three methods are in general more accurate than the last one [55], but they require material samples with small and precise geometries, which many times may not contain all the necessary constituents of a typical construction material. The free-space technique is non-destructive and particularly useful for inhomogeneous structures such as brick and reinforced concrete walls; thus is the suitable choice for indoor propagation application.

The free-space reflection and transmission technique involves a sample of the material under test being placed between a transmit and a receive antenna, and the measurement of the attenuation and phase shift of the detected signal. The assumption is that a uniform plane wave is normally incident on the planar surface of the material under test, and that the physical dimensions of the surface are large enough such that diffracted rays from the

edges of the sample can be neglected. The accuracy of this method depends strongly on the antenna beam width, antenna positioner, sample holder, and geometry of the experiment.

Muqaibel *et al.* in [54] employed the free-space technique to examine propagation of ultrawideband (UWB) signals through walls made of typical building materials and then evaluate the capabilities and limitations of UWB (3.1 – 10.6 GHz) wireless communication technology. In contrast to what happens to narrowband signals, UWB signals are not only attenuated, but also suffer distortion due to dispersive properties of the wall. In fact, UWB signals suffer more distortions than narrowband signals while propagating through walls because each spectral component of the signal undergoes a different amount of delay and attenuation, since the dielectric constants of wall materials are frequency dependent.

Grosvenor *et al.* [55] also used the time-domain free-field technique to measure the dielectric constant and loss tangent of the following construction materials: polycarbonate, gypsum (gyproc), plywood, a brick wall, and a concrete wall. Another common aspect of these two works [54], [55] is the use of the time gating technique, useful for isolating the front and back surface responses and removing spurious signals from the measured data. Table 2.4 shows a summary of electrical properties of some construction materials found in the literature. More information can be found in [56].

Table 2.4: Electrical properties of construction materials.

MATERIAL	Muqaibel *et al.* [54]	Grosvenor *et al.* [55]	Cuinas, I. and Sanchez, M.G. [57]	Bertoni [58]
Drywall (gyproc)	$\varepsilon_r{}' = 2.44$ $\tan(\delta) < 0.005$ 2 – 11 GHz	$\varepsilon_r' = 2.41 - 2.6$ $\varepsilon_r'' = 0.209 - 0.301$ 0.9 – 5.5 GHz	$\varepsilon_r{}' = 2.02$ 5.8 GHz	-
Office partition	$\varepsilon_r{}' = 0.6 - 1.3$ $\tan(\delta) = 0.04 - 0.1$ 2 – 11 GHz	-	-	-
Structure wood	$\varepsilon_r{}' = 2.1 - 2.2$ $\tan(\delta) = 0.06 - 0.11$ 2 – 11 GHz	-	-	-
Wooden door	$\varepsilon_r{}' = 2.1$ $\tan(\delta) = 0.05 - 0.06$ 2 – 11 GHz	-	-	$\varepsilon_r' = 1.5 - 2.1$ 3 GHz
Plywood	$\varepsilon_r{}' = 2.4 - 2.5$ $\tan(\delta) = 0.1 - 0.18$ 2 – 11 GHz	$\varepsilon_r' = 3.67 - 3.81$ $\varepsilon_r'' = 0.157 - 0.162$ 0.9 – 5.5 GHz	-	-
Glass	$\varepsilon_r{}' = 6.7$ 2 – 8 GHz	-	$\varepsilon_r{}' = 6.06$ 5.8 GHz	$\varepsilon_r' = 3.8 - 8$ 3 GHz
Styrofoam	$\varepsilon_r{}' = 1.1$ 2 – 11 GHz	-	-	-
Brick	$\varepsilon_r{}' = 3.7 - 4.6$ $\tan(\delta) = 0.07$ 2 – 8 GHz	$\varepsilon_r' = 3.88 - 4.26$ $\varepsilon_r'' = 0.455 - 0.515$ 0.9 – 5.5 GHz	$\varepsilon_r{}' = 3.58$ 5.8 GHz $\varepsilon_r{}'(max) = 4.33$	$\varepsilon_r' = 4$ 3 GHz
Concrete block	$\varepsilon_r{}' = 3.7 - 4.6$ $\tan(\delta) = 0.07$ 2 – 7 GHz	-	-	-
Concrete wall	$\varepsilon_r{}' = 9.2$ 2 – 8 GHz	$\varepsilon_r' = 7.63 - 9.54$ $\varepsilon_r'' = 1.266 - 1.806$ 0.9 – 5.5 GHz	-	-
Polycarbonate	-	$\varepsilon_r' = 2.82 - 2.89$ $\varepsilon_r'' = 0.028 - 0.064$ 0.9 – 5.5 GHz	-	-

2.4 Statistical Models and Analysis

In this section we will define the distributions which are used to model the measured fast fading in the indoor environments considered in this thesis. Moreover, we outline the basic theory for two important methods of parameter estimation: the maximum likelihood estimation (MLE) method and the γ-based moment method (MM). Finally, we describe

the Anderson-Darling goodness-of-fit test used to quantify the extent to which fast fading can be represented by a specific distribution.

2.4.1 Rayleigh Distribution

The Rayleigh distribution is usually used to model the fast fading in an indoor environment dominated by multipath propagation, or rather, with no dominant field contribution. Furthermore, the electromagnetic waves that reach a specific region, through different paths, are assumed to have a homogeneous phase distribution. The Rayleigh distribution that describes the electric field strength has a pdf given by [12], [14], [59]

$$p(x) = \frac{x}{\sigma^2} \cdot \exp\left(-\frac{x^2}{2\sigma^2}\right) \quad x \geq 0 \tag{2.20}$$

where x is the electric field strength at the receiver, and $2\sigma^2$ the mean power of the multipath field. The effect of the σ parameter is demonstrated in Figure 2.7. Low sigma is an almost deterministic signal with small deviations from the peak, whereas high sigma means wider distribution and more signal variability.

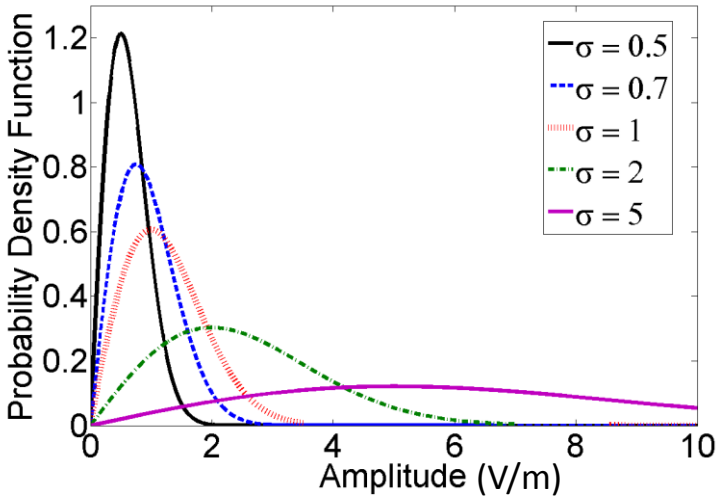

Figure 2.7: Rayleigh distribution probability density function.

2.4.2 Ricean Distribution

The Ricean distribution is widely used to characterize the fast fading and accounts for a dominant field component which is usually that of the LOS wave, but just as for the Rayleigh distribution, it assumes the multipath components to be approximately equal in amplitude and uniformly distributed in phase. The pdf of the Ricean distribution is given by [12], [14], [59], [60]

$$p(x|\nu,\sigma) = \frac{x}{\sigma^2} \cdot \exp\left(-\frac{x^2+\nu^2}{2\sigma^2}\right) \cdot I_0\left(\frac{x\nu}{\sigma^2}\right) \qquad r \geq 0 \qquad (2.21)$$

where x is the electric field strength at the receiver, ν the amplitude of the dominant component, $2\sigma^2$ the mean power of the multipath field, and $I_0(\cdot)$ the modified Bessel function of the first kind and zero order. The Ricean *K*-factor is defined as

$$K = \frac{\nu^2}{2\sigma^2} \tag{2.22}$$

When there is no dominant component, that is, $K = 0$, the Ricean distribution reduces to a Rayleigh distribution. References [31], [53] have described the Ricean distribution as

$$p(E) = \frac{2(K+1)E}{\Omega} \cdot \exp\left(-K - \frac{(K+1)E^2}{\Omega}\right) \cdot I_0\left(2E\sqrt{\frac{K(K+1)}{\Omega}}\right) \tag{2.23}$$

where *E* is the electric field strength and I_0 the modified Bessel function. *K* is the Ricean *K*-factor which is defined by

$$K = \frac{E_{dir}^2}{E_m^2} \tag{2.24}$$

where E_{dir} is the dominant component and E_m is the multipath component. Ω is given by

$$\Omega = (E_{dir}^2 + E_m^2) \tag{2.25}$$

The higher the value of the *K*-factor, the stronger the influence of the dominant component, which causes the peak of the probability density function to appear at the

value of the dominant electric field strength component, with small random variations. On the other hand, for regions far from the transmit antenna, which are usually characterized by a *K*-factor that is less or equal to unity, the dominant field strength is comparable to that of the multipath. This characterizes a field strength that is highly random. As a conclusion, the knowledge of the *K*-factor provides an insight into the distribution of the field in the region surrounding the receiver.

The effect of the dominant and multipath components on the Ricean distribution is demonstrated in Figure 2.8. We can see the effect of the direct and multipath components on the shape of the distribution. For a fixed multipath components, we see that the direct field component changes the position of the distribution peak; whereas for a fixed direct component and varying multipath component, the effect is on the spread of the distribution. This makes sense because the multipath components is the one responsible for the total field variation.

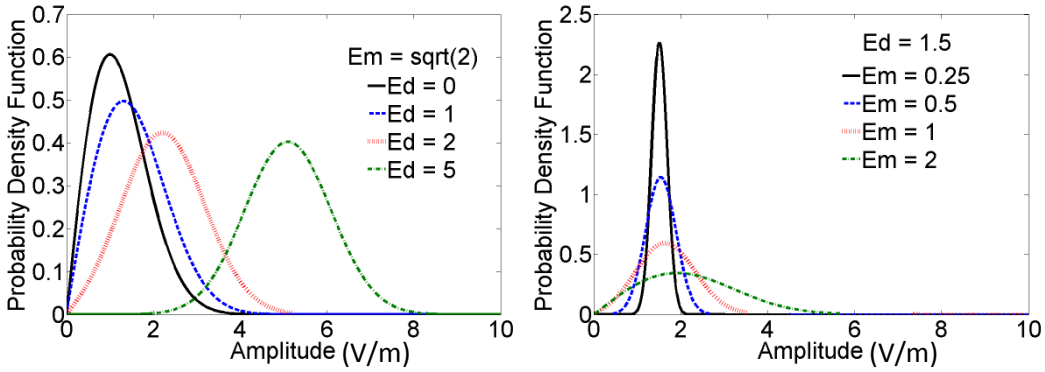

Figure 2.8: Ricean distribution probability density function.

2.4.3 Nakagami Probability Distribution

The Nakagami distribution is a more general distribution which, with the choice of appropriate parameters, can approximate both the Ricean and Rayleigh distributions [12], [14], [59]. The Nakagami distribution has the following probability density function:

$$p(x|m,\Omega) = \frac{2m^m}{\Gamma(m)\Omega^m} \cdot x^{2m-1} \cdot \exp\left(-\frac{m}{\Omega}x^2\right) \quad x \geq 0 \; and \; m \geq 0.5 \qquad (2.26)$$

where, x is the envelope amplitude of the received signal, $\Omega = \langle x^2 \rangle$ is the time-averaged power of the received signal, and $m = E[x^2]/var[x^2]$ is a unitless quantity that is the inverse of the normalized variance of x^2, $\Gamma(\cdot)$ is the Gamma function, and $E[\cdot]$ represents statistical expectation. When $m = 1$, a Rayleigh distribution is obtained. Large values of m signifies strong dominant component. The effect of the shape parameter m is demonstrated in Figure 2.9. As we can see, the shape parameter changes both the peak position and the spread of the distribution.

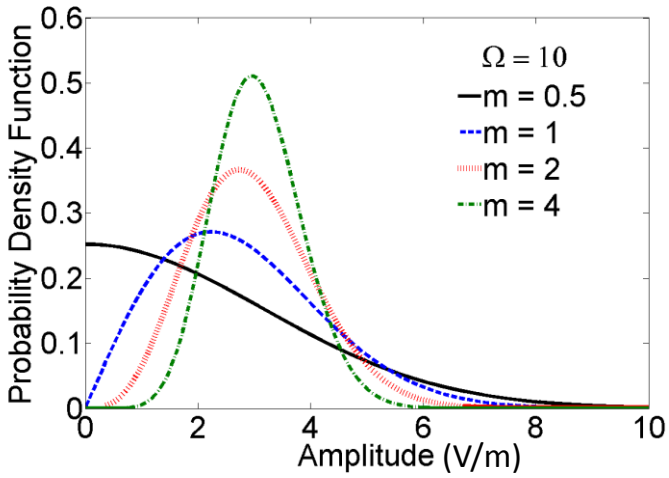

Figure 2.9: Nakagami distribution probability density function.

2.4.4 Weibull Probability Distribution

The Weibull distribution is characterized by its scale and shape parameters α and β, and has the following pdf:

$$p(x|\alpha,\beta) = \frac{\beta}{\alpha} \cdot \left(\frac{x}{\alpha}\right)^{\beta-1} \cdot \exp\left(\left(-\frac{x}{\alpha}\right)^{\beta}\right) \qquad x \geq 0 \; and \; \alpha,\beta \geq 0 \qquad (2.27)$$

The effect of the shape parameter is demonstrated in Figure 2.10. Note that when $\beta = 1$ the distribution becomes the Exponential distribution, and when $\beta = 2$ it becomes the Rayleigh distribution. This shows how versatile the Weibull distribution is.

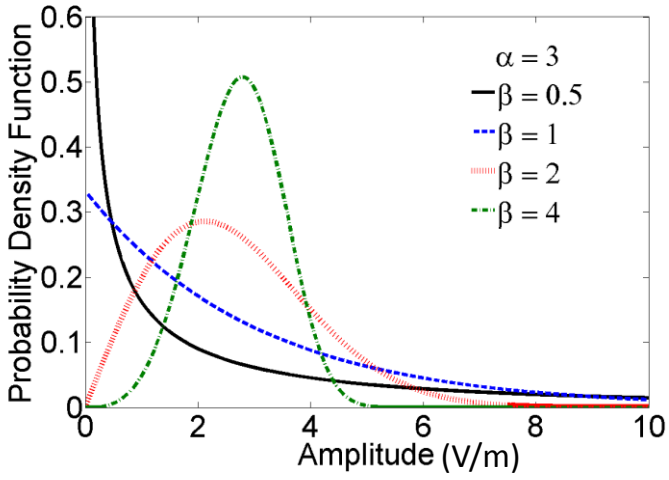

Figure 2.10: Weibull distribution probability density function.

2.4.5 Parameter Estimation: Maximum-Likelihood Estimation (MLE)

The distributions described in the previous section have parameters, and are fully specified only when we have values for each parameter. However, in practice, we rarely know the true value of the parameter for each distribution, and thus an estimate that provides the distribution best fit to the collected data is a common approach to the problem. In this thesis, this is achieved through the following parameter estimation methods: the maximum likelihood estimation (MLE) [61], and the γ-based moment method (MM) [62].

The maximum likelihood method selects as its estimate the parameter value that maximizes the probability of the collected data [61]. In other words, for a fixed set of data and underlying statistical model, the MLE method selects the set parameters that maximizes the likelihood function. A probability density function, $f(x|\theta)$, maps x to the probability of observing the value x for some fixed parameter θ. This can be written as

$$f(x|\theta) = \frac{f(\theta|x)f(x)}{f(\theta)} \quad . \tag{2.28}$$

We can reverse (2.28) to obtain the likelihood function of the collected data, which is a function of θ and is denoted by $L(\theta|x)$. In other words, for a likelihood function, the collected data is fixed and the parameters of the distribution are variables. Since the data values are independent and identically distributed, we can write

$$L(\theta|x) = \prod_{j=1}^{n} f(\theta|x_j) \quad . \tag{2.29}$$

We then obtain the maximum likelihood estimate by finding the value for which

$$\frac{\partial}{\partial\theta} L(\theta|x) = \frac{\partial}{\partial\theta}\left\{\prod_{j=1}^{n} f(\theta|x_j)\right\} = 0 \quad . \tag{2.30}$$

Since (2.30) involves a product of terms, the log likelihood function is usually used in order to make the computation of the derivative more convenient. Consider the following example adapted from [61].

Let $\boldsymbol{E}_n = (E_1, E_2, \ldots, E_n)$ be the observed electric field strengths and assume that the field is a Gaussian random variable. Our goal is to estimate the normal distribution parameters from the set of electric field data: the mean $\theta_1 = \mu$ and variance $\theta_2 = \sigma_E^2$. The likelihood function must be maximized with respect to the two parameters. The pdf of the jth observation is given by [61]

$$f_E\left(\theta_1, \theta_2 \middle| E_j\right) = \frac{1}{\sqrt{2\pi\theta_2}} e^{-(E_j-\theta_1)/2\theta_2} \quad . \tag{2.31}$$

The log likelihood function is given by

$$\begin{aligned}\ln L(\theta_1, \theta_2 | E_1, E_2, \ldots, E_n) &= \sum_{j=1}^{n} \ln f_E(\theta_1, \theta_2 | E_j) \\ &= -\frac{n}{2} \ln 2\pi\theta_2 - \sum_{j=1}^{n} \frac{(E_j - \theta_1)^2}{2\theta_2} \quad .\end{aligned} \tag{2.32}$$

We take derivatives with respect to the parameters and set the results equal to zero:

$$\frac{\partial}{\partial \theta_1} \sum_{j=1}^{n} \ln f_E(\theta_1, \theta_2 | E_j) = -\frac{1}{\theta_2} \left[\sum_{j=1}^{n} E_j - n\theta_1 \right] = 0 \tag{2.33}$$

$$\frac{\partial}{\partial \theta_2} \sum_{j=1}^{n} \ln f_E(\theta_1, \theta_2 | E_j) = -\frac{1}{2\theta_2} \left[n - \frac{1}{\theta_2} \sum_{j=1}^{n} (E_j - \theta_1)^2 \right] = 0 \quad . \tag{2.34}$$

Therefore, the maximum likelihood estimators are:

$$\theta_1 = \frac{1}{n} \sum_{j=1}^{n} E_j \tag{2.35}$$

$$\theta_2 = \frac{1}{n} \sum_{j=1}^{n} (E_j - \theta_1)^2 \quad . \tag{2.36}$$

Thus, θ_1 is the sample mean and θ_2 is the biased sample variance. Note that as *n* becomes large, θ_2 approaches the unbiased variance.

2.4.6 Parameter Estimation: γ-based Moment Method (MM)

Abdi *et al.* [62] present a γ-based MM method for estimating the *K* Ricean parameter from a data set containing total electric field strength values. As for the Ω parameter the authors used the MLE method which is straightforward to implement and given by

$$\Omega = \frac{1}{n}\sum_{j=1}^{n} e_j^2 \tag{2.37}$$

where e_j is the signal envelope.

As for the *K* parameter, based on the general expression for the *l*th-order moment of the Ricean distribution, we can write [62]

$$\gamma = \frac{2K+1}{(K+1)^2} \ . \tag{2.38}$$

Solving for *K*, we obtain

$$K = \frac{\sqrt{1-\gamma}}{1-\sqrt{1-\gamma}} \tag{2.39}$$

where γ is defined as

$$\gamma = \frac{V[e^2]}{(E[e^2])^2} \tag{2.40}$$

$V[\cdot]$ denotes variance and $E[\cdot]$ the expectation.

So, the procedure to compute the *K* parameter from a set $\{e_i\}$ starts with the calculation of the following three moments:

$$E[e] = \frac{1}{n}\sum_{j=1}^{n} e_j$$

$$E[e^2] = \frac{1}{n}\sum_{j=1}^{n} e_j^2 \tag{2.41}$$

$$E[e^4] = \frac{1}{n}\sum_{j=1}^{n} e_j^4 \quad .$$

Then we calculate

$$\Omega = E[e^2] \tag{2.42}$$

and

$$K = \frac{\sqrt{2(E[e^2])^2 - E[e^4]}}{E[e^2] - \sqrt{2(E[e^2])^2 - E[e^4]}} \quad . \tag{2.43}$$

This method is applied to the data collected for this thesis and compared to the MLE method.

2.4.7 Anderson-Darling Test

To quantify the extent to which fast fading data can be represented by a candidate or hypothesized probability distribution, a goodness-of-fit test must be employed. The Anderson-Darling (AD) test is based on a comparison of the hypothesized cumulative distribution function $F(x)$ with the empirical cumulative distribution function $F_n(x)$ [63]. This test is an alternative to the Kolmogorov-Smirnov and Chi-Squared goodness-of-fit tests. It is also more powerful than the Kolmogorov-Smirnov because it gives more weight to the differences between the tails of the functions. The class of quadratic empirical distribution function (EDF) tests is given by [63]

$$T_n = n \int_{-\infty}^{\infty} [F_n(x) - F(x)]^2 \, \psi(x) dF(x) \tag{2.44}$$

where $\psi(x)$ is a weight function. Notice that when $\psi(x) = 1$ we obtain the Cramé-von Mises (CVM) test statistics W_n^2, and when

$$\psi(x) = \frac{1}{F(x)(1 - F(x))} \tag{2.45}$$

we obtain the AD test statistics A_n^2

$$A_n^2 = n \int_{-\infty}^{\infty} \frac{[F_n(x) - F(x)]^2}{F(x)\big(1 - F(x)\big)} dF(x) \ . \tag{2.46}$$

For computation purposes the following equation is used [63], [64], [65], [66], [67],

$$A_n^2 = -n - \sum_{i=1}^{n} \frac{2i-1}{n} \left[\ln\left(F(X_i)\right) + \ln(1 - F(X_{n+1-i}))\right] \tag{2.47}$$

where $\{X_1, X_2, \ldots, X_n\}$ are the ordered data and n is the number of data points in the sample.

Differences in shape between the hypothesized distribution and the empirical distribution have a direct impact on the AD test statistic. It is only when this difference is greater than that expected by random chance, for a specific significance level, that the AD test rejects the null hypothesis, leading to the conclusion that the data cannot be describe by the hypothesized distribution.

In this thesis the parameters of the hypothesized distributions are estimated by the MLE method, and the p-value of the AD test is computed with MATLAB command *adtest* [67]. This test can be configured to compute the p-value analytically or by means of the asymptotic distribution of the test statistic. Since the sample data analyzed in this thesis have more than 120 data points, the asymptotic distribution is chosen.

The next chapter describes the automated measurement system used in this work.

Chapter 3: Measurement System

In this chapter we describe an automated measurement system which was designed and built to sample the electric field strength in an indoor environment. The system automatically places a receive antenna at the desired location and then records electric field strength readings on an SD card. This project started as a collaboration with a Capstone 490 group of undergraduate students in a 2011/2012 project to design and build the mechanical parts of the system, as well as some of the electrical parts [68]. At this stage, my main role was to supervise the three undergraduate students and provide them with the system's specifications and overall design. The next phase of the project, which involved an improved design and the construction of the entire measurement system, was carried out by Mr. Vincent Mooney Chopin, who was one of the initial undergraduate students, and me. Even though both of us have participated in every aspect of the system, Vincent's main contribution was in the implementation of various parts of the antenna positioners, the programming, and the integration of the subsystems; whereas my main contribution was the detection system, especially the RF aspect of it. This chapter is divided into three parts. In the first one, we describe the entire measurement system, in the second we discuss the electromagnetic environment of interest, and in the third we give emphasis to the detection system.

3.1 Subsystems Overview

As mentioned above the measurement system automatically positions an antenna, samples electric field strengths and records the data on an SD card. The automated measurement system consists of three subsystems: a moving platform (Line Follower), a horizontal 2D scanner, and a detection system, as illustrated in Figure 3.1.

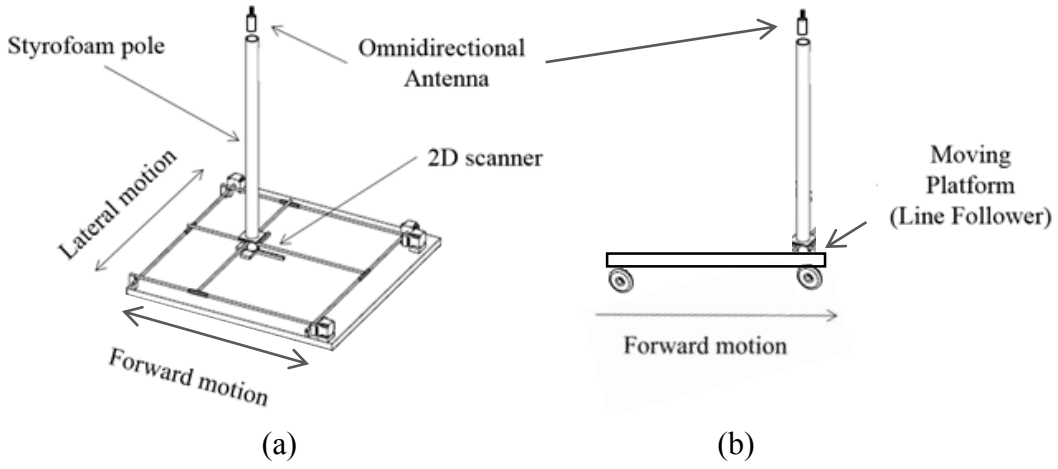

Figure 3.1: Measurement system overview. (a) 2D scanner. (b) Line follower.

These subsystems were designed and built so that they can be used to measure electric field strength for a variety of indoor propagation experiments. The 2D scanner can be mounted on the line follower platform and scan a 2D grid for each position of the line follower, or they can be operated independently of one another. The Line Follower is a battery operated moving platform capable of following a path as long as 50 m (forward movement) in precise steps of 1 cm or larger. The horizontal 2D scanner could be sited on top of the platform or used independently, and is capable of moving in the forward

and lateral directions in precise steps that can be as small as 0.1 cm. The measurement window is defined by the user and can be as large as 70 by 70 cm. A Styrofoam pole is used to place the omnidirectional receive antenna at the desired height, and serves as a support for parts of the detection system and cable.

3.1.1 Mechanical Design and Electrical Setup of the Controllers

Figure 3.2 shows the block diagram of the entire measurement system, which provides a more detailed description of the interactions between the subsystems. All subsystems communicate with the master controller by means of CAT 5e twisted pair cables and RJ45 connectors. Moreover, the CAT 5e cables carry DC power as well as the serial peripheral interface (SPI) bus. The user interacts with the master controller by means of a keypad and a liquid-crystal display (LCD), as shown in Figure 3.3. The experiment setup is configured by following the instructions on the display and selecting the appropriate options for each experiment. The first step is to choose whether the Line Follower or the 2D scanner or both of them are going to be used. Next, the user defines the parameters of the experiment such as the measurement window and the spacing between measurement points. Then the system waits for the user to click on the start button, and gives the user a few seconds to leave the environment where the experiment takes place. The Line Follower moves to the starting point or the 2D scanner moves the Styrofoam pole to the starting point and then stops and wait.

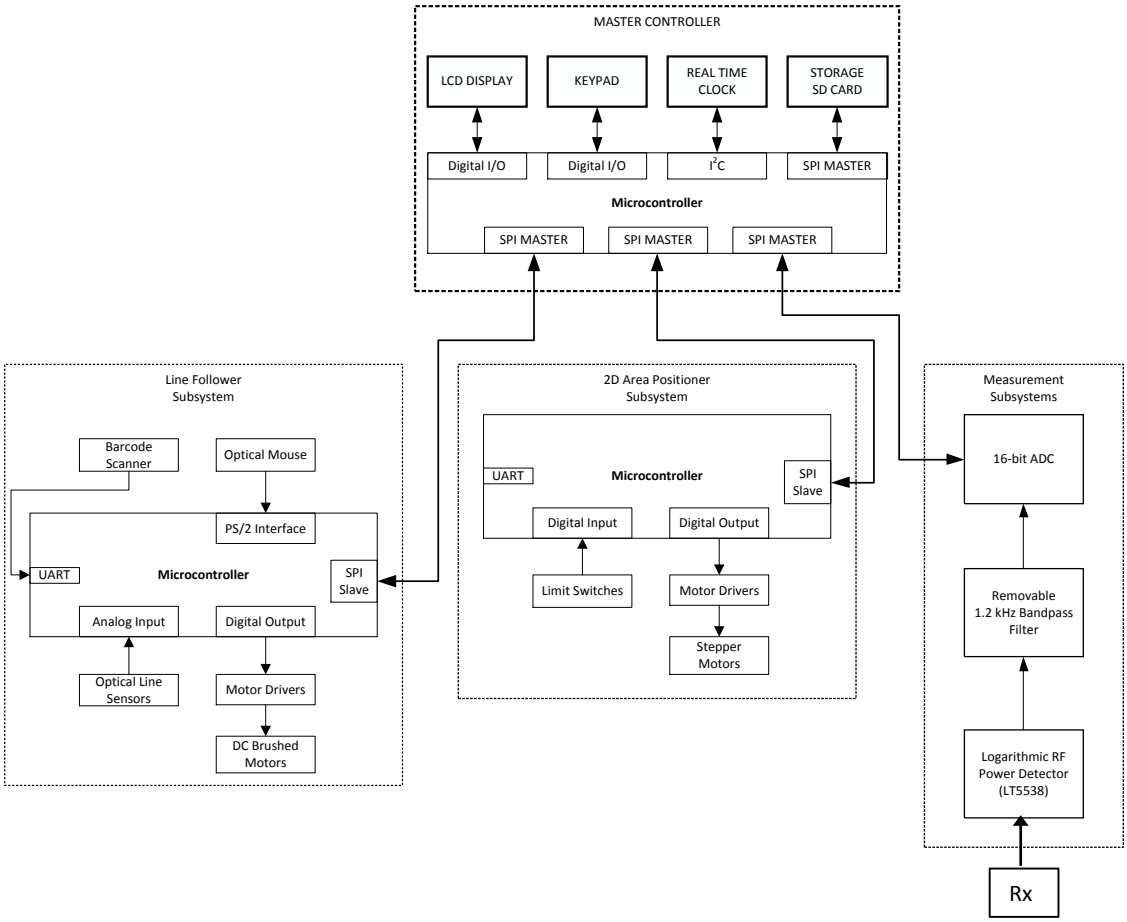

Figure 3.2: Block diagram of the measurement system.

Figure 3.3: Master controller.

The electric field strength of a modulated signal is sampled by an omnidirectional antenna and sent into a power detector, and next into an extremely narrow bandpass filter centered at 1.2 kHz. There is a peak detector at the output of the 1.2 kHz filter, which recovers the power of the sampled field. Finally, this constant-value signal is sent into an analog-to-digital converter (ADC) and then to the master controller which stores the data on a secure digital (SD) card. The positioning system moves the antenna to the next measurement point and this procedure starts over and repeats until the whole experiment is complete.

3.1.2 Line Follower

The Line Follower, shown in Figure 3.4, is an automated subsystem designed to follow a straight-line path in precise steps defined by the user. Its main application is to position an antenna at points along the path for field strength measurements in indoor environments.

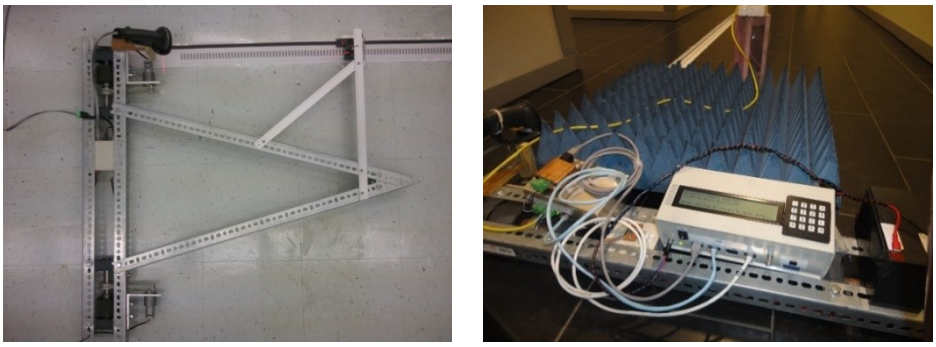

(a) (b)

Figure 3.4: Line Follower. (a) Top view of the line follower platform. We can see the line detector on the upper right corner of the figure and the bar code reader to the left. (b) Master controller, battery, and detection system on top of the line follower.

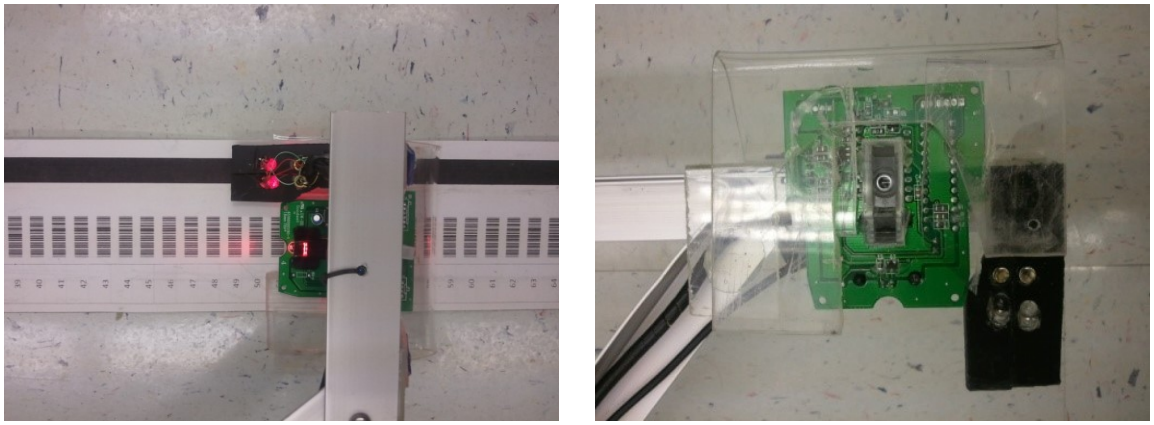

Figure 3.5: Bar code tape, line detector, and optical sensor.

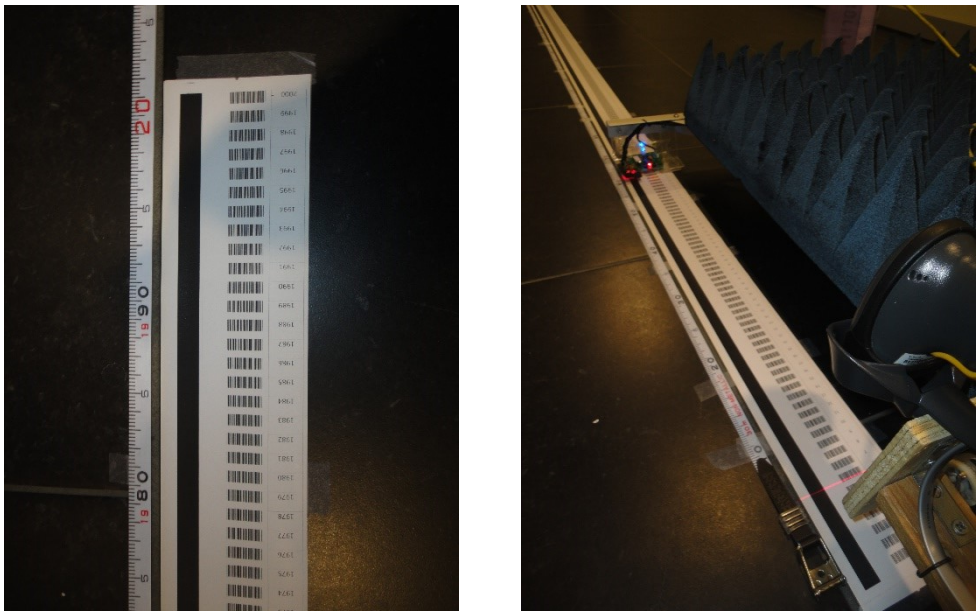

Figure 3.6: Bar cade tape and bar code reader.

The Line Follower subsystem is essentially a moving platform that is capable of following a straight-line path, positioning the antenna, and carrying a relatively heavy payload such as the 2D scanner and detection system. The user can define the spacing

between measurement point to be as small as 1 cm, and the path can be as long as 50 m. The system uses a very practical tape as a guide, Figures 3.5 and 3.6, and reads barcodes off the tape to acquire information on its position relative to the starting point of the experiment, usually the position of the transmit antenna. The Line Follower stops immediately as soon as it reads the desired barcode. In this way, there is no cumulative error in position as the Line Follower moves farther and farther from the starting point. The accuracy in the position depends only on the width of the laser used to read the barcodes, which is approximately 1 mm, and on the printer used to print the barcodes and black line. The printer creates an accumulated error of 3 mm per meter, which must be compensated by properly placing the tape on the floor. In doing so, the accumulated error over a 20-m path is about 2 mm. This subsystem has been extensively tested, and it can position the receive antenna at any point along the tape with an accuracy of ± 1 mm and no cumulative error. The black line printed on the tape is used to steer the moving platform so that it follows a straight line path. Two light-emitting diodes (LED) illuminate the tape and the reflected signals are detected by the line detector, comprised of two phototransistors, and used to correct the trajectory of the Line Follower. Simultaneously, an optical sensor from a computer mouse is used as a position feedback and controls how straight the robot moves.

The line follower can operate in a standalone mode, or can be connected by a cable to a computer and controlled remotely, as when used for instance inside an anechoic chamber, where being able to control the system from outside is a desirable feature. Figure 3.7 shows the block diagram of the Line Follower for its standalone mode.

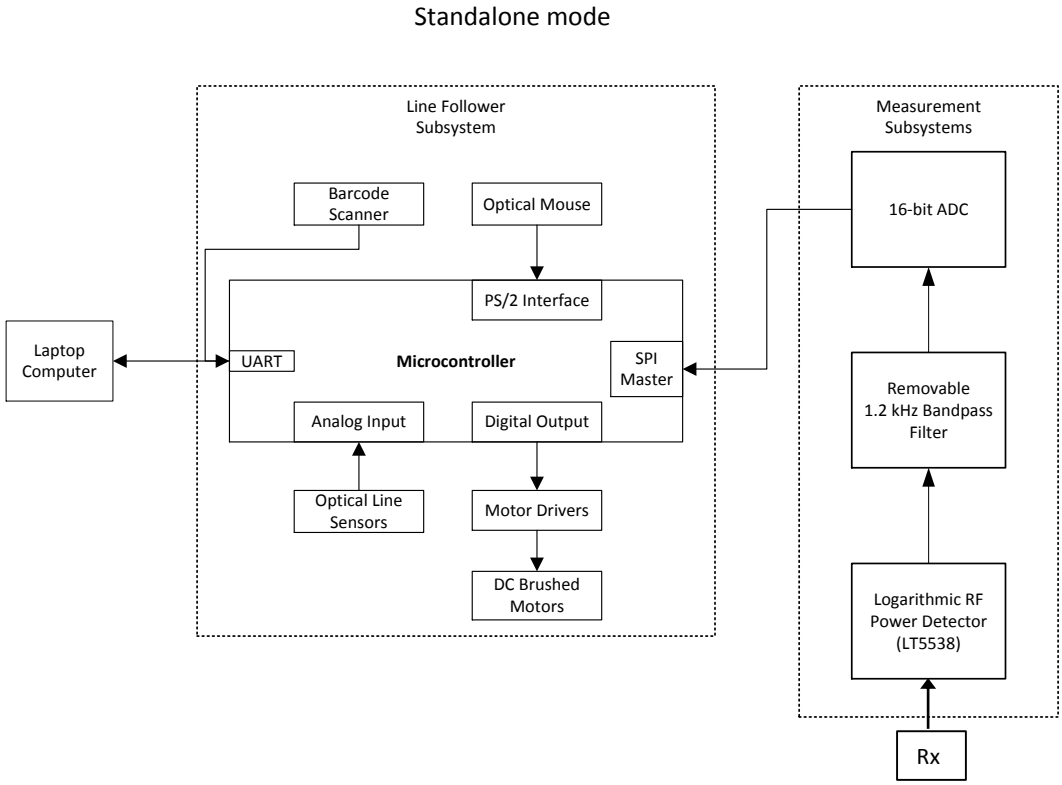

Figure 3.7: Block diagram of the Line Follower (standalone mode).

3.1.3 2D Scanner

The 2D Scanner is a subsystem designed to position an antenna at any point in a horizontal plane of size 70 by 70 cm, as illustrated in Figure 3.8. This positioning system is comprised of four lead screws each connected to a stepper motor. The pair of motors associated to the movement in one direction are connected in parallel so that the corresponding lead screws experience the same torque, thus causing the smooth rod oriented perpendicularly to the pair of lead screws to displace equally. It is this perpendicular smooth rod that pushes the base of the Styrofoam pole in the direction parallel to the pair of lead screws in question.

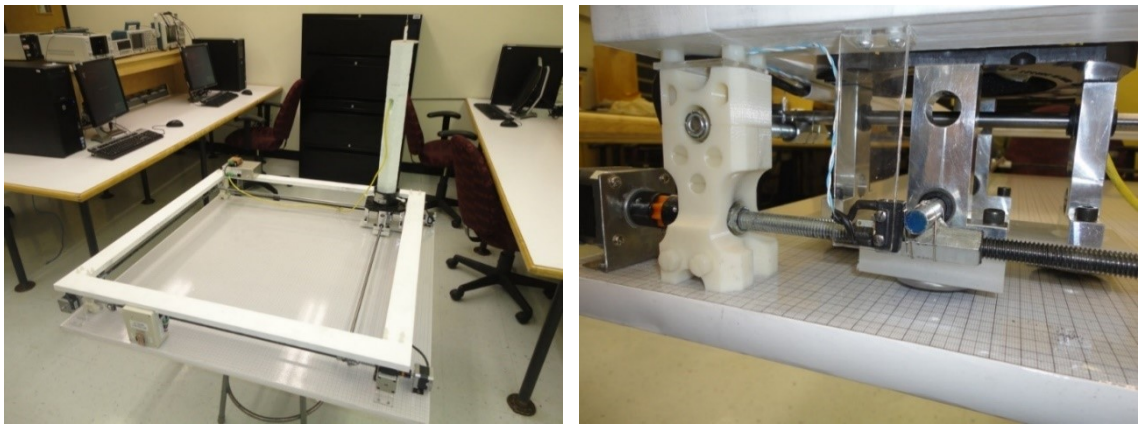

Figure 3.8: 2D Scanner.

The same applies to the other pair of stepper motors for the movement in the other direction. This is a very accurate system since the position accuracy depends on the size of the lead screw thread and also on the step size of the stepper motor. Each step of the motor represents a linear distance of 0.008 mm.

A Styrofoam pole is used to carry a receive antenna because its dielectric constant is about 1.03, almost free space, and thus does not scatter radio waves much. Observe that there is a cable, almost parallel to the pole, trailing from below the antenna. It is expected that this cable will be excited by the direct field and, consequently, scatter omnidirectionally in a horizontal plane, and that some of the scattered energy could find its way to the receive antenna via reflection from a nearby wall. As will be demonstrated in the following chapters, the agreement between measurements and simulations suggests that the scattered waves from the cable is at worst a secondary effect.

As we can see, the wooden base of the scanner is covered with a water-resistant plastic sheet with a millimeter square grid printed on it. This sheet has proven to be of great importance in the squaring of the lead screws and to the experiment alignment. Figure 3.8 also shows one of the corners of the scanner, where we can see a limit switch for protection purposes, which stops the system in case it is hit. Furthermore, the base of the Styrofoam pole sits on three ball casters that allow the sliding of the base. We also see two smooth rods going through the base in perpendicular directions. These are the rods that transfer movement to the base. Figure 3.9 shows the scanner controller.

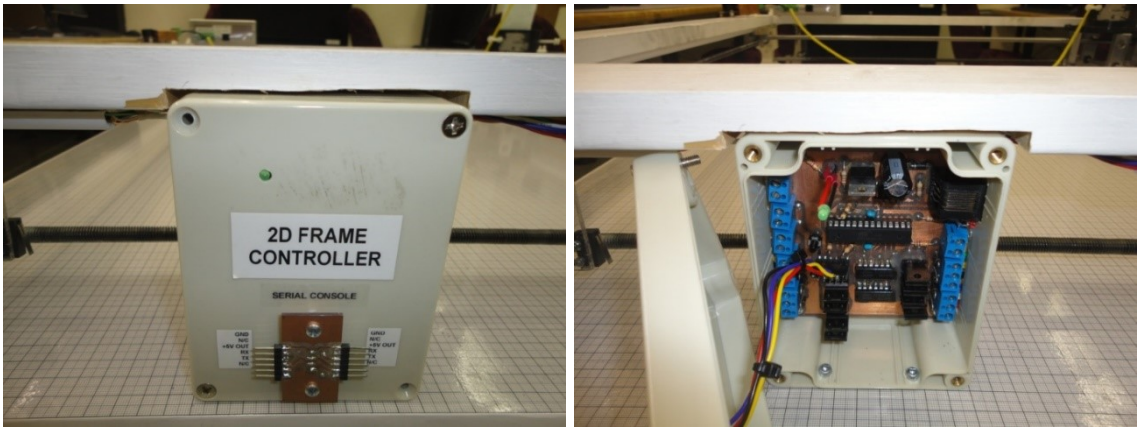

Figure 3.9: 2D Scanner controller.

The 2D Scanner can either operate autonomously in its standalone mode, or be connected by a cable to a computer and controlled externally. Figure 3.10 shows the block diagram of the 2D Scanner for its standalone mode.

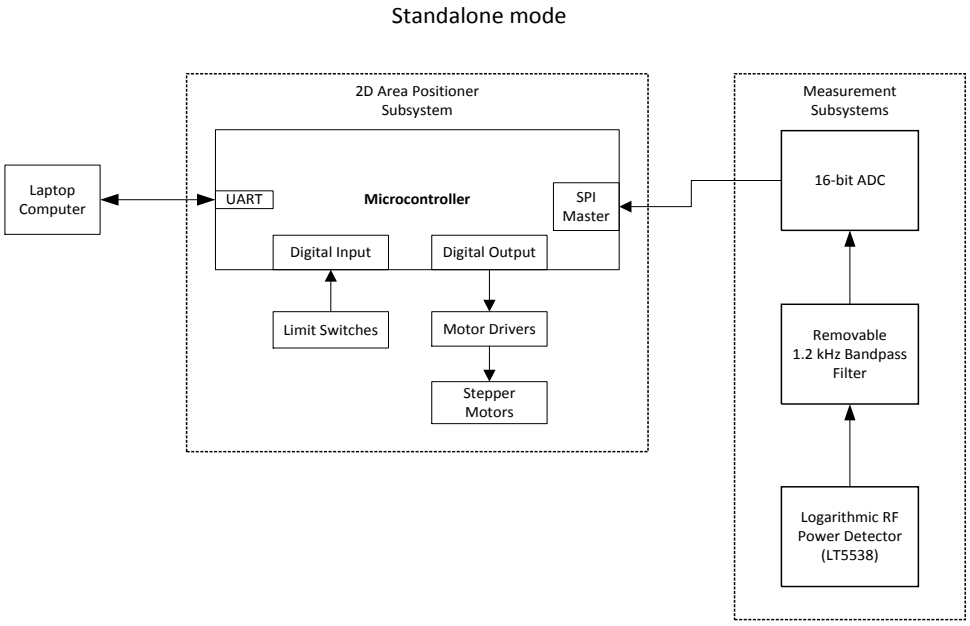

Figure 3.10: Block diagram of the 2D Scanner (standalone mode).

3.2 Electromagnetic Environment

The frequencies of interest in this work are in the 2.4 GHz WLAN band. Because the goal is to measure the electric field strength at points along a path or over a grid in a real indoor environment, which in most cases is covered by the one or more channels of the 2.4 GHz WLAN, the selection of an appropriate experiment frequency is paramount. Ideally, we would choose a frequency that lies in between two of the channels in order to minimize the chance of interference between the experiment signal and the building's wireless network. The 2.45 GHz frequency falls in between the channels 6 and 11, which are non-overlapping channels for the 2.4 GHz WLAN; thus being a suitable choice of frequency for this study.

To verify this assumption, a spectrum analyzer was used to measure the electromagnetic activity in one of the indoor environments considered in this work (15th floor of EV Building). The spectrum analyzer was setup to measure RMS power levels and to hold the maximum reading for each frequency in a range from 2.3 to 2.6 GHz. The analyzer was moved throughout the floor and measurements were taken over a period of 10 minutes. This allowed us to clearly see that the activity at 2.45 GHz was almost non-existent, and confirmed that this frequency was indeed adequate. The result is shown in Figure 3.11. The highest power level detected in the 10 min time window was -68.25 dBm, which is almost the noise floor (-72 dBm) of the detection system used in this work. Notice the need for a bandpass filter centered at 2.45 GHz. It would prevent unwanted signals to add to the power reading of the wanted signal.

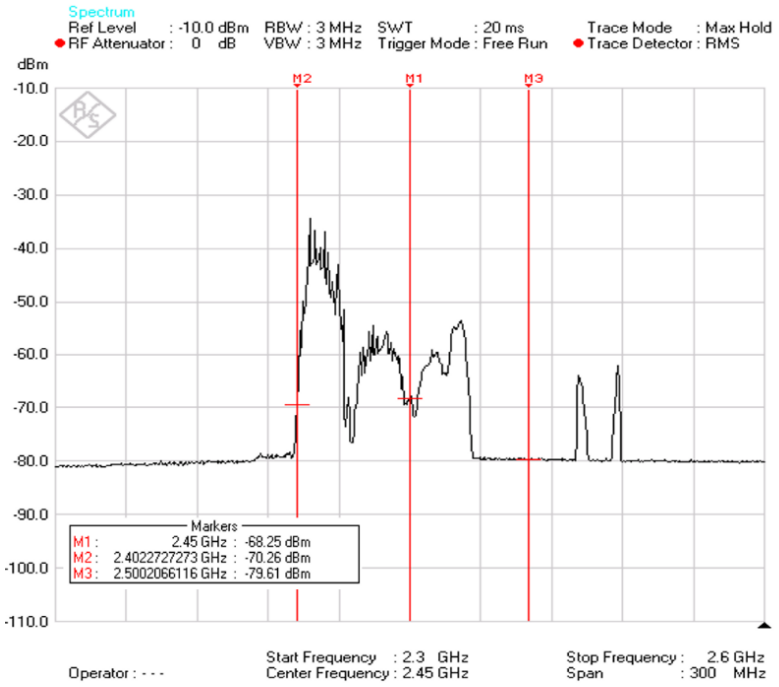

Figure 3.11: Electromagnetic activity on the 15th floor of the EV Building.

3.3 Detection System

As mentioned above, the detection system is presented separately because it is my main contribution to the entire system. The detection system consists of an omnidirectional antenna, a coupled-line filter centered at 2.45 GHz, a power detector (LT5538) [69], a 1.2 kHz bandpass filter, a peak detector, an ADC converter, and a storage media device (SD card), as illustrated in Figure 3.12.

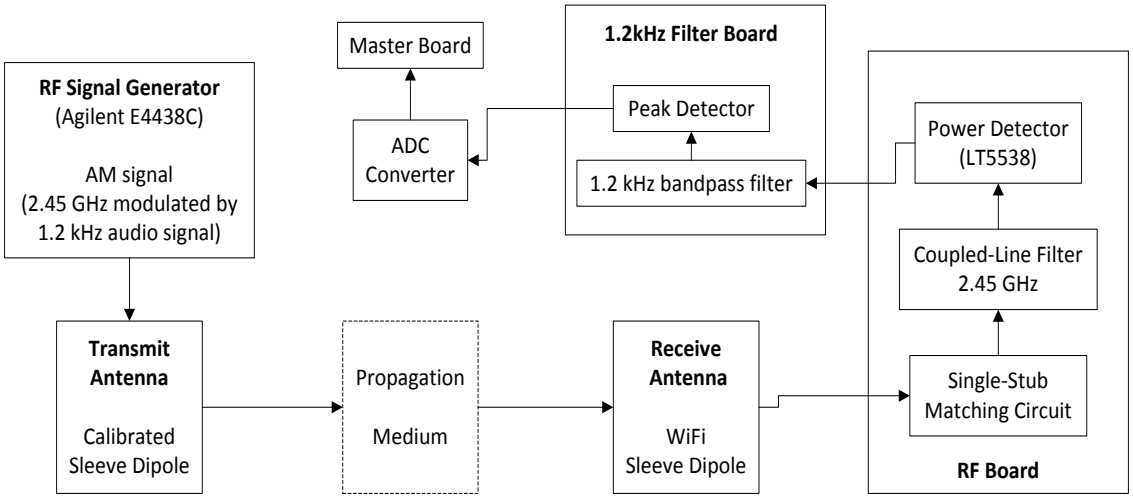

Figure 3.12: Block diagram of the detection system.

3.3.1 Receive Antenna

An omnidirectional receive antenna is used in every experiment presented in this thesis. The reason is that we are interested in measuring the contributions of rays coming from every direction in an indoor environment. The chosen WiFi sleeve dipole antenna is shown in Figure 3.13, and its reflection coefficient in Figure 3.14.

(a) (b) (c)

Figure 3.13: (a) Receive WiFi sleeve dipole antenna. (b) Antenna on top of a Styrofoam pole. The plastic disc supports the antenna mechanically. (c) Antenna in its horizontal configuration.

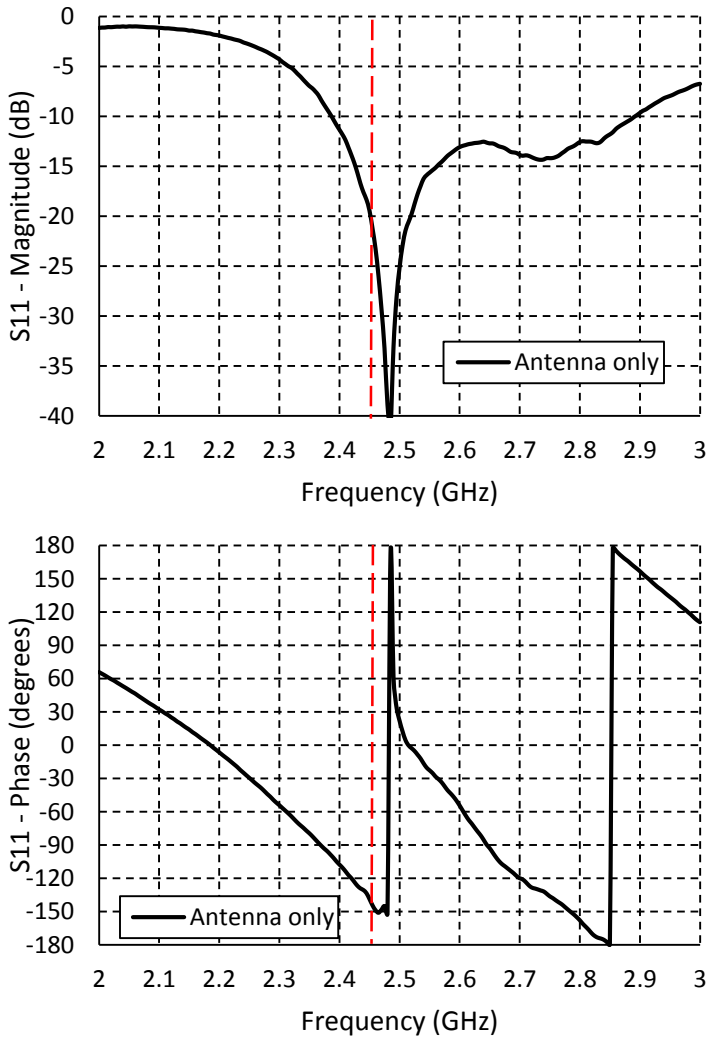

Figure 3.14: Reflection coefficient of the receive antenna (measurement).

3.3.2 Single-Stub Matching Circuit

Even though we can see that the receive antenna has a good match in the 2.45 GHz, in Figure 3.14, this antenna picks up signals relatively well in the range from 2.4 to 2.9 GHz. An open-circuited single-stub matching circuit was designed and implemented to shift the return loss magnitude minimum to 2.45 GHz and decrease the antenna bandwidth. The matching circuit is shown in Figure 3.15, and the reflection coefficient in Figure 3.16. We can see that the antenna is now very well matched to 50 Ohms.

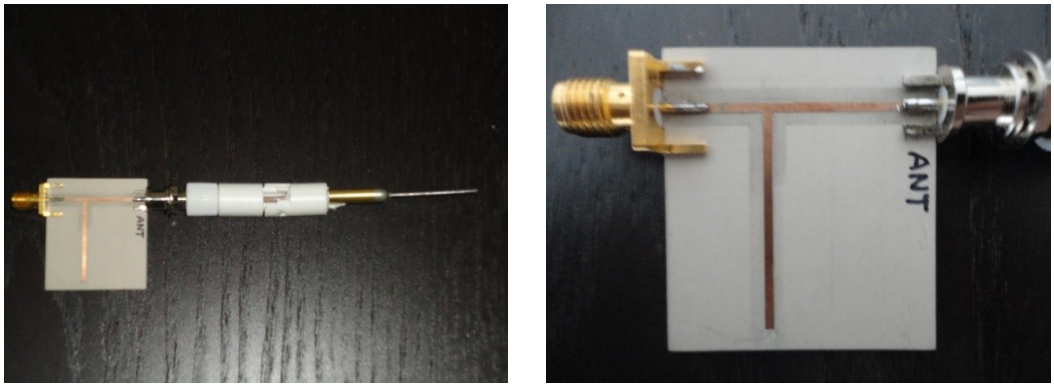

Figure 3.15: Single-stub matching circuit.

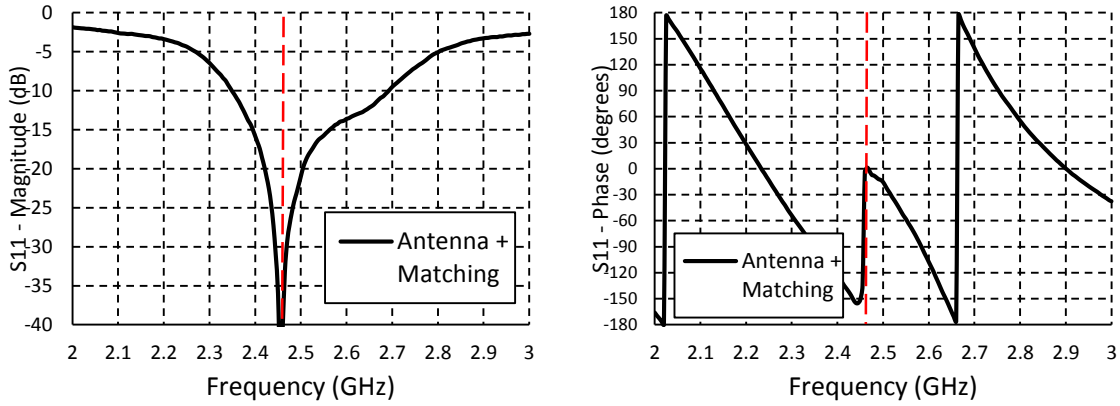

Figure 3.16: Reflection coefficient of the antenna with the matching circuit (measurement).

3.3.3 Coupled-Line Filter

In order to remove unwanted signals present in an indoor environment such as those created by the building's wireless network, a narrow bandpass filter centered at 2.45 GHz is needed. A coupled-line filter was designed for this purpose and is shown in Figure 3.17. Due to the size of the line sections and the separation between them, only a narrow band of frequencies is transmitted through the coupled line sections. Since the signal propagates within the substrate of the filter board, a loss is expected. The return and insertion losses of the filter are shown in Figure 3.18. The -10 dB bandwidth of the filter is 40 MHz.

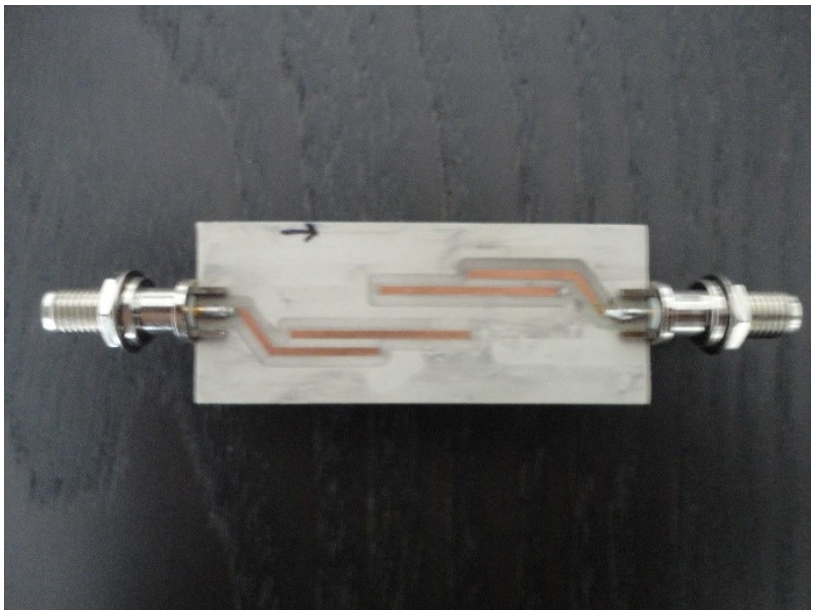

Figure 3.17: Coupled-line bandpass filter.

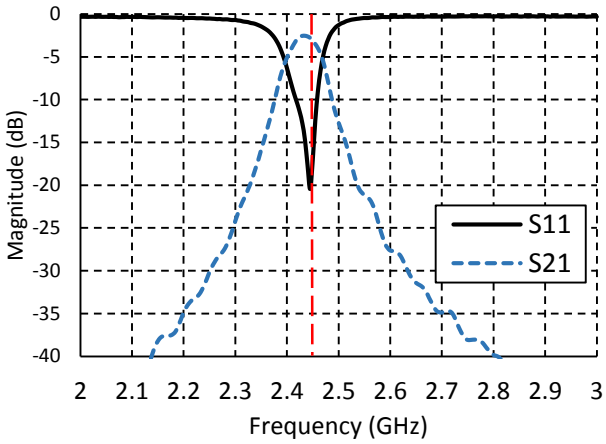

Figure 3.18: Return and insertion losses of the coupled line filter (measurement).

3.3.4 Antenna, Matching Circuit, and Coupled-Line Filter

The reflection coefficient at the input of the couple-line filter when connected to the matching circuit and antenna is shown in Figures 3.20 and 3.21, for the cases where the antenna is in its vertical and horizontal configurations, respectively.

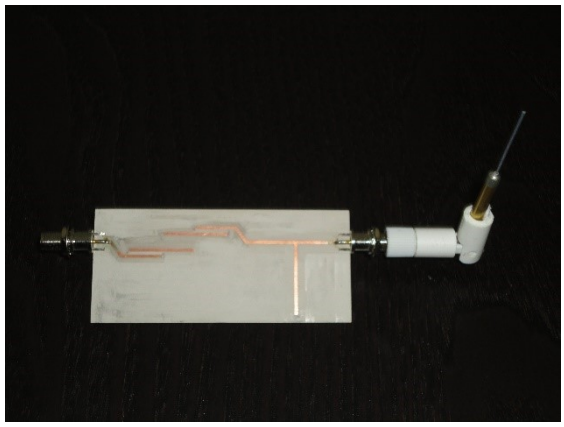

Figure 3.19: Antenna, matching circuit, and coupled-line filter.

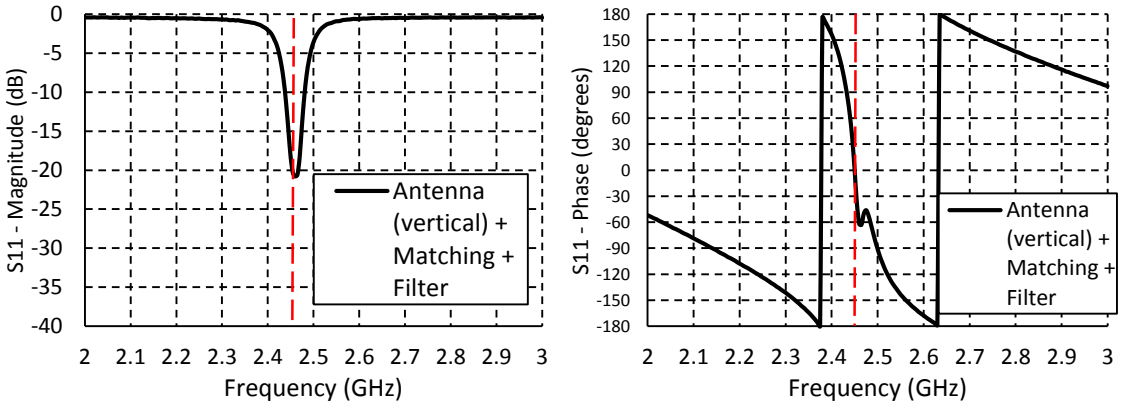

Figure 3.20: Reflection coefficient at the input of the filter for the antenna in the vertical configuration (measurement).

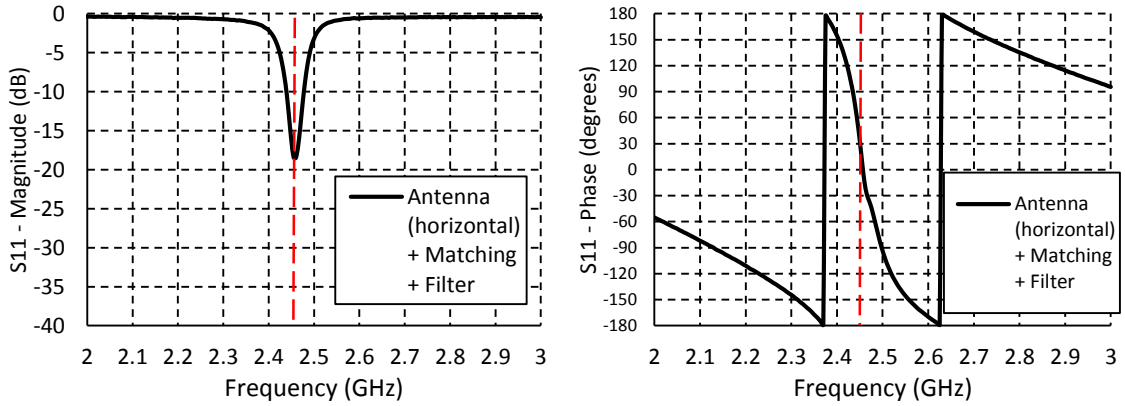

Figure 3.21: Reflection coefficient at the input of the filter for the antenna in the horizontal configuration (measurement).

3.3.5 Power Detector

The power detector used to measure our 2.45 GHz signal modulated with a 1.2 kHz audio signal is the LT®5538 provided by the Linear Technology Corporation [69]. It is a 40 MHz to 3.8 GHz monolithic logarithmic RF power detector with a wide linear dynamic range of 75 dB and a detection sensitivity of -72 dBm. This dynamic range is obtained by

using cascaded RF limiters and RF detector [69]. The detector outputs an accurate linear DC voltage (within ± 1 dB) that is proportional to the input RF signal in dBm for the full temperature range. So, the output voltage of the detector is proportional to the input power. Figure 3.22 shows the power detector connected to the shielded RF board.

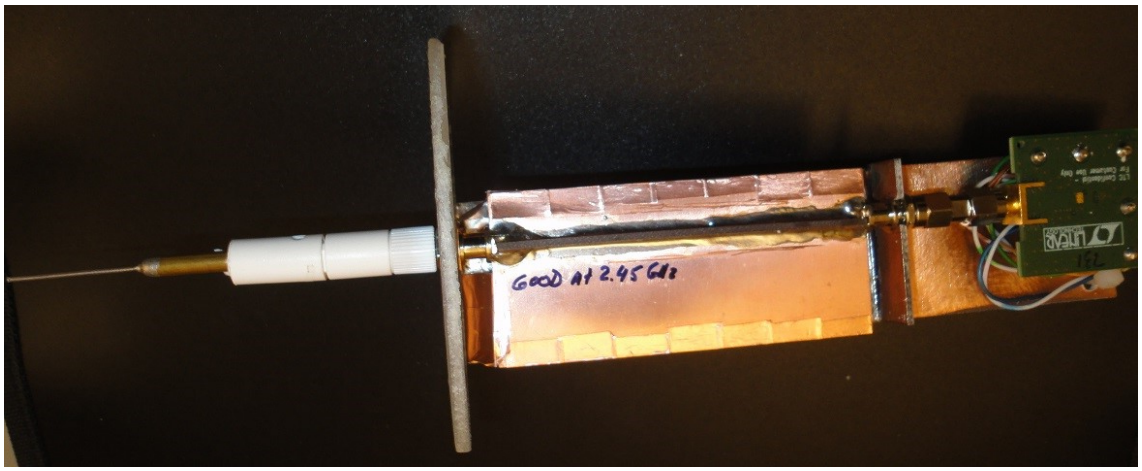

Figure 3.22: Power detector connected to the shield RF board. On the left we see the Wifi antenna, in the middle the shielded RF box, and on the right the power detector.

3.3.6 1.2 kHz Filter Board and ADC Converter

The 1.2 kHz filter board is shown in Figure 3.23. The output signal leaving the power detector is the 1.2 kHz audio signal with a DC offset. It is then sent into a very narrow bandpass filter centered at 1.2 kHz, Figure 3.24, which removes the noise in our signal considerably, since the noise power is proportional to the bandwidth. Then a peak detector circuit measures the amplitude of this signal and sends this information to the ADC converter which in turn sends the data to either the master board or to a computer.

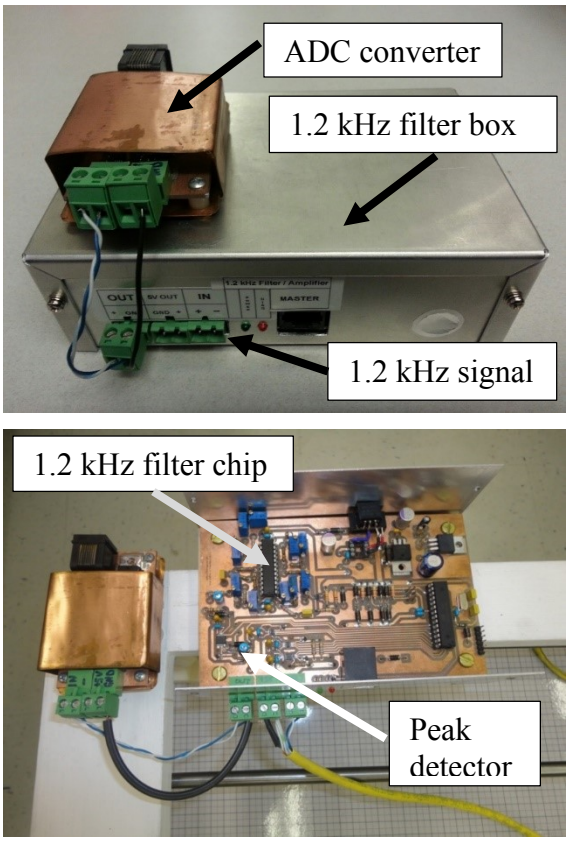

Figure 3.23: 1.2 kHz filter board and ADC converter.

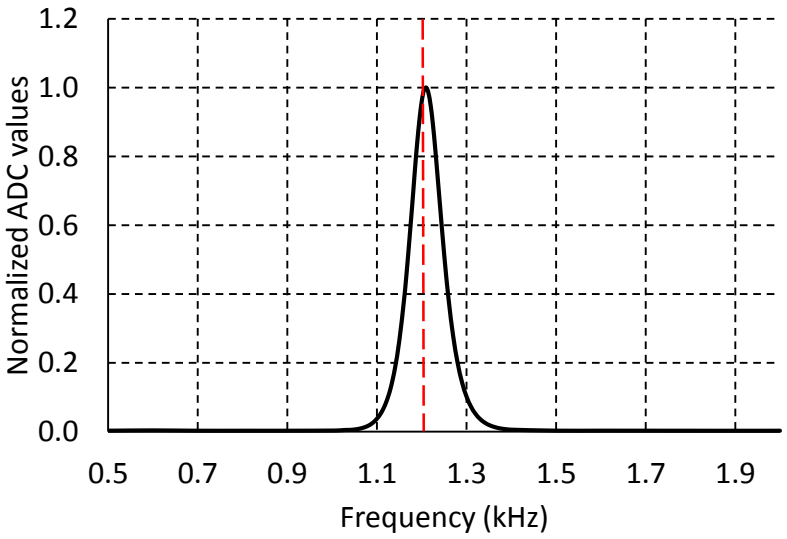

Figure 3.24: 1.2 kHz bandpass filter response.

In order to find a relationship between the ADC values stored on the SD card and the power levels of the signal at the antenna port of the RF board, the port is connected straight to an RF signal generator (Agilent E4438C) and the curve shown in Figure 3.25 is obtained. Notice that the matching stub cannot be removed from the RF board, so the impedance at that port is not 50 Ohms when the antenna is not connected. The reflection coefficient of the port (antenna port) is measured at 2.45 GHz, and the reflected power is then subtracted from the value of power set on the RF signal generator. All the losses in the detection system are taken into account in this calibration curve. The dynamic range of the system is 60 dB.

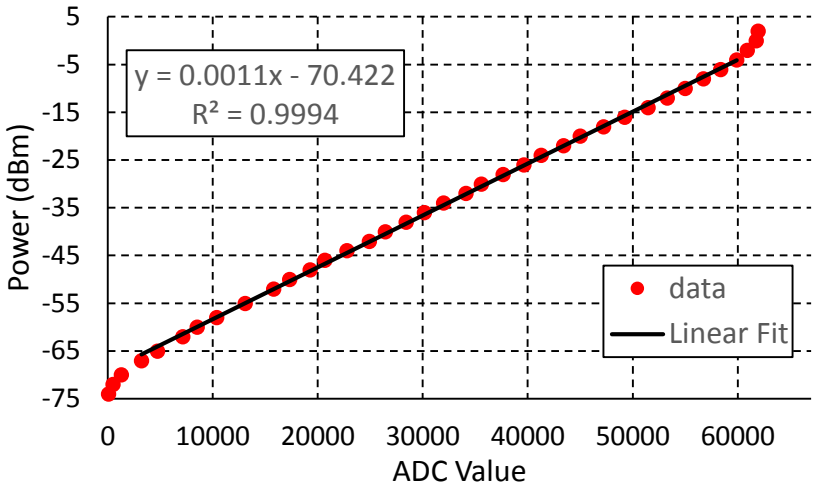

Figure 3.25: Relationship between power and ADC value.

3.3.7 Free-Space Measurement: Calibration to 100 mW

Many portable wireless communication devices radiates a maximum output power of about 100 mW. For this reason, all the simulations presented in this work consider a transmit antenna radiating 100 mW. However, the RF signal generator (Agilent E4438C)

is set to 7 dBm for all of the experiments conducted in this work. This power level is much less than the 100 mW. Therefore, a conversion factor that raises the measured electric field strength to the level of the field strengths obtained with simulation is needed.

To solve this problem, a free-space experiment is conducted in a shielded anechoic chamber. The transmit antenna is fixed and the receive antenna is moved by the 2D scanner along a straight line radially away from the transmitter. Since there is no reflective surfaces inside the chamber and the floor is covered with RF absorbers, this experiment mimics a free-space condition which is the only scenario that we are absolutely certain to be exactly reproducible by ray-tracing simulation. Then, the best fit to the measured data is compared to the simulated curve, as illustrated in Figure 3.26.

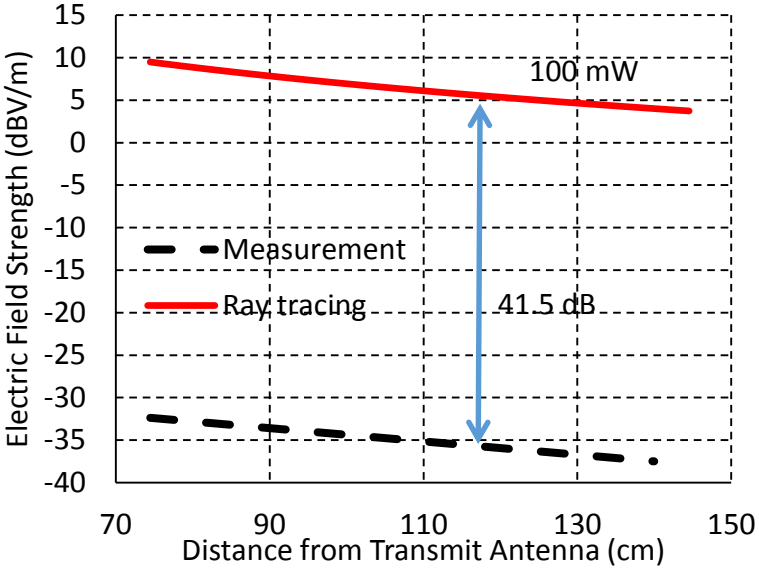

Figure 3.26: Calibration factor. It raises the measured data to the level of the simulated data.

This concludes our description of the measurement system. It should be noted that the power level calibration procedure discussed above does not apply to measurements presented in Chapters 4 and 5. But it is extensively used in the experiments described in Chapters 8 and 9.

In the next chapter we present a method for measuring the dielectric constant of wall construction materials. This method involves measurements with the 2D scanner and detection system described in Chapter 3.

Chapter 4: Dielectric Constant Measurement: Parallel-Path Method

In this chapter we describe our method [34] for measuring the dielectric constant of wall construction materials. This technique, referred to as parallel-path technique, falls into the category of free-space methods and relies on measurement of electric field strength along several paths parallel to the surface of the wallboard panel under test. Furthermore, this method takes into account a range of angles of incidence, as opposed to the approaches used in [55], [54], and [56], which sample normal incidence only. These authors use two broadband horn antennas, one on each side of a slab made of the material under test, and aligned with the propagation path normal to the slab. Although free-space measurement is not as precise as coaxial or cavity measurements [55], it is more suitable for the characterization of heterogeneous wall constructions for indoor propagation [54].

Grosvenor *et al.* [55] reported the dielectric constant of gyproc material to vary from 2.4 to 2.6 over a frequency range from 0 to 6 GHz. The imaginary part of the relative permittivity varies from 0.209 to 0.301 (loss tangent ≈ 0.11). They use a vector network analyzer (VNA) to measure the scattering parameters, and apply time domain gating to isolate the front and back surface responses of the material samples from the environment. Then, the reflection and transmission coefficients are determined and compared to those obtained from a plane-wave model. Parameters of the model are varied so as to obtain the best fit. Muqaibel *et al.* [54] found the gyproc dielectric constant to be approximately 2.4 and the loss tangent less than 0.01 from 2 to 11 GHz, by using a VNA

to measure the insertion transfer function that accounts for multiple reflections from the interior of the slab, for cases in which time gating does not produce satisfactory results. Then, the transmission coefficient is obtained, allowing the extraction of the dielectric constant. Thajudeen *et al.* [56] measure the dielectric constant of several wall constructions by using a VNA and associated Agilent 85071E dielectric constant measurement software. They obtained for the gyproc material a dielectric constant of 2.2 from 1 to 3 GHz, but do not report the loss tangent for this material.

In our method, the dielectric constant is determined by measuring the electric field strength along several paths parallel to the surface of the wallboard panel. The interference between the field of the direct ray and of the reflected ray gives rise to a series of maxima and sharp minima along the path, which are sensitive to the dielectric constant and the wallboard thickness. Comparing GO simulations with the measured field strength for various dielectric constant values allows the best-fit value to be found, as described in the following.

To illustrate the proposed technique, we measure the dielectric constant of gyproc wallboard panels of two different thicknesses, and of a wooden door. In this work, these materials are approximated as lossless because, for example, the skin depth at 2.45 GHz for a material with dielectric constant 2.3 and loss tangent 0.11 is 23.4 cm, much larger than the gyproc sheet thickness of 1.5 cm. Consequently, there is not sufficient material thickness for the wave to be attenuated significantly. The reflected field is not sensitive to small conductivity values for such a thin sheet of low-loss material. This is the reason

why Grosvenor et al. [55] found the measurement of the imaginary part of the complex permittivity to be less accurate than that of the real part.

Gyproc wall construction uses two gyproc wallboards separated by an interior air space, and is simulated in geometrical optics using the plane-wave reflection coefficient for a structure with three layers [32], [33]. Measurements are made of the field strength along a path parallel to the wall surface, and compared with GO simulations which takes into account reflections internal to the gyproc panels. Agreement validates both the measured dielectric constant and the use of the plane-wave reflection coefficient of a layered structure to model reflection from the wall in geometrical optics calculations, also shown in [34].

4.1 Experiment Set-up

Power at 2.45 GHz from an RF signal generator (Agilent E4438C) was radiated by a sleeve dipole antenna. Fields were received by another sleeve dipole antenna connected to a coupled-line filter, and then sent to a peak detector (LT5538) [69] from which power readings were taken and converted into electric field strength readings, as described in section 4.2. The measurements were taken in an anechoic chamber with RF absorber on the walls, ceiling and most of the floor. The floor itself has vinyl tiles over plywood, with a copper mesh underneath.

Figure 4.1 shows the set-up inside the anechoic chamber, consisting of a wall panel, a transmit antenna in a fixed location, and a moving receive antenna carried by a 2D

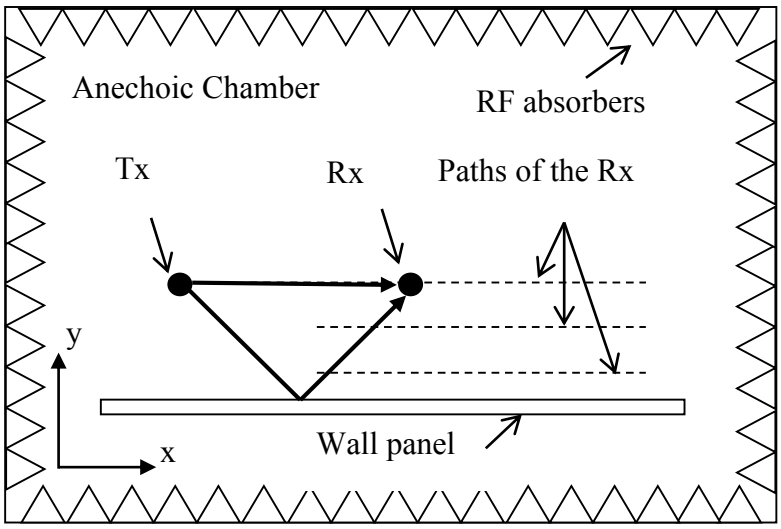

Figure 4.1: Experiment set-up. Single reflection.

scanner in precise 0.5 cm steps along a 65 cm straight line path parallel to the panel. Both transmit (Tx) and receive (Rx) antennas were either vertically or horizontally oriented, and their heights were kept constant at 81 cm above the floor. Both antennas were sufficiently far from the edges of the panel so that the diffracted fields could be ignored. This scenario is very simple because each receiver location sees only the direct ray from the transmitter and the reflected ray from the panel.

Omnidirectional transmit and receive antennas were used because the angle of transmission and arrival of the ray reflected from the panel varies with position along the path. The field strength along the path depends on the reflection coefficient of the panel as the angle of incidence on the wall panel varies. In all the parallel-path experiments, the distance of the Tx from the panel surface was kept constant at 50 cm. The distance of the Tx from the edge of the panel was 70.7 cm. Finally, the distances of the receive paths from the panel surface were 20, 30, 40, 50 and 70 cm.

The simulated field strengths were computed with a half-wave dipole transmitter radiating 1 mW. However, in the measurements, the radiated power was not known. Thus, the measured field strengths were scaled to match the simulated data as described in the following.

4.2 Single-Layered Panels

4.2.1 Metal Panel

The purpose of the metal panel measurement is to establish the scale factor for scaling the measured data in all the path measurements that follow. A metal panel is ideal for this goal because of its well-known reflection coefficient of minus one which is due to the high conductivity of metal. The field strength radiated by a vertically polarized transmit antenna was measured on a path located 30 cm from the metal panel. Then, a scale factor was determined to minimize the root-mean-square error (RMSE) between the measurement and the geometrical-optics simulation.

Figure 4.2 compares the measured and simulated results in dB relative to 1 V/m. The RMSE value is 0.98 dB. Using the same scale factor for the path located 70 cm from the panel, the RMSE is 0.6 dB. Since the same radiated power was used in all the measurements presented in this chapter, the same scale factor was used to scale all the measured data.

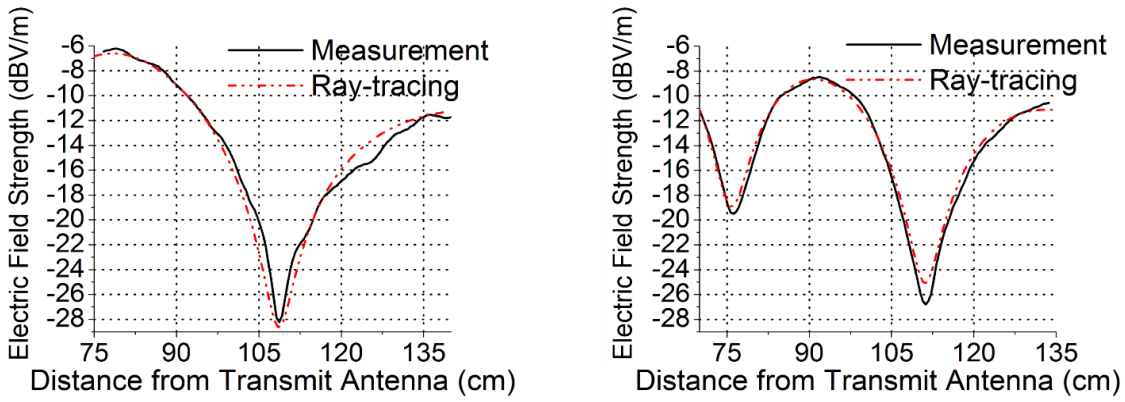

Figure 4.2: Metal panel. Distance from Rx path to the panel: (a) 30 cm; (b) 70 cm.

4.2.2 Gyproc Wallboard (1.5 cm thick)

A gyproc panel of thickness 1.5 cm replaced the metal panel and field strength measurements were taken for paths separated 20, 30 and 70 cm from the panel, with both Tx and Rx vertically polarized. The paper layer covering the gyproc slab is so thin, approximately $\lambda/10000$ at 2.45 GHz, that it has no effect on the measurement. The panel was positioned with an accuracy of ± 3 mm, which is less than $\lambda/20$ at 2.45 GHz. The measured field strength was scaled with the factor determined from the metal panel experiment. To find the dielectric constant of the gyproc, the field strength was calculated with GO using the panel thickness of 1.5 cm, and varying the dielectric constant from 1.7 to 3. The best match of the GO simulation to the measurement was obtained with a dielectric constant of 2.25. Figures 4.3(a), (b) and (c) show the measured and simulated results for the 1.5 cm thick panel at path separations of 20, 30 and 70 cm. The figure shows simulations for different values of dielectric constant, and illustrates that there are substantial changes as the dielectric constant is varied.

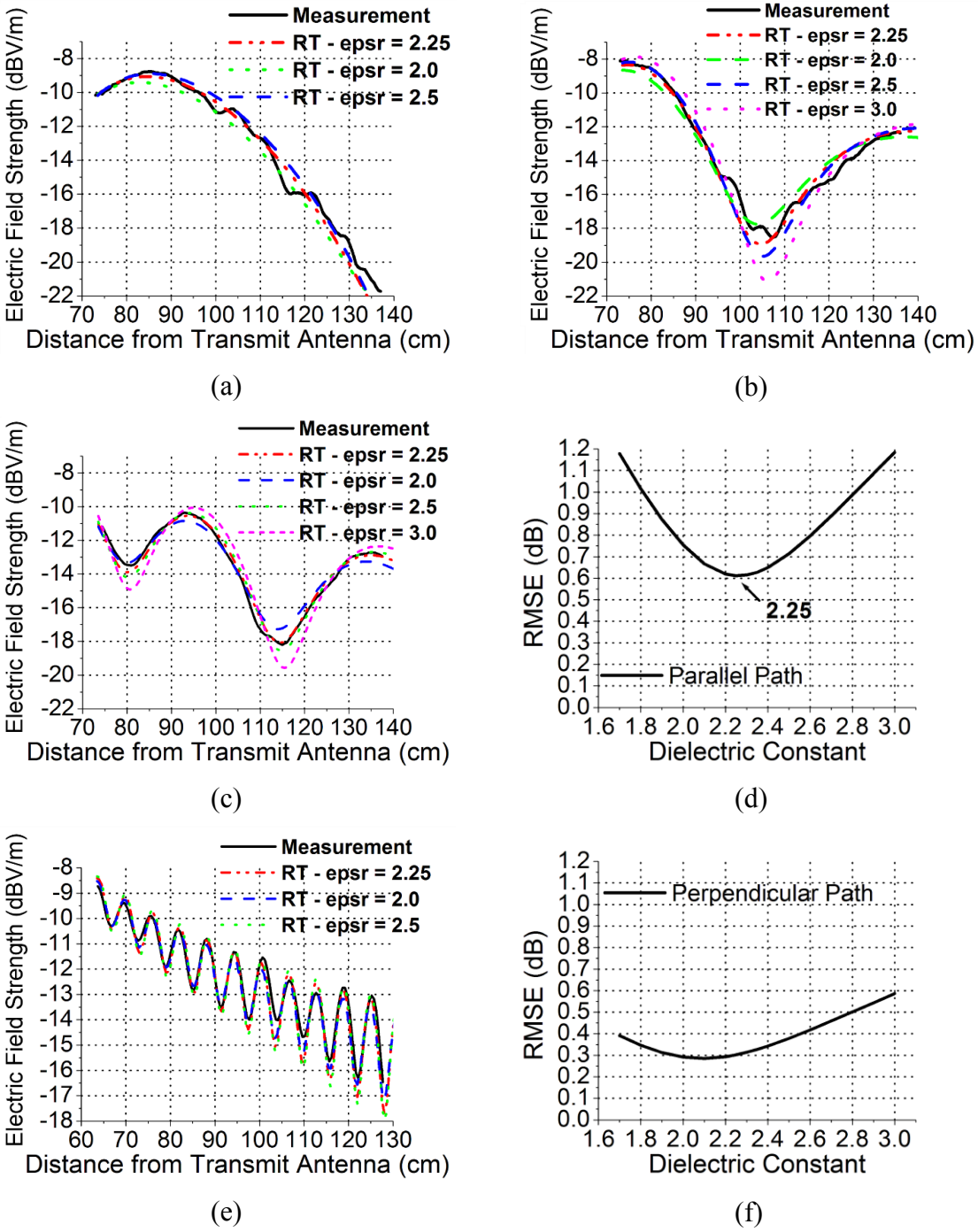

Figure 4.3: 1.5 cm thick gyproc wallboard. Distance from Rx path to the panel: (a) 20 cm; (b) 30 cm; (c) 70 cm. (d) RMSE as a function of dielectric constant for the parallel path located 30 cm from the panel. (e) Normal incidence. Comparison among ray-tracing (RT) simulation data for different dielectric constant values. (f) RMSE as a function of dielectric constant for the path perpendicular to the panel.

Figure 4.3(d) shows the RMSE between the measured field at 30 cm and the GO simulation as function of dielectric constant. The RMSE curve shows a clear minimum at 2.25 with a value of 0.6 dB. Figure 4.3(e) considers a path perpendicular to the surface of the gyproc panel. The normal incidence measurement was used as confidence check that the measurement setup is correct and that the dielectric constant obtains agreement for a different geometry. The Tx antenna was 142 cm from the surface. Figure 4.3(e) also shows that the field strength along the path resembles a standing wave. The disagreement between 100 and 115 cm is probably associated with a slight curvature of the gyproc panel; it was not perfectly flat and plane. The figure shows little difference between the GO simulations as the dielectric constant is changed from 2.0 to 2.25 to 2.5. By visual inspection of Figure 4.3(e) only, it is hard to tell which simulated curve best fits the measured data. Figure 4.3(f) shows the RMSE as a function of dielectric constant for the normal-incidence case. Smaller changes in RMSE as the dielectric constant changes are seen in this case than in the parallel-path case. There is a clear minimum at 2.1 where the RMSE is 0.30 dB. Since the RMSE is much more sensitive to dielectric constant for the parallel-path case, the value from Figure 4.3(d) is the best estimate, with a value of 2.25.

4.2.3 Gyproc Wallboard (1.27 cm thick)

To further investigate whether or not our estimate of the dielectric constant remains the same for a different gyproc slab, a thinner panel from the same manufacturer, of thickness 1.27 cm, was tested. The results are shown in Figure 4.4, and the same value of 2.25 was obtained, with maximum RMSE of 0.52 dB for the case in which the distance from the Rx path to the panel was 30 cm. As can be seen in Figures 4.4(a), (c), and (e),

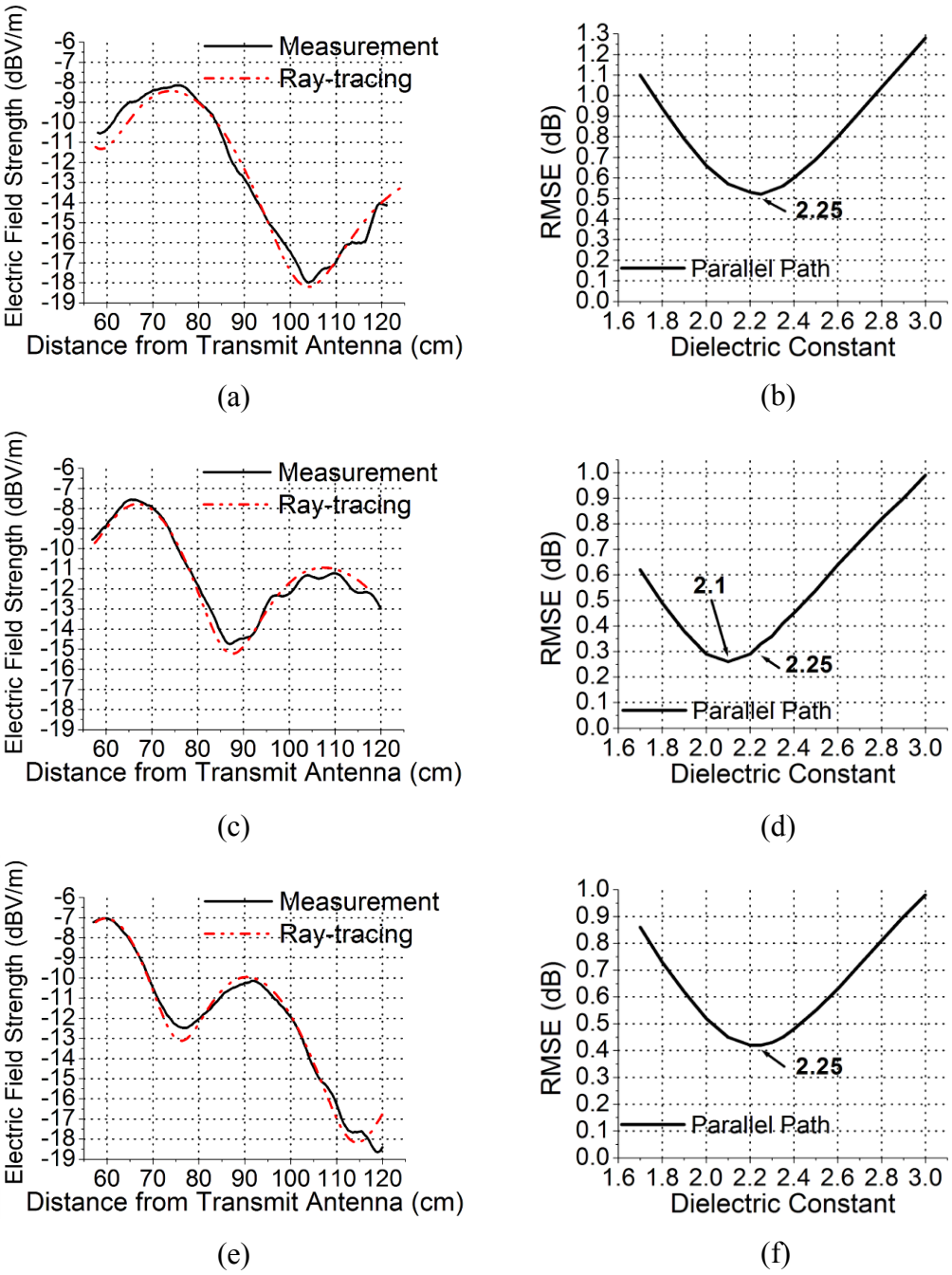

Figure 4.4: 1.27 cm thick gyproc wallboard. (a) Distance from Rx path to the panel is 30 cm; (b) RMSE as a function of dielectric constant for the parallel path located 30 cm from the panel. (c) Distance from Rx path to the panel is 40 cm. (d) RMSE as a function of dielectric constant for the parallel path located 40 cm from the panel. (e) Distance from Rx path to the panel is 50 cm. (f) RMSE as a function of dielectric constant for the parallel path located 50 cm from the panel.

there is excellent correspondence between measured data and simulated data obtained with a dielectric constant of 2.25. It should be noted in Figure 4.4 (d) that the minimum RMSE is found for a dielectric constant of 2.1 instead of 2.25. However, this result is observed for only one of the cases, and the difference between the corresponding RMSEs is only about 0.03 dB.

This experiment confirms that 2.25 is indeed a good estimate of the dielectric constant for a gyproc slab, since it resulted in the best match between measured data and simulated data for all the different geometries considered, as well as for the two different thicknesses of the panels.

4.2.4 Wooden Door

The experiment was repeated with both Tx and Rx vertically polarized, to determine the dielectric constant of the material of a 4.5-cm-thick wooden door. Figure 4.5 shows the measured and simulated results for a dielectric constant of 2.7, which obtained the best agreement between the simulations and measurements at three distances from the door. In this case, the maximum RMSE was 0.4 dB for the case in which the distance from the Rx path to the door was 30 cm. Notice that the minimum RMSE occurs for dielectric constant values of 2.65 and 2.7. However, the difference between the corresponding RMSE values is less than 0.01 dB for all cases, and is also within the RMSE interval corresponding to the resolution of the detection system. Therefore, since these estimates are equivalent, we chose to use 2.7 as the dielectric constant of this particular wooden door for subsequent experiments.

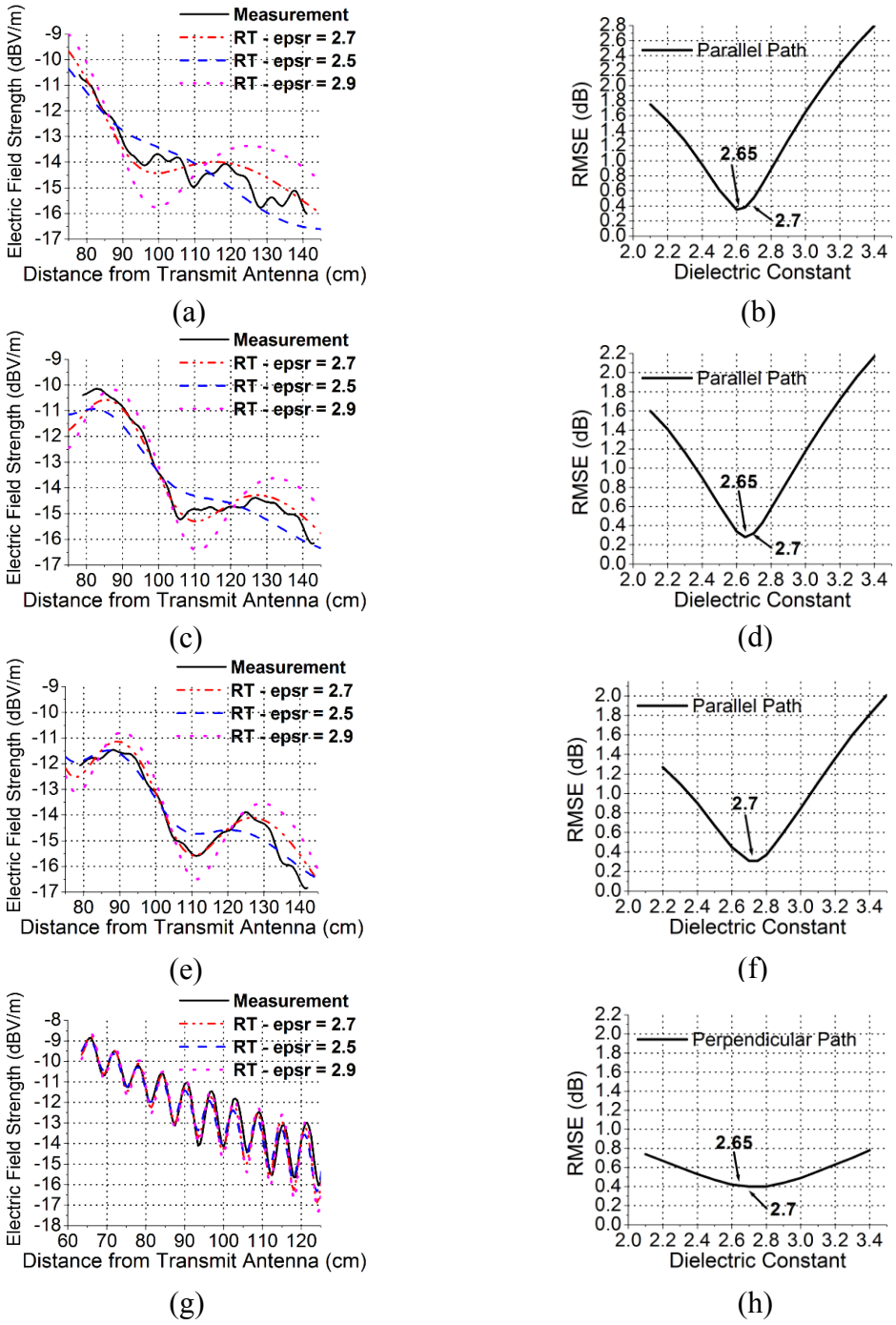

Figure 4.5: Wooden door. (a) Distance from Rx path to the panel is 30 cm; (b) RMSE as a function of dielectric constant for the parallel path located 30 cm from the panel. (c) Distance from Rx path to the panel is 50 cm. (d) RMSE as a function of dielectric constant for the parallel path located 50 cm from the panel. (e) Distance from Rx path to the panel is 70 cm. (f) RMSE as a function of dielectric constant for the parallel path located 70 cm from the panel. (g) Normal incidence. (h) RMSE as a function of dielectric constant for the path perpendicular to the panel.

Once again the normal incidence measurement is shown to be less sensitive to variation in the dielectric constant, Figures 4.5(b), (d), (f), (h). Yet, it is useful as a confidence check as well as for providing an initial range of possible values.

4.3 Three-Layered Wall

Figure 4.6 simulates an interior wall with two 1.5-cm-thick gyproc panels separated by an 8.9-cm air space. Styrofoam spacers were used instead of wood or metal studs to eliminate scattering from studs, a topic treated in Chapter 5. The field strength was measured along parallel paths located 20, 30, 50 and 70 cm from the surface of the wall on the same side as transmit antenna, as well as along paths located 25 and 70 cm from the wall on the other side of the wall. Transmit and receive antennas were both either vertically or horizontally (y-direction) positioned, as illustrated in Figure 4.1. The objective is to verify that the GO code accurately predicts the reflection from and transmission through the surface of a wall built with gyproc panels using the previously-measured dielectric constant of 2.25.

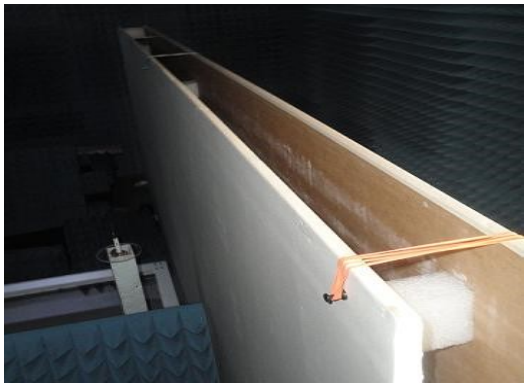

Figure 4.6: Three-layered wall.

4.3.1 Reflection

Figure 4.7 compares measured and simulated results for the perpendicular-polarized case. The RMSEs are 0.95, 1.32, 1.43, and 1.27 dB, for the case in which the Rx path distances from the wall are 20, 30, 50, and 70 cm, respectively. The measured results are very sensitive to the position of the layered wall relative to the Tx antenna and measurement path, as well as to the air spacing between the gyproc slabs. A position error of a few millimeters over the 2.4-m-long layered wall can make a significant difference in the measured field strength and accounts for some of the error in Figure 4.7.

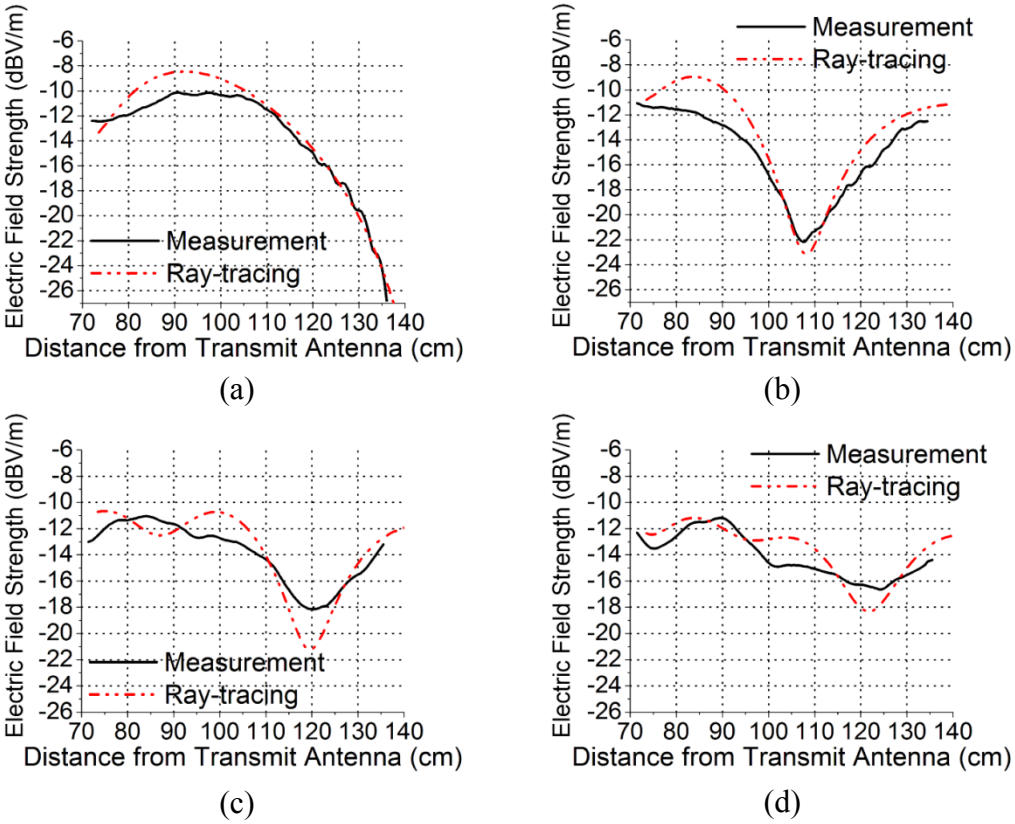

Figure 4.7: Three-layered wall results. Direct plus reflected rays for perpendicular-polarized wave. Distance from Rx path to the wall: (a) 20 cm; (b) 30 cm; (c) 50 cm; (d) 70 cm.

Figure 4.8 shows what happens when the polarization is changed to horizontal. Both transmit and receive antennas were oriented in the y-direction as shown in Figure 4.1, hence they were parallel to the plane of incidence.

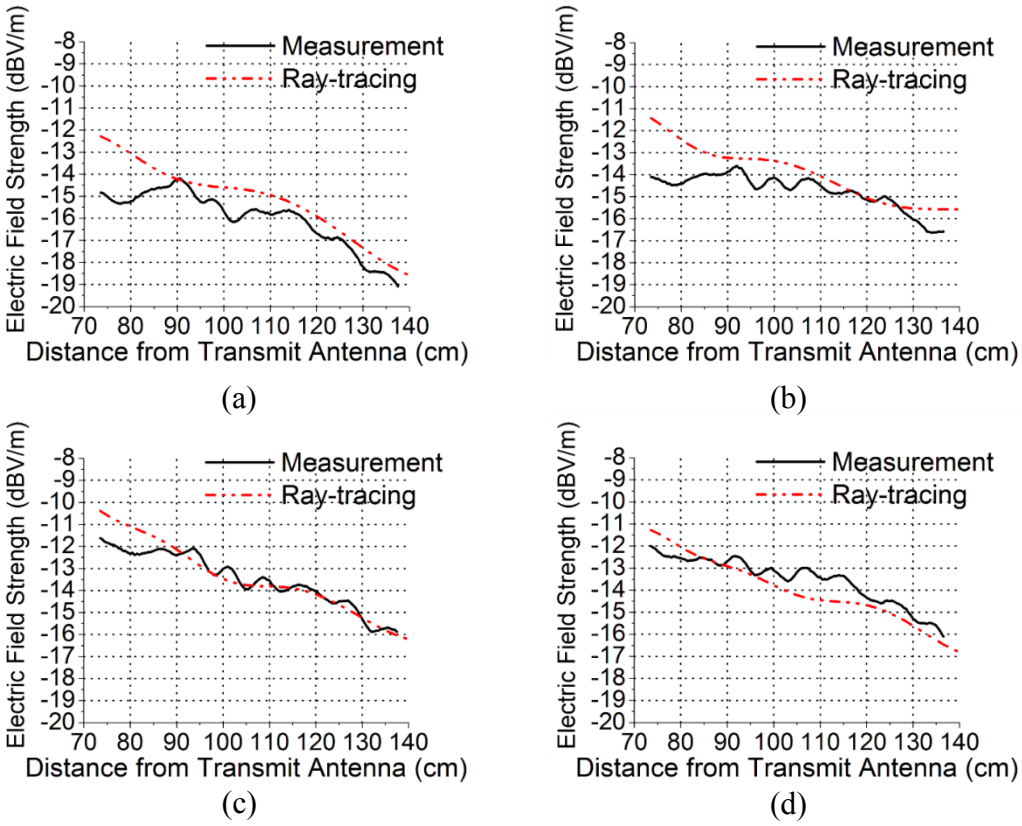

Figure 4.8: Three-layered wall results. Direct plus reflected rays for parallel-polarized wave. Distance from Rx path to the wall: (a) 20 cm; (b) 30 cm; (c) 50 cm; (d) 70 cm.

It should be noted that even though the measurement system does not perform optimally at this configuration, because of the metal RF box located right under the receive antenna inside the Styrofoam pole, we still managed to obtain reasonable agreement between measurement and simulation. Another important aspect of the antennas in this configuration is their radiation patterns, as opposed to what happens when the antennas

are vertically oriented and at the same height. Remember that we are comparing measurements taken with a sleeve dipole to simulations using the fields radiated by a half-wave dipole. Thus, small differences were expected for this case due to differences in the E-field patterns of these types of antennas.

4.3.2 Transmission

Figure 4.9 shows the experiment set-up for the transmission experiment. The purpose of this experiment is to verify whether the plane-wave transmission coefficient is a good model for the layered wall, and whether the dielectric constant measured with the parallel-path method works for this different experiment.

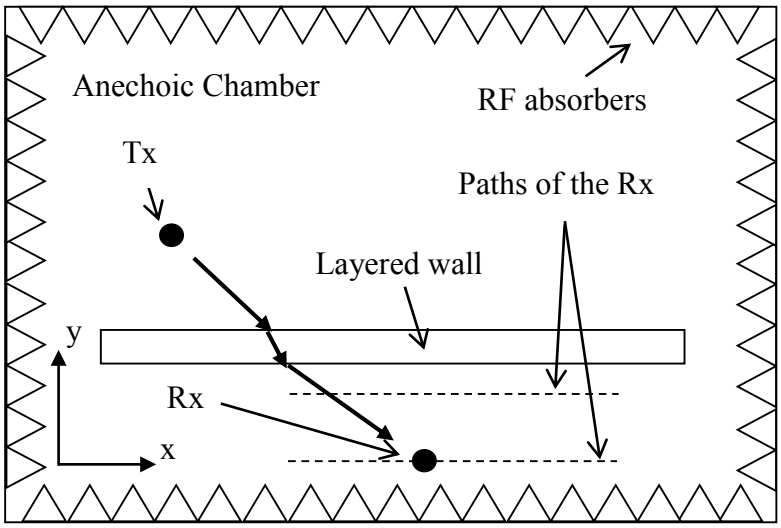

Figure 4.9: Experiment set-up. Transmission.

Figure 4.10 shows the transmitted fields through the three-layered wall along paths parallel to the wall 25 and 75 cm away from the surface of the wall. Both perpendicular and parallel polarized waves were considered. Figure 4.10(a) shows the results for a path 25 cm from the wall for perpendicular polarization, and Figure 4.10(b) for the same path but for parallel polarization.

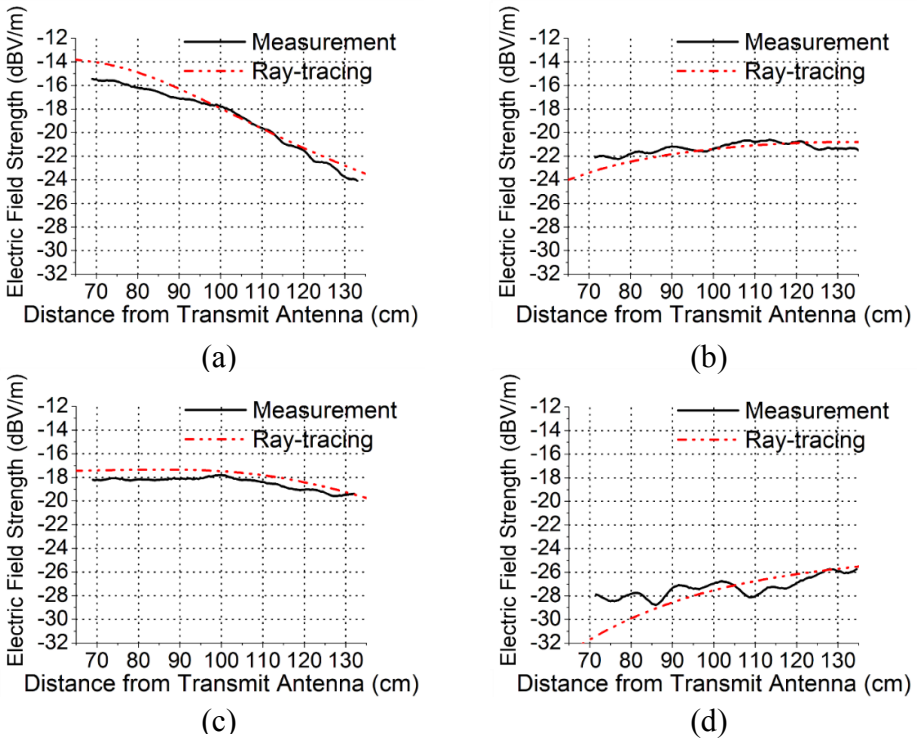

Figure 4.10: Three-layered wall results. Transmitted electric field strength. (a) 25 cm from the wall – perpendicular polarization; (b) 25 cm from the wall – parallel polarization; (c) 70 cm from the wall – perpendicular polarization; (d) 70 cm from the wall – parallel polarization.

Figures 4.10(c) and (d) show the two polarizations for a path 70 cm from the wall. This measurement tests the agreement between the measurement and the simulation for transmission through a layered wall. The conclusions are the following: the layered wall

transmission coefficient is a reasonable model of the three-layered wall, and the dielectric constant measured by the parallel-path method works for the transmission measurements.

4.4 Conclusion

We presented the parallel-path method for measuring the dielectric constant of panels of materials such as gyproc and wood. The receiver moves along a path parallel to the panel surface. The reflected ray from the panel surface samples the reflection coefficient as a function of angle of incidence, and allows for a more accurate estimation of the dielectric constant when compared to that obtained with a normal incidence measurement. The dielectric constants at 2.45 GHz for gyproc was found as 2.25, and for wood as 2.7. Measurements were done to validate the use of plane-wave reflection and transmission coefficients for a layered medium to approximate the case of spherical wave incidence. The conclusion is that the geometrical optics approximation, for both perpendicular and parallel polarizations, obtain reasonable agreement with measurements.

Chapter 5: Controlled Multipath Environments

In this chapter we describe the controlled multipath environments used to study the fast fading and the extent to which it can be predicted with GO. The controlled environments are built in a shielded anechoic chamber to eliminate unwanted reflections such as those from walls, ceiling and floor; as well as to prevent the building's wireless network from contaminating the measurements. A few reflecting surfaces are introduced to control the amount of reflection in a given experiment. By knowing the electrical properties of the surface materials and the precise geometry of the experiment, we can identify the strong and weak aspects of the GO model [27] before we employ it in a real indoor environment, whose geometry and material properties of walls, floor, ceiling, and objects are rarely precisely known.

First, in order to assess how well the GO code accounts for reflections from the floor and to study the extent to which the floor affects the net field, an experiment conducted in a shielded anechoic chamber is discussed. This was necessary because preliminary results suggested that reflections from the floor were responsible for some of the discrepancies found between measurement and simulation. Then, a multipath environment is described, the measured and computed field strength distributions are compared point-by-point, and the result of the statistical analysis of the fast fading is examined. Finally, we introduce metal studs in between two gyproc panels and measure their effect on the electric field strength point by point along a straight path.

5.1 Effect of the Floor on the Net Electric Field Strength

In this section the reflected ray from the floor is shown to have a significant contribution to the electric field strength, and 3D geometrical optics simulation is proven to properly model the floor and account for reflections from it. Notice that in the previous experiments the floor was covered with RF absorber. Here, the floor is taken into account.

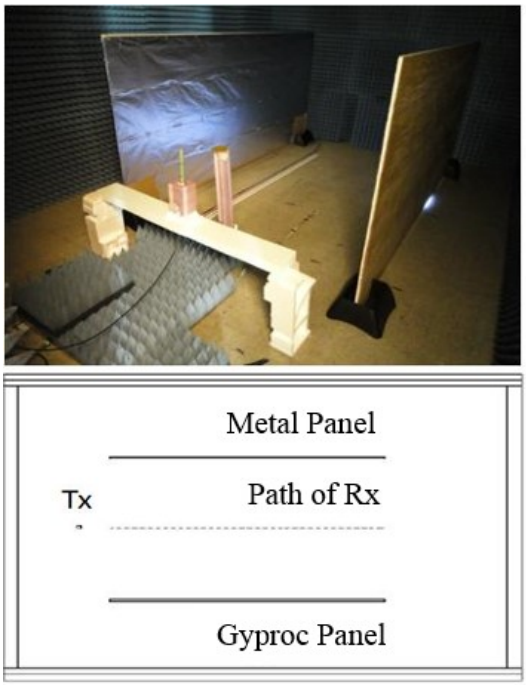

Figure 5.1: Two-panel experiment. A metal panel parallel to a gyproc panel.

Figure 5.1 shows a controlled environment consisting of two parallel flat surfaces, a metal panel and a gyproc panel of thickness 1.5 cm, separated by a distance of 150 cm. The floor is highly reflective because it contains a metal grid below its tiles, thus it was considered as metal in the simulation. As for the gyproc panel, its dielectric constant was

measured to be 2.25 at 2.45 GHz, as discussed in chapter 4. Both transmit and receive antennas were vertically polarized, and their heights were kept constant at 72 cm above the floor. The transmit antenna was fixed and the receive antenna was moved along a straight line, radially away from the transmit antenna and parallel to both walls, by the Line Follower robot in steps of 1 cm.

Power at 2.45 GHz from an RF signal generator (Agilent E4438C) was radiated by a calibrated sleeve dipole antenna. The RF signal was amplitude modulated with a 1 kHz square wave. Fields were received by a monopole antenna on a circular ground plane of a diameter of 8 cm, and with a diode detector connected between the antenna element and the ground plane, as illustrated in Figure 5.2. For this experiment only, the demodulated signal at 1 kHz was amplified and sent to an SWR meter (HP 415 E) from which electric field strength readings were taken. This measurement system was semi-automated. The SWR meter had to be calibrated to a reference field level which was chosen in such a way to make the best use of the meter's dynamic range. Thus, 0 dB corresponds to the field level at the point closest to the transmitter.

Figure 5.2: Monopole Antenna with a diode detector and an amplifier circuit.

5.1.1 Measurement and Simulation

Two situations are considered here: in the first one, measured data is compared to simulation in which the floor is not included; whereas in the second one, the floor is included. The measured data is the same for both cases and does include the floor.

As for the GO simulation, this scenario is complex in terms of number of reflected rays that reach the receive antenna, given that there are multiple reflections between the parallel panels. Therefore, it is fundamental to include enough reflected rays in the simulation in order to properly predict the field strength. The number of rays taken into account is determined by the user by choosing a threshold or minimum field strength. The lower the threshold is, the more rays are considered, thus the longer the computational time is. The idea is to keep decreasing the threshold until no change is observed in the field strength. In this experiment the threshold used was 18 dB below isotropic level, which led to total of 12 reflections.

Figure 5.3(a) compares measured to simulated data and shows reasonably good agreement between them, despite the fact that there is no floor in the simulation. But, by taking a closer look at the minima and maxima in Figure 5.3(a), as well as at the region beyond 80 cm, the curves seem to be slightly shifted. Moreover, in the simulation result, a maximum instead of a minimum appears at 110 cm, suggesting that there are other contributions to the field that could perhaps fix these disagreements.

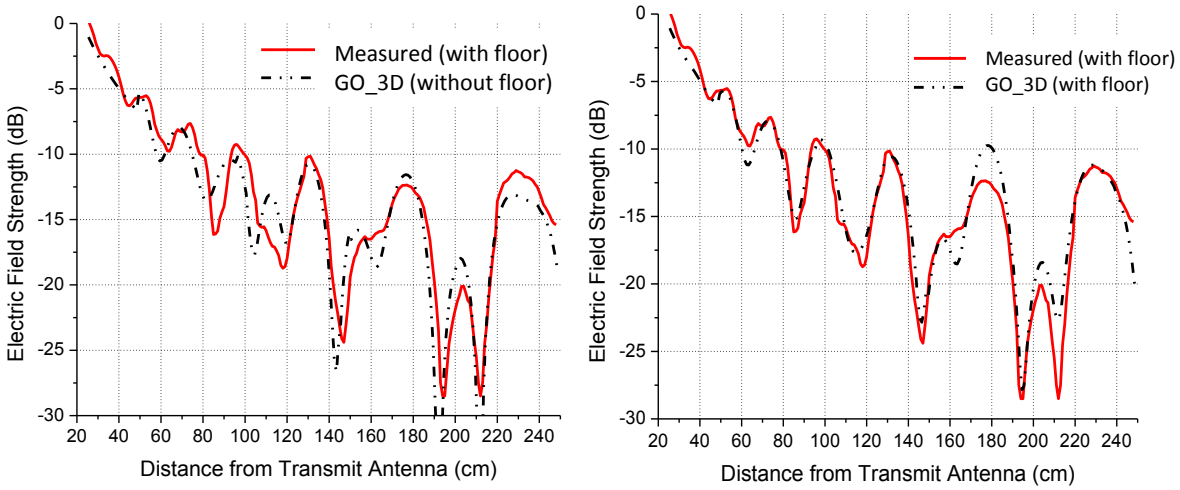

(a) (b)

Figure 5.3: Comparison between measurement and GO simulation. The field strength is in dB relative to the field strength at the point closest to the transmitter. (a) Ray reflected from the floor is not taken into account in the simulation. (b) Ray reflected from the floor is taken into account in the simulation.

The floor was then included in the geometrical optics simulation and the result is shown in Figure 5.3(b). The agreement now is significantly better since all maxima and minima locations are the same for both measurement and simulation. We can also see that the disagreements in Figure 5.3(a) were fixed, including that at 230 cm. However, there is still a 2 dB difference at 178 cm which might have been due to the presence of the moving platform carrying the receiving antenna, since at that location it might have blocked a strong ray reflected from the floor that would have reached the receiving antenna.

This shows not only the effect of the rays reflected from the floor on the resultant field and that geometrical optics can also be used to accurately calculate the specular reflection from the floor, but also that a 2D ray-tracing model would not have been enough to

accurately predict field strength in such a complex scenario, not to mention conventional indoor environments.

This section discusses the effect of the floor on the electric field strength in an indoor environment and the use of a 3D-geometrical-optics-based model for predicting the field. It shows the importance of either including the rays reflected from the floor in the calculation or suppressing these rays in the measurements by putting RF absorber panels on the floor. Besides, this experiment shows that geometrical optics is a good approximation to model electromagnetic field propagation at 2.45 GHz for LOS cases.

5.2 Fast Fading in a 65 by 65 cm Region

5.2.1 Experiment Set-up

Three regions in the vicinity of the transmit antenna are considered in this subsection, in attempt to emulate a situation in which a person carrying a communication device is in proximity to a medical equipment. Such a scenario is the one with highest probability of EMI occurrence.

Figures 5.4 and 5.5 show the controlled multipath environment built inside the anechoic chamber, which consists of two parallel planar "walls" separated by a distance of 152 cm, and of a planar wooden door which is positioned perpendicular to the walls. Notice that in Figure 5.4 the door is in the back of the room, 3.02 m away from the transmitter, and does not block the line-of-sight path from the transmitter to the measurement regions;

whereas in Figure 5.5 the door is only 1.145 m away from the transmitter, and so the measurement region is at non-line-of-sight to the transmitter. One wall is a 1.5-cm-thick gyproc panel and the other is a three-layered wall consisting of two 1.5 cm thick layers of gyproc and a 9.8 cm thick central layer of air. The gyproc panels and the wooden door were modeled as low-loss materials with measured dielectric constants of 2.25 and 2.7, respectively, at 2.45 GHz [34], [56]. Both transmit (Tx) and receive (Rx) antennas were vertically polarized, and their heights were kept constant at 81 cm above the floor.

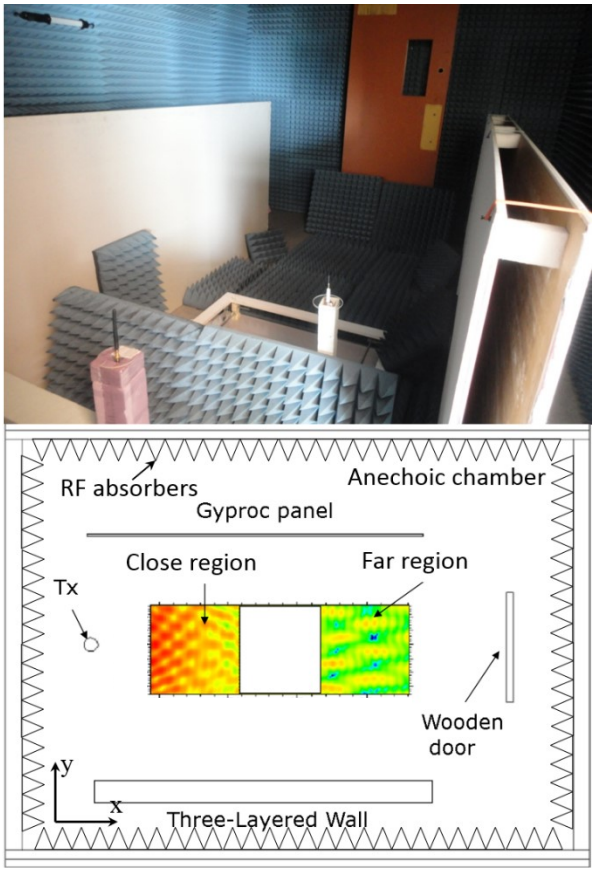

Figure 5.4: The controlled multipath environment in an anechoic chamber for the LOS cases.

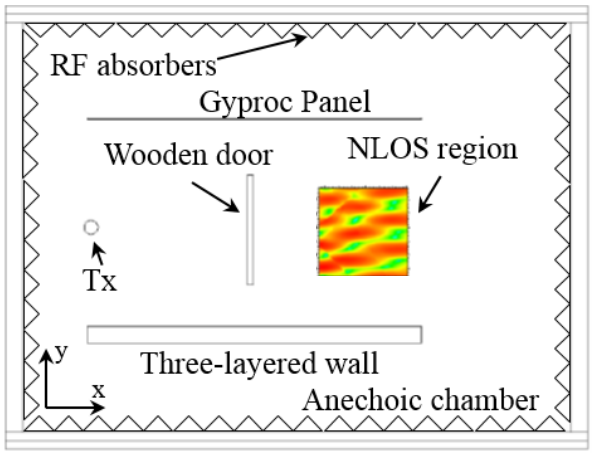

Figure 5.5: The controlled multipath environment in an anechoic chamber for the NLOS case.

The transmit antenna was in a fixed position, and the receive antenna was moved on a 65 by 65 cm horizontal plane in steps of 1 cm for the LOS cases, generating a total of 4225 field measurements; and on a 65 by 61 cm plane for the NLOS case, generating 3965 field measurements. Two regions were considered for the LOS case: centered 1.50 m from the transmit antenna or "close", and 2.48 m away from the antenna or "far". As for the NLOS case, the measurement region was also centered between the gyproc wall surfaces, with its center located 2.48 m away from the Tx and 1.29 m from the back surface of the door. Omnidirectional transmit and receive antennas were used because the angles of transmission and of arrival of the ray reflected from the walls vary with position across the region.

Power at 2.45 GHz from an RF signal generator (Agilent E4438C) was radiated by a sleeve dipole antenna. Fields were received by another sleeve dipole antenna connected to a coupled-line filter, and then sent to a peak detector (LT5538), as described in chapter

3, from which power readings were taken and converted into electric field strength readings.

5.2.2 Measurement and Simulation

The radiated power by most mobile devices are limited to around 100 mW. Therefore, for the purposes of this study, the simulated field strengths were computed with a half-wave dipole transmitter radiating 100 mW. In the measurements, the radiated power was unknown. Therefore, the measured field strengths were scaled to match the simulated data by multiplying the measured data by a scale factor. This factor was determined from the ratio of the measured to the simulated medians of a 25 by 25 cm sub-region of the close region closest to the Tx, where the contribution of the direct field was highest. The same scale factor was used to scale the measured data corresponding to the LOS and NLOS regions far from the Tx.

The controlled multipath environment illustrated in Figures 5.4 and 5.5 is fairly complex in that a large number of rays can contribute to the field at any point in the region of interest. There are paths with a single reflection from one of the walls, paths with two reflections, one from each wall; and paths with multiple reflections back and forth between the walls. In addition, there are paths including reflection from the wooden door, and reflections from the walls and the door. The interference of the fields associated with all these ray paths results in the multipath field. Then the interference of the direct field with the multipath field gives rise to the fast fading in the region of measurement.

Figures 5.6 and 5.7 compare the measured and simulated results in dB relative to 1 V/m. Figure 5.6 depicts the electric field strength in the region close to the Tx in Figure 5.4, whereas Figure 5.7 depicts the field in the region far from the Tx, and close to the wooden door. At both distances, there appears to be excellent correspondence between measurement and 3D geometrical optics simulation, with the locations of maxima and minima predicted by ray-tracing in agreement with those found by measurement. The degree of agreement can be assessed with the root-mean-square error (RMSE) between the measured and simulated field strengths. For the close region the RMSE is 0.30 V/m for a field strength range from 0 to 7 V/m; and for the far region it is 0.31 for a field range from 0 to 3 V/m. These RMSE values are not very small when compared to the field range, and shows the difficulty in getting point-by-point agreement.

Figure 5.8 compares the measured and simulated results in dB relative to 1 V/m for the NLOS case. Again, excellent correspondence between measurement and 3D geometrical optics simulation is observed. The RMSE between the measurement and the simulation is 0.39 V/m for a field strength range from 0 to 3 V/m. Notice that there is a GO shadow boundary in the figure corresponding to the simulated data. This shadow boundary would disappear if edge diffraction from the wooden door were accounted for.

Figures 5.9 and 5.10 show that the empirical cumulative distribution functions obtained from the measured and simulated data are very similar for the LOS close region and are almost identical for the LOS far region and NLOS region.

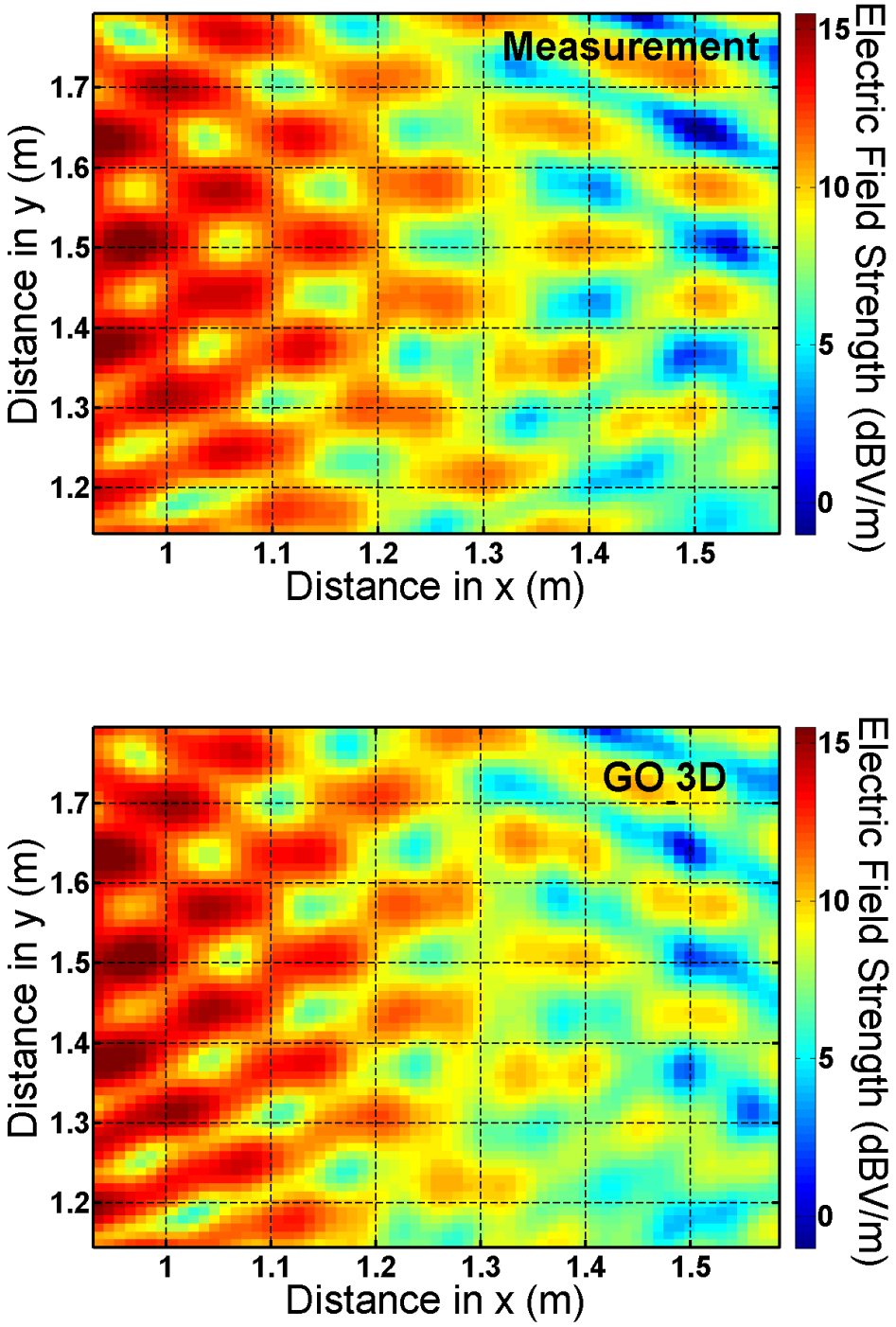

Figure 5.6: Comparison between measurement (top) and 3D geometrical optics simulation (bottom) for the region close to the transmit antenna in Fig. 5.4.

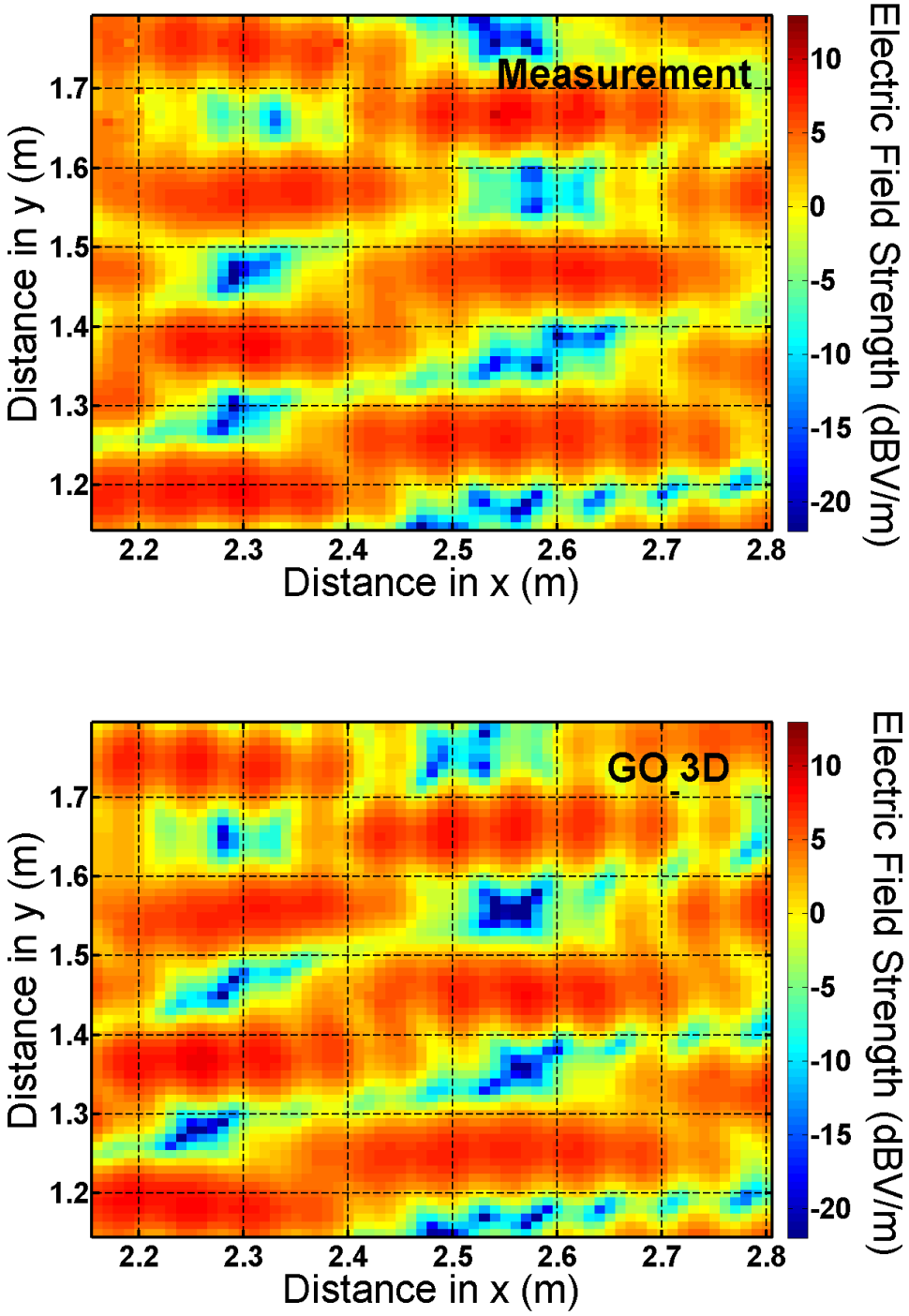

Figure 5.7: Comparison between measurement (top) and 3D geometrical optics simulation (bottom) for the region far from the transmit antenna in Fig. 5.4.

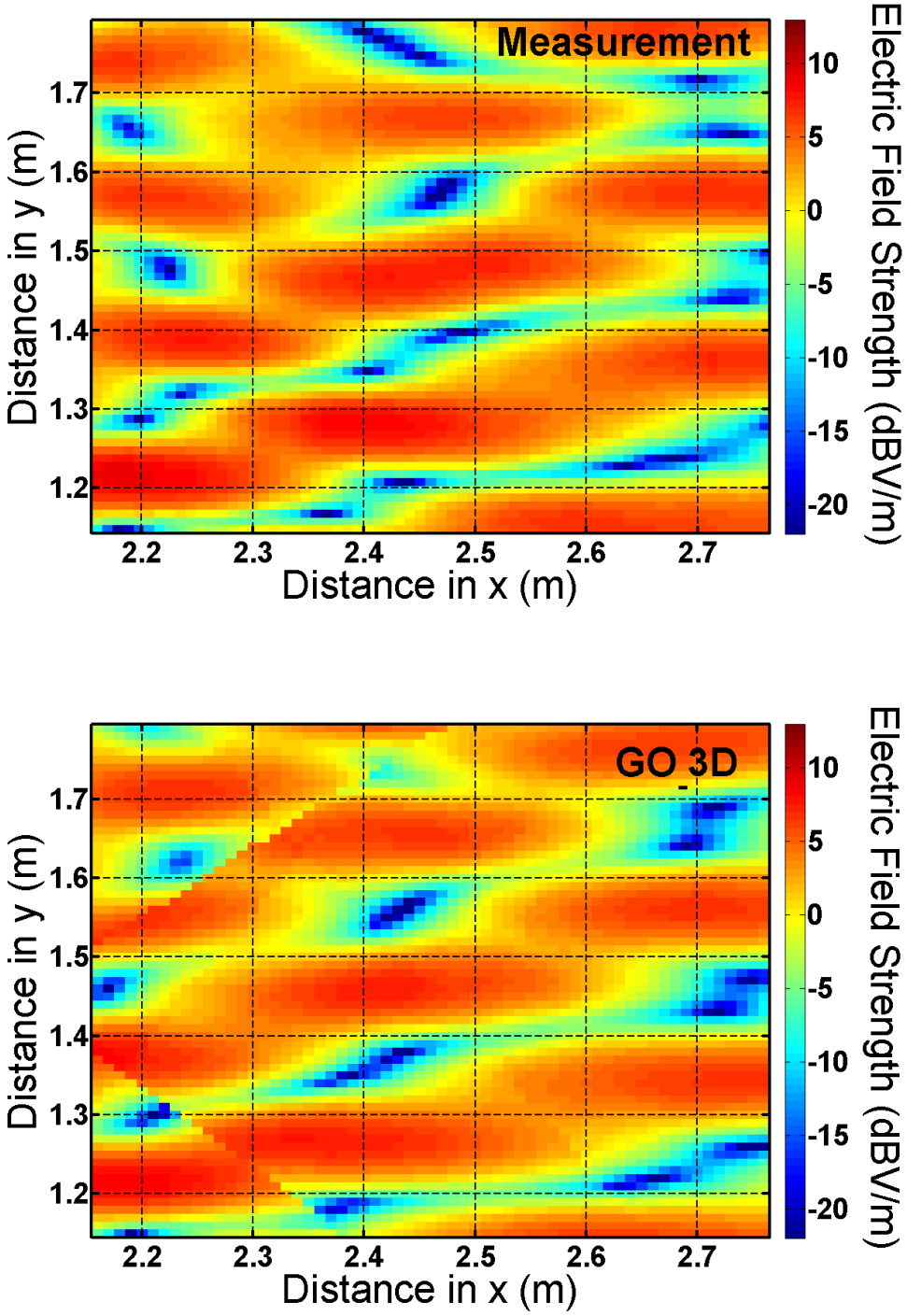

Figure 5.8: Comparison between measurement (top) and 3D geometrical optics simulation (bottom) for the region in Fig. 5.5.

Despite the difficulty in attaining point-by-point agreement and the existence of a shadow boundary for the NLOS case, the GO computation still managed to predict the statistics of the field.

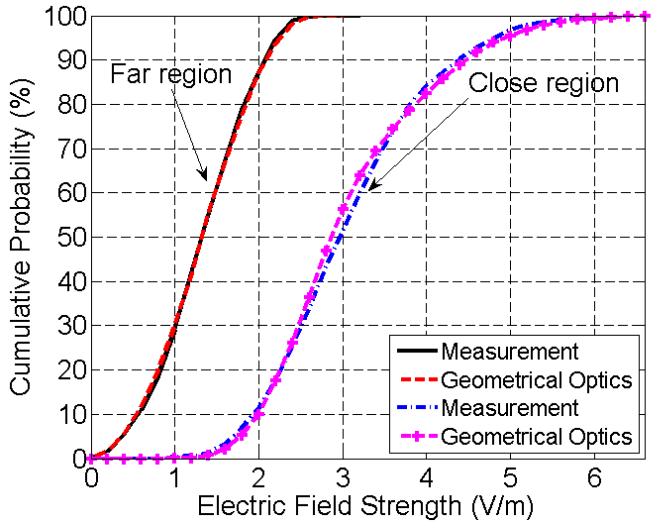

Figure 5.9: Measured and simulated cumulative distribution functions for LOS regions.

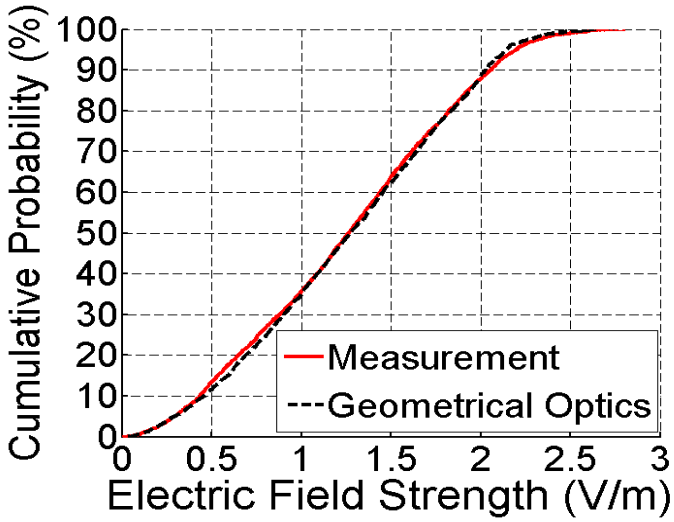

Figure 5.10: Measured and simulated cumulative distribution functions for NLOS region.

In order to objectively assess to what extent these CDFs are similar, the Friedman's test [70] for two related samples was applied to each case with a significance level of 5%. This is a nonparametric test of the following null hypothesis: the distributions of the two related samples are the same. Friedman's test is sensitive to differences in median, dispersion, skewness, and so forth. For the LOS regions close to and far from the Tx, a p-value of 0.52 and 1.0 was obtained, respectively; whereas for the NLOS region, the p-value was 0.63. Since the p-values are greater than 0.05, we conclude that the distributions are the same.

Thus, geometrical optics is suitable for predicting the local fast fading of the field for site-specific environments, provided that the geometry of the scenario and the electrical properties of the walls are known.

5.3 Metal Studs

5.3.1 Three-Layered Wall with Metal Studs

In order to study the effects of reflected and diffracted rays created by metal studs on the net field strength, a point-by-point comparison of measured field strengths along a path parallel to a three-layered gyproc wall, with and without metal studs in between the gyproc slabs, is made. The experiment set-up is shown in Figure 5.11. This gyproc wall consists of two 1.5-cm gyproc panels and of a 10-cm internal air layer. It contains 4 metal studs separated by 40 cm.

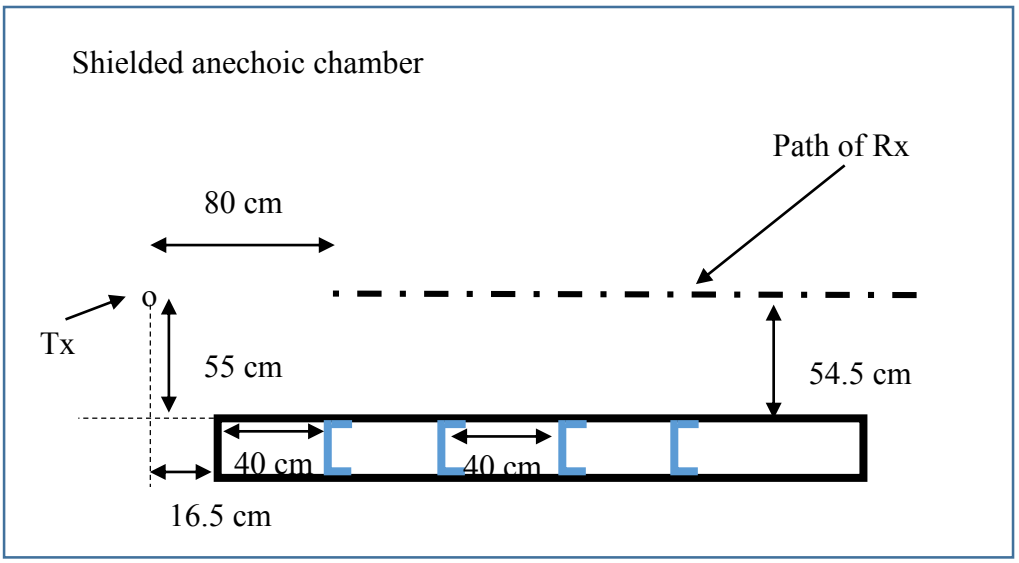

Figure 5.11: Experimental set-up for the three-layered wall with metal studs.

Measurements were taken along a 230-cm long path of receivers in steps of 1 cm. The measurement system used in this experiment was the one described in Chapter 3. The field strength readings were scaled to the simulated fields according to the calibration curve in Figure 3.26.

Figure 5.12(a) compares measured data (no stud) with GO simulation. We can see that the GO code successfully models the three-layered wall without metal studs. This was also shown in chapter 4. The small differences are due to the difficulty in keeping the 2.4-m long gyproc panels perfectly aligned and parallel. It was observed during the measurement campaign that variations of 0.5 cm in the spacing between the gyproc layers affected significantly the field strength between 80 and 140 cm. The position of the minimum was affected more strongly by errors in the alignment of the gyproc slabs and in the distance from the parallel path of receivers to the wall. With this in mind, we could

also attribute the small differences observed in Figure 5.12(a) to the non-perfectly flat gyproc panels.

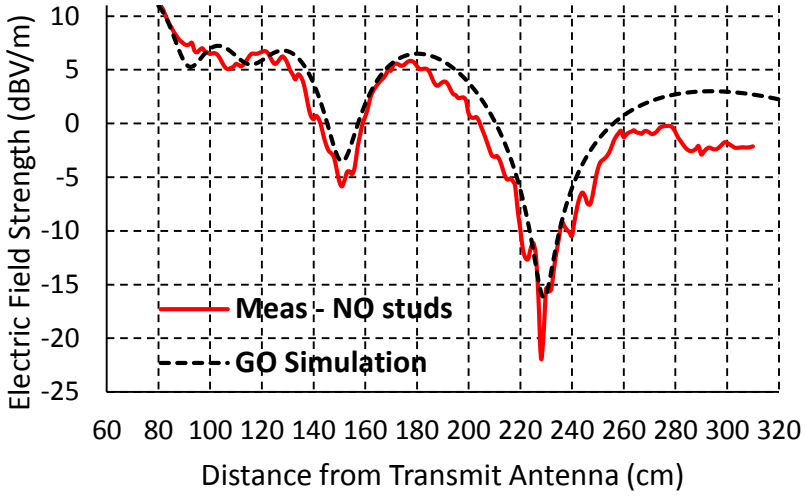

(a)

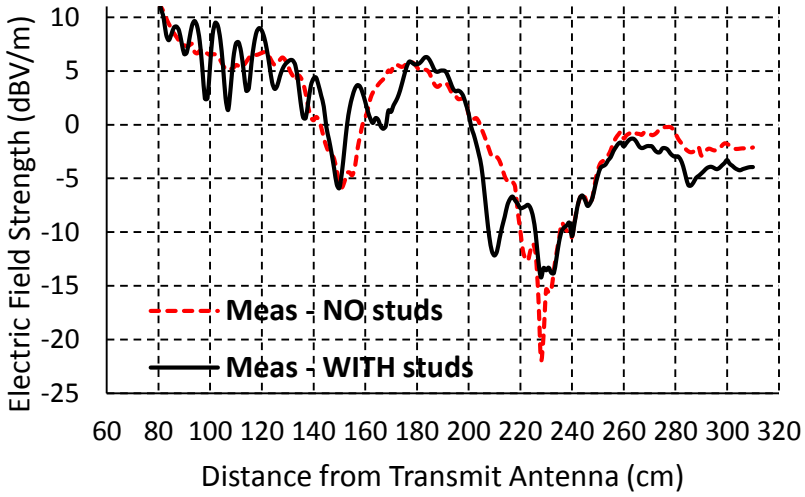

(b)

Figure 5.12: (a) Comparison between measurement (no stud) and GO simulation. (b) Comparisons between measurement (no stud) and measurement (with stud).

Figure 5.12(b) shows what happens when four metal studs are inserted in between the gyproc slabs. As we can see, reflected and diffracted rays created by the studs cause additional variation on top of the GO field, as expected. It is clear that the GO model does not capture variation caused by diffracted rays. However, it does capture the average field level and the overall behavior of the field strength.

5.4 Conclusion

The first conclusion is that reflections from the floor have to be eliminated by covering the floor with RF absorber. This was done for the measurements presented later in the chapter.

Geometrical optics can be used for predicting the fast fading of the field for site-specific environments at 2.45 GHz, provided that the geometry of the scenario and the electrical properties of the reflective surfaces are known. Moreover, besides being computationally less expensive than UTD, GO is useful to capture the statistics of the fast fading.

Finally, it is also shown that reflected and diffracted rays created by the studs cause additional variation on top of the GO field. Thus, GO fails to predict field strength point by point in the presence of metal studs. In spite of that, it does capture the average field level and the overall behavior of the field strength.

Chapter 6: Statistical Analysis of the Fast Fading in a Controlled Environment

The small-scale spatial variations of the electric field or "fast fading" in an indoor propagation environment are often calculated by ray tracing, and then modeled with a probability distribution. In this chapter, the Anderson-Darling test, described in the literature review chapter, is used to test four probability distributions for goodness-of-fit to the measured data presented in Chapter 5, Figures 5.6, 5.7, and 5.8. The statistical distributions considered in this work are the following: Ricean, Normal, Nakagami, and Weibull distributions.

Since closely-spaced measured data points are correlated, a correlation coefficient is used to estimate how far apart data points should be so that they are almost independent, and the set of 4000 points is thinned to roughly 200 points. Six subsets of the original 4000 points are compared, and Friedman's test is used to show that the subsets have the same statistics. Then the MLE method is used to find the best fit for each of the four probability distributions to the entire set of 4000 points. The Anderson-Darling test is used to assess whether each probability distribution can represent the data. For all three scenarios, any of the four probability distributions is shown to be suitable to represent any of the subsets of measured data points, given that the parameters of the distribution are chosen by the MLE method. The conclusion is that, besides being computationally less expensive than UTD, GO is shown to be sufficiently accurate to capture the statistics of the fast fading, even from sparse set of computed or measured data points; and that the

fast fading can be represented by any of the four probability distributions. Finally, we introduce metal studs in between two gyproc panels and measure their effect on the statistics of the fast fading.

6.1 Statistical Distributions

In this section, the Anderson-Darling test [64], [65], [67] is used to assess the goodness of fit of four probability distributions to the measured data. Figure 6.1 shows the histogram of the measured electric field strength in the LOS regions of Figure 5.4 in comparison to the Ricean, Normal, Nakagami, and Weibull distributions. All the 4225 measured data points and the MLE method [71] were used to find the best fit for each distribution. Figure 6.2 shows the fits obtained with MLE method for the NLOS data of Figure 5.5. These hypothesized distributions are the ones used later on in the Anderson-Daring test because they are the best statistical model for each type of distribution since they were obtained with the entire set of data. By visual inspection of Figures 6.1and 6.2, it is hard to tell which distribution best represents the data. The Anderson-Darling test provides an objective assessment of whether each distribution can represent the data.

The Anderson-Darling hypothesis test assumes that the measured data is obtained from mutually independent observations. However, the electric field strength is spatially correlated over short distances, so is not independent. For this reason, a subset of the measured data consisting of points sufficiently separated to be independent must be used.

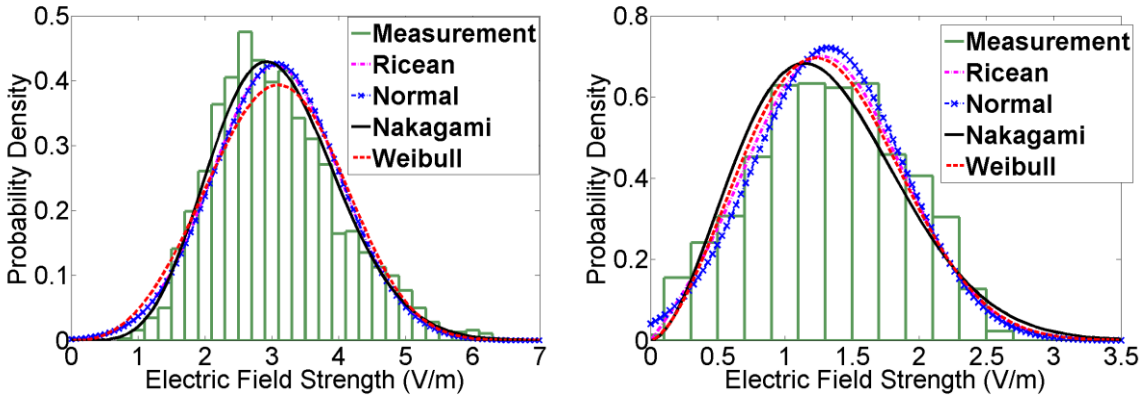

Figure 6.1: Histogram of the measured data containing a total of 4225 points. (a) LOS close region. (b) LOS far region.

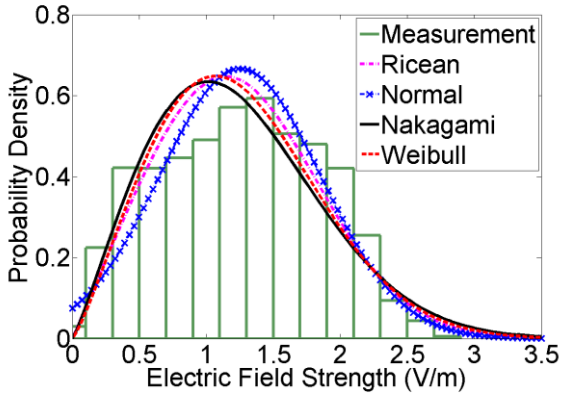

Figure 6.2: Histogram of the measured data containing a total of 3965 points for the NLOS region.

The correlation coefficient is a function of the spatial separation between measurement points, and is given by [12], [72]

$$\rho(\Delta x) = \frac{E\{(u - E\{u\})(v - E\{v\})\}}{\sqrt{var\{u\}}\sqrt{var\{v\}}} \tag{6.1}$$

where $E\{\cdot\}$, $var\{\cdot\}$, are expectation and variance, respectively, u and v are linear values of the field strength, and Δx is the spatial separation. If the correlation coefficient is less or equal to 0.5, the measured data is considered almost uncorrelated [12], [72]. Figures 6.3 and 6.4 graph the mean correlation coefficient of the measured electric field strength for the LOS cases and NLOS case, respectively. Notice that the mean correlation coefficient is different in the x and y directions.

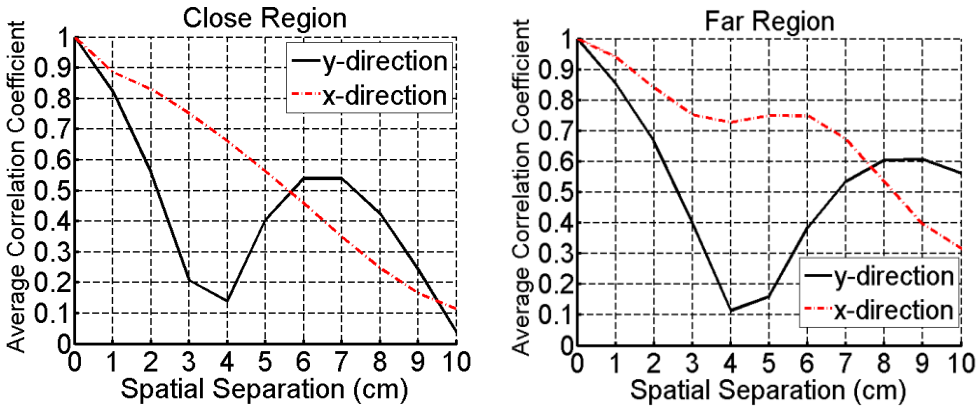

(a) (b)

Figure 6.3: Correlation coefficient as a function of spatial separation between sample elements for the LOS cases.

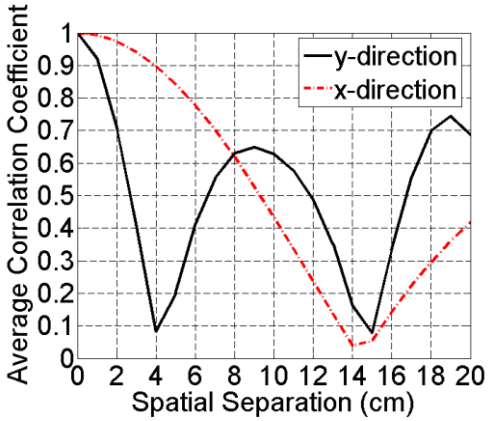

Figure 6.4: Correlation coefficient as a function of spatial separation between sample points for the NLOS case.

For the LOS cases, the correlation coefficient is less than 0.5 for a spatial separation of 6 cm in the x-direction and 3 cm in the y-direction for the close region; and 8 cm in the x-direction and 3 cm in the y-direction for the far region. Thus, in order to run a goodness-of-fit test to verify whether or not the data follow a specific known distribution, a subset of the initial 4225 field measurements was obtained for each region. Field values corresponding to positions spaced 6 cm apart in the x-direction and 3 cm apart in the y-direction for the close region were selected for a total of 210 mutually independent points, and to positions spaced 8 cm apart in the x-direction and 3 cm apart in the y-direction for the far region for a total of 168 mutually independent points. As for the NLOS case, the correlation coefficient is less than 0.5 for a spatial separation of 9 cm in the x-direction and 3 cm in the y-direction. Thus, field values corresponding to positions spaced 9 cm apart in the x-direction and 3 cm apart in the y-direction were selected for a total of 154 mutually independent points.

Six subgroups of 210, 168, and 154 mutually independent points were selected from the full data set in order to study whether the data distribution depends on the subgroup. For example, for the NLOS case, a subgroup including the point at x = 1, y = 1 is shown in blue in Figure 6.5. The red subset is shifted by 1 cm in x and 1 cm in y from the blue set, the black x mark subset is shifted 2 cm in x and 0 cm in y, while the orange subset is shifted 3 cm in x and 1 cm in y. The green subset is shifted 5 cm in x and 0 cm in y, and finally the black plus sign mark subset is shifted 6 cm in x and 1 in y. Within each subset the data points are uncorrelated. There are more possible subsets of data.

Figure 6.6 shows the histograms of two of the subgroups with the fitted known distributions Ricean, Normal, Nakagami, and Weibull, for the NLOS case. The parameters of the distributions were found by using the MLE method [71]. Even though the histograms are visually slightly different, we can see that the best fits for each of the

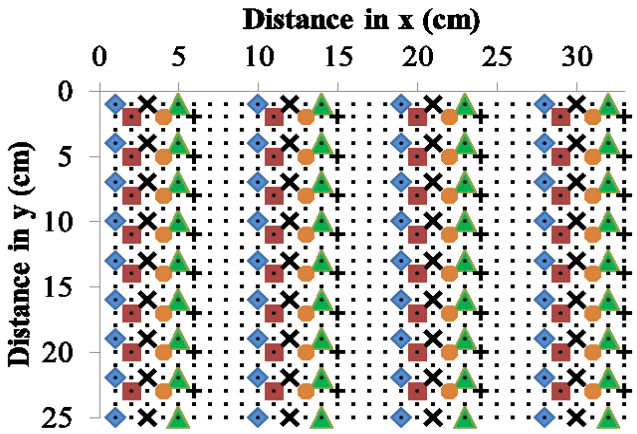

Figure 6.5: Illustration of the selection procedure of the subgroups containing mutually independent measured points.

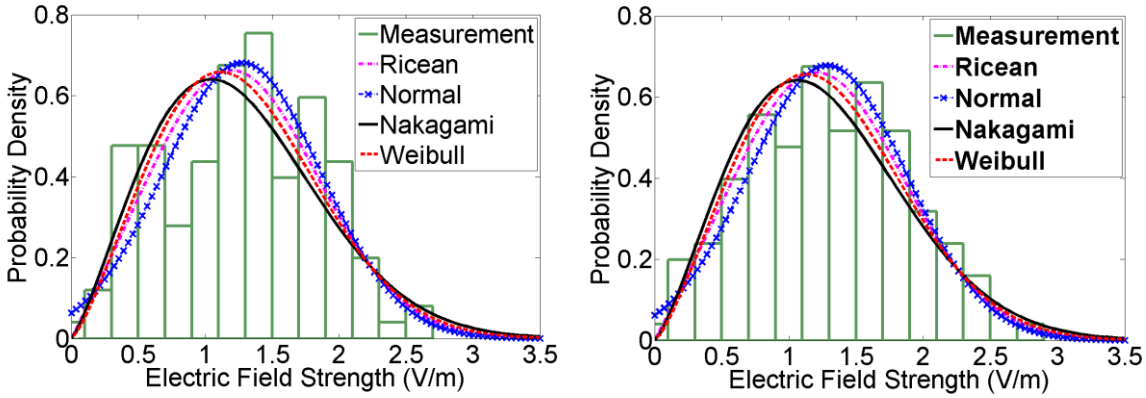

(a) (b)

Figure 6.6: Histograms of two of the six related NLOS subgroups, each with 154 mutually independent points.

four probability distributions are very similar for these two subgroups, and also to the distributions in Figure 6.2 fitted using all 3965 data points.

Another way to compare the fitted distributions in Figure 6.6 to those in Figure 6.2 is by looking at their CDFs, shown in Figure 6.7. The CDFs corresponding to the LOS cases are shown in Figure 6.8.

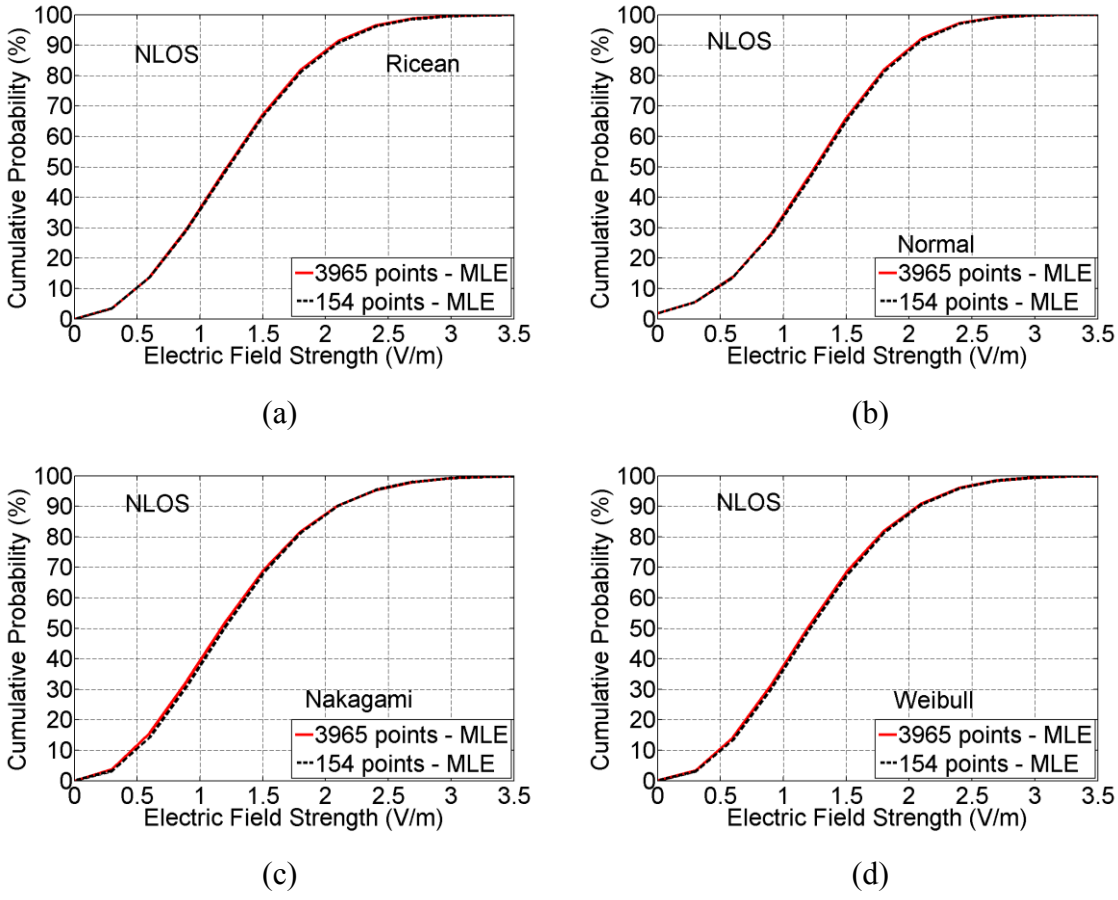

Figure 6.7: Comparison between the Rician CDFs corresponding to the data containing 3965 and 154 points for the NLOS case. The parameters of the distribution were obtained by using MLE mehod.

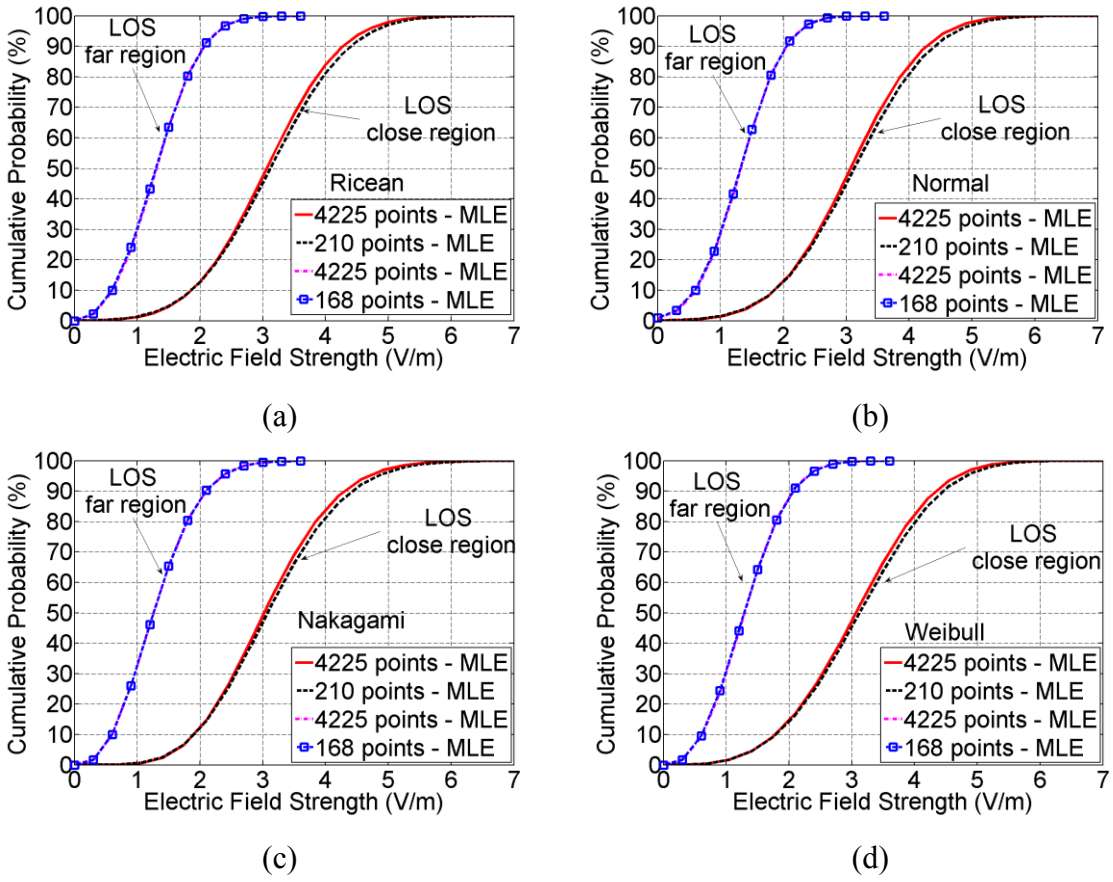

Figure 6.8: Comparison between the Ricean CDFs corresponding to the data sets containing 4225 and 210 or 168 points for both LOS cases. The parameters of the distribution were obtained by using MLE method.

In order to assess whether or not the distributions of all six subgroups are significantly different, the Related-Samples Friedman's Two-Way Analysis of Variance by Rank test was applied [70]. For the LOS close region, the result of the test showed a p-value less than 0.05 for two of the subgroups, which means that two out of six subgroups are statistically different. For the LOS far region and NLOS region, the p-values are 0.69 and 0.904, respectively; which means that the data supports the null hypothesis that the six subgroups have the same distributions at 5% significance level for all the cases.

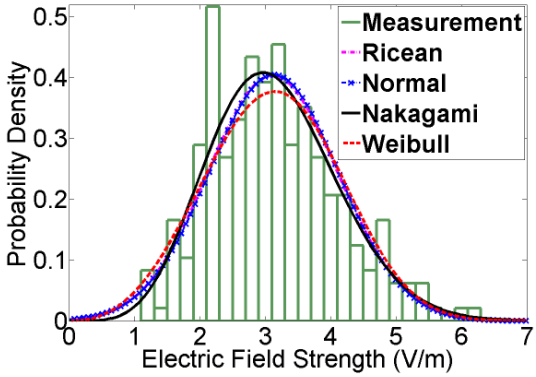

Figure 6.9: Histogram of the data corresponding to a LOS subregion close to the Tx. Spatial separation of 6 cm in the x-direction, spatial separation of 3 cm in the y-direction, and sample size of 210 elements.

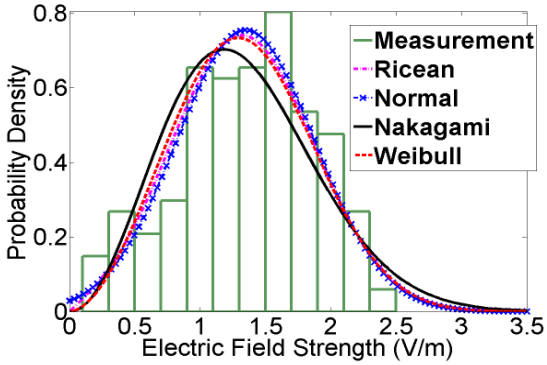

Figure 6.10: Histogram of the data corresponding to a LOS subregion far from the Tx. Spatial separation of 8 cm in the x-direction, spatial separation of 3 cm in the y-direction, and sample size of 168 elements.

Figures 6.9 and 6.10 show the histogram of the data of one of the subgroups with the fitted distributions for both the LOS close region and the LOS far region, respectively. As can be seen, an accurate statistical model can be derived from a rather sparse data set of 150 to 200 points. Therefore, it is not necessary to measure or calculate the field at 4000 points in order to determine the statistical behavior of the field. As few as 150 points are sufficient.

Again, by visual inspection of Figures 6.9 and 6.10, it is hard to tell which distribution best represents the data or whether a specific distribution represents the data at all, even for cases in which the approximation is reasonably tight. The hypothesis test provides an objective assessment.

6.2 Statistical Test

Figures 6.11, 6.12, and 6.13 compare the Anderson-Darling statistics for the four distributions for the LOS close region, LOS far region, and NLOS region, respectively. The Anderson-Darling test measures the distance between the CDF of the measured data and the CDF of the hypothesized distribution. Therefore, the hypothesis distribution that results in the smallest Anderson-Darling test statistic is the one that provides the best fit to the data. We accept the null hypothesis that the data can be represented by the hypothesized distribution if the Anderson-Darling test statistic falls below the 5% significance level indicated by the solid line. It is important to keep in mind that the significance level is the risk to discard the null hypothesis when it is true. In other words, it is the tolerance for making a Type I error when the null hypothesis is true [61]. Although the sample sizes of the subgroups are 210, 168, and 154, the hypothesized distributions to which this data were compared were obtained from the entire data containing 4225 and 3965 points.

For the LOS close region, 5 out of 6 subgroups are well represented by all four distributions at the 5% significance level, as shown in Figure 6.11. Notice that even

though two of the subgroups are statistically different from the rest, as discussed previously, they can still be represented by any of these distributions.

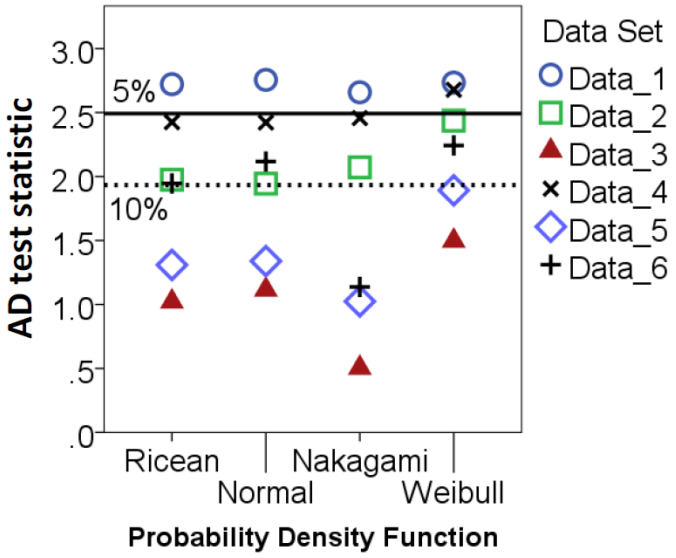

Figure 6.11: Anderson-Darling goodness-of-fit test for the LOS close region. The solid and dotted lines are the thresholds corresponding to 5% and 10% significance levels, respectively.

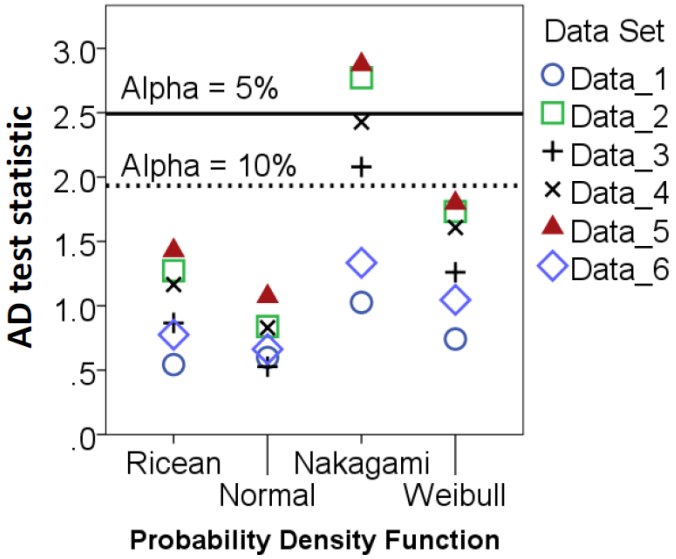

Figure 6.12: Anderson-Darling goodness-of-fit test for the LOS far region. The solid and dotted lines are the thresholds corresponding to 5% and 10% significance levels, respectively.

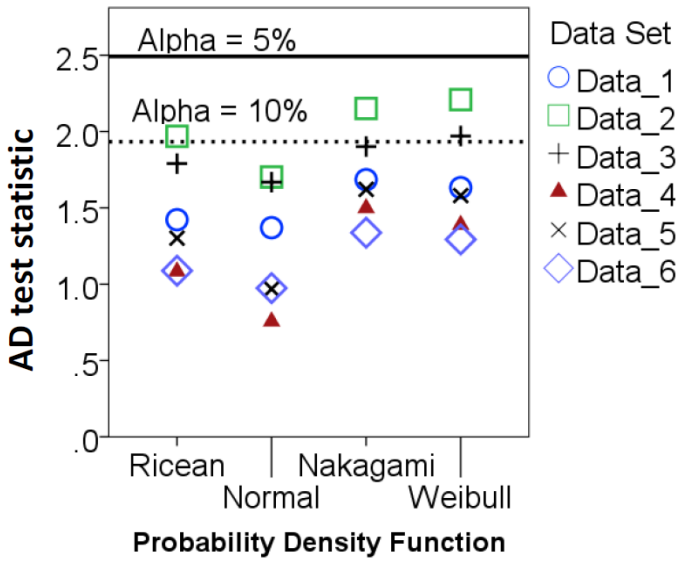

Figure 6.13: Anderson-Darling goodness-of-fit test for the NLOS case. The solid and dotted lines are the thresholds corresponding to 5% and 10% significance levels, respectively.

As for the LOS far region, the Anderson-Darling test results are shown in Figure 6.12. We can see that all four distributions can be used to model the majority of the data, and that the Ricean and Normal distributions are the ones that provide the best fit for field strength distribution in this region. Finally, for the NLOS case, Figure 6.13, all six subgroups are well represented by the four pdfs at the 5% significance level, and five of the six by all four at the 10% level.

Therefore, the data supports the hypothesis that the fast fading in a region in the vicinity of the transmitter in a multipath environment can be modeled equally well with the Ricean, Normal, Nakagami, or Weibull distributions. For the field samples of the experiments presented in this chapter, the Ricean and Normal distributions are the ones that best fit all six data subsets for all the cases.

6.3 Metal Studs

Gyproc walls are commonly used in modern buildings, and an accurate electromagnetic characterization of a three-layered wall consisting of two 1.5-cm-thick gyproc panels separated by an 8.9 cm air space is presented in chapter four. In this section, four metal studs separated by 40 cm are inserted in between the gyproc layers, as illustrated in Figure 6.14. This scenario is essentially that in Figure 5.4, except for the metal studs. We measure the effect of metal studs on both the electric field strength and its statistics. The measurement procedure is the same as that discussed in subsection 5.2.1.

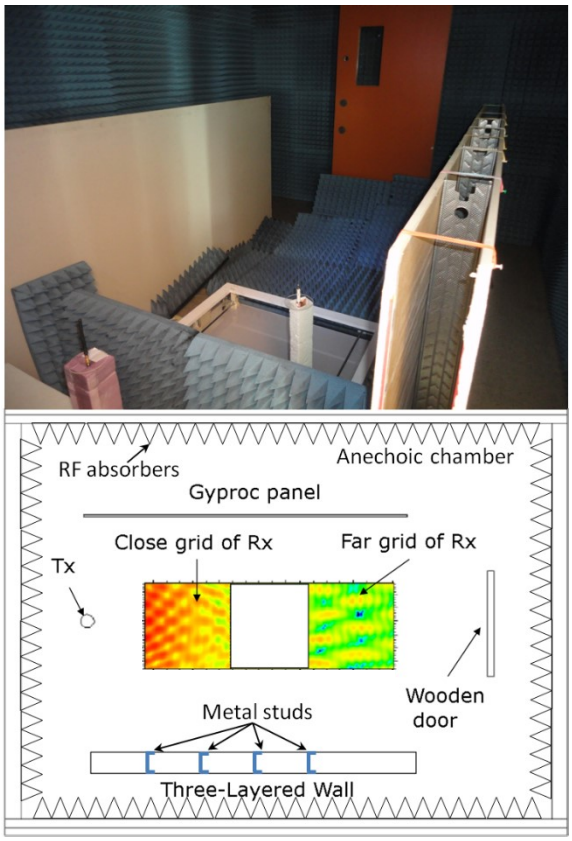

Figure 6.14: Experimental set-up. Inclusion of metal studs.

6.3.1 Effect of Metal Studs on the Field Statistics

Figure 6.15 compares the measured data with metal studs to both the measured and GO-simulated data without studs for the LOS region close to the transmitter; whereas Figure 6.16 shows the comparison for the LOS far region. As we can see in Figures 6.15 and 6.16, the metal studs do affect the field distribution in the region since the locations of the maxima and minima have changed, as well as the field strength. Notice how the metal studs spread the energy in the multipath field across and beyond the region.

This happens through diffraction, which is not taken into account in the GO model. The effect of diffracted rays are more prominent in the LOS far region though. Nevertheless, the overall field distribution is not strongly affected. Having said that, the idea is to assess the effect of diffracted rays on fast fading, and the extent to which the fast-fading statistics can be correctly predicted with a GO model only, without having to resort to more complex and computationally expensive models such as UTD.

Figure 6.17 shows the CDFs based on 4225 and 242 points for both regions. We can see that, in spite of the presence of metal studs, the GO model seems to be a sufficiently good approximation to the fast fading for the LOS close region. Nevertheless, a small difference between the CDFs is observed. As for the LOS far region, the results suggest that the GO model does not seem to lead to a good prediction of the fast fading.

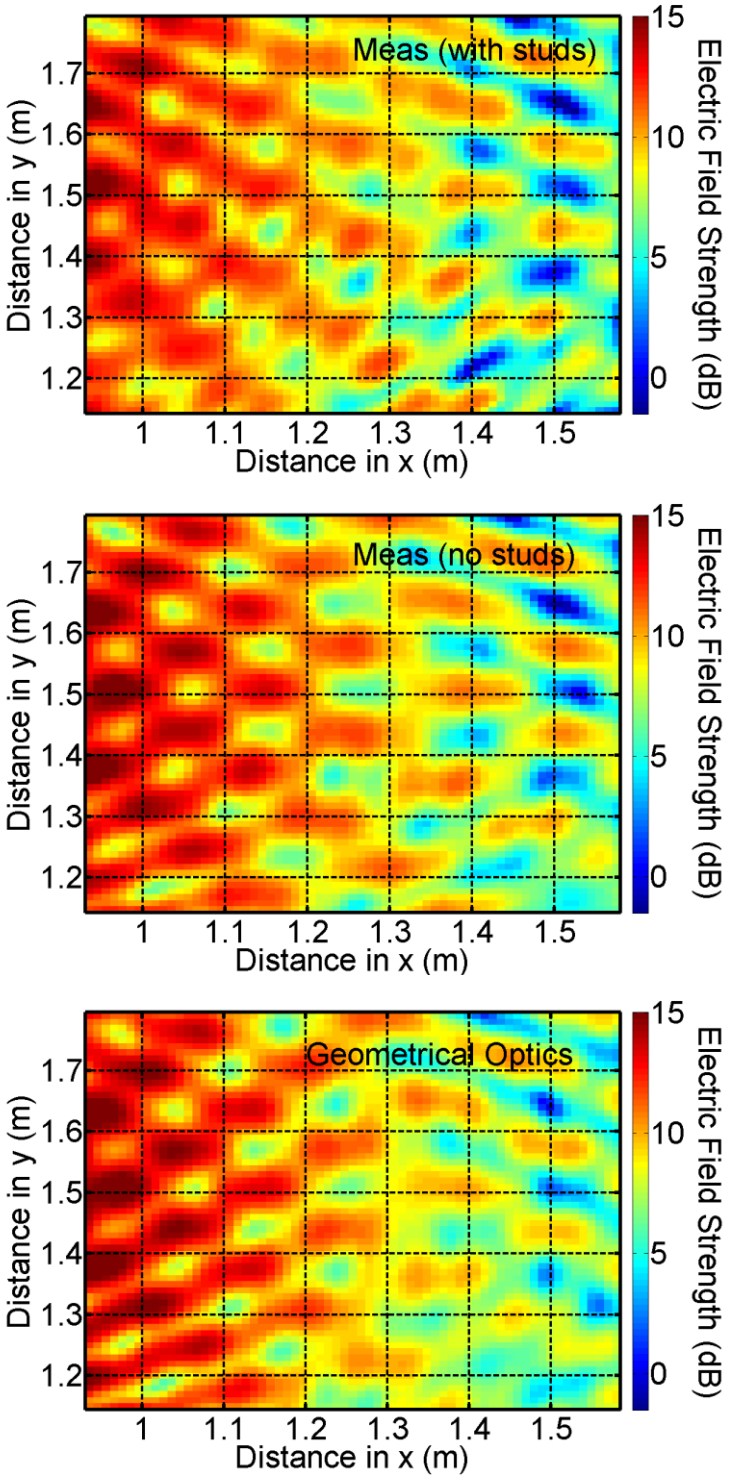

Figure 6.15: Comparison among measurement with metal studs (top), measurement without metal studs (center), and 3D geometrical optics simulation with no metal studs (bottom) for the region close to Tx in Fig. 6.14.

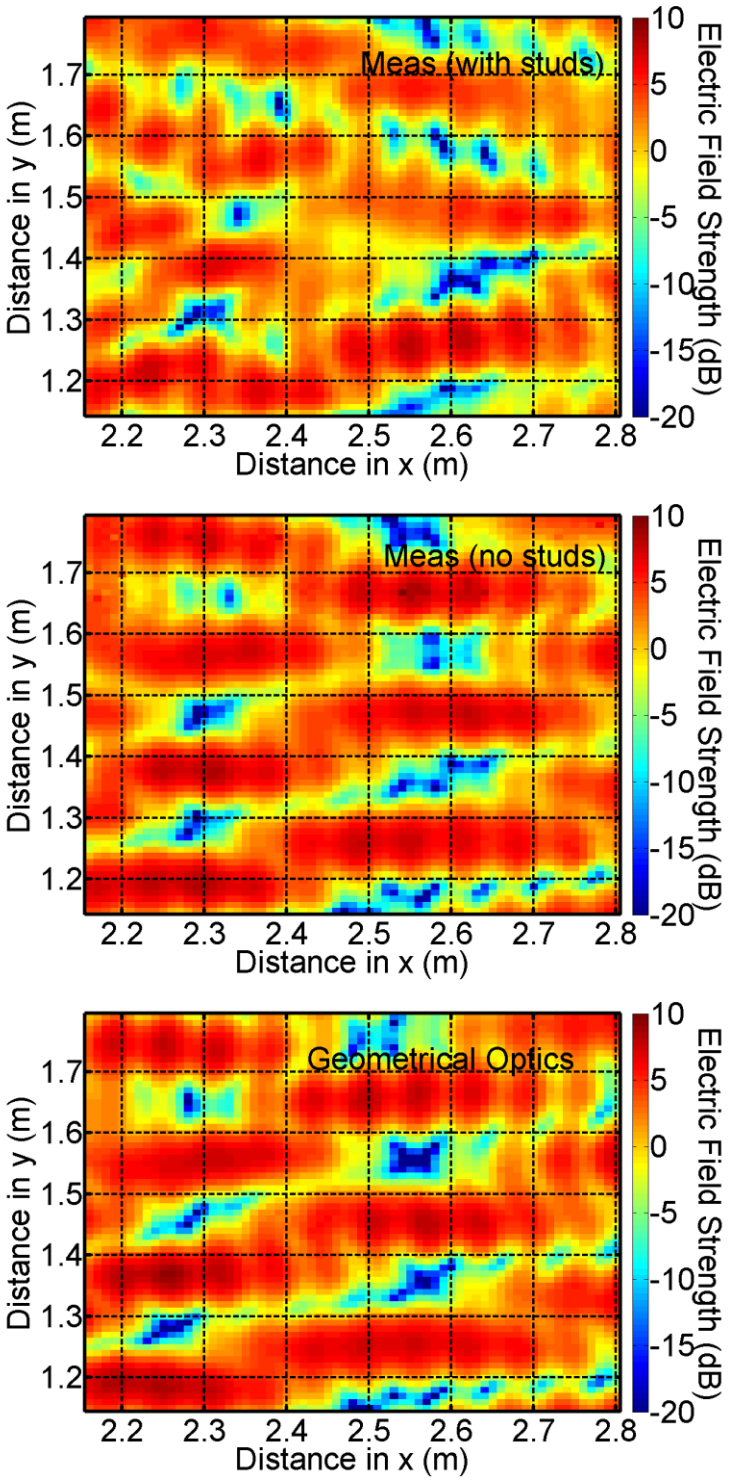

Figure 6.16: Comparison among measurement with metal studs (top), measurement without metal studs (center), and 3D geometrical optics simulation with no metal studs (bottom) for the region far from Tx in Fig. 6.14.

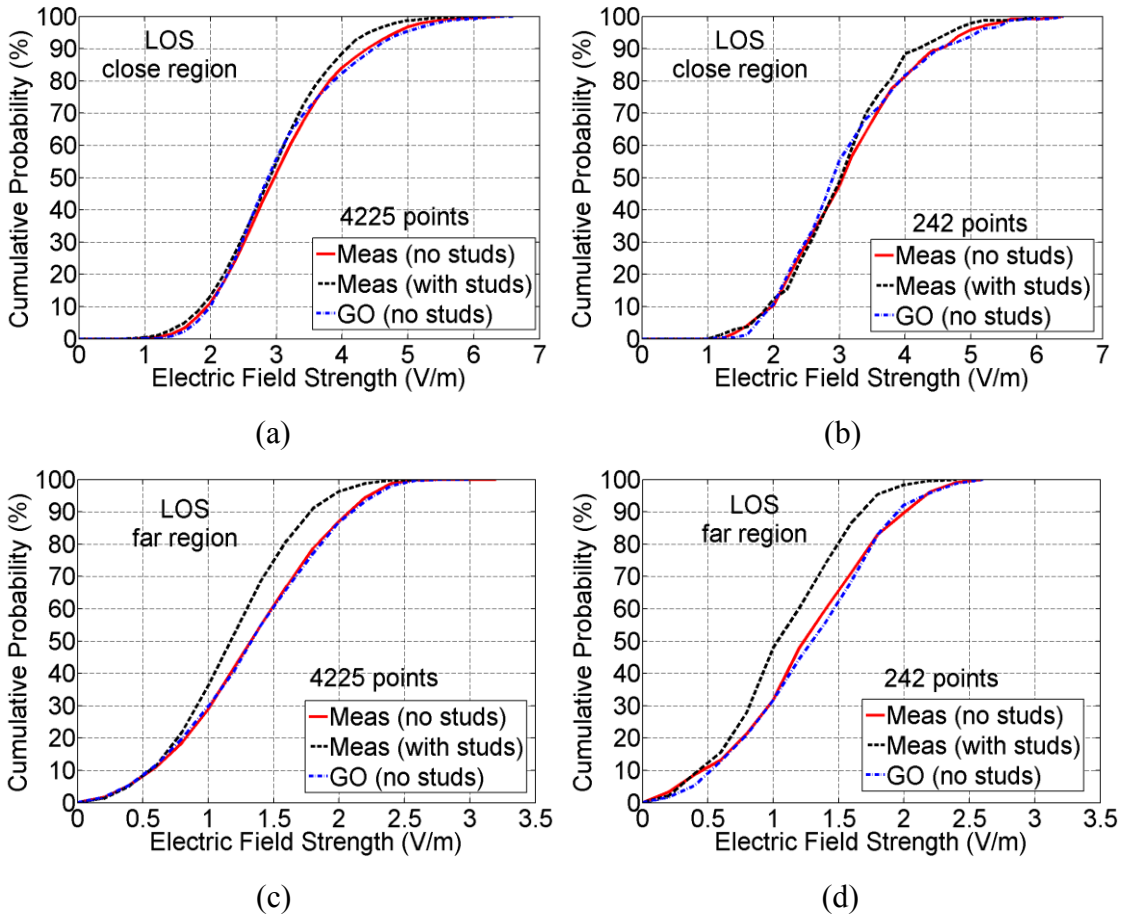

Figure 6.17: Comparison of CDFs obtained from measurement with metal studs, without metal studs, and from GO simulation for the LOS close region.

A statistical test is needed to objectively assess whether or not the observed differences in the CDFs are significant. Statistical tests usually require the data to be obtained from mutually independent observations. However, the electric field strength is spatially correlated for short distances. As explained in chapter 6, points separated by 6 cm in the x-direction and by 3 cm in the y-direction are uncorrelated. Therefore, a subset of 242 measured points is taken from the 4225 measured points. Since many such subsets are possible, we studied 8 different subsets. Each set of data from the simulation group was

compared to all of the sets in the measurement group. The number of possible combinations is thus 64. Because these sets are related, as a result of the sampling process, the Related-Samples Friedman's Two-Way Analysis of Variance by Rank [70] was applied to the data. 39% of the statistical tests for the LOS close region turned out to show statistically significant differences, at 5% significance level, between measurement and simulation; whereas 64 % was obtained for the LOS far region.

These results objectively say that, in the presence of metal studs, a GO model has a good chance to predict the fast-fading statistics correctly for regions within 2 m from the transmitter. For close regions the direct field is much stronger than the scattered field from the studs, so omitting the latter is reasonable. However, for regions farther than 2 m from the transmitter, scattering from the metal studs plays a significant role. Therefore, the conclusion is that since the GO analysis ignores the metal studs, it is not sufficient to adequately capture the statistics of the fast fading.

6.4 Conclusion

We conclude that the fast fading can be equivalently represented by the Ricean, Normal, Nakagami, and Weibull distributions. Besides, an accurate statistical model can be derived from a rather sparse data set of 150 to 200 points, using the MLE method for estimating the distribution parameters.

We also conclude that diffracted rays due to metal studs in gyproc walls do exert a significant effect on the statistics of the fast fading. Since the GO analysis ignores the

metal studs, GO analysis is not sufficiently adequate to capture the statistics of the fast fading. However, this effect can be ignored when the region of interest is about 2 m from the transmitter. Keep in mind, that this conclusion is based on an experiment conduct nearby a gyproc wall with metal studs. The results suggest that diffracted rays from metal studs may not play an important role in regions far from the walls.

Chapter 7: Estimation of the Ricean Parameters

In this chapter the data from the controlled multipath environment described in Chapter 5 and further analyzed in Chapter 6 is used to investigate how many samples of the electric field strength are needed for an accurate estimation of the parameters of a Ricean probability distribution. We have seen in chapter 6 that when both the full set of about 4000 data points and the set of about 200 points are considered, a Ricean CDF is a good fit to the measured data. In this chapter, a new method for estimating the Ricean distribution parameters is presented and compared to known methods, such as the MLE and the MM, for different sample sizes. It is shown that, when using the proposed method for estimating the Ricean parameters as few as 9 data points obtain a reasonable fit for the LOS region well separated from the transmitter and for the NLOS region (Figures 5.4 and 5.5), but at least 36 data points are required to obtain a satisfactory fit of the Ricean CDF for the LOS region close to the transmitter.

7.1 Proposed Method

The Ricean probability distribution is discussed in the literature review chapter. References [31], [53], and [62] have used the Ricean distribution in the following form:

$$p(E) = \frac{2(K+1)E}{\Omega} \cdot exp\left(-K - \frac{(K+1)E^2}{\Omega}\right) \cdot I_0\left(2E\sqrt{\frac{K(K+1)}{\Omega}}\right) \qquad (7.1)$$

where E is the electric field strength and I_0 the modified Bessel function. K is the Ricean K-factor which is defined by

$$K = \frac{E_{dir}^2}{E_m^2} \tag{7.2}$$

where E_{dir} is the dominant component and E_m is the multipath component. Ω is given by

$$\Omega = (E_{dir}^2 + E_m^2) \quad . \tag{7.3}$$

However, these authors have each developed a different way of estimating the Ricean distribution parameters (7.2) and (7.3). For instance, Ardavan *et al.* [31] use GO and Sabine's method to compute the direct and multipath fields at a single point in space and then estimate the Ricean parameters from (7.2) and (7.3). Abdi *et al.* [62] compare two MM-based estimators of the parameters: the μ-based and γ-based estimators. The computation of the latter is presented in the literature review chapter. In contrast to the methods employed in [29] and [31], the γ-based estimator relies on total field strength data rather than on direct and multipath field data. Finally, we use GO in [29] to calculate the direct and multipath field strengths at N evenly-spaced points across a 65 by 65 cm region and then use their medians in (7.2) and (7.3). This method works well for regions far from the transmitter, but presents a problem when used to model the fast fading in regions within 2 m from the transmitter such as the LOS close region shown in Figure 5.4.

Usually, the variability of the field is thought of as caused by the multipath component only. This assumption holds for regions sufficiently far from the antenna, where the variability of the direct field over the 65 by 65 cm area is small. But for regions close to the transmit antenna, the direct field varies strongly across the region. To account for this variation the formulas for K and Ω are modified and become

$$K = \frac{\hat{E}_{dir}^2}{\left(\hat{E}_m + std(E_{dir})/2\right)^2} \tag{7.4}$$

$$\Omega = \left(\hat{E}_{dir}^2 + \left(\hat{E}_m + std(E_{dir})/2\right)^2\right) \tag{7.5}$$

where $\hat{E}_{dir}$ is the median of the direct field strength, $\hat{E}_m$ is the median of the multipath field strength, and $std(E_{dir})$ is the standard deviation of the direct field strength.

It should be noted that this correction affects the model only for regions close to the transmitter because the standard deviation of the direct field becomes very small for regions far from the transmitter, in which case (7.4) and (7.5) becomes (7.2) and (7.3), respectively, using the median field strength rather than the field value at a single point.

Essentially, the proposed method consists of finding the median direct field and the median multipath field over the N data points, then using (7.4) and (7.5) to estimate K and Ω.

7.2 Electric Field Distribution as a Function of Sample Size

Figure 7.1 shows a boxplot of nine sets of field strength samples of different sizes for each of the cases illustrated in Figures 5.4 and 5.5: the LOS close region case, the LOS far region case, and the NLOS case. With a sample spacing of 1 cm there are about 4000 samples; with a 2 cm spacing, about 1000 samples, and so forth. The boxplot helps visualize differences in how data are distributed [70]. The horizontal solid line in each box represents the sample median. The bottom and top of the box represents the 25th and 75th percentiles, respectively. That means that 50% of the data lie within the box. When the data are normally distributed, 95% of the data points are expected to lie within the region defined by the whiskers.

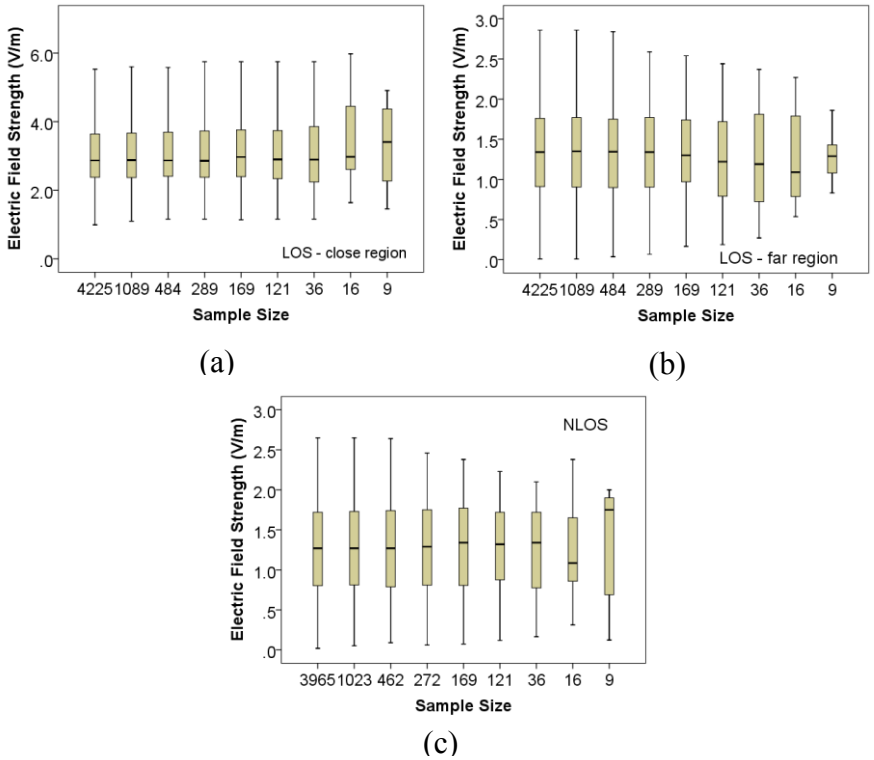

Figure 7.1: Boxplots. Comparison of the E-field distributions for different sample sizes.

The total field is comprised of the direct and multipath components, thus the conclusions drawn from Figure 7.1 can be extrapolated to the direct and multipath fields. Since the electric field distribution does not necessarily follow a normal distribution, we use the estimated median of the field strength as a measure of central tendency.

Figure 7.1 shows that as the sample size decreases, the change in the median field strength from about 4000 samples to 36 samples is only 0.87% for the LOS close case, 11.2% for the LOS far case, and 5.51% for the NLOS case. This suggests that the median value will lead to an accurate Ricean distribution based on only 36 samples. With 16 or 9 samples, larger changes in the median are seen for the NLOS case. Notice how the median and mean field values in the far regions are substantially smaller than that in the close region. In the NLOS case, the door did not block the direct field substantially because of its low dielectric constant.

In the following, we investigate how many data points are required for an accurate fit of the Ricean model to the fast fading behavior. The Ricean CDF found using the maximum likelihood method based on about 4000 data points will serve as a reference for assessing Ricean distributions based on far fewer data points, evaluating K and Ω using equations (7.4) and (7.5) and median field strengths.

7.3 Comparison of CDFs for Different Sample Sizes

The question above can be answered by comparing the CDFs as shown in Figure 7.2. The CDF based on measured data is shown as a solid red line and is very close to the CDF using about 4000 field samples computed with GO, shown with short black dashes. The squares show the Ricean best fit using MLE [71] and all the GO samples, and is very close to the CDF obtained with the GO data itself. The blue dashed line shows the Ricean distribution using (7.4) and (7.5) based on 36 evenly-spaced data points from GO, and the green dashes show the Ricean CDF using only 9 evenly-spaced data points. The 9 and 36 point curves are almost the same. In the NLOS case, at low field strength of 0.5 to 1 V/m, these curves are slightly below the CDF based on the full data set; and at high field strengths of 1.5 to 2 V/m, these CDFs are slightly higher. For the LOS case the curves for 36 and 9 points are very close to the original GO data.

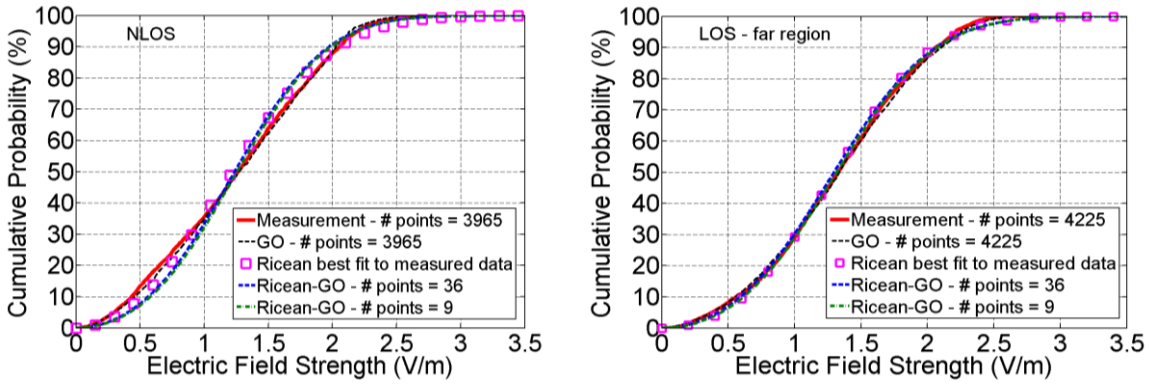

(a) (b)

Figure 7.2: Comparison of empirical CDF, simulated CDF with largest sample size, CDF based on the MLE best fit, CDF based on the proposed method with 36 points, and CDF based on the proposed method with 9 points. (a) NLOS case. (b) LOS far case.

Hence the Ricean model can be accurately estimated with sample sizes as small as 36 or even 9 points for a 65 by 65 cm region at 2.45 GHz for these two cases.

Now, let us examine the LOS close region case by first looking at what happens when (7.2) and (7.3) are used to estimate the Ricean parameters, and then when (7.4) and (7.5) are used. Figure 7.3 shows the measured CDF (red curve) and the CDF calculated by GO (black dashes), both using 4225 points, and the curves are very close, and statistically equivalent. The Ricean best fit obtained by the MLE and the 4225 points computed by GO (squares) is also very similar to the measurement. So the data for the LOS close region can be represented accurately by a Ricean distribution, as discussed in the previous subsection. However, the Ricean CDF based on 36 data points (blue dashes) or 9 points (green dashes) is not a good fit. Even if all 4225 data points are used to estimate the median direct and median multipath field for use with (7.3) and (7.4), the CDF does not agree with that based on MLE.

Figure 7.4 graphs the CDFs created with the Ricean parameters obtained from the median direct and multipath fields using (7.4) and (7.5). With 36 data points (blue dashed curve) the CDF is a good fit to the Ricean maximum-likelihood best fit (squares). Thus, the proposed method solves the problem for the LOS close region. However, 9 data points is too few to achieve a reasonable match.

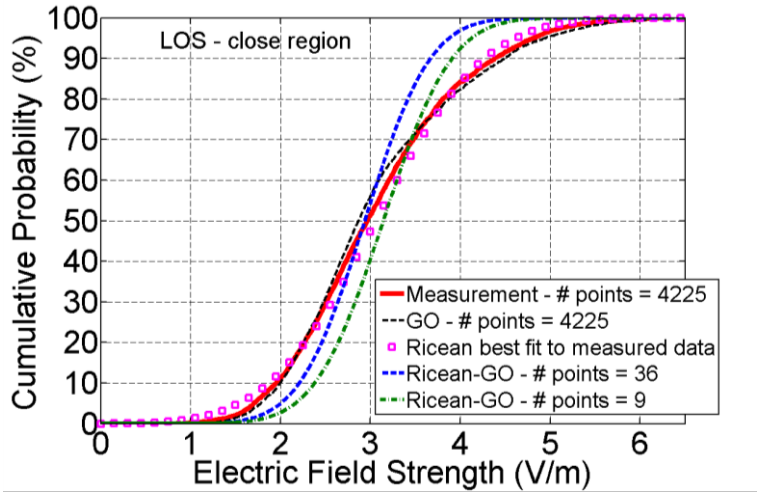

Figure 7.3: Comparison of empirical CDF, simulated CDF with largest sample size, CDF based on the MLE best fit, CDF based on the proposed method with 36 points, and CDF based on the proposed method with 9 points for the LOS close region case using (7.2) and (7.3).

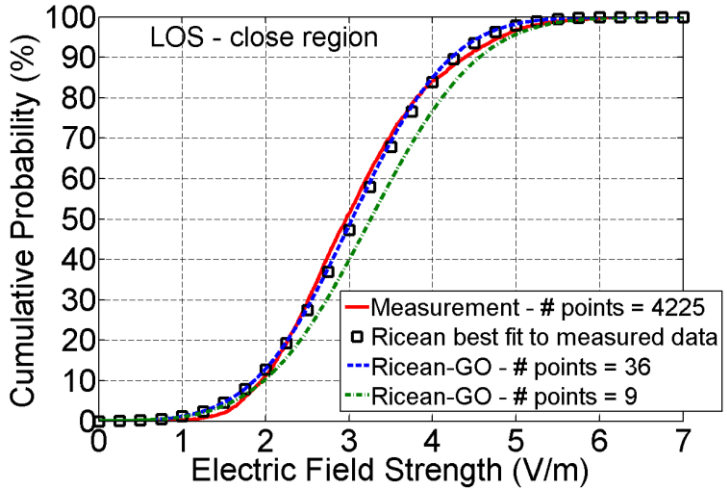

Figure 7.4: Comparison of empirical CDF, simulated CDF with largest sample size, CDF based on the MLE best fit, CDF based on the proposed method with 36 points, and CDF based on the proposed method with 9 points for the LOS close region case using (7.4) and (7.5).

In summary, to avoid computing field strength values at thousands of closely spaced points, fast fading can be modeled with a Ricean probability distribution. This subsection investigates the number of field samples needed to estimate the Ricean parameters for LOS regions both close to and well separated from the transmitter, and for NLOS regions. A good Ricean model is found in all three cases with 36 data points over a 65-cm square region at 2.45 GHz. Fewer data points can be used with some reduction in the fit of the Ricean model to the measured data. Simple formulas give the values of the Ricean parameters for the NLOS region and the LOS region well separated from the transmitter, but fail when the LOS region is very close. In the proposed method these formulas are modified and lead to a good fit of the Ricean model to the true fast fading behavior.

7.4 Comparison of Parameter Estimation Methods

In this subsection the proposed method is compared to both the maximum-likelihood method (MLE) [71] and the moment method (MM) [62] for different sample sizes. In terms of complexity, the proposed method and the MM method are equivalent, and both these methods are less complex that the MLE method. It is shown that these three methods for estimating the Ricean parameters perform quite well for samples with at least 36 data points evenly-spaced across an area of 65 by 65 cm at 2.45 GHz; and that the proposed method outperforms the MM and MLE methods when samples with as few as 9 points are considered.

Table 7.1 compares the Ricean parameter obtained with these methods. As we can see, the estimate of the Omega parameter is essentially the same for all methods, regardless of the sample size. On the other hand, the estimate of the *K*-factor varies depending on the method used, especially for the samples with 9 points.

Figure 7.5 compares the CDFs corresponding to each method for samples containing 36 data points, whereas Figure 7.6 considers samples with 9 points. From these figures we conclude that the proposed method is as good as the MLE and MM methods for sample with at least 36 points, even though it is fairly simple and easy to implement. Figure 7.6 shows that although the CDFs based on the three methods with only 9 points are very similar for the LOS close region, it should be noted that none of them agrees well with the CDF based on measurements. This leads to a minimum recommended sample size of 36 for regions within 2 m from the transmitter. Moreover, the proposed method is shown to be better for regions far from the transmitter when only 9 points are used.

In order to get 36 points evenly spaced across a 65 by 65 cm region, the spacing between points must be 12 cm. At 2.45 GHz, the wavelength is 12.24 cm. So, it is curious that the minimum number of points that results in reliable Ricean models happens to be about one wavelength, regardless of the method used to estimate the Ricean parameters and of the distance between the transmitter and the region of interest. To obtain 9 points evenly spaced, the spacing between points must be 25 cm. It is interesting that the proposed method resulted in good Ricean models for regions far from the transmitter when points spaced apart about two wavelengths were used.

Table 7.1: Ricean parameters obtained with different methods.

LOS close region

	MLE		MM		Proposed method	
Sample size	K	Ω	K	Ω	K	Ω
4225	4.54	10.29	3.10	10.37	5.89	9.50
210	4.17	10.75	2.88	10.65	5.65	9.82
36	4.20	10.64	3.02	10.87	4.61	10.13
9	3.38	10.87	3.70	12.19	4.43	11.70

LOS far region

	MLE		MM		Proposed method	
Sample size	K	Ω	K	Ω	K	Ω
4225	1.78	2.05	2.08	2.10	1.56	2.06
168	1.64	2.05	1.72	2.08	1.59	2.07
36	1.39	1.94	1.35	1.94	1.64	2.04
9	6.71	1.84	9.20	1.75	1.75	2.11

NLOS region

	MLE		MM		Proposed method	
Sample size	K	Ω	K	Ω	K	Ω
3965	0.96	1.93	1.71	1.92	1.52	1.90
154	0.90	1.96	1.80	1.91	1.53	1.93
36	1.62	1.94	2.57	1.88	1.57	1.89
9	0.06	2.10	2.55	2.22	1.68	1.93

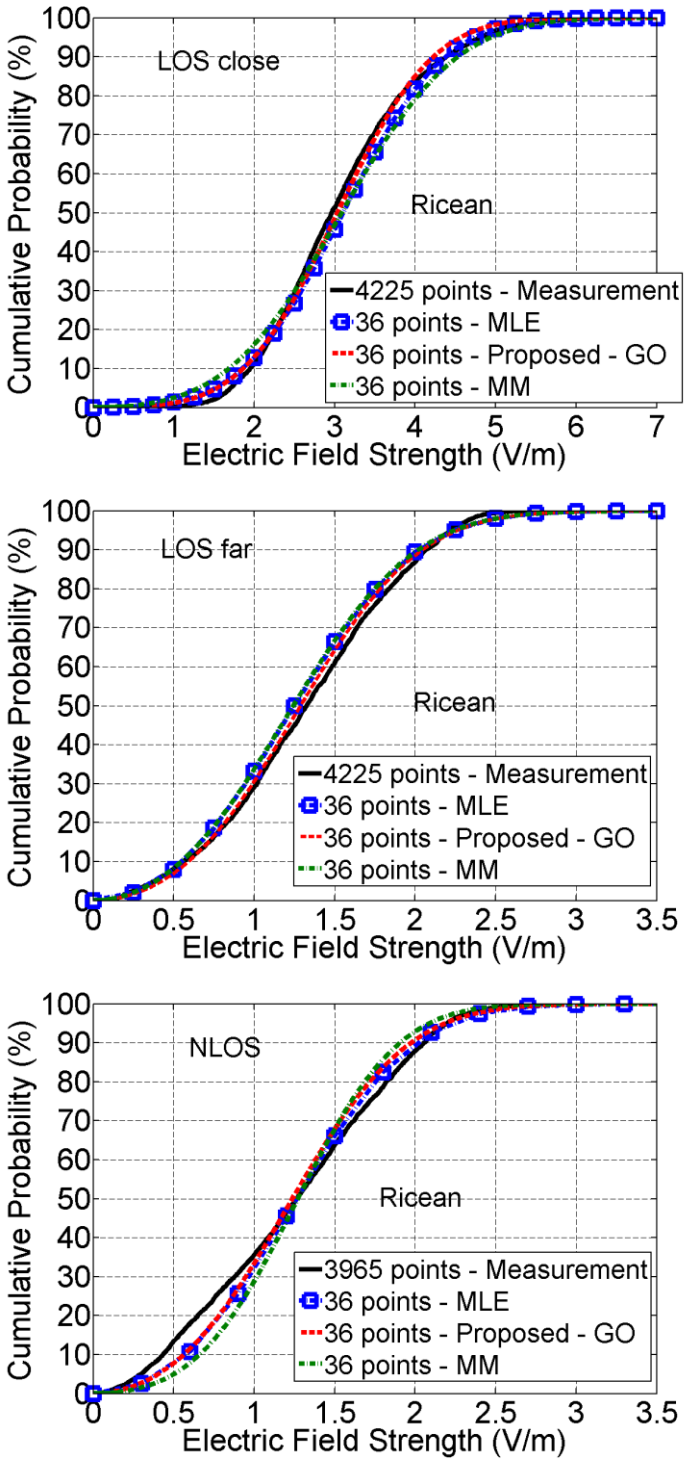

Figure 7.5: Comparison of CDFs obtained with different methods with 36 data points.

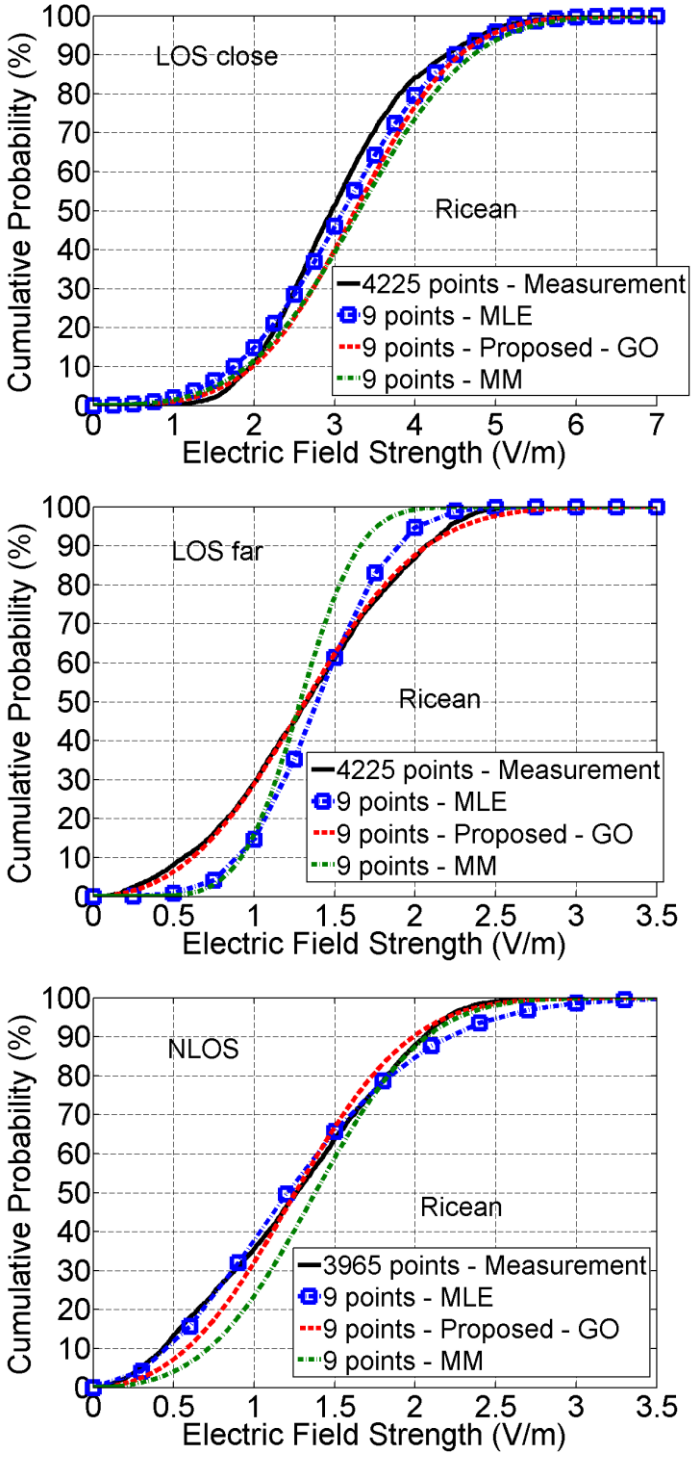

Figure 7.6: Comparison of CDFs obtained with different methods with 9 data points.

7.5 Conclusion

After showing that the fast fading can be represented by any of the four distributions, as discussed in Chapter 6, we focus on the Ricean distribution because of its simplicity and physical interpretation. A new and simpler method for estimating the Ricean parameters is proposed and shown to be as good as the MLE and the MM methods when at least 36 data points evenly spaced across a 65 by 65 cm region are considered. It is superior when as few as 9 points are used for regions well separated from the transmitter. Besides, the proposed method solves the problem previously encountered when treating regions close to the transmitter.

We recommend that the spacing between data points be about one wavelength for a reliable Ricean model for any distance from the transmitter, even though very good approximations can be obtained with a separation as large as two wavelengths.

Chapter 8: Electric Field Strength in a Corridor

In this chapter we study electromagnetic wave propagation in a long corridor by means of measurements, GO simulation, Sabine's method, and statistical analysis. We have demonstrated in Chapters 5, 6, and 7 that GO simulation is sufficient as basis for predicting the statistics of the spatial variation of the field, and that we can attain an accurate prediction of the fast fading from a data set of about 200 points for the scenarios considered in the controlled multipath environment. Moreover, we have seen that the Ricean, Normal, Nakagami, and Weibull distributions are equally good to model fast fading, and chosen the Ricean distribution to work with due to its simplicity and physical meaning. Furthermore, we have demonstrated that the Ricean parameters can be estimated from as few as 36 data points evenly spaced on a 65 by 65 cm region by using the MLE, MM, or proposed-GO estimation methods. The latter method showed superior performance when only 9 data points were considered.

Here, we apply the same methods and techniques to a real indoor scenario, a corridor on the 15^{th} floor of the EV building at Concordia University, shown in Figure 8.1. Modern hospitals use gyproc walls with embedded metal studs, therefore their building structure is represented by this corridor. Electromagnetically, corridors are interesting environments and have been observed in some situations to act as overmoded waveguides [42], [73]. We start by presenting the statistical analysis of the measured electric field strength at ten regions throughout the corridor and show that the Ricean, Normal, Nakagami, and Weibull distributions provide statistical models that are statistically

equivalent for all the 10 regions. For this real scenario, the Normal distribution provides the worst of all best-fits to the measured data when compared to the best-fit based on the other distributions. Then we show that GO simulation, together with MLE, MM, or the proposed-GO method, can be used to predict the statistics of the electric field strength for most of the ten cases in the corridor, although many of the environment features, such as metal studs, cannot be included in the GO model. Besides, we show that the path loss can be accurately predicted with both ray-tracing technique and the Sabine method.

8.1 Electric Field Strength Distribution on a 65 by 65 cm Region

This experiment was conducted on the 15th floor of the EV building at Concordia University. Measurements of electric field strength were taken at ten different locations throughout the corridor. The purpose of this experiment was to find the best statistical model for the distribution of the field in a square region that is about 5 wavelengths in size at 2.45 GHz. Furthermore, we wanted to compare measurement to GO simulation, and show that a good Ricean model could be obtained from GO calculations for this particular type of real scenario. Finally, we compared path loss models obtained by measurement, GO simulation, and Sabine method. Figure 8.1 shows the corridor.

Figure 8.2 shows the model of the floor plan used in both the GO and the Sabine simulations, with the ten measurement regions represented by the squares. Notice that there are 8 LOS and 2 NLOS regions.

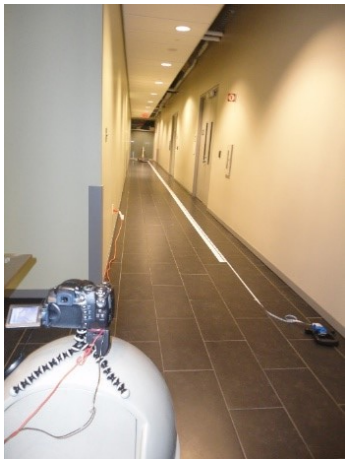

Figure 8.1: Corridor on the 15th floor of the EV Building.

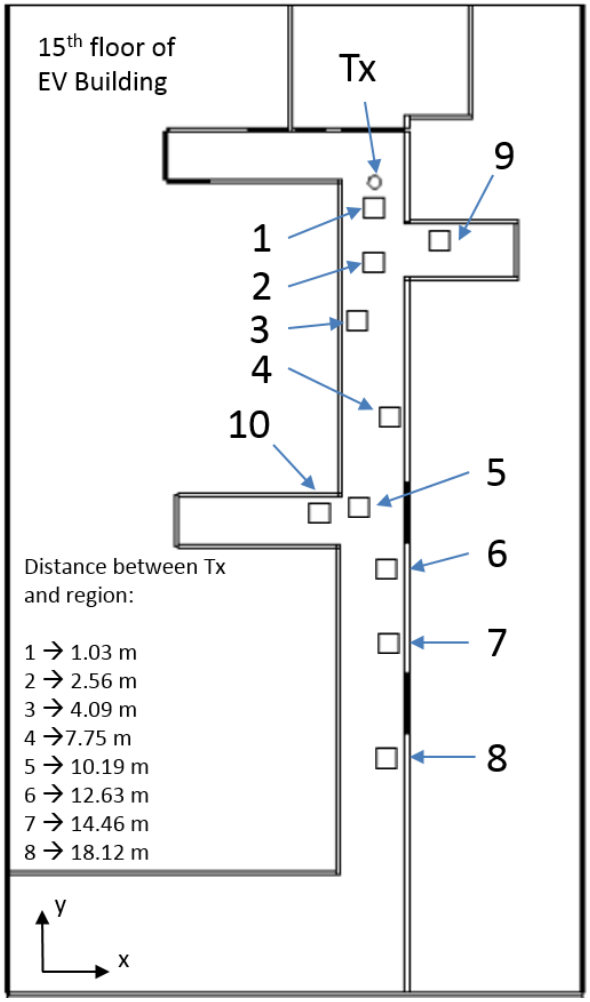

Figure 8.2: Model of the floor plan of the 15th floor.

The distance from the transmitter to the center of each region is indicated at the bottom left corner of Figure 8.2. The corridor is 1.82-m wide and over 20-m long with a ceiling height of 2.98 m. The walls were modeled as layered structures containing two 1.5-cm-thick gyproc ($\varepsilon_r = 2.25, \sigma = 0$ mS/m) panels separated by a 9.5-cm-thick air layer. The metal doors, wooden doors, metal door frames, and glass walls were all included in the model. Both the floor and ceiling were modeled as a 30-cm-thick concrete layer ($\varepsilon_r = 9.2, \sigma = 204$ mS/m).

We have explained in Chapter 6 that the electric field strength observations must be independent if we are to apply the Anderson-Darling test of goodness of fit. We have also learned that this condition is met when the sample points are spaced 3 cm apart in the x-direction and 6 cm apart in the y-direction, using the coordinate directions in Figure 8.2. Thus, in this experiment, we use the 2D scanner measurement system to take electric field strength measurements in a 65 by 65 cm region in steps of 3 cm in the x-direction and 6 cm in the y-direction for a total of 242 sample points. The experiment setup is shown in Figure 8.3.

This measurement system is described in more detail in Chapter 3. The transmitter was a calibrated sleeve dipole antenna which was fixed in position, 90 cm from the left wall and 92 cm from the right wall, vertically oriented and kept at a height of 1.47 m above the floor. The receiver was a vertically oriented WiFi sleeve dipole antenna and was also at a height of 1.47 m above the floor. The simulations considered a vertically oriented half-wave dipole antenna radiating 100 mW. As the radiated power was much less than 100

Figure 8.3: Corridor experiment. Measurement setup. This figure shows the xy positioner, which scans the probe on top of the Styrofoam pole over a 65 by 65 cm area. The photo at left looks towards the Tx from position 2, and the one in the center from position 6. The photo at right shows some details of the receive sleeve dipole.

mW and not precisely known, the calibration method described in section 3.3.7 was applied to bring the power level of the measured data to that of the simulated.

8.1.1 Statistical Analysis of the Measured Data

In each region in Figure 8.2 the field strength was measured at 242 points spaced 6 cm apart in the y-direction and 3 cm apart in the x-direction. The field strengths were expected to be uncorrelated. To verify that these observations are indeed uncorrelated so that the Anderson-Darling test can be applied, Figure 8.4 shows the average correlation coefficient, given by (6.1), of the measured data for regions 2 and 3. The same results were found for the other regions. As can be seen in Figure 8.4, the average correlation coefficient is less than 0.5 at 3 cm in the x-direction and at 6 cm in the y-direction. Hence, we consider the 242 data points to be independent [72].

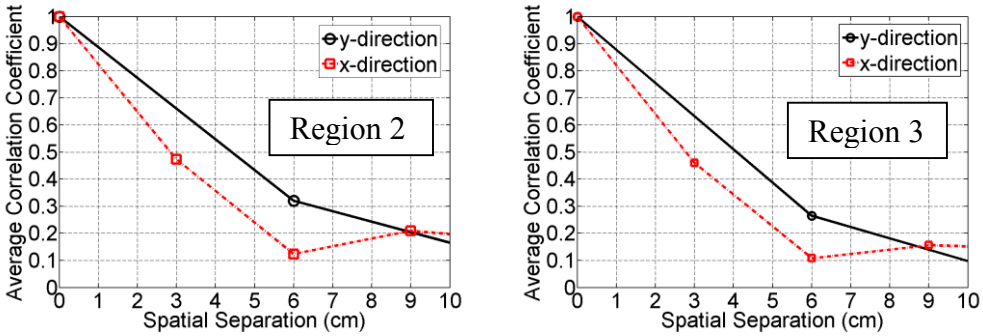

Figure 8.4: Correlation coefficient for corridor experiment.

Figures 8.5 and 8.6 show the histogram of the measured electric field strength for the LOS and NLOS regions in Figure 8.2. They also show the Ricean, Normal, Nakagami, and Weibull best fits obtained with the MLE method and all the 242 uncorrelated data points for each region. It is interesting to see that the histograms and curves get narrower as we move away from the transmitter. This expresses the fact that as the distance increases the probability of high field strengths decreases dramatically. By visual inspection, all the four distributions seem to be good statistical models for the measured data, and we cannot tell which one is the best. The Anderson-Darling goodness-of-fit test is an objective test used to assess whether a data set follows a specific distribution. This test is also used in chapter 6 and is described in more detail in chapter 2. In short, the Anderson-Darling test measures the distance between the CDF of the measured data and the CDF of the hypothesized distribution. Therefore, the hypothesis distribution that results in the smallest Anderson-Darling test statistic is the one that provides the best fit to the data. We accept the null hypothesis that the data can be represented by the hypothesized distribution if the Anderson-Darling test statistic falls below the 5% significance level. We should keep in mind that the significance level is the risk to

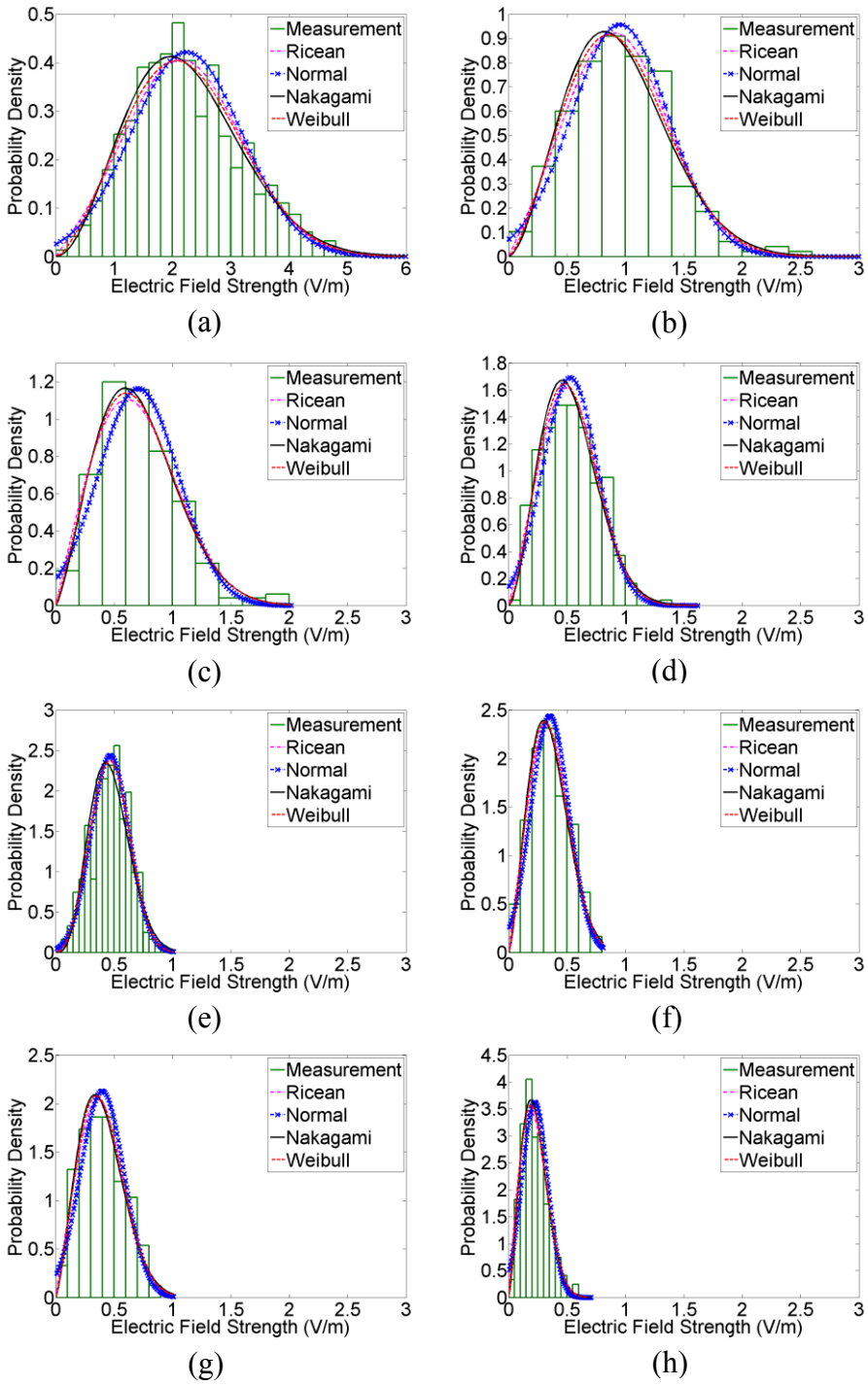

Figure 8.5: Histograms with best-fit distributions obtained with MLE method and all the 242 uncorrelated data points. LOS regions: (a) region 1. (b) region 2. (c) region 3. (d) region 4. (e) region 5. (f) region 6. (g) region 7. (h) region 8.

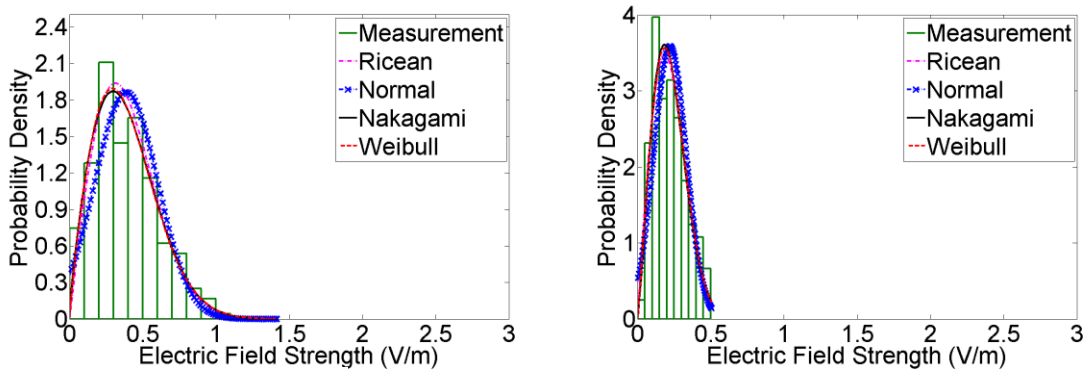

Figure 8.6: Histograms with best-fit distributions obtained with MLE method and all the 242 uncorrelated data points. NLOS regions: (a) region 9. (b) region 10.

discard the null hypothesis when it is true. In other words, it is the tolerance for making a Type I error when the null hypothesis is true [61].

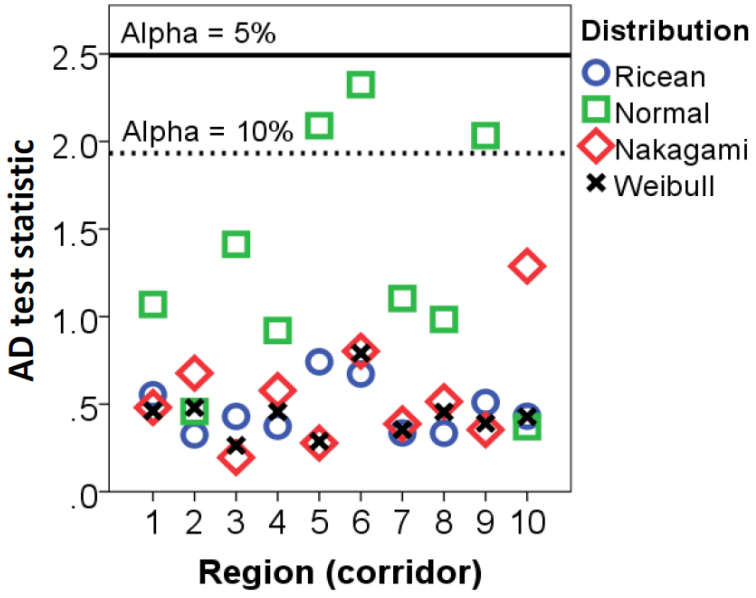

Figure 8.7: Anderson-Darling test for the corridor experiment.

Figure 8.7 compares the Anderson-Darling test statistic for the four distributions, for each region, and shows that it falls below the 5% significance level for all the regions regardless of the distribution. This result means that the fast fading in the real indoor scenario considered in this chapter, a corridor, can be equivalently described by these four statistical models, each based on one of the four distributions, since no statistical difference was obtained. Even though we cannot reject the null hypothesis that the data follow the Normal distribution, we can see that the Normal best-fits are constantly worse than those based on the Ricean, Nakagami, and Weibull.

8.1.2 Geometrical Optics Considerations

The GO_3D program includes in the computation of the field strength all image sources that may have a field strength of T dB below the isotropic level, where T is a threshold value chosen by the user. The program computes the "isotropic level field strength" corresponding to the power radiated by the source. Then, it estimates the field strength that an image source might contribute assuming the 1/distance divergence of the spherical wave, and using the distance from the image source to the observer. However, no accounting is made for reflection coefficient. Thus, when a threshold of $T = 15$ dB is chosen, the program includes all image sources that would produce a field strength (ignoring reflection coefficients) stronger than the isotropic level minus the threshold in dB. This is conservative because reflection coefficients reduce the fields of image sources, which results in many image sources that do not produce field strengths stronger than the isotropic level minus the threshold, T, being taken into account in the

simulation. If all the reflection coefficients were unity, then all the images would give the required field strengths.

In the GO model of the hallway, the threshold value used to control the number of ray paths was 25 dB. As a consequence, the model took into account ray paths with up to 15 reflections. Even though rays with more than 3 or 4 reflections do not contribute significantly to the net field strength, it is important to note that when the threshold value is increased the model does not add just low field strength rays, but also rays that could have significant field strengths. Therefore, increasing the threshold value in the GO model does not necessarily add only insignificant rays. This is shown in Figure 8.8 which graphs the field strength of each ray versus the corresponding path length for the center points in regions 1 and 4 in Figure 8.2. Notice that as the threshold value increases more rays are taken into account.

We can see in Figure 8.8(a) that the direct path has a length of 1 m and a field strength of 6.5 dBV/m. At 2 m we see a one-reflection path with field strength of -5.3 dBV/m. Moreover, there are two reflection paths with lengths of 3 m and field strengths of about -21 dBV/m; and two paths with lengths of about 3.8 m with field strengths of -11 and -12 dBV/m. Notice that the squares in Figure 8.8 correspond to a threshold of 10 dB, but many rays that are much smaller in field strength than 15 dB below the direct ray are found (This is not the definition of threshold, which is T dB below the isotropic level). This is because the criterion to decide whether or not an image source should be included is based on distance only, and does not take into account the reflection coefficient.

Increasing the threshold to 15 dB (circles) introduces a few more rays that have field strengths that may be significant, shown as circles with crosses but no squares. For example there is a ray path of length 14 m and field strength of about -25 dBV/m. Further increasing the threshold to 20 dB (crosses) adds a few ray paths (crosses only) that may have significant field strengths, such as the cross at 7 m and field strength of -26 dBV/m, and many ray paths with much smaller field strengths. Many of these rays have paths with many reflections and thus do not contribute the field strength. But a few of them have field strengths of about -29 dBV/m, such as those with path lengths of 5, 7, 14, and 16 m in Figure 8.8(a). As for region 4, the direct path has a length of 7.75 m and a field strength of about -10 dBV/m, as shown in Figure 8.8(b). We can also see significant field strengths of about -20 dBV/m for path lengths of 8 and 9 m.

Another way to look at the data of Figure 8.8 is to organize the rays according to the number of reflections and the associated field strengths, as shown in Figure 8.9. We can see the field strength of direct field (0 reflection), and then of all individual rays with 1 reflection, 2 reflections and multiple reflections that reach the center point of regions 1, 4, and 8 in Figure 8.2. A decrease in field strength of 20 dB represents a decrease of 0.1 on a linear scale or one-tenth. Hence, Figure 8.9 shows that two reflections are needed to include all rays with field strengths in the range of 20 dB below the field strength of the direct field, Figures 8.9(a) and (c); and that 3 reflections are needed in Figure 8.9(b). Notice that there are rays with 1 and 2 reflections that have comparable field strengths to the direct ray for regions 4 and 8. We can also see that there are a lot of rays with up to five reflections in the range of 0.01 to 0.1 V/m (-40 to -20 dBV/m).

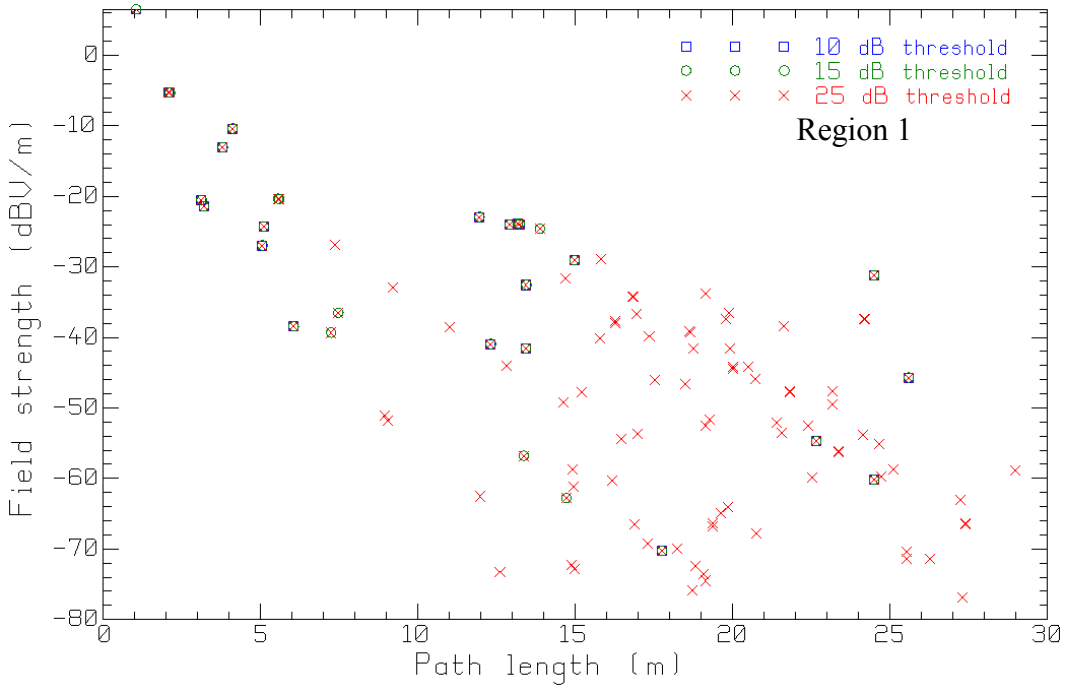

(a)

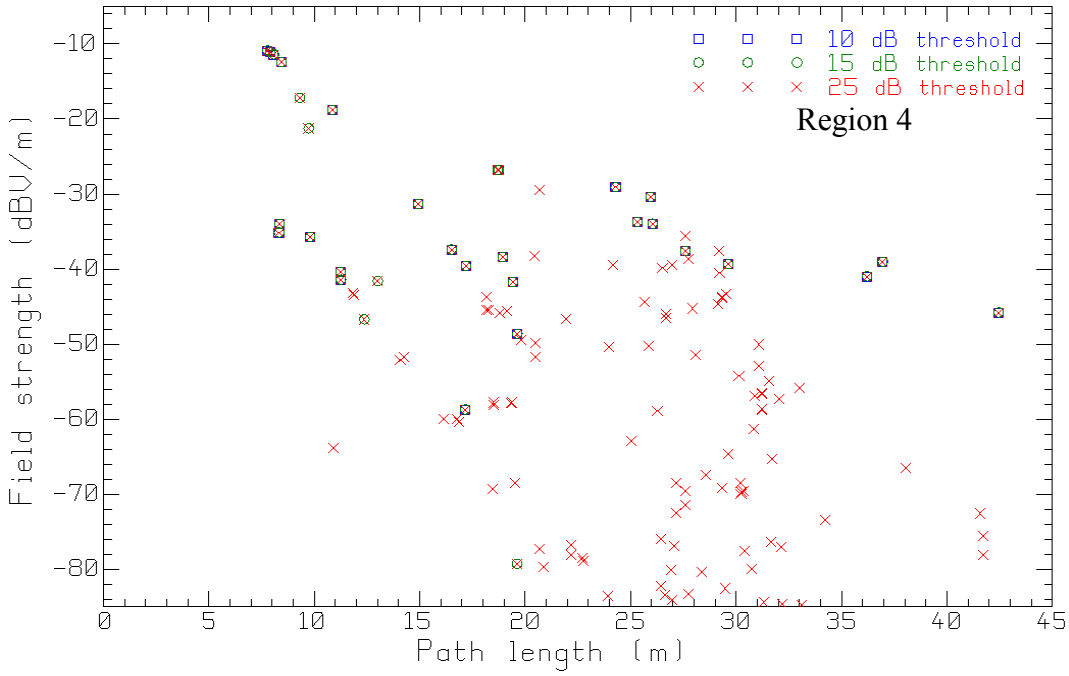

(b)

Figure 8.8: Effect of the threshold value on the number of rays taken into account in the GO model. (a) Region 1. (b) Region 4.

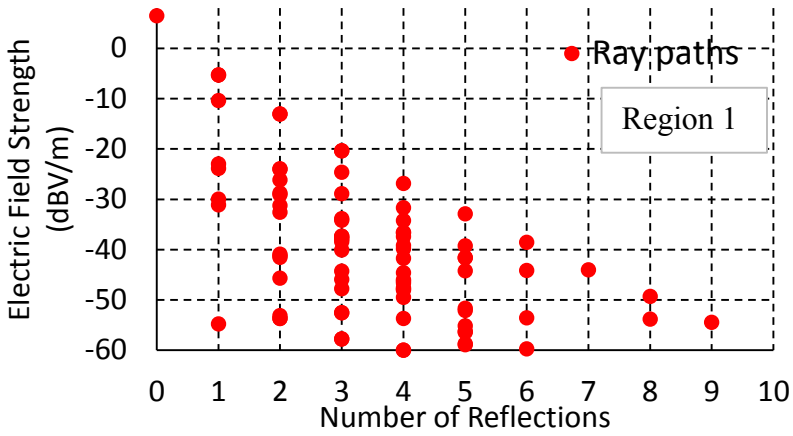

(a)

(b)

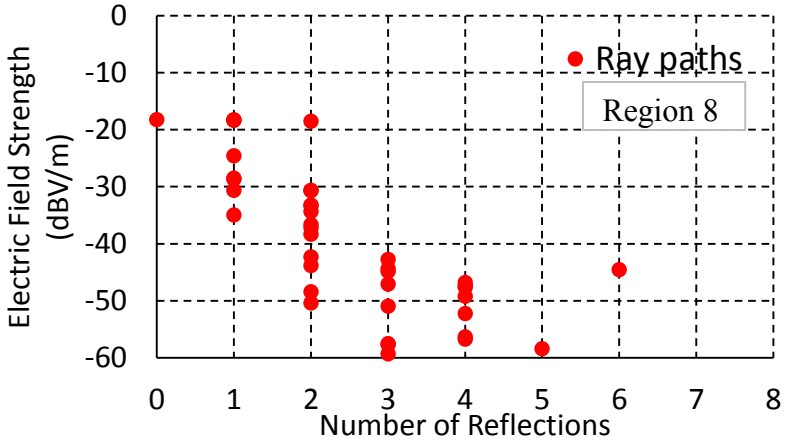

(c)

Figure 8.9: Field strength as a function of number of reflections. (a) Region 1. (b) Region 4. (c) Region 8.

Figure 8.10 shows the power density in the direct field and in all the rays with 1 or more reflections for regions 1, 4, and 8. Observe in Figure 8.10(a) the linear decline in power density as the number of reflections increases. In this case, 84.23% of the power is in the direct field, 97.29% in the direct ray plus rays with one reflection, 99.43% in the direct, one-reflection and two-reflection rays, and 99.9% in the rays with up to three reflections including the direct ray. Therefore, ray paths with more than three reflections have negligible impact on the net field strength, except at points where we find the minima of the interference pattern.

At the center of the region 4, the power density in the rays with one reflection is greater than that in the direct ray. So, as the receiver gets farther and farther away from the transmitter, the multipath field component becomes comparable to that of the direct field, and many times is the dominant component. In this case, the power density in the direct ray comprises 23.89% of the total power density at that point. 73.02% of the power density is in the direct rays plus rays with one 1 reflection, 91.35% in the direct ray, one-reflection and two-reflection rays, and 99.45% in the direct ray plus rays with up to 3 reflections. Therefore, in this case, the rays with one reflection are the ones carrying most of the power. Again, rays with more than three reflections could be discarded without a compromise on accuracy. However, rays with up to five reflections are necessary to accurately predict the minima of the interference pattern in the region, as shown in Figure 8.9(b) and (c) where we can see that there are significant five-reflection rays that are less than 40 dB below than the field strength of the direct ray. Choosing to use up to three-

reflection rays only would result in a less accurate prediction of the statistics of the field strength distribution.

The further the receiver gets from the transmitter, the more important the multipath component becomes because most of the power density is in the multipath field, mainly in the one- and two-reflection rays. This can also be observed in Figures 8.10(c) which shows the power density at the center of region 8 in Figure 8.2.

Finally, observe that one reflection reduces the field strength by a factor equal to the reflection coefficient magnitude. Imagine that we have an average reflection coefficient, Γ. Then, N reflections reduce the field strength by Γ^N, or on a dB scale, by $20N\log(\Gamma)$. Since power is proportional to E^2, the power is $10\log(\Gamma^{2N})$, which is also $20N\log(\Gamma)$. This is seen in the power vs number of reflections graph in Figure 8.10. Estimating the average reflection coefficient would allow us to choose the number of reflections to include in the GO calculation to account for field strengths that are greater than a pre-set number of dB below the largest reflected power. This could be a better way to define the threshold in the GO_3D program.

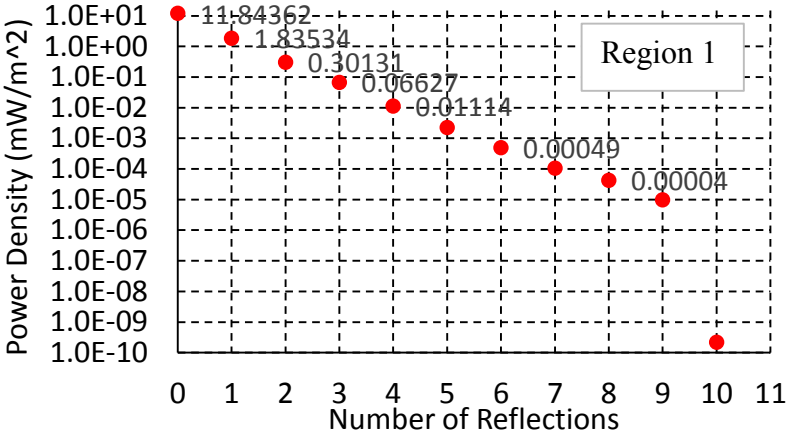

(a)

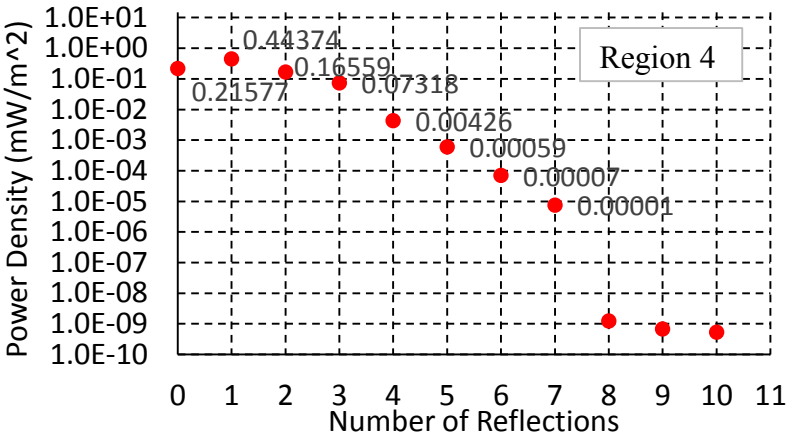

(b)

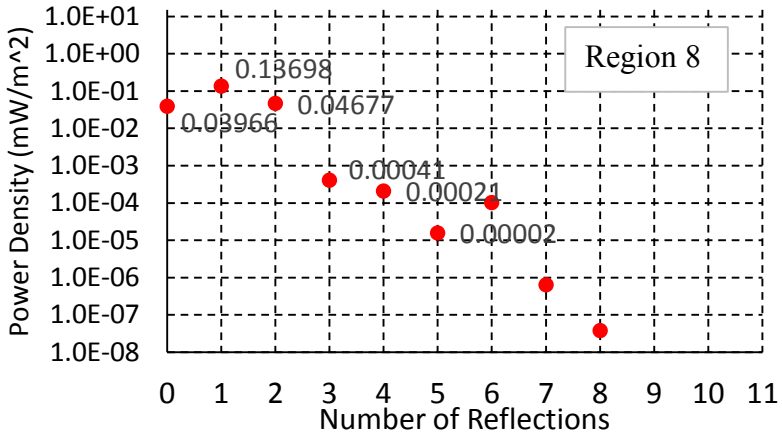

(c)

Figure 8.10: Total power density as a function of number of reflections. (a) Region 1. (b) Region 4. (c) Region 8.

8.1.3 Ricean Model Obtained by Geometrical Optics

In this section, we compare the measured electric field strengths to those predicted by GO simulation. We also compare the MLE, MM, and proposed methods of estimation of the Ricean parameters when only 36 or 9 evenly-spaced data points across a 65 by 65 cm region are considered. Figure 8.11 shows the field maps for region 1 in Figure 8.2.

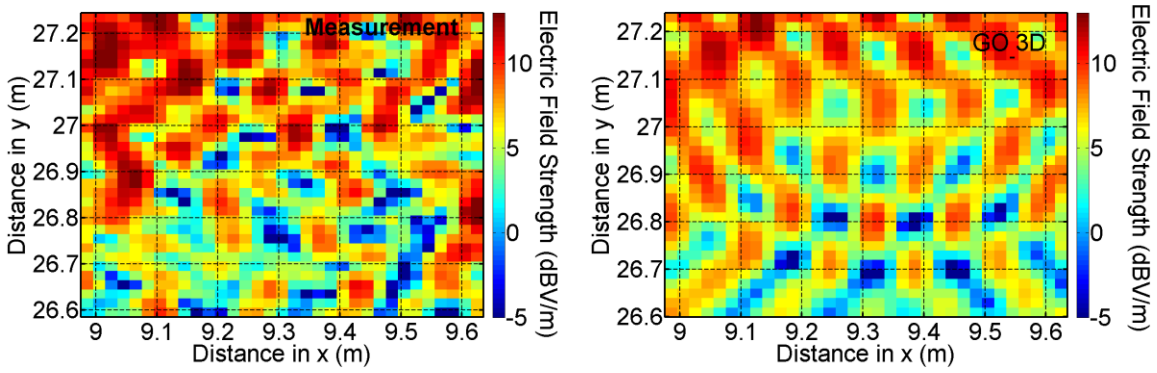

(a) (b)

Figure 8.11: Electric field strength map for region 1. (a) Measurement, (b) GO simulation.

The separation between data points is 2 cm in both x- and y-directions. As we can see, there is correlation between measurement and GO simulation, but the measured field seems less organized than the simulated, with peaks slightly stronger and more counts of very low field values. This result was expected and resembles that of the metal studs in the controlled environment, shown in chapter 6. The presence of metal studs in the corridor walls, which are not taken into account in the GO simulation, seems to cause the rapid variations seen in Figure 8.11(a). Besides, the effect of the metal studs is stronger in region 1 than in regions far from the transmitter because of the relatively small (near-

normal) angle of incidence of the rays undergoing multiple reflections between the two walls. This geometry favors the incidence of a rays on the surface and edges of the metal studs and, therefore, the generation of stronger reflected and diffracted rays, as demonstrated in section 5.3.

Figure 8.12 compares the measured and simulated CDFs, as well as the CDFs obtained by estimating the Ricean parameters with 36 and 9 data points using the MLE, MM, and proposed-GO methods. The proposed-GO estimation method is described in section 7.1. As we can see, the statistics of the fast fading obtained with measurement and simulation differ somewhat. There is a difference of 10% at the upper tail of the distributions. The three estimation methods, MLE, MM, and the proposed-GO, are successful in reproducing the statistics of the simulated fast fading when 36 points are considered. But the CDF computed with 9 data points is not nearly close to the measurement as that with 36 data points.

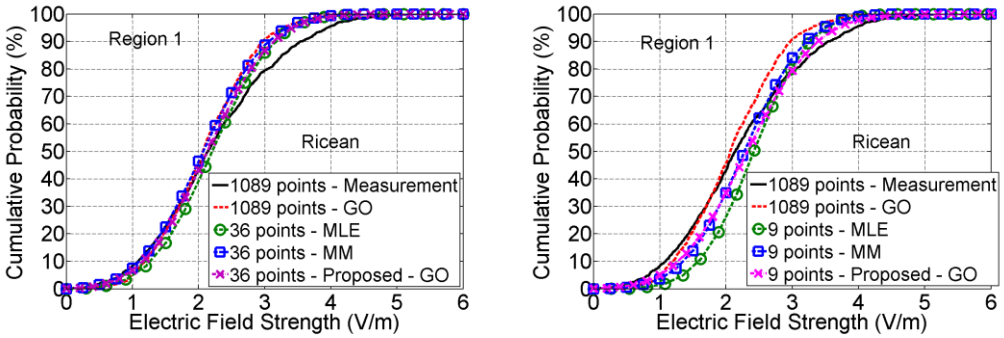

(a) (b)

Figure 8.12: Comparison of CDFs for region 1 of Figure 8.2. (a) 36 data points, (b) 9 data points.

This suggests that for regions close to the transmitter, the separation between sample points should be around one wavelength. This conclusion is in agreement to that reached in the controlled environment. Table 8.1 compares the Ricean parameters. Despite the huge reduction in sample size, all three methods provide similar Ricean parameters with 36 data points. It should be noted that the estimates of the Ω parameter given by MLE and MM methods are the same for all regions. This is due to the fact that this parameter is obtained from the second moment (2.41) which is also is the maximum likelihood estimator.

Table 8.1: Ricean parameters. Region 1 of corridor experiment.

Region 1 (Corridor)

	MLE		MM		Proposed method	
Sample size	K	Ω	K	Ω	K	Ω
1089	3.54	4.87	3.31	4.87	3.52	5.52
36	3.70	5.41	3.31	5.42	3.34	5.61
9	6.10	6.31	4.72	6.31	3.49	6.57

Figure 8.13 compares the measured and simulated CDFs, as well as the CDFs obtained by estimating the Ricean parameters with 36 and 9 data points using the MLE, MM, and proposed-GO methods for regions 2 and 3 in Figure 8.2. As we can see, the agreement between measurement and GO simulation is much better for regions 2 and 3, despite the model's inaccuracies and simplicity. Moreover, the proposed estimation method is shown to be better than the MLE and MM methods, especially when only 9 points are considered. Tables 8.2 and 8.3 show the Ricean parameters for regions 2 and 3,

respectively. Notice how the CDFs move to the left as the separation between the transmitter and the center of each region increases.

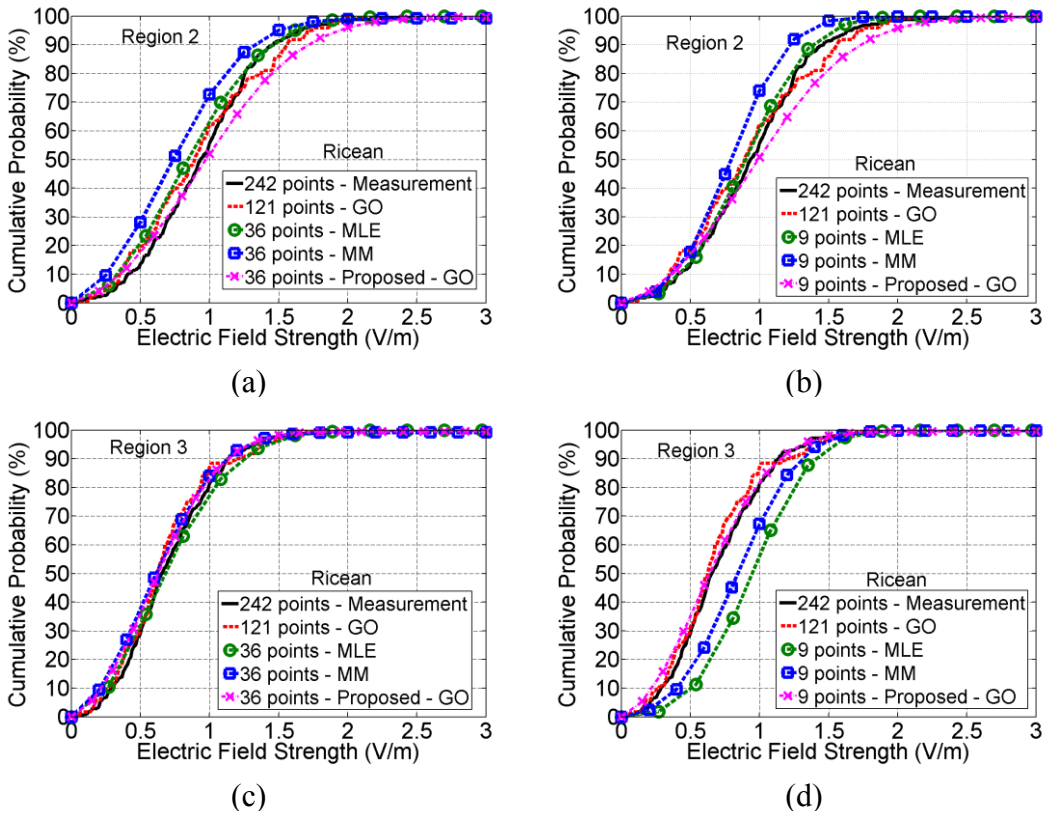

Figure 8.13: Comparison of CDFs for regions 2 and 3 of Figure 8.2.

Table 8.2: Ricean parameters. Region 2 of the corridor experiment.

Region 2 (Corridor)

	MLE		MM		Proposed method	
Sample size	K	Ω	K	Ω	K	Ω
121	0.59	1.07	0.77	1.07	0.94	1.49
36	0.80	0.94	1.035	0.94	0.94	1.49
9	2.11	0.95	3.05	0.95	0.99	1.52

Table 8.3: Ricean parameters. Region 3 of the corridor experiment.

Region 3 (Corridor)

	MLE		MM		Proposed method	
Sample size	K	Ω	K	Ω	K	Ω
121	0.00042	0.58	0.39	0.57	0.79	0.65
36	0.0016	0.66	0.84	0.66	0.78	0.65
9	3.01	1.02	2.7	1.02	0.78	0.67

Besides, notice how little the effect of sample size is on the Ricean parameters estimated with the proposed method. Caution must be taken when using the MM method (2.38) to estimate the Ricean *K*-factor for small values of field strength because it can lead to complex-valued estimates. When the expectation, $(E[e^2])^2$, is less than the variance, $V[e^2]$, γ becomes greater than 1 in (2.38). In such cases, the absolute value of $1-\gamma$ is used in (2.38). Although this correction causes (2.38) to be no longer a solution of (2.37), it prevents the problem of complex-valued *K*-factors and still provides a good estimate of this parameter.

Figure 8.14 compares the measured and simulated CDFs, as well as the CDFs obtained by estimating the Ricean parameters with 36 and 9 data points using the MLE, MM, and proposed methods for regions 4 and 5 in Figure 8.2. As we can see, an even better agreement between the measurement and GO simulation was obtained for region 4 when compared to the previous regions. On the other hand, this is not seen for region 5. In fact, there is no agreement at all, which is disappointing given that an agreement similar to those of region 3 and 4 was expected.

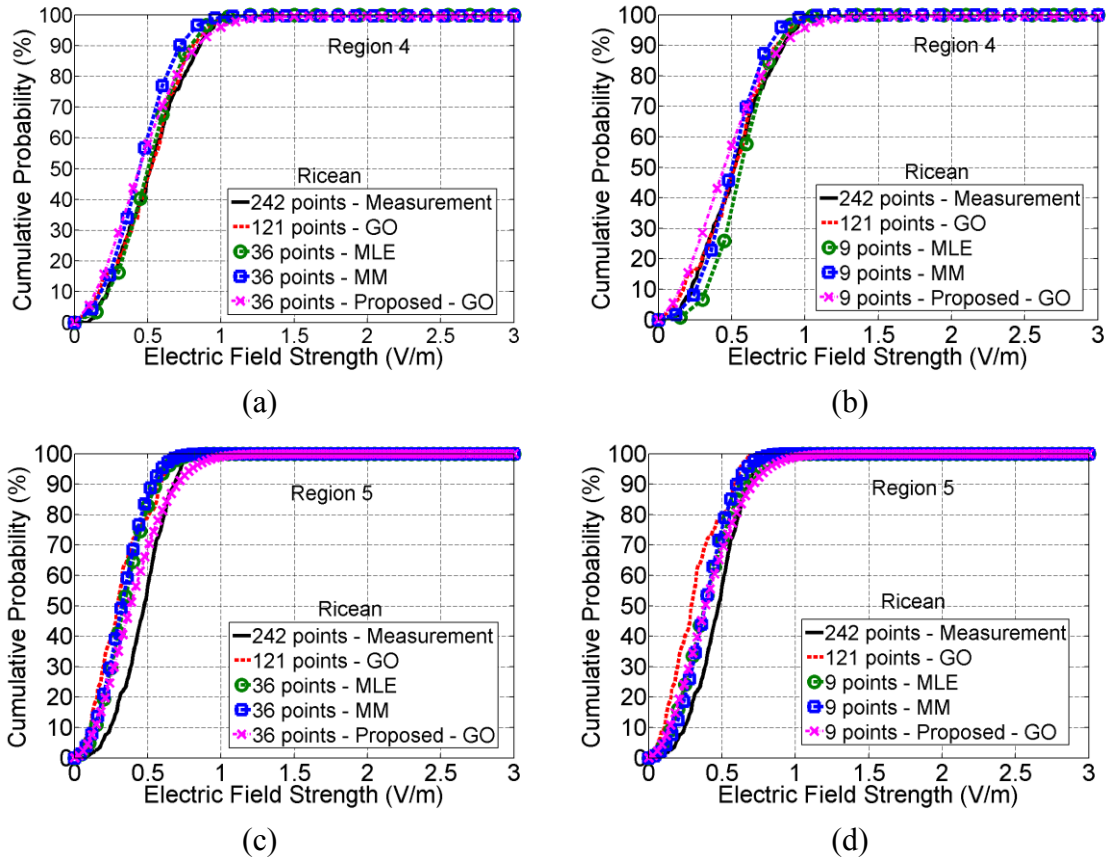

Figure 8.14: Comparison of CDFs for regions 4 and 5 of Figure 8.2.

Observe in Figure 8.14(c) and (d) that both the measured and the GO simulated CDFs have comparable slopes. However, the measured mean field is larger than that of GO, which suggests that the scaling of the measured field to the simulation level might have gone wrong. Since the same calibration factor was used to raise the measured data of all regions to the simulation level, and that agreement was obtained for other regions, this is a possible but not very likely explanation. It should also be pointed out that as the regions get farther and farther from the transmitter, the field level becomes lower and lower, hence the errors in the measurement system, as well as due to the simplified model of the

floor plan, and approximate values of electrical properties of materials become more noticeable.

As for the estimation methods, we can see that they all lead to a reasonably good Ricean model of the simulated data, especially for the cases in which 36 data points are used. The Ricean parameters are compared in Tables 8.4 and 8.5.

Table 8.4: Ricean parameters. Region 4 of the corridor experiment.

Region 4 (Corridor)

	MLE		MM		Proposed method	
Sample size	K	Ω	K	Ω	K	Ω
121	1.19	0.31	1.62	0.31	0.31	0.34
36	1.95	0.30	2.00	0.30	0.31	0.34
9	4.17	0.35	3.40	0.35	0.31	0.35

Table 8.5: Ricean parameters. Region 5 of the corridor experiment.

Region 5 (Corridor)

	MLE		MM		Proposed method	
Sample size	K	Ω	K	Ω	K	Ω
121	0.03	0.13	0.14	0.13	0.26	0.22
36	1.01	0.14	1.47	0.14	0.26	0.22
9	0.82	0.19	2.12	0.19	0.26	0.23

Figure 8.15 compares the measured and simulated CDFs, as well as the CDFs obtained by estimating the Ricean parameters with 36 and 9 data points using the MLE, MM, and proposed methods for regions 6, 7, and 8 in Figure 8.2. Observe that a shift of the measured mean field strength to the right when compared to the CDF obtained from GO is present in the CDFs corresponding to regions 6, 7, and 8. Although the slopes of the curves in Figure 8.15(a) for region 6 are all similar, this is not the case for regions 7 and 8. This means that not only the measured mean field strength is greater than that of the GO, but also that the measured multipath component is larger. This suggests that the model of the sidewalls might not be correct, since the multipath component depends on the reflection coefficient of the sidewall, which in turn depends on the thickness of the gyproc slabs and of the air layer, as well as on the electrical properties used in the simulation.

However, it should be noted that the model does not include any furniture, metal cabinets, shelves, and lab equipment that might be on the other side of the sidewalls, which may affect to the multipath component. A counterargument is that the path along the corridor is so long that the reflection coefficient is at nearly grazing incidence and should approach unity in magnitude. So, what is behind the sidewalls should not matter at those regions.

Notice that for the region 8 in Figure 8.15(c), both the MLE and the MM methods resulted in CDFs that are slightly better representations of the GO CDF than that obtained

with the proposed method. However, the estimation methods are similar for regions 6 and 7.

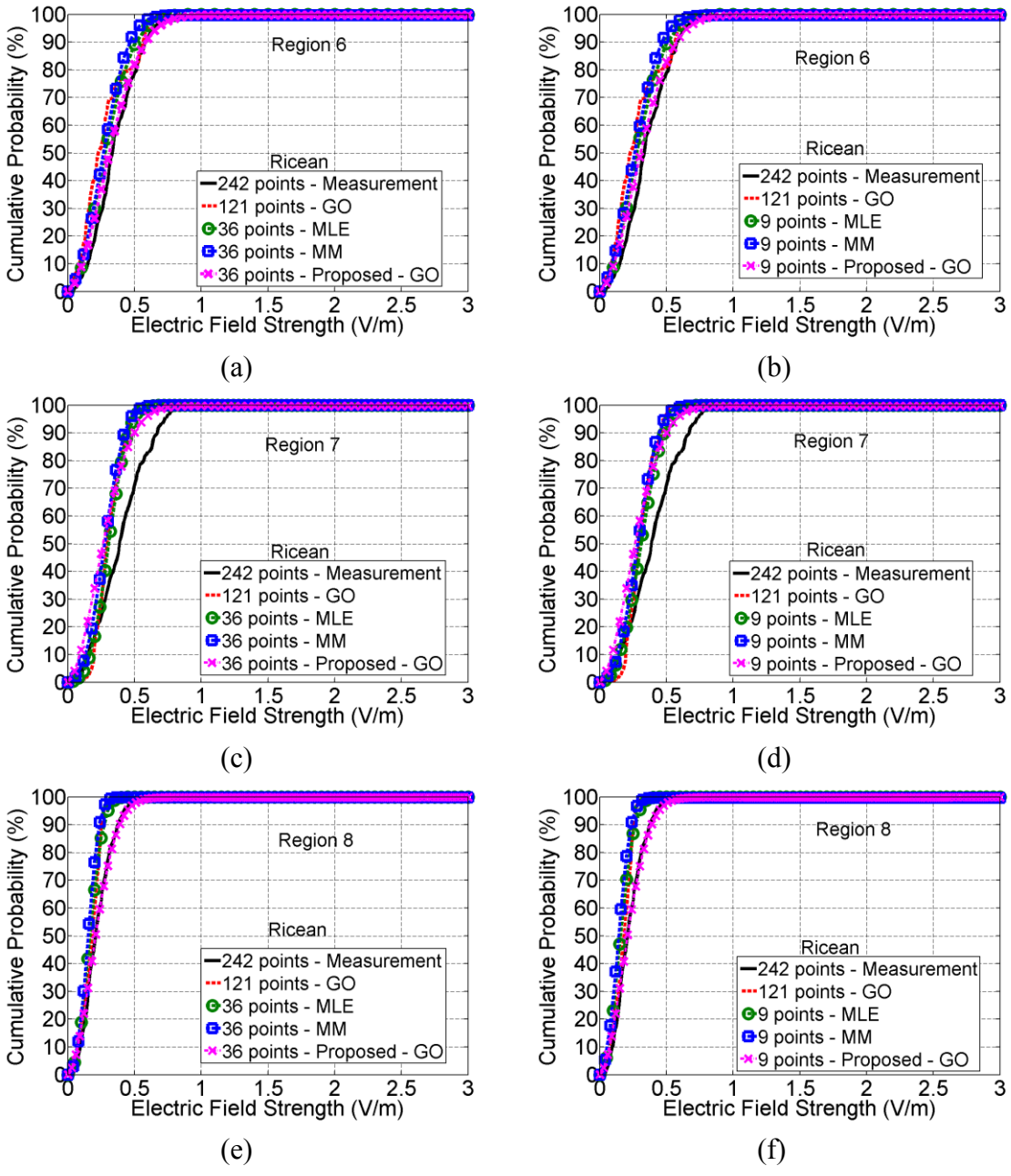

Figure 8.15: Comparison of CDFs for regions 6, 7, and 8 of Figure 8.2.

The Ricean parameters corresponding to regions 6, 7, and 8 are compared for the three different estimation methods in the Tables 8.6, 8.7, and 8.8, respectively.

Table 8.6: Ricean parameters. Region 6 of the corridor experiment.

Region 6 (Corridor)

	MLE		MM		Proposed method	
Sample size	K	Ω	K	Ω	K	Ω
121	0.001	0.11	1.22	0.11	0.24	0.16
36	<0.001	0.11	1.13	0.11	0.24	0.16
9	<0.001	0.11	0.90	0.11	0.25	0.15

Table 8.7: Ricean parameters. Region 7 of the corridor experiment.

Region 7 (Corridor)

	MLE		MM		Proposed method	
Sample size	K	Ω	K	Ω	K	Ω
121	4.41	0.11	3.97	0.11	0.25	0.12
36	2.96	0.11	2.73	0.11	0.25	0.12
9	1.90	0.11	2.62	0.11	0.25	0.12

Table 8.8: Ricean parameters. Region 8 of the corridor experiment.

Region 8 (Corridor)

	MLE		MM		Proposed method	
Sample size	K	Ω	K	Ω	K	Ω
121	2.21	0.034	3.36	0.034	0.27	0.07
36	1.37	0.034	2.70	0.034	0.27	0.07
9	0.89	0.032	1.73	0.032	0.27	0.07

For these eight LOS regions, the GO model proved to be useful for the estimation of the statistics of fast fading for most cases, even though point-by-point agreement was never expected; given the simplified model of the floor plan, errors in the positioning of the receive antenna, and in the model of the walls. We also see that 36 points evenly-spaced across a 65 by 65 cm region lead to more reliable CDFs than when only 9 points are considered. Besides, the estimation methods are shown to have comparable performances for 7 out of the 8 cases for 36 points; whereas caution must be taken with only 9 points. Therefore, we recommend that at least 36 points be used for reliable estimation of the statistics of the fast fading for real indoor environments.

As for the NLOS regions, Figure 8.16, compares the measured and simulated CDFs, as well as the CDFs obtained by estimating the Ricean parameters with 36 and 9 data points using the MLE, MM, and proposed methods for regions 9 and 10 in Figure 8.2. The agreement between the measured and simulated CDFs in Figure 8.16(a) is surprisingly good because at that deep shadow we would expect diffraction to play an important role, as is the case for region 10 in Figure 8.16(b).

It is important to point out that the walls of the corridor have internal metal studs which block the transmitted field that would reach region 10 due to the very oblique angles of incidence on the hallway wall surfaces. Consequently, in the measurement, there cannot be a transmitted field in region 10. In contrast, in the simulation, the GO_3D code accounts for the transmitted field through the three-layer wall, but does not model the

blocking of the studs and diffraction. As a result, the GO model provides a poor representation of the region 10.

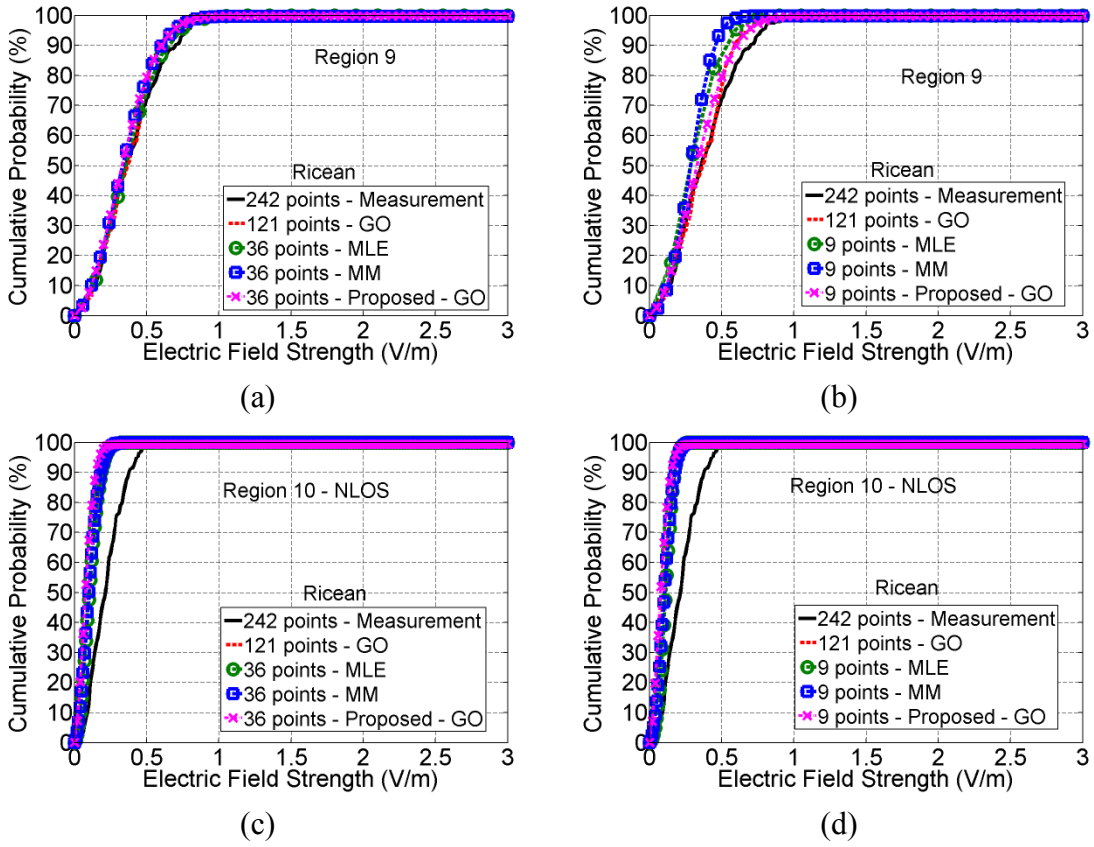

Figure 8.16: Comparison of CDFs. Comparison of CDFs for NLOS regions 9 and 10 of Figure 8.2.

Once again, the use of 36 data points in the estimation of the Ricean parameters resulted in better CDFs. Tables 8.9 and 8.10 compare the Ricean parameters obtained by the MLE, MM, and proposed estimation methods.

Table 8.9: Ricean Parameters. Region 9 of the corridor experiment.

Region 9 (Corridor)

	MLE		MM		Proposed method	
Sample size	K	Ω	K	Ω	K	Ω
121	0.71	0.17	0.85	0.17	0.49	0.17
36	0.001	0.18	0.62	0.18	0.48	0.17
9	0.0001	0.12	2.21	0.12	0.48	0.17

Table 8.10: Ricean parameters. Region 10 of the corridor experiment.

Region 10 (Corridor)

	MLE		MM		Proposed method	
Sample size	K	Ω	K	Ω	K	Ω
121	0.36	0.014	0.37	0.014	0.021	0.019
36	0.01	0.015	0.26	0.015	0.038	0.011
9	1.99	0.015	1.13	0.015	0.041	0.011

8.1.4 Path Loss Model

The electric field strength associated with the path loss model is given by [16]

$$E(r) = \frac{E_0}{r^{n/2}} \tag{8.1}$$

where $E_0 = \sqrt{\eta_0 D P_t/(4\pi)}$ is the field strength at 1 m from the transmitter. When $n = 2$ we obtain the free-space attenuation, and when $n < 2$ the attenuation decreases at a rate less than would be expected in free space.

In our experiment, the mean electric field of each LOS region is used to analyze the behavior of the slow fading and to derive the path loss exponent by using the least-square method. Figure 8.17 shows the electric field as a function of distance from the transmitter and the center of the regions.

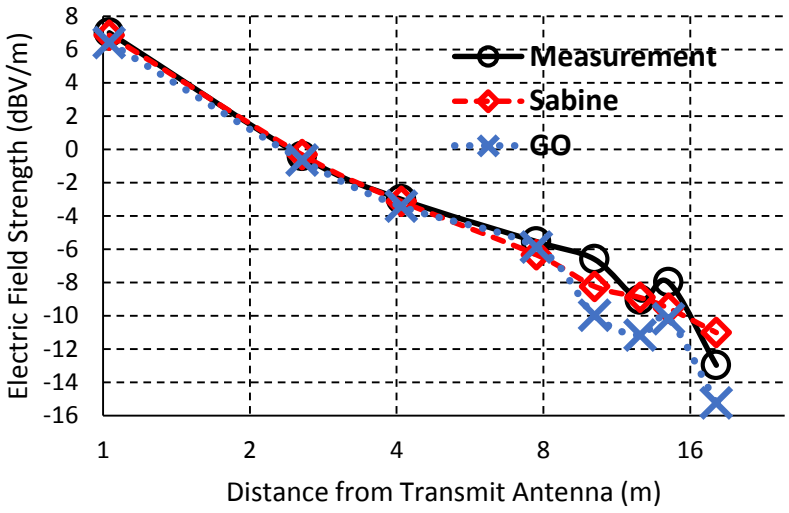

Figure 8.17: Mean electric field strength as a function of distance from the transmitter.

As we can see the Sabine method with the exponential correction results in a path loss very similar to that obtained by measurement. The curve obtained with GO differs by about 2 dB from the others for regions beyond 10 m from the transmitter. Yet, GO successfully predicts the rise in the mean field around 14 m, also observed in the measured curve. The path loss exponents obtained by measurement, GO simulation, and Sabine method is shown in Table 8.11.

Table 8.11: Path loss exponent. Area measurements.

Method	Measurement	GO simulation	Sabine
Path loss exponent	1.394	1.588	1.384

8.2 Electric Field Strength along a Straight Path

In this section we study both fast fading and slow fading along a 20-m long straight path in the corridor on the 15th floor of the EV Building at Concordia University, shown in Figures 8.1 and 8.18. The purpose of this experiment was to compare point by point the measured electric field strength and that obtained with GO simulation. Moreover, we wanted to compare the measured slow fading with those predicted by GO and Sabine models. Figure 8.19 shows the model of the floor plan used in the simulations, with the path of receivers represented by the dashed line.

Figure 8.18: This figure shows the corridor on the 15th floor of the EV Building, and the line-follower "robot" carrying the receive antenna, with the transmit antenna in the background.

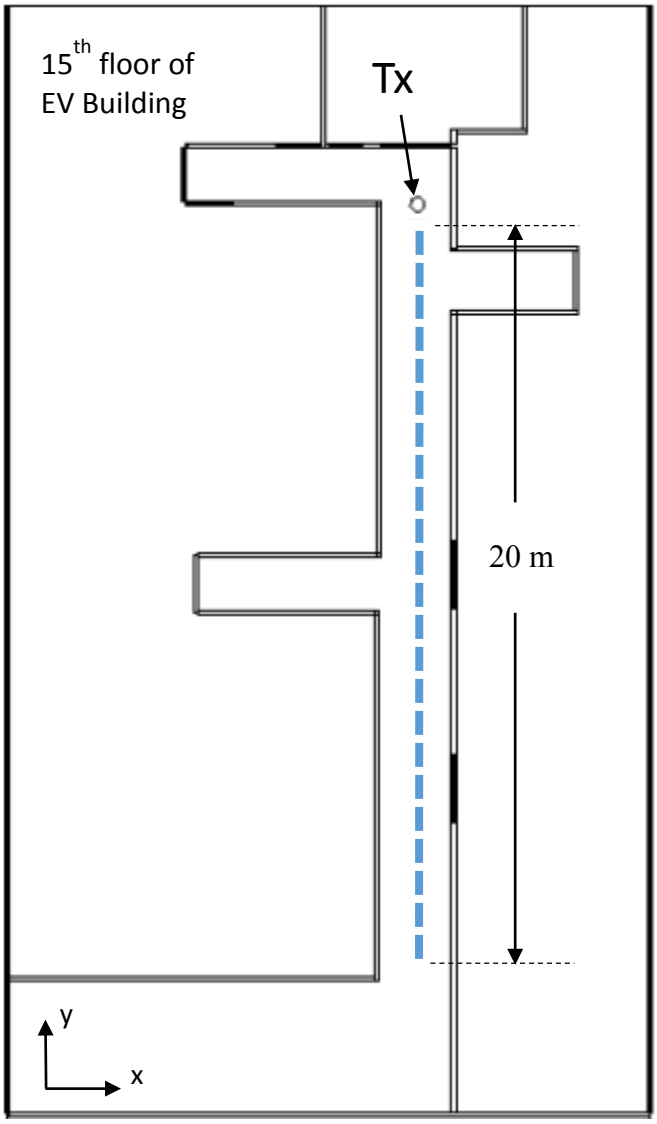

Figure 8.19: Model of the floor plan of the 15th floor of the EV Building. Line measurement.

Electric field strength measurements were taken along this 20-m long path every 1 cm. The corridor is 1.82-m wide and over 20-m long with a ceiling height of 2.98 m. The walls were modeled as layered structures containing two 1.5-cm-thick gyproc ($\varepsilon_r = 2.25, \sigma = 0$ mS/m) panels separated by a 9.5-cm-thick air layer. Metal doors, wooden

doors, metal door frames, and glass walls were all included in the model. Both the floor and ceiling were modeled as a 30-cm-thick concrete layer ($\varepsilon_r = 9.2, \sigma = 204$ mS/m). Figure 8.20 shows the measurement setup in the corridor.

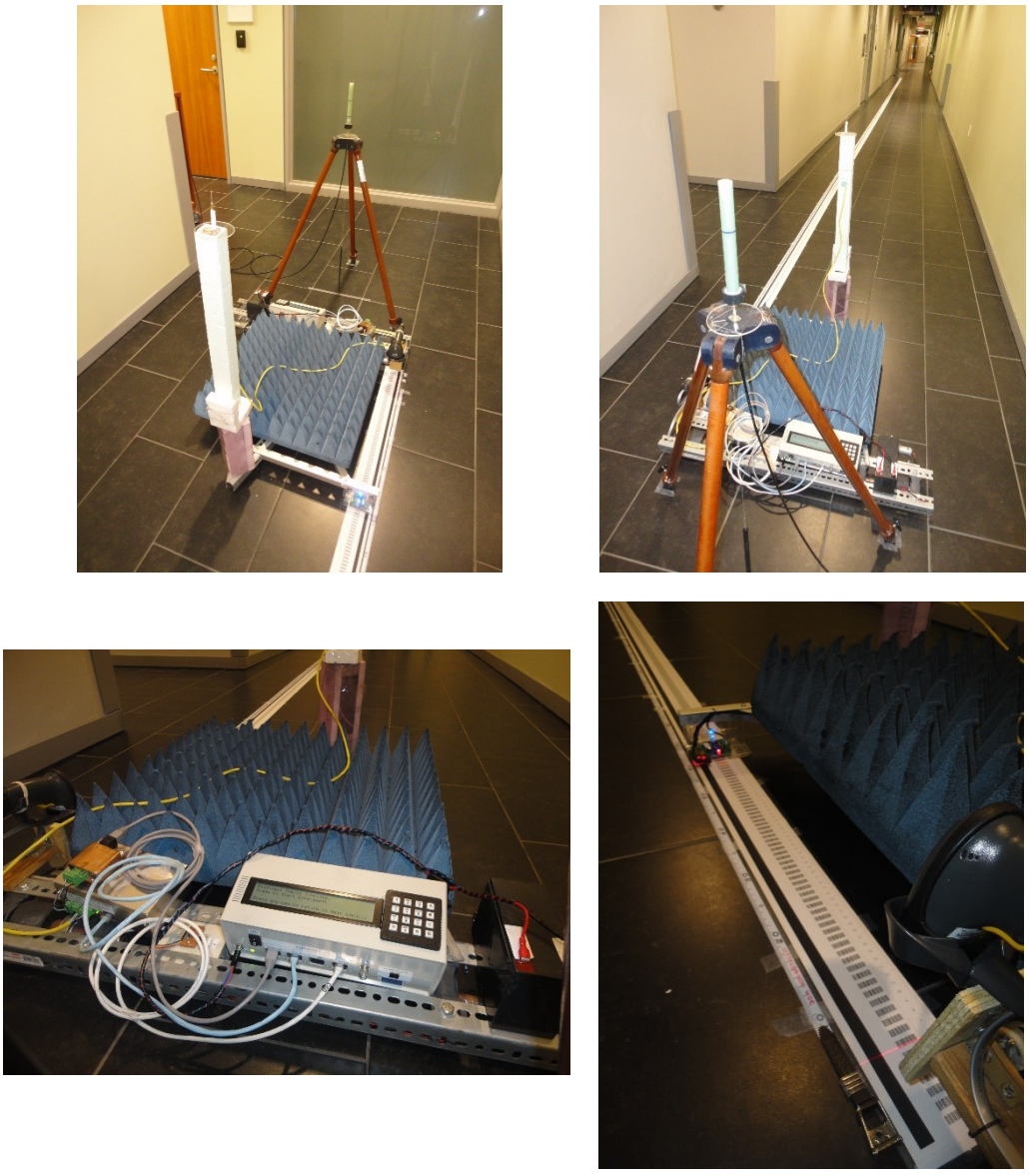

Figure 8.20: Experiment setup for the field measurement along a path in a corridor.

This measurement system used for this experiment was the Line Follower robot described in more detail in Chapter 3. The transmitter was a calibrated sleeve dipole antenna which was fixed in position, 92 cm from the left wall and 90 cm from the right wall, vertically oriented and kept at a height of 1.14 m above the floor. The receiver was a vertically oriented WiFi sleeve dipole antenna and was at a height of 1.015 m above the floor. The distance from the straight path of receivers to the left and right walls were 93.5 and 88.5 cm, respectively. The simulations considered a vertically oriented half-wave dipole antenna radiating 100 mW. As the radiated power was much less than 100 mW and not precisely known, the calibration method described in Section 3.3.7 was applied to bring the power level of the measured data to that of the simulated. In the GO simulation, a threshold value of 25 dB was used to control the number of rays. Consequently, rays with up to 15 reflections were taken into account in the computation of the total electric field strength at a single point. Even though more computation was done than was necessary, the results were still correct GO calculations. As discussed in Section 8.1.2, rays with more than 3 reflections could be discarded.

Figure 8.21 compares point by point the measured electric field strength to that obtained with GO simulation. We can see that there is reasonable agreement up to 8 m. In this section of the path the fast variation of the simulated field is mainly due to reflections from the big glass wall in the back of the corridor, close to the transmitter, which together with the direct field from the transmitter creates the standing wave pattern. As for the even faster variation observed in the measured curve, not only the big glass wall plays an

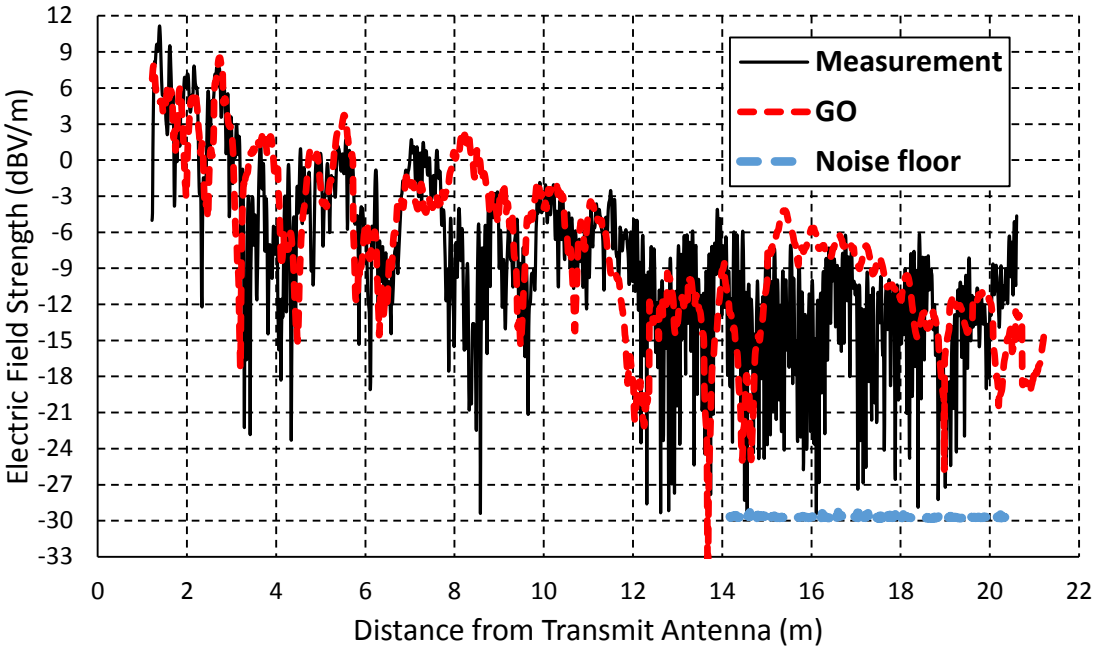

Figure 8.21: Point-by-point comparison between measured and GO simulated electric field strength.

important role, but also the metal studs in the interior of the sidewalls, just as observed in the area measurements. The discrepancy at around 8.5 m might be due to a strong reflection from the floor or ceiling, which may not have been captured well in the simulation because both the floor and the ceiling were modeled as a 30-cm-thick concrete layer.

Another possible explanation is the possibility of existence of structures such as metal cabinets, shelves, and lab equipment on the other side of the sidewalls. These structures are not taken into account in the model and could very well have a strong effect on the net field in the corridor. Then, from 9 to 11 m we have agreement again. Beyond 12 m

we apparently enter in a different regime, and no agreement is observed whatsoever. Notice that the field levels are still well above the noise floor, represented by the dashed blue line at the bottom of the Figure 8.21.

Figure 8.22 compares the slow fading of the electric field strength by displaying the moving average of the measured and GO curves of Figure 8.21 for an averaging window of 65 cm, approximately 5 wavelengths in size. Furthermore, Figure 8.22 also graphs the mean electric field strength obtained with the Sabine method as a function of distance from the transmitter.

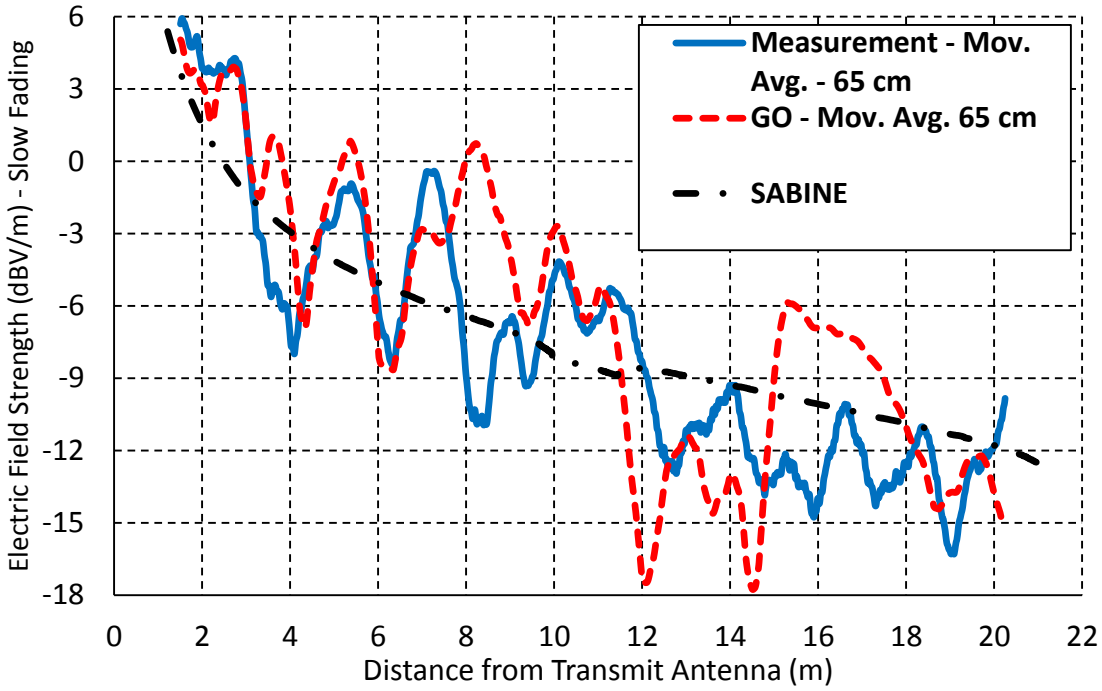

Figure 8.22: Slow fading. Electric field strength as a function of distance from the transmitter.

The Sabine method with the exponential correction provides a very good model for the mean electric field strength in a long corridor. We can also see that an average window of approximately 5 wavelengths is not enough to completely remove the fast fading. However, it allows us to compare the trend of the measured and GO simulated curves. In contrast to the results of the area experiment, in this experiment both the GO and Sabine simulations resulted in slightly overestimated mean electric field strengths in the section of the path beyond 15 m. Finally, the least-square method was applied to these three curves in order to obtain the power law best fit, and consequently the path loss exponent. Table 8.12 compares the path loss exponents obtained from measurement, GO simulation, and Sabine method.

Table 8.12: Path loss exponent. Line measurement.

Method	Measurement	GO simulation	Sabine
Path loss exponent	1.682	1.630	1.288

By comparing Tables 8.11 and 8.12, we see that the path loss exponents of 1.394 and 1.682 obtained by measurements differ somewhat, with a relative error of 17%. On the other hand, both the GO and the Sabine simulations resulted in very close (relative error less than 10%) predictions of the path loss exponent regardless of the type of measurement, whether over an area or along a straight path. A conclusion in common to

both experiments is that the path loss exponent is less than 2 (free space), which is expected for this type of real indoor environment because of the presence of the multipath components of the field, which cause the field to decrease slower than it would in free space.

8.3 Conclusion

Just as for the experiments conducted in the shielded anechoic chamber discussed in Chapters 5, 6, and 7, the statistics of the fast fading can be modeled by any of the following four distributions: Ricean, Normal, Nakagami, and Weibull. However, for the corridor experiment the Normal distribution constantly resulted in the worst fit to the measured data, despite the fact that the Normal model was not significantly different from the measured data.

In this chapter, we conclude that rays with up to three reflections are the ones carrying over 98% of the power that reaches the receiver. However, up to five-reflection rays are necessary to accurately predict the minima of the interference pattern in the regions. We showed that it is necessary to use a high threshold value to be able to include some important rays.

Then, focus was again given to the Ricean distribution because of its simplicity and physical interpretation. The new and simpler proposed method for estimating the Ricean parameters was shown to be as good as the MLE and the MM methods when at least 36 data points evenly spaced across a 65 by 65 cm region are considered. In contrast to the

conclusion in Chapter 7, for the long corridor scenario we recommend the use of at least 36 data points in order to reliably estimate the Ricean parameters. Besides, the use of only 9 points was shown to be inadequate for this purpose. In addition, we conclude that proposed method solves the problem previously encountered when treating regions close to the transmitter even for this real indoor scenario.

We also conclude that point-by-point agreement between measurement and GO simulation is very hard if not impossible to attain, but that GO can still provide a good and useful prediction of the statistics of the fast fading for LOS regions, despite the fact that it ignores diffracted rays and is usually applied with a simplistic model of the site geometry and objects in the interior. On the other hand, GO was not expected to work for the NLOS cases where diffracted rays play an important role.

As for the slow fading and path loss exponent, we conclude that the Sabine method with the exponential correction is a very good and efficient method for predicting the mean electric field strength in indoor environments and thus the path loss exponent, and that the GO model can also be used to predict the slow fading and path loss exponent provided that an averaging window much larger than 5 wavelengths is used in the line type of experiment and at least 36 points evenly spaced across a 65 by 65 cm region in the area type of experiment.

Chapter 9: Electric Field Strength in a Laboratory Room

In this chapter we study radio-wave propagation in a laboratory room by means of measurements, GO simulation, Sabine's method, and statistical analysis, just as we did in the previous chapter for the long corridor scenario. We have demonstrated in Chapters 5 and 6 that GO simulation is sufficient to predict electric field strength in a controlled scenario, and that we can accurately attain the statistics of the fast fading from a data set of about 200 points. Then, in Chapter 7, we chose the Ricean distribution to model fast fading, and showed that its parameters can be estimated from as few as 36 data points evenly spaced on a 65 by 65 cm region by using the MLE, MM, or proposed-GO estimation methods. Finally, in Chapter 8, we applied the same methods and techniques to investigate indoor propagation on a real indoor scenario, a long corridor.

We now consider a conventional rectangular laboratory room, the H853 microwave laboratory on the 8th floor of the Hall building at Concordia University. We start by presenting the statistical analysis of the measured electric field strength at four regions along a path and show that the Ricean, Normal, Nakagami, and Weibull distributions provide statistical models that are statistically equivalent for all the 4 regions, especially for regions farther than 3 m from the transmitter. For this real scenario, the Nakagami distribution clearly provides the best-fit to the measured data for regions close to the transmitter. Then we show that GO simulation, together with MLE, MM, or the proposed-GO method, can be used to predict the statistics of the electric field strength for

two of the cases, and that clutter has a major impact on the propagation of the radio waves. Besides, we show how clutter can affect the prediction of path loss by the ray-tracing technique and Sabine method.

9.1 Electric Field Strength Distribution on a 65 by 65 cm Region

This experiment was conducted in the microwave lab on the 8th floor of the Hall building at Concordia University. Measurements of electric field strength were taken at four different locations in the room, radially away from the transmitter, as shown in Figure 9.2. The purpose of this experiment was to find the best statistical model for the distribution of the field in a square region that is about 5 wavelengths in size at 2.45 GHz. Furthermore, we wanted to compare measurement to GO simulation, and see whether a Ricean model can be obtained from GO calculations for this particular type of real indoor environment with lots of clutter. Finally, we compared path loss models obtained by measurement, GO simulation, and Sabine method. Figure 9.1 shows the laboratory room.

Figure 9.1: Microwave Lab on the 8th floor of the Hall Building. The photo shows that the file cabinet with instruments stored on top of them near the Tx. Both antennas are positioned at a height greater than the height of the file cabinet.

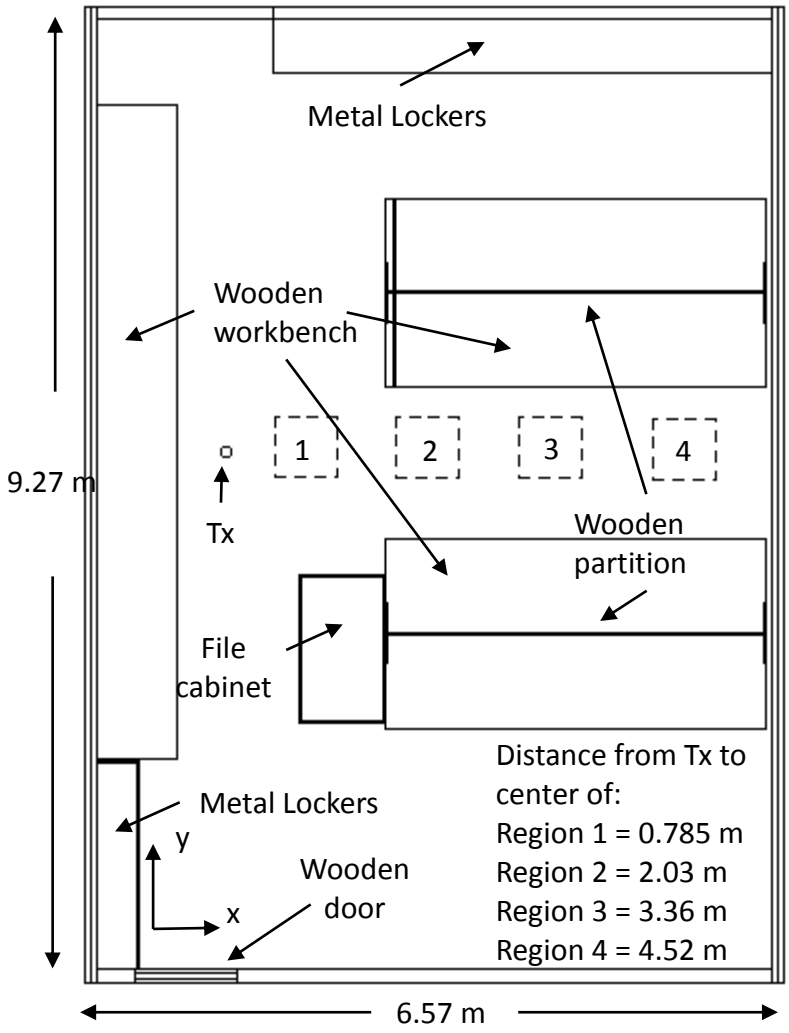

Figure 9.2: Model of the microwave lab H853.

Figure 9.2 shows the model of the floor plan used in both the GO and the Sabine simulations, with the four measurement regions represented by the squares. The distance from the transmitter to the center of each region is indicated at the bottom right corner of Figure 9.2. The room is 6.57-m wide and 9.27-m deep, with a ceiling height of 3.75 m. The rectangular room has old cinder-block walls which were modeled as layered structures containing two 1.5 cm of concrete ($\varepsilon_r = 5.37, \sigma = 149.5$ mS/m), 0.8 cm of brick ($\varepsilon_r = 4.38, \sigma = 18.5$ mS/m) [16], a center air layer 7.8 cm thick, and symmetric

layers of brick and concrete. Metal lockers, wooden doors, wooden workbenches, and wooden partitions were all included in the model. However, clutter such as lab equipment and objects were not included in the model. Both the floor and ceiling were modeled as a 30-cm-thick concrete layer ($\varepsilon_r = 9.2, \sigma = 204$ mS/m). The electrical properties of the materials used in this experiment to model the room walls, ceiling, and floor, were found in the literature rather than being measured.

In this experiment, we used the 2D scanner measurement system to take electric field strength measurements in a 65 by 65 cm region in steps of 6 cm in the x-direction and 6 cm in the y-direction, as indicated in Figure 9.2, for a total of 121 sample points. The experiment setup is shown in Figure 9.3.

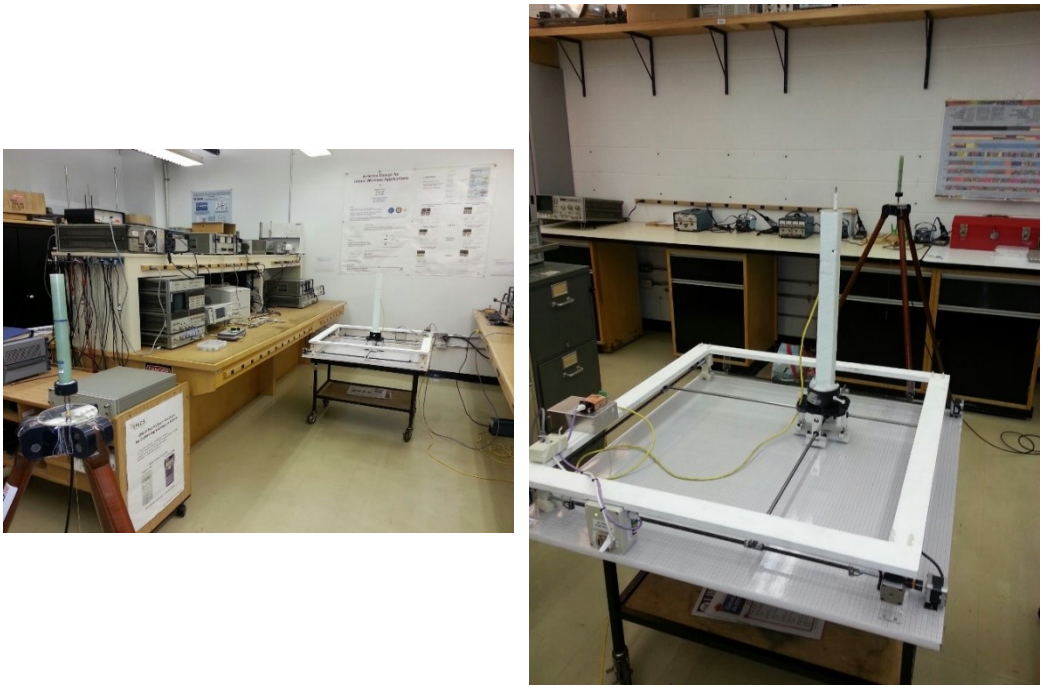

Figure 9.3: Experiment in the microwave lab H853. Measurement setup. The photo shows the xy positioner and the Styrofoam pole used to move the receive antenna.

This measurement system is described in more detail in chapter 3. The transmitter was a calibrated sleeve dipole antenna which was fixed in position, 125.5 cm from the left wall and 505.5 cm from the bottom wall, and was vertically oriented and kept at a height of 1.47 m above the floor. The receiver was a vertically oriented WiFi sleeve dipole antenna and was also at a height of 1.47 m above the floor. The simulations considered a vertically oriented half-wave dipole antenna radiating 100 mW. Just as for the corridor experiment, the radiated power was much less than 100 mW and not precisely known, so the calibration method described in section 3.3.7 was applied to bring the power level of the measured data to that of the simulated.

9.1.1 Statistical Analysis of the Measured Data

For all the four regions in Figure 9.2 we measure the field strength at 121 data points, and we expected the measured field strengths to be uncorrelated. To verify that the data points are indeed uncorrelated so that the Anderson-Darling test can be applied, Figure 9.4 shows the average correlation coefficient, given by (6.1), of the measured data for the four regions considered. As can be seen the average correlation coefficient is less than 0.5 at 6 cm in both the x- and y-directions for regions 2, 3, and 4. Hence, we consider the 121 data points to be independent [72]. For region 1, the closest to the transmitter, the data is almost uncorrelated in the x-direction. That is a result of the relatively strong direct field propagation radially away from the transmitter in the x-direction, and the fact that there is no strong reflections coming from the sides in this region, as opposed to the cases in the anechoic chamber and in the corridor. Since the data is almost uncorrelated and the correlation coefficient does not change much for points spaced 6 cm or 12 cm apart, and

in order to maintain a large number of sample points, we decided to keep all the 121 data points for this regions as well.

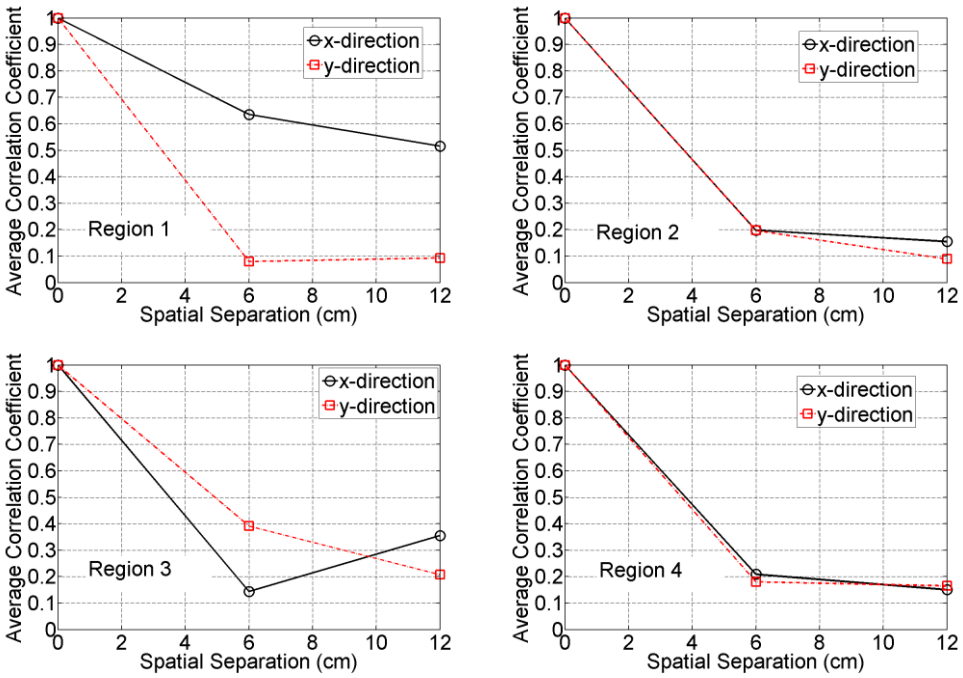

Figure 9.4: Correlation coefficient for corridor experiment.

Figure 9.5 shows the histogram of the measured electric field strength in the regions in Figure 9.2. They also show the Ricean, Normal, Nakagami, and Weibull best fits obtained with the MLE method and all the 121 uncorrelated data points for each region. By visual inspection, all the four distributions seem to be good statistical models for the measured data, and we cannot tell which one is the best. The Anderson-Darling goodness-of-fit test provides an objective assessment of whether or not a data set follows a specific distribution. This test is also used in chapter 6 and 8, and is described in more detail in chapter 2.

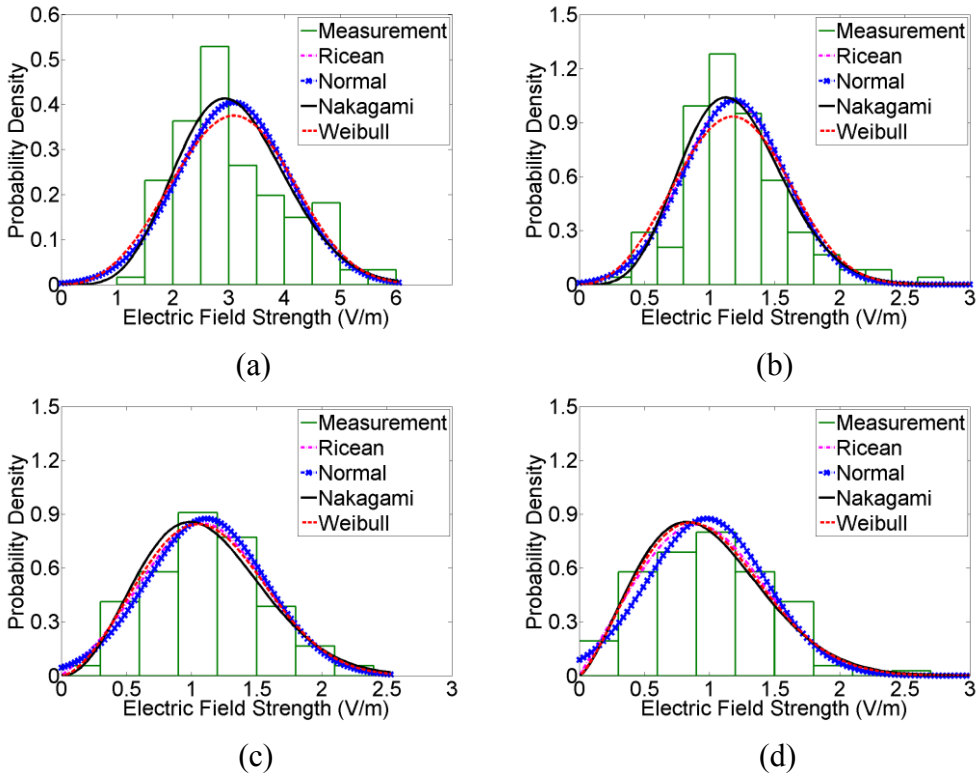

Figure 9.5: Histograms with best-fit distributions obtained with MLE method and all the 121 uncorrelated data points. (a) region 1. (b) region 2. (c) region 3. (d) region 4.

In summary, the Anderson-Darling test measures the distance between the CDF of the measured data and the CDF of the hypothesized distribution. Therefore, the hypothesized distribution that results in the smallest Anderson-Darling test statistic is the one that provides the best fit to the data. We fail to reject the null hypothesis, that the data can be represented by the hypothesized distribution, if the Anderson-Darling test statistic falls below the 5% significance level.

Figure 9.6 compares the Anderson-Darling test statistic for the four distributions, for each of the four regions, and shows that it falls below the 5% significance level in all cases regardless of the distribution. This result means that the fast fading in the real indoor

scenario considered in this chapter, a laboratory room, can be equivalently described by these four statistical models, each based on one of the four distributions, since no statistical difference was obtained. However, we clearly see that the Nakagami distribution provides the best fit to the measured sample data in regions 1 and 2 of this particular experiment.

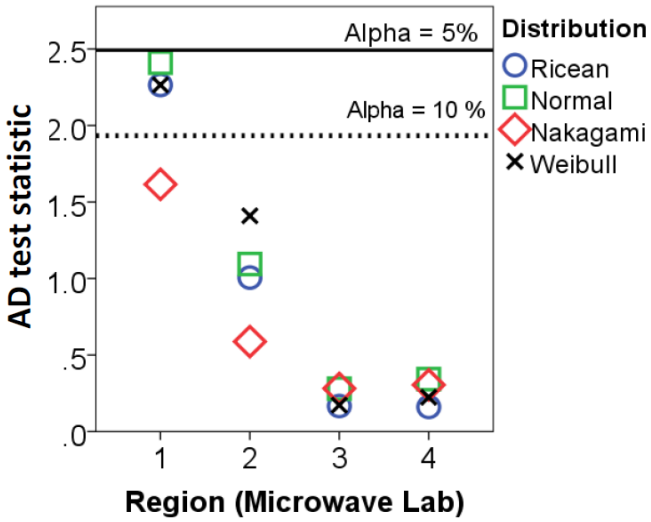

Figure 9.6: Anderson-Darling test for the corridor experiment.

9.1.2 Ricean Model Obtained by Geometrical Optics

In this section, we compare the measured electric field strengths to those predicted by GO simulation. We also compare the MLE, MM, and Proposed-GO methods of estimation of the Ricean parameters when only 36 or 9 evenly-spaced data points across a 65 by 65 cm region are considered. The threshold value used in the GO simulations for this scenario was 20 dB, and rays with up to 16 reflections were taken into account. Figure 9.7

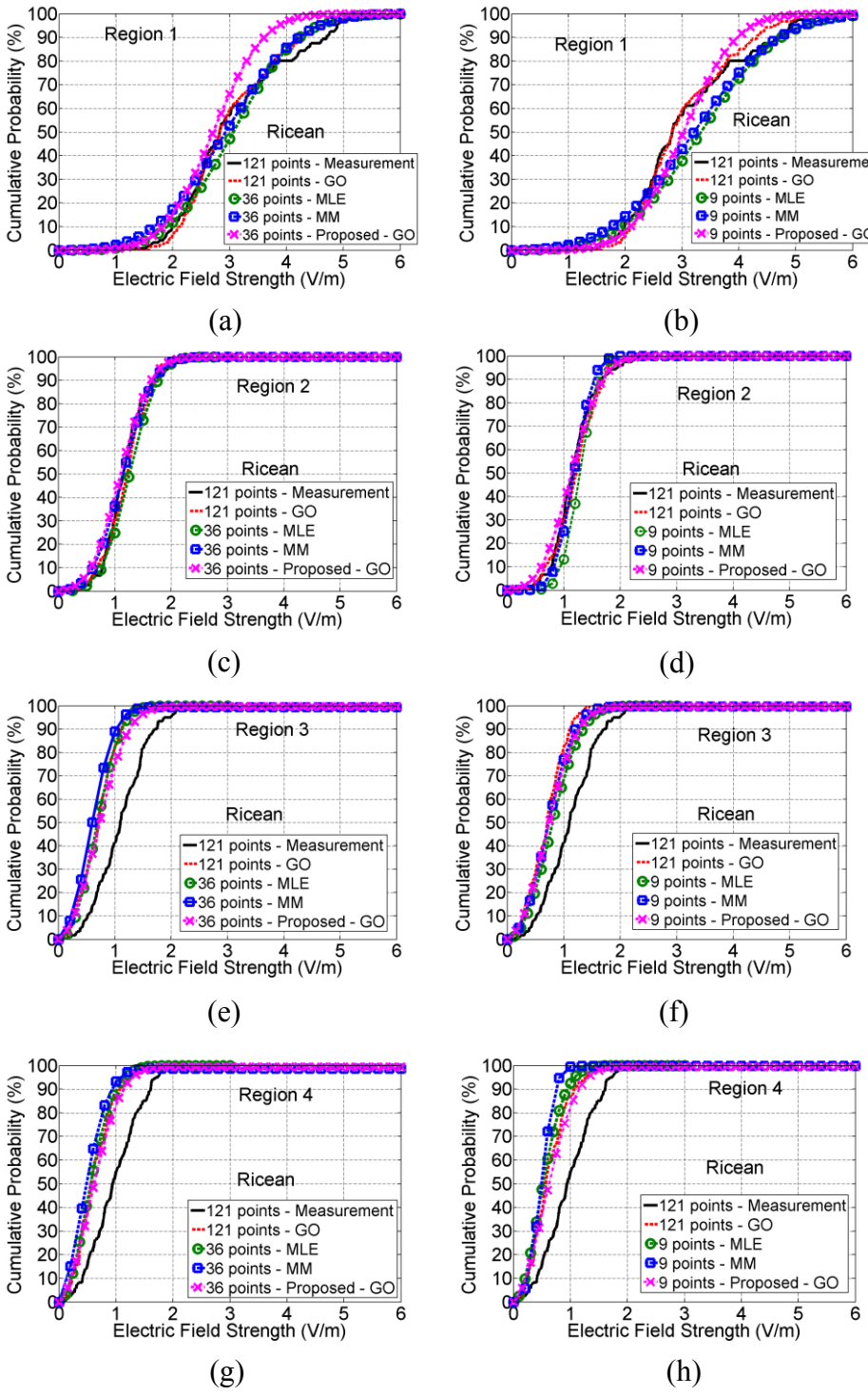

Figure 9.7: Comparison of CDFs obtained with 36 and 9 data points for the four regions in Figure 9.2.

compares the measured and simulated CDFs, as well as the CDFs obtained by estimating the Ricean parameters with 36 and 9 data points using the MLE, MM, and proposed-GO methods. The proposed-GO estimation method is described in section 7.1. As we can see, the statistics of the fast fading obtained with measurement and simulation differ just slightly for regions 1 and 2. There is a less than 10% difference at the upper tail of the distributions of region 1, and almost no difference for region 2. The MLE and MM methods are successful in reproducing the statistics of the simulated fast fading in region 1 when at least 36 points are considered, whereas the proposed-GO method fails. The contribution of the multipath component was underestimated and in turn caused the corresponding CDF to have a greater slope. In comparison to the results of the experiments in the anechoic chamber and corridor, this disagreement means that the contribution of the multipath to the field in the region closest to the transmitter is greater for the laboratory environment than for the corridor and the controlled scenario built in the anechoic chamber.

As for region 2, the three estimation methods are very similar in performance, which can also be seen by comparing the Ricean parameters in Tables 9.1 and 9.2. Despite the huge reduction in sample size, all three methods provide similar Ricean parameters with 36 data points. We can see that the Ricean parameters estimated with 36 data points agree very well with those obtained by measurements, as opposed to what happens with 9 data points. This suggests that for regions 1 and 2, relatively close to the transmitter, the separation between sample points should be around one wavelength. This conclusion is in

agreement to those reached in the controlled environment and in the long corridor experiments.

Table 9.1: Ricean parameters estimated by measurement.

Ricean parameters estimated from measurement and MLE method		
	Sample size = 121	
Region	K	Omega
1	4.06	10.49
2	3.80	1.57
3	1.89	1.45
4	1.04	1.16

Table 9.2: Comparison of Ricean parameters for the H853 room experiment. Regions 1 and 2. The parameters are estimated from GO-simulated data.

Region 1 (Microwave Lab)

	MLE		MM		Proposed method	
Sample size	K	Ω	K	Ω	K	Ω
121	5.916	9.935	4.894	9.935	8.135	8.572
36	4.936	10.244	3.821	10.244	7.199	8.266
9	3.885	12.359	3.308	12.359	8.102	10.172

Region 2 (Microwave Lab)

	MLE		MM		Proposed method	
Sample size	K	Ω	K	Ω	K	Ω
121	3.884	1.621	3.846	1.621	3.138	1.572
36	4.525	1.748	3.424	1.748	3.077	1.568
9	11.77	1.719	9.965	1.719	3.198	1.664

Table 9.3: Comparison of Ricean parameters for the H853 room experiment. Regions 3 and 4.

Region 3 (Microwave Lab)

	MLE		MM		Proposed method	
Sample size	K	Ω	K	Ω	K	Ω
121	1.352	0.587	1.660	0.587	1.110	0.826
36	1.395	0.595	1.510	0.595	1.110	0.824
9	1.079	0.829	1.800	0.829	1.170	0.837

Region 4 (Microwave Lab)

	MLE		MM		Proposed method	
Sample size	K	Ω	K	Ω	K	Ω
121	0.270	0.486	0.365	0.486	0.604	0.640
36	0.001	0.442	0.577	0.442	0.605	0.637
9	0.001	0.386	3.644	0.386	0.602	0.658

As for region 3 and 4, we see in Figure 9.7 that GO simulation fails to predict the statistics of the fast fading. Just as the results for regions 6, 7, and 8 of the corridor experiment, the GO results are underestimated. In other words, the mean values of field strength are constantly being underestimated by the GO model. The reason for this becomes much clearer in this experiment because we can see the amount of clutter in the laboratory room, which is not modeled in the simulation, Figures 9.1 and 9.3. This means that the vertical wooden partitions on top of the workbenches do not represent the clutter well. The surfaces of the workbenches in Figure 9.2 are well below the level of the antennas. Ray paths that join the transmitter to the receiver would be complicated, using reflection from the workbench to the side wall of the room and then to the Rx. This is a

long path with two reflections. Therefore, we would not expect the surface of the workbenches to have much effect on the GO calculation. Another interesting point is that the clutter does not seem to be attenuating the field, which suggests that the clutter in this particular room is not made of lossy dielectric and lossy metal materials. The AC power strips, instrument cords, lab equipment and so forth are likely to be responsible for the observed difference between measurement and GO simulation in this case, by making multipath stronger in the considered regions.

It should be noted that even though GO simulation did not agree with measurements for regions 3 and 4, the estimation methods based on the simulated data did result in CDFs that represent the simulated data.

The conclusion is that the main reflective surfaces included in the GO model seem to have been well modeled because agreement between measurement and GO simulation was obtained for regions 1 and 2. Since there are no major reflective structures close to regions 3 and 4, we must conclude that the obtained disagreement between measurement and GO simulation is caused by clutter. Therefore, for this particular scenario with a lot of clutter, GO is not enough to accurately predict the statistics of the fast fading. Interestingly enough, Austin *et al.* in [42] could not accurately predict the slow fading of the field in the presence of clutter even with a much more sophisticated simulation tool based on 3D FDTD, given the random nature of clutter. However, Trueman *et al.* in [46] obtained good agreement between measured and GO-simulated slow fading (RMSE of 0.9 dB and max error difference of 2.1 dB at a single point) for a very similar experiment

to the one presented in this chapter, but with field strengths taken along a straight line path instead of over areas. The reason for the slightly better agreement between measurement and simulation obtained in [46] when compared to the results presented in the next section, is that the authors used the local-area-average field strength to predict the slow fading. Since they took measurements along a line, they used a 70-cm window to compute the local-area-average field. It should be noted that the local-area-average field strength is computed by averaging the local field strength on a power basis, and in this case along a straight path. As shown in the next section, the local-area-average field strength leads to larger values than the simple linear average, and tends to provide better agreement to measured data.

In the next section, we consider the slow fading of the field and how it is affected by clutter.

9.1.3 Slow Fading and Path Loss Model

As described in Chapter 8, the electric field strength associated with the path loss model is given by [16]

$$E(r) = \frac{E_0}{r^{n/2}} \tag{9.1}$$

where $E_0 = \sqrt{\eta_0 D P_t/(4\pi)}$ is the field strength at 1 m from the transmitter.

In our experiment, the mean electric field of each region is used to analyze the behavior of the slow fading and to derive the path loss exponent by using the least-square method.

Figure 9.8 shows the electric field as a function of distance from the transmitter and the center of the regions.

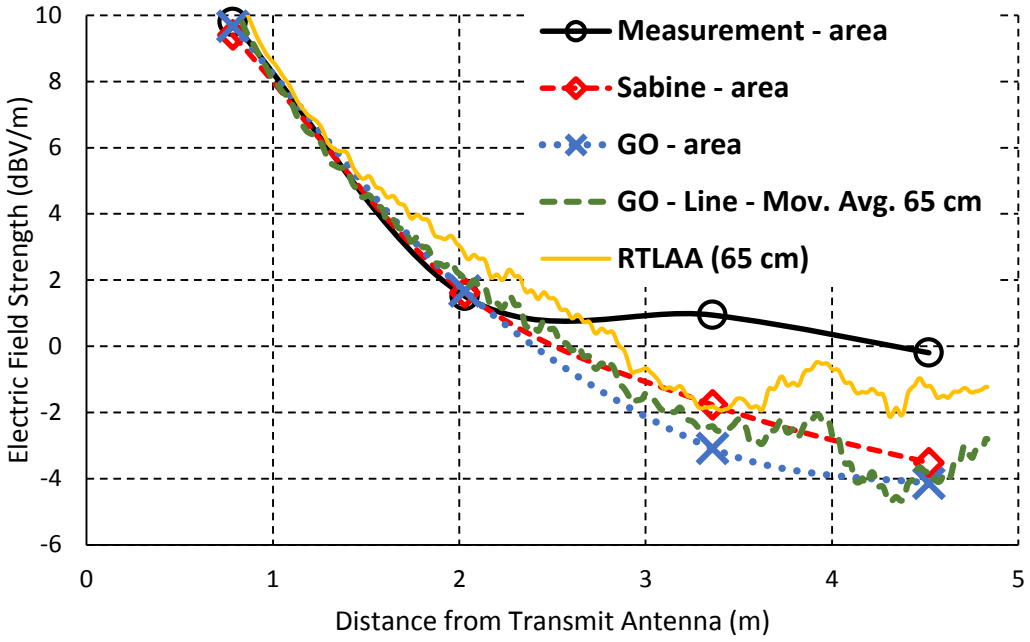

Figure 9.8: Mean electric field strength as a function of distance from the transmitter. The first three curves are based on measurement and simulation over an area, the fourth one on the linear moving average obtained from GO simulation along a straight line path crossing the center of each region at steps of 1 cm, and the last one on the ray-tracing local area average (RTLAA) described in *[46]* .

As we can see, the results are similar to those of the corridor experiment. GO simulation was used to predict the field strength along a straight line path that passes by the center of each region at steps of 1 cm. A 65-cm window was used to obtain the slow fading along the path, and the result agrees with those obtained by GO and Sabine simulations based on data points across an area. The slow fading obtained by GO differs by about 4 dB from that obtained by measurement in regions 3 and 4. Notice that the ray-tracing local area average (RTLAA) described in [46] results in higher values of mean field than the

linear moving average, and in this case provided an improved agreement to measured data. The path loss exponent obtained by measurement, GO simulation, and Sabine method is shown in Table 9.4. The GO-based loss pass exponent agrees well with the Sabine method estimate. However, both estimates are underestimates the measured data. As expected, GO and RTLAA provided the closest estimate of the measured path loss exponent.

Table 9.4: Path loss exponent. Area measurements.

Method	Measurement (area)	GO Simulation (area)	Sabine Method (area)	GO simulation (along a path – moving average) Least-square method)	GO simulation (along a path – RTLAA) Least-square method)
Path loss exponent	1.31	1.88	1.71	1.83	1.56

Neither the GO nor the Sabine simulation predicted the slow fading accurately in this indoor environment with lots of clutter. This was expected for the GO simulation based on the measured mean field strength observed in the measured CDFs for regions 3 and 4, shown in Figure 9.7. Perhaps, if a more detailed model of the laboratory room, which included more clutter, were used with the Sabine method, we would get a better estimation of the mean electric field strengths in each region. However, the random nature of clutter shows the limitations of deterministic models. The clutter would have to be treated statistically and then added to the deterministic model. Despite the

disagreement in the path loss exponent obtained by these three methods, the common feature present in all of the predictions is that the slow fading decreases more slowly than it would in free space. This is expected for indoor propagation environments because of the contribution of the multipath field.

9.2 Conclusion

Just as for the experiments discussed in Chapters 5, 6, 7, and 8 the statistics of the fast fading can be modeled by any of the following four distributions: Ricean, Normal, Nakagami, and Weibull. However, for the measured samples of the experiment in the laboratory room, the Nakagami distribution clearly resulted in the best fit to the measured data for the two regions closest to the transmitter, despite the fact that the other statistical models based on the Ricean, Normal, and Weibull were found to be not significantly different from the measured data. Besides, all the four distributions provided very good fits the regions farther than 3 m from the transmitter. Focus was again given to the Ricean distribution because of its simplicity and physical interpretation. The new and simpler proposed method for estimating the Ricean parameters was shown to be as good as the MLE and MM methods when at least 36 data points evenly spaced across a 65 by 65 cm region were considered for regions 2, 3, and 4. However, the new method did not provide a good Ricean model for the closest region to the transmitter, as it had done for the experiments in the anechoic chamber and in the long corridor. Just as in the long corridor case, we recommend the use of at least 36 data points in order to reliably estimate the

Ricean parameters in a rectangular indoor environment. The use of only 9 points were shown to be inadequate for this purpose.

We also conclude that point-by-point agreement between measurement and GO simulation is very hard to attain, but that GO can still provide a good and useful prediction of the statistics of the fast fading for scenarios with some clutter, but is not sufficient in the presence of lots of clutter such as lab equipment.

As for the slow fading and path loss exponent, we conclude that the Sabine method with the exponential correction does not provide an accurate prediction of the slow fading in the presence of clutter, despite having produced results similar to those obtained with GO simulation and being a very efficient and fast method for predicting the mean electric field strength in indoor environments, as demonstrated in the experiment in the long corridor. The measured, GO-estimated, and Sabine-estimated loss exponents did not agree in this case, but all of them captured to a certain extent the effects of the multipath field.

Finally, in the presence of clutter, a more detailed model of the environment is required to successfully predict the important statistics of the electric field strength distribution with a deterministic model. Regions containing clutter could be modeled with FDTD, and this solution could be added to that of the entire room obtained with GO.

Chapter 10: Conclusion

The purpose of this thesis was to study the spatial variation of the electric field strength in indoor environments by means of measurements, computer simulated propagation models, and statistical analysis. It was hypothesized that the development of statistical models for an accurate characterization of the fast fading would be an important step towards the solution of the problem of EMI in critical-care medical equipment caused by wireless communication systems. In this chapter, we summarize our approaches and the main results presented in this thesis, and then we make recommendations for future work.

10.1 Summary of the Work

In the modeling of electrically large electromagnetics problems, the computational cost of full-wave solvers makes them impractical for most cases, and thus high-frequency techniques such as GO and UTD are preferred. Our simulated models were based on GO and Sabine method. Even though GO is much faster and practical for indoor propagation applications than FDTD and MoM, it does not account for diffraction, and can still require extensive computer resources and computation time depending on the complexity of the model, the number of reflections considered, and number of points where the field is computed. Statistical probability distributions are also often used to characterize the field variation. Thus, accurate statistical models based on known probability distributions and on a modest number of field strength values computed with GO over a sparse grid of points become attractive for indoor propagation applications. With that in mind, the

objectives of this thesis were to validate the GO models, both of a controlled environment and of two real indoor scenarios at 2.45 GHz against measurement, and compare the results point-by-point and in terms of their statistics. We found that point-by-point agreement is hard to attain, especially in real environments, but that the GO calculations match the statistics of the measured field for most cases. Furthermore, we wanted to find the best probability distribution to represent the electric field strength variation, and we found that the Ricean, Normal, Nakagami, and Weilbull are equally good to represent the measured data for most of the cases considered in this work. Then, we studied the effect of the number of points over a horizontal grid on the estimation of the parameters of the Ricean probability distribution, and showed that data points spaced by about 1 wavelength (36 points for the 65x65 cm region at 2.45 GHz) resulted in accurate and reliable estimates of the Ricean parameters, and that as few as 9 points could be satisfactory. Finally, we studied the slow fading of the field in two real indoor environments in terms of measurement, GO simulation, and Sabine method. We found reasonable agreement between the methods, except in the presence of clutter such as lab equipment.

We studied radio-wave propagation in indoor environments and rapid variation of the electric field strength at 2.45 GHz over a dense grid of points in a 65 by 65 cm region, as well as at points separated by 1 cm along a 20-m long straight line path. We chose to base our modeling of the fast fading on GO simulations. Point-by-point agreement was difficult to get even for the experiment conducted in the controlled environment which was built inside a shielded anechoic chamber. Still, we observed very good correlation

between GO simulation and measurement, given that the model predicted accurately the position of the maxima and minima. As for the statistics of the field, a much better agreement than that of point-by-point was obtained for all the cases, whether in the controlled environment or in the real indoor scenarios.

This thesis presents a comparative study of the ability of the four statistical distributions, namely the Ricean, Normal, Nakagami, and Weibull distributions, to represent the measured data. These distributions are commonly used to model the fast fading of the field strength in indoor environments. We have found that all the four distributions can represent the data well. This comparison was based on a large number of measured data points for the controlled multipath scenario and the two real indoor environments, a long corridor and a conventional laboratory room. The Anderson-Darling goodness-of-fit test was used as an objective tool for comparing the fit of different statistical distributions to the measured data. Our results showed that the Ricean, Normal, Nakagami, and Weibull distributions are equally good to represent the measured data for 100% of the cases considered in this work, since statistical difference was not observed. However, it should be noted that for real indoor environments the Normal distribution consistently provided the worst fit to the data, whereas the Nakagami distribution resulted in the best fit for the regions close to the transmitter in the experiment conducted in the laboratory room, which has a rectangular geometry. The Ricean distribution provided a very good fit to the measured data for 100% of the cases. Given its simplicity and physical interpretation, it was chosen to be further investigated and combined with GO simulations to model the fast fading from a reduced number of data points.

We presented a method for measuring the dielectric constant of construction materials, which was successfully applied to gyproc slabs and a wooden door. The method is based on GO and on electric field strength measurements taken along a straight line path parallel to the surface of the material under test. We found the dielectric constant of a gyproc slab and of a wooden door to be 2.25 and 2.7, respectively. These values were then used in the validation of the GO model of a three-layer wall and in the model of a controlled multipath environment. Agreement between measurements and GO simulation was obtained in both cases.

Metal studs placed in between two gyproc slabs were demonstrated to significantly affect the electric field strength distribution in the vicinity of the structure, to an extent where a GO model is no longer sufficient to provide reliable and accurate predictions neither of the field strength at a point nor of the field statistics. Comparison between measurement and GO simulation suggests that reflected and diffracted rays, created at the edges of each metal stud, would have to be incorporated in the model. This hypothesis could be verified in a future work.

We also described a new simple method to estimate the Ricean parameters from a sample containing 36 data points evenly-spaced across a 65 by 65 cm horizontal region, and then compared its performance to those of the MLE and MM methods. The data points were based on GO simulations. For the experiments conducted inside the shielded anechoic chamber, the new estimation method was proven to have comparable performance to MLE and MM methods for 36 data points and to be superior when only 9 data points

were considered. For the experiments in the real indoor environments, 36 data points or more are recommended to obtain an accurate estimation of the Ricean parameters, regardless of the estimation method chosen. For most cases the new method provided estimations of the measured CDF that were similar to those obtained by the MLE and MM methods, except for the region closest to the transmitter in the experiment conducted in the laboratory room. In general, for situations where GO simulation provides accurate predictions of the mean electric field strength in a 65 by 65 cm region, this new simple estimation method can be applied to obtain a statistical model of the fast fading.

The modeling of the slow fading in the 20-m long corridor was based on both GO simulation and Sabine method, and was satisfactorily predicted by both of them, except towards the end of the corridor where the field level was too low and more susceptible to being affected by structures not taken into account in the model. The Sabine method performed slightly better at this region than the GO model. The path loss exponents predicted by measurements over an area and along a straight line path differ by 17%. It should be noted that the exponential correction was used in the Sabine method. As for the slow fading in the rectangular laboratory room, the agreement between area measurement, and computer simulations was not as good as that for the corridor experiment for the regions farthest from the transmitter. This is due to the abundant presence of clutter such as lab equipment in the room. Clutter cannot be modeled very well in practice by any deterministic model, therefore a statistical model of the clutter itself should be added to the deterministic model. FDTD could be used to model clutter in more detail, but the model would be tedious to construct and require long execution

times. Despite the discrepancies between measurement and computer simulation, an excellent agreement between GO simulation and Sabine method was obtained, which once again showed the power of the Sabine method.

With the discussion on the results of the experiments conducted in the shielded anechoic chamber, in the long corridor, and in the laboratory room, we conclude our study on indoor propagation, more precisely on the rapid spatial variation of the electric field in indoor environments. The next section includes some recommendations for future work.

10.2 Recommendations and Future Work

We will now examine the limitations of our research, which leads to recommendations for future work.

In Chapter 3, we presented an automated measurement system that samples electric field strength at a single frequency only, 2.45 GHz. This allowed us to measure the field strength in the steady state. If the RF detector could be replaced by a portable spectrum analyzer which can be made to communicate with the master board of the measurement system, a frequency sweep type of measurement could be taken, and information on the impulse response of a channel, the power profile, and the rms delay spread could be obtained. For broadband type of measurements, both the transmit and receive antennas would have to have superior bandwidth than those used for narrowband experiments or experiments at a single frequency. Frequency-domain type of experiment would be a natural extension of the present work.

In Chapter 4, we described a method based on GO and on the automated measurement system for measuring the dielectric constant of wall constructions. The method was applied to gyproc slabs of different thicknesses and to a wooden door, and was proven to provide accurate results. For a future work, this method could be further explored and applied to different types of wall constructions such as brick walls, concrete walls, and layered walls. The method could also be used to estimate an average dielectric constant, and thus reflection coefficient, of walls with unknown internal structures. The average dielectric constant would take into account the effects of all the interaction mechanisms of the incident wave with the wall and its internal structures.

In Chapter 5, we described an experiment conducted in a controlled multipath environment which was built inside a shielded anechoic chamber. For the scenarios considered, the effect of diffraction was observed to be negligible, especially in the prediction of the statistics of the field, despite the fact that a NLOS region was considered. However, we saw that reflected and diffracted rays from the metal studs do considerably affect not only the electric field strength prediction at a point nearby the wall, but also the prediction of the field statistics. A future work that would successfully incorporate the model of the metal studs into the existing GO code, would lead to a significant contribution to the field of indoor propagation.

In Chapter 7, we presented a Ricean parameter estimation method based on 36 data points evenly spaced over a 65 by 65 cm area. The Ricean models are then used to represent the electric field variation in the corresponding area. This easy and

computationally inexpensive method could be applied to the estimation of risk of exceeding immunity of critical-care medical equipment in several regions of a hospital floor plan.

In Chapter 8, we observed that for a NLOS region relatively close to the transmitter, the GO model successfully predicted the statistics of the field, despite the fact that diffracted rays from the wall corner had been expected to play a major role. However, GO alone did not predict the statistics of the field for a NLOS region about 10 m away from the transmitter. In this case, it was expected because the contribution of the diffracted rays from the wall corner was comparable or stronger than that of the reflected rays that underwent multiple reflections before reaching that area. The incorporation of diffraction into the existing GO model, in a way that the user could select the edges to be considered in the computation, would result in improved agreement between measurement and computer simulation, without increasing the execution time substantially.

In Chapter 9, we saw the effect of clutter in the prediction of both the fast fading and slow fading. Given the random nature of clutter, it is very difficult to model clutter with deterministic models only. A detailed model could be made with FDTD, but the execution time would be very long. If a field level factor which represents the effect of clutter in a room could be estimated statistically and then added to the deterministic model, a better agreement between measurement and computer simulation would be obtained for indoor environments such as the rectangular room described in Chapter 9.

Based on these suggestions, we can see that improvement in the modeling of radio wave propagation is of great importance for the field of indoor propagation. Since a measurement campaign would be expensive and time-consuming, a computer model based on GO would make the study of the risk of exceeding immunity feasible, which would be a substantial benefit.

10.3 Conclusion

We have studied radio-wave propagation in indoor environments at 2.45 GHz. Our focus has been on the spatial distribution of the electric field strength in a 65 by 65 cm region and along a straight line path. We have characterized the fast fading of the field with a Ricean distribution whose parameters were efficiently found by GO simulation at a modest number of points across a region. The results were validated against measurements in controlled and real indoor environments.

References

[1] K.-S. Tan, I. Hinberg and J. Wadhwani, "Electromagnetic interference in medical devices: health Canada's past and current perspectives and activities," in *Proc. IEEE Int. Symp. on Electromagn. Compat*, Montreal, QC, Canada, Aug. 2001, pp. 1283-1288, vol.2.

[2] C. K. Tang, L. C. F. K. H. Chan and S. W. Leung, "Electromagnetic interference immunity testing of medical equipment to second- and third-generation mobile phones," *IEEE Trans. Electromagn. Compat,* vol. 51, no. 3, pp. 659-664, Aug. 2009.

[3] M. F. Chimeno and F. Silva, "Mobile phones electromagnetic interference in medical environments: a review," in *Proc. IEEE Int. Symp. on Electromagn. Compat.*, Fort Lauderdale, FL, USA, July 25-30, 2010, pp. 311-316.

[4] G. Calcagnini, P. Bartolini, M. Floris, M. Triventi, P. Cianfanelli, G. Scavino, L. Proietti and V. Barbaro, "Electromagnetic interference to infusion pumps from GSM mobile phones," in *Proc. IEEE IEMBS 26th Annu. Int. Conf. Engineering in Medicine and Biology Society*, Sep. 1-5, 2004, pp. 3515-3518.

[5] "International electrotechnical commission: medical electrical equipment - Part 1-2: General requirements for safety - Collateral standard: Electromagnetic compatibility - Requirements and test.," 1999.

[6] "ANSI: American national standard recommended practice for an on-site, ad hoc test method for estimating radiated electromagnetic immunity of medical devices to specific radio-frequency transmitters," 1997.

[7] D. Davis, Indoor radio-wave behavior at 850 and 1900 MHz with electromagnetic compatibility application in hospitals: an experimental, theoretical, statistical and morphological characterization, Montreal, Quebec: PhD Thesis, McGill University, 2003.

[8] D. Davis, B. Segal and T. Pavlasek, "Can minimal-separation criteria ensure electromagnetic compatibility in hospitals?," *Biomed. Instrum. Technol.,* vol. 33, no. 5, pp. 411-416, Sep-Oct 1999.

[9] D. Davis, B. Segal, A. Cinquino, K. Hoege, R. Mastrocola and T. Pavlasek, "Electromagnetic compatibility in hospital corridors," in *Proc. IEEE Int. Symp. Electromagn. Compat.* , Seatle, WA, USA, pp. 268-272, Aug. 2-6, 1999.

[10] K.-S. Tan and I. Hinberg, "Radiofrequency susceptibility tests on medical equipment," in *Proc. IEEE IEMBS 16th Annu. Int. Conf. Engineering in Medicine and Biology Society*, Baltimore, MD, USA, Nov. 3-6, 1994.

[11] J. B. Andersen, T. S. Rappaport and S. Yoshida, "Propagation measurements and models for wireless communications channels," *IEEE Commun. Mag.,* vol. 33, no. 1, pp. 42-49, January 1995.

[12] H. Hashemi, "The indoor radio propagation channel," *Proc. of IEEE,* vol. 81, no. 7, pp. 943-968, July July 1993.

[13] A. A. M. Saleh and R. A. Valenzuela, "A statistical model for indoor multipath propagation," *IEEE Journal on Selected Areas in Communications,* vol. 5, no. 2, pp. 128-137, February 1987.

[14] T. Sarkar, Z. Ji, K. Kim, A. Medouri and M. Salazar-Palma, "A survey of various propagation models for mobile communication," *IEEE Antennas and Propagation Magazine,* vol. 45, no. 3, pp. 51-82, June 2003.

[15] W. K. Tam and V. N. Tran, "Propagation modelling for indoor wireless communication," *Electronics & Communication Engineering Journal,* vol. 7, no. 5,

pp. 221-228, October 1995.

[16] C. W. Trueman, D. Davis and B. Segal, "Relationship between the path loss exponent and the room absorption for line-of-sight communications.," *Journal of Applied Computational Electromagnetics Society (ACES),* vol. 24, no. 4, pp. 361-367, Aug. 2009.

[17] T. S. Rappaport, Wireless Communications: Principles & Practice, Upper Saddle River, NJ: Prentice Hall PTR, 1996.

[18] F. Dagefu and K. Sarabandi, "Analysis and modeling of near-ground wave propagation in the presence of building walls," *IEEE Transactions on Antennas and Propagation,* vol. 59, no. 6, pp. 2368 - 2378, June 2011.

[19] C. A. Balanis, Advanced Engineering Electromagnetics, Wiley, 1989.

[20] R. P. Torres, S. Loredo, L. Valle and M. Domingo, "An accurate and efficient method based on ray-tracing for the prediction of local flat-fading statistics in picocell radio channel," *IEEE Journal on Selected Areas in Communications,* vol. 19, no. 2, pp. 170-178, Feb. 2001.

[21] F. Saez de Adana, O. G. Blanco, I. G. Diego, J. P. Arriaga and M. F. Catedra, "Propagation model based on ray tracing for the design of personal communication systems in indoor environments," *IEEE Transactions on Vehicular Technology,* vol. 49, no. 6, pp. 2105-2112, Nov. 2000.

[22] V. Degli-Esposti, G. Lombardi, C. Passerini and G. Riva, "Wide-band measurement and ray-tracing simulation of the 1900-MHz indoor propagation channel: comparison criteria and results," *IEEE Transactions on Antennas and Propagation,* vol. 49, no. 7, pp. 1101 - 1110, July 2001.

[23] G. E. Athanasiadou and A. R. Nix, "A novel 3-D indoor ray-tracing propagation model: the path generator and evaluation of narrow-band and wide-band predictions," *IEEE Transactions on Vehicular Technology,* vol. 49, no. 4, pp. 1152-1168, Jul. 2000.

[24] S. Loredo, L. Valle and R. P. Torres, "Accuracy analysis of GO/UTD radio-channel modeling in indoor scenarios at 1.8 and 2.5 GHz," *IEEE Antennas and Propagation Magazine,* vol. 43, no. 5, pp. 37-51, Oct. 2001.

[25] Y. Chang-Fa, W. Boau-Cheng and K. Chuen-Jyi, "A ray-tracing method for modeling indoor wave propagation and penetration," *IEEE Transactions on*

Antennas and Propagation, vol. 46, no. 1998, pp. 907-919, June 1998.

[26] W. L. Stutzman and G. A. Thiele, Antenna Theory and Design, Hoboken, NJ: John Wiley & Sons, Inc., 2012.

[27] C. W. Trueman, "Three-dimensional Geometrical optics code for indoor propagation," *J. Appl. Comput. Electromagn. Soc.,* vol. 17, no. 2, pp. 134-144, July 2002.

[28] T. F. C. Leao and C. W. Trueman, "Small-scale fading determination with a ray-tracing model, and statistics of the field," in *Proc. IEEE AP-S Int. Symp. Antennas Propag.*, Chicago, IL, USA, Jul. 8-14, 2012.

[29] T. F. C. Leao, V. M. Chopin and C. W. Trueman, "Statistics of the electric field strength in a controlled multipath environment," in *Proc. IEEE AP-S Int. Symp. Antennas Propag.*, Orlando, FL, USA, July 7-13, 2013.

[30] T. F. C. Leao and C. W. Trueman, "Ray-tracing prediction of the fast fading in an indoor environment and validation by measurement," in *Proc. IEEE CCECE*, Montreal, QC, Canada, Apr. 29-May 2, 2012.

[31] M. Ardavan, C. W. Trueman and K. Schmitt, "A sabine-rice approximation for the risk of exceeding immunity," *in Proc. IEEE AP-S Int. Symp. Antennas Propag.,* July 3-8, 2011.

[32] J. H. Richmond, "Efficient recursive solution for plane and cylindrical multilayers," Ohio State University Electro Science Lab, Tech. Rep. 1968-1, Aug. 1965, prepared for Bureau of Naval Weapons (AD 624191), Contract 65-0329-d.

[33] E. H. Newman, "Plane multilayer reflection code," Ohio State University Electroscience Lab, Tech. Rep. 712978-1, Jul. 1980, prepared for Lockheed Missiles and Space Co. Inc., Sunnyvale, Va, Subcontract dB50C6160F.

[34] T. F. C. Leao, V. M. Chopin and C. W. Trueman, "Electromagnetic characterization of a gyproc slab by measurement and 3D geometrical optics simulation," *IEEE Antennas and Wireless Propagation Letters,* vol. 12, pp. 1570-1573, Dec. 2012.

[35] D. Davis, B. Segal and C. W. Trueman, "Ray optical simulation for indoor corridor propagation at 850 MHz and 1900 MHz," in *Proc IEEE AP-S Antennas Propag. Wireless Commun. Conf.*, Waltham, MA,USA, pp. 81-86, Nov. 6-8, 2000.

[36] J. Zhao, R. Paknys and C. Trueman, "Efficient reflection and transmission dyad multiplication for 3D geometrical optics," *IEEE Transactions on Vehicular Technology ,* vol. 52, no. 5, pp. 1412 - 1414 , Sep 2003.

[37] C. W. Trueman, R. Paknys, J. Zhao, D. Davis and B. Segal, "Ray tracing algorithm for indoor propagation," in *Proc. Annual Review of Progress in Applied Computational Electromagnetics*, Monterey, California, USA, pp. 493-500, March 2000.

[38] W. Honcharenko and H. L. Bertoni, "Transmission and reflection characteristics at concrete block walls in the UHF bands proposal for future PCs," *IEEE Transactions on Antennas and Propagation,* vol. 42, no. 2, pp. 232-239, February 1994.

[39] C. L. Holloway and P. L. Perini, "Analysis of composite walls and their effects on short-path propagation modeling," *IEEE Transactions on Vehicular Technology,* vol. 46, no. 3, pp. 730-738, August 1997.

[40] Z. Ji, T. K. Sarkar and B. H. Li, "Analysis of the effects of walls on indoor wave propagation using the FDTD method," *Microwave and Opitical Technology Letters,* vol. 29, no. 1, pp. 19-21, 2001.

[41] A. C. M. Austin, M. J. Neve, G. B. Rowe and R. J. Pirkl, "Modeling the effect of nearby buildings on inter-floor radio-wave propagation," *IEEE Transactions on Antennas and Propagation,* vol. 57, no. 7, pp. 2155-2161, July 2009.

[42] A. C. M. Austin, M. J. Neve and G. B. Rowe, "Modeling propagation in multifloor buildings using the FDTD method," *IEEE Transactions on Antennas and Propagation,* vol. 59, no. 11, pp. 4239-4246, November 2011.

[43] W. Ying, S. Safavi-Naeini and S. K. Chaudhuri, "A hybrid technique based on combining ray tracing and FDTD methods for site-specific modeling of indoor radio wave propagation," *IEEE Transactions on Antennas and Propagation,* vol. 48, no. 5, pp. 743-754, May 2000.

[44] Z. Sandor, L. Nagy, Z. Szabo and T. Csaba, "3D ray launching and moment method for indoor propagation purposes," in *Proc. IEEE 8th Int. Symp. Personal, Indoor and Mobile Radio Commun.*, Helsinki, Finland, Sep. 1-4, 1997.

[45] A. Parsa, Electromagnetic analysis of a finite reinforced concrete slab, Montreal, Quebec: PhD Thesis, Concordia University, 2008.

[46] C. W. Trueman, D. Davis, B. Segal and W. Muneer, "Validation of Fast Site-Specific Mean-Value Models for Indoor Propagation," *ACES Journal: Applied Computational Electromagnetics Society,* vol. 24, no. 3, pp. 312-323, June 2009.

[47] C. W. Trueman, S. S. Muhlen, D. Davis and B. Segal, "Field strength estimation in indoor propagation by the Sabine method," in *Proc. 24th Annual Review of Progress in Applied Computational Electromgnetics*, Niagara Falls, ON, Canada, 2008.

[48] L. E. Kinsler, A. R. Frey, A. B. Coppens and J. V. Sanders, Fundamentals of Acoustics, New York: Wiley, 2000.

[49] C. W. Trueman, FINDEMI User's Guide, version D1c, Dec. 2010.

[50] S. Guerin, Y. Guo and S. Barton, "Indoor propagation measurements at 5 GHz for HIPERLAN," in *Proc. IEEE 10th Int. Antennas Propag. Conf.*, Edinburgh, Scotland, pp. 306-310, April 14-17, 1997.

[51] R. Tingley and K. Pahlavan, "Space-time measurement of indoor radio propagation," *IEEE Transactions on Instrumentation and Measurement,* vol. 50, no. 1, pp. 22 - 31 , February 2001.

[52] K. Haneda, J.-i. Takada and K.-i. Takizawa, "Evaluation of signal quality improvement with rake reception using an ultrawideband indoor area propagation measurement," *IEEE Antennas and Wireless Propagation Letters,* vol. 7, pp. 337 - 340, October 2008.

[53] W. Muneer, Rician-K factor study for temporal and spatial variations, Montreal, Quebec: Master Thesis, Concordia University, 2007.

[54] A. Muqaibel, A. Safaai-Jazi, A. Bayram, A. Attiya and S. Riad, "Ultrawideband throught-the-wall propagation," *IEE Proc.-Microw. Antennas Propag.,* vol. 152, no. 6, pp. 581-588, December 2005.

[55] C. A. Grosvenor, R. T. Johnk, J. Barker-Jarvis, M. D. Janezic and R. B., "Time-domain free-field measurements of the relative permittivity of building materials," *IEEE Transactions on Instrumentation and Measurement,* vol. 58, no. 7, pp. 2275-2282, July 2009.

[56] C. Thajudeen, A. Hoorfar and F. Ahmad, "Measured complex permittivity of walls with different hydration levels and the effect on the power estimation of TWRI target returns," *Progress in Electromagnetic Research B,* vol. 30, pp. 177-199, May

2011.

[57] I. Cuinas and M. G. Sanchez, "Measuring, modeling, and characterization of indoor radio channel at 5.8 GHz," *IEEE Trans. Veh. Technol.,* vol. 50, no. 2, pp. 526-535, 2001.

[58] H. L. Bertoni, Radio propagation for modern wireless systems, NJ: Prentice Hall , 2000.

[59] M. D. Yacoub, "Fading distributions and co-channel interference in wireless systems," *IEEE Antennas and Propagation Magazine,* vol. 42, no. 1, pp. 150 - 160, 2000.

[60] N. A. Goodman and K. L. Melde, "The impact of antenna directivity on the small-scale fading in indoor propagation," *IEEE Transactions on antennas and propagation,* vol. 54, no. 12, pp. 3771-3777, 2006.

[61] A. Leon-Garcia, Probability, Statistics, and Random Processes for Electrical Engineering, Upper Saddle River, NJ: Pearson Prentice Hall, 2008.

[62] A. Abdi, C. Tepedelenlioglu, M. Kaveh and G. Giannakis, "On the estimation of the K parameter for the Rice fading distribution," *IEEE Communications Letters,* vol. 5, no. 3, pp. 92-94, March 2011.

[63] O. Thas, Comparing Distributions, New York, NY: Springer, 2010.

[64] T. W. Anderson and D. A. Darling, "Asymptotic theory of certain "goodness of fit" criteria based on stochastic processes," *The Annals of Mathematical Statistics,* vol. 23, no. 2, pp. 193-212, June 1952.

[65] M. A. Stephens, "Asymptotic results for goodness-of-fit statistics with unknown parameters," *The Annals of Statistics,* vol. 4, no. 2, pp. 357-369, Mar. 1976.

[66] M. A. Stephens, "EDF statistics for goodness of fit and some comparisons," *Journal of the American Statistical Association,* vol. 69, no. 347, pp. 730-737, Sep. 1974.

[67] "MathWorks, R2013b documentation: Anderson-Darling test.," February 2014. [Online]. Available: http://www.mathworks.com/help/stats/adtest.html#btrbl9w-1.

[68] V. Mooney-Chopin, J. Lemire and H. Saad, Concordia University, ELEC/COEN

490 report : Volumetric field strength measurement system, March 2012.

[69] "Linear Technology," 2013. [Online]. Available: http://cds.linear.com/docs/en/datasheet/5538f.pdf.

[70] "IBM SPSS Statistics for Windows, Version 20. Armonk, NY: IBM Corp.," [Online].

[71] "MathWorks, R2013b documentation: Maximum likelihood estimates," February 2014. [Online]. Available: http://www.mathworks.com/help/stats/mle.html.

[72] F. Babich and G. Lombardi, "Statistical analysis and characterization of the indoor propagation channel," *IEEE Transactions on Communications,* vol. 48, no. 3, pp. 455-464, March 2000.

[73] D. Porrat and D. C. Cox, "UHF propagation in indoor hallways," *IEEE Trans. Wireless Commun.,* vol. 3, no. 4, pp. 1188-1198, Jul. 2004.